



Università degli Studi di Cagliari

Facoltà di Scienze

Dipartimento di Fisica

Dottorato di Ricerca in Fisica

Settore Scientifico Disciplinare FIS/01

XXVII Ciclo

Light Conversion Processes in Lanthanide-based Molecular Materials

PhD Thesis of:
Flavia Artizzu



Supervisor: Prof. Francesco Quochi

Co-supervisor: Prof. Paola Deplano

Coordinator:

Prof. Paolo Ruggerone

A. A. 2013/2014

A mia madre

Light Conversion Processes in Lanthanide-based Molecular Materials

Abstract

This work is mainly focused on the investigation and processing of luminescent molecular complexes of lanthanide ions (Ln), for the development of efficient near infrared (NIR)-emitting materials. In the light of a detailed understanding of the chemical/photophysical properties of the special class of lanthanide quinolinolato complexes, as prototype molecular materials for NIR applications, two main aspects have been taken into consideration for a progress in this field: i) (multi-) functional NIR-emissive heterolanthanide complexes and ii) lanthanide-doped sol-gel glasses as NIR-emissive optical materials.

Heterometallic assemblies, containing two or more different lanthanide cations as carriers of distinctive functionalities, represent promising materials where different physical properties can coexist or be in interplay thanks to intermetallic communication. A thorough discussion on heterolanthanide assemblies, pointing out the general strategies to achieve the desired (multi-) functionalities in these systems, is provided herein.

In this framework, heterolanthanide Er/Yb systems have attracted significant interest for Er^{3+} sensitization through resonance energy transfer (RET) from Yb^{3+} leading to enhancement of Er^{3+} NIR emission at 1.5 μm in glass host Yb-Er co-doped optical fiber amplifiers. A strategy to achieve composition control and homogeneity in such materials resorts to the encapsulation of Er and Yb in the same molecule to afford intermetallic communication between lanthanide ions sitting at short distance in a discrete polynuclear architecture. Fully efficient Yb-to-Er RET at molecular level is firstly demonstrated in the mixed-lanthanide Yb_2ErQ_9 complex (Q = quinolinol ligand), and, as an extension of these studies, the investigation of the full photocycle leading to narrow-band NIR emission in a series of heterolanthanide $\text{Er}_x\text{Yb}_{3-x}$ quinolinolato compounds, on variation of metal composition and molecular stoichiometry, has been performed. Moreover, the first example of a tri-lanthanide discrete polynuclear molecule containing three NIR-emissive lanthanide ions: Nd^{3+} , Yb^{3+} and Er^{3+} , is presented. The NdYbErQ_9 complex was investigated as a potential broad-band NIR emitter where the intensities of the three different main emissions from each lanthanide ion can be finely tuned on varying metal composition.

The investigation of the processing potential of luminescent lanthanide complexes through doping into inorganic or polymeric host matrixes is of crucial interest for the development of optical devices (amplifiers, optical waveguides, OLEDs, etc.). To this purpose, studies on the incorporation of an Yb quinolinolate complex into a silica sol-gel glass, with a thorough account of the photophysical properties of this hybrid material, have been performed. Promising results on silica thin films doped with heterolanthanide Er/Yb quinolinolates are also presented as a molecular approach to achieve controlled light conversion in NIR-emissive optical materials.

Table of Contents

Introduction

1. General Introduction	3
2. State of the Art	4
3. Heterolanthanide Assemblies	6
4. Doped Silica Glasses	9
References	10

Paper 1

<i>Tailoring Functionality through Synthetic Strategy in Heterolanthanide Assemblies</i>	14
--	----

Paper 2

<i>Fully Efficient Direct Yb-to-Er Energy Transfer at Molecular Level in a Near-Infrared Emitting Heterometallic Trinuclear Quinolinolato Complex</i>	27
Supporting Information	35

Paper 3

<i>Light Conversion Control in NIR-Emissive Optical Materials based on Heterolanthanide Er_xYb_{3-x} Quinolinolato Molecular Components</i>	43
Supporting Information	59

Paper 4

<i>Ln_3Q_9 as a Molecular Framework for Ion-Size-Driven Assembly of Heterolanthanide (Nd, Er, Yb) Multiple Near-Infrared Emitters</i>	71
Supporting Information	79

Table of Contents

Paper 5

<i>Silica Sol–Gel Glasses incorporating Dual-Luminescent Yb Quinolinolato Complex: Processing, Emission and Photosensitising Properties of the ‘Antenna’ Ligand</i>	105
Supporting Information	115

Conclusions and Perspectives

1. Conclusions	121
2. Perspectives	123

Introduction

Light Conversion Processes in Lanthanide-based Materials

1. General Introduction
2. State of the Art
3. Heterolanthanide Assemblies
4. Doped Silica Glasses

1. General Introduction

The relevance and strategic importance of lanthanide (Ln) ions in several fields ranging from high-technology to biomedical applications is nowadays highly recognized, and has brought these elements to be included in the list of “critical metals”, materials whose availability is essential but vulnerable to politically or economically driven fluctuations in supply.¹ Their very peculiar luminescent and magnetic properties, related to the nature of their 4f core-like electrons, have attracted remarkable interest for the development of, for example, MRI contrast agents, catalysts, magnetic materials with large anisotropy and reduced quantum tunneling of the magnetization, supermagnets, luminescent materials for solar energy conversion, optical imaging, bioprobes, sensors, display and lighting technology, lasers, optical fibers and amplifiers.²⁻³

In particular, lanthanide ions’ photoluminescence represents a very attractive feature as it originates from parity-forbidden intra-shell 4f-4f transitions resulting in a high color purity and long radiative lifetime. Moreover, the emission color depends on the nature of the lanthanide ion but is largely independent of its chemical environment. Different luminescent lanthanide ions can therefore be selected on dependence of the specific purpose for which they are intended, as UV, visible or near infrared (NIR) emitters. A Dieke diagram illustrating the energy levels of 4f electrons of some luminescent lanthanide ions is reported in Figure 1.

Yb^{3+} , Nd^{3+} and Er^{3+} play a special role in optical fiber technologies operating in the

near infrared, as their emission covers, respectively, the so-called first (1 μm), second (1.33 μm) and third (1.55 μm) optical communication windows. In order to compensate signal losses in optical fibers (due to coupling and propagation losses) and achieve optical amplification in the waveguide, the guiding core can be doped with lanthanide ions. In particular, erbium-doped fiber amplifiers (EDFAs), operating in the third telecom window, have already been implemented in optical fiber systems, and erbium-doped waveguide amplifiers have also been demonstrated in glass⁴ and crystal⁵ hosts.

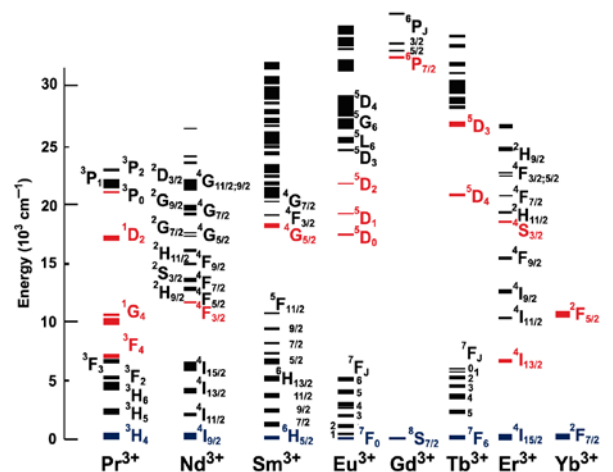


Figure 1. Dieke diagram for some luminescent lanthanide ions. Emissive and ground levels are highlighted in red and blue, respectively.

A disadvantage of this technology stems from the weak intrinsic absorptivity of lanthanide ions and their very low solubility in all inorganic matrices, resulting in long and expensive amplifiers. A promising strategy to overcome these drawbacks resorts to the encapsulation of the lanthanide ion by a “light harvesting” organic ligand which allows optical pumping and provides good solubility in the host material. Excited-state processes leading to lanthanide emission sensitization through an organic ligand are shown in Figure 2.

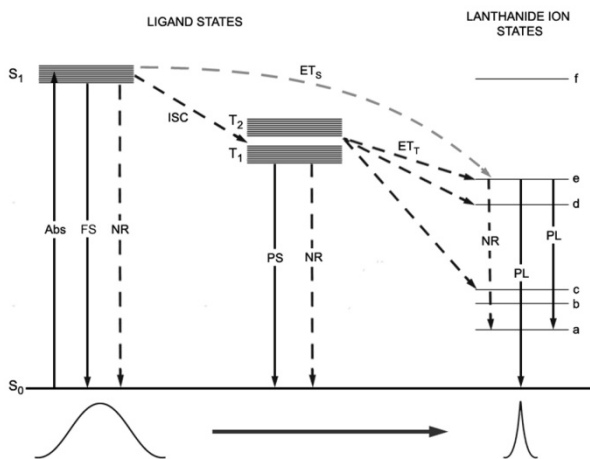


Figure 2. Jablonski diagram depicting the sensitization mechanism of a Ln ion through resonance energy transfer from an organic ligand. The ligand is photo-excited to the singlet level S_1 , then intersystem-crossing (ISC) occurs to lower-lying excited triplet states (T_1, T_2) that are suitable to feed the Ln^{3+} upper levels by direct energy transfer (ET). Alternatively, ligand-to-metal ET can occur directly from the S_1 state. FS = fluorescence; PL=photoluminescence; NR=non-radiative decay; PS=phosphorescence.

Moreover, the ligand can shield the ion from additional coordination from the solvent or impurities in the matrix, which could quench the luminescence. Such lanthanide complexes could enable the realization of a new generation of low-cost optical amplifiers in the centimeter-length scale, featuring superior optical and mechanical figures of merit, and are suitable for the fabrication of photonic integrated circuits.⁶

This work is inserted into this general framework, and mainly focused on the chemical/photophysical investigation and processing of NIR-luminescent complexes of lanthanide ions, for the development of efficient NIR-emitting materials.

2. State of the Art

Among the several complexes extensively investigated as emitting materials in the last decade, the interest in lanthanide complexes with the 8-quinolinolato (Q) ligand and its derivatives, as low cost emitting materials in the near-infrared region, followed the demonstration of the first electrically-excited IR emitter based on the erbium complex, formerly formulated as ErQ_3 , in analogy with the structurally characterized AlQ_3 (Figure 3).⁷

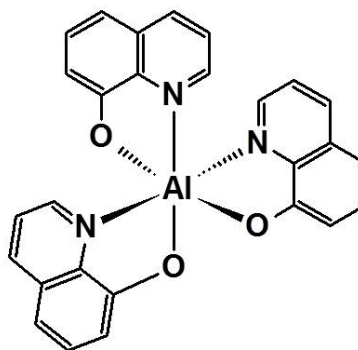


Figure 3. Molecular structure of AlQ_3 .

Photoluminescence studies on this and similar complexes have shown lifetimes much shorter than the natural radiative lifetime of the $Er^{3+} {}^4I_{13/2} \rightarrow {}^4I_{15/2}$ transition at 1540 nm. The unexpectedly short lifetime (in the 2 μs range) and the low quantum yield have been ascribed to the presence of CH groups of the Q-ligand and OH groups of water molecules possibly present in the first coordination sphere and supposed to be the most important IR quenchers. This implied that in ErQ_3 the ligand was unable to protect the ion from further coordination by solvent or moisture. The reason of the low quantum yield claimed for a quantitative understanding of IR quenching mechanisms in these materials and several contributions have been provided to help

clarify this point.⁸ This has led in some instances to questionable assignments of the deactivation mechanisms affecting the luminescence properties of lanthanide quinolinolates.

In the last decade there has been a considerable effort in the strive for a detailed understanding of the structure/property relationship in this class of complexes. Remarkable advances in the field were made after a full reinvestigation of the synthetic procedures and molecular structural studies which pointed out the extremely versatile coordination chemistry of lanthanide quinolinolates.⁹ This allowed to fully understand and quantify the quenching mechanisms affecting NIR luminescence in these compounds on the basis of a detailed structural and spectroscopic characterization.

Among the investigated lanthanide quinolinolates, particular relevance has to be given to the molecular structure of the erbium complex with the Q ligand, which consists of a trinuclear edifice of formula Er_3Q_9 , where the three metal ions are fully coordinated by nine ligands (Figure 4).^{9b}

In Er_3Q_9 , where the coordination sphere is completely saturated by the ligands, the role of water in quenching phenomena is definitely ruled out and non-radiative deactivation processes can be only ascribed to the ligand CH groups in the vicinity of the metal ion. Structural and spectroscopic data allowed the quantitative evaluation of the rate of the Förster's vibrational deactivation¹¹ of erbium luminescence in Er_3Q_9 by CH groups through the determination of the erbium and CH absorption cross-section, the overlap integral between the erbium emission and CH absorption spectra, and the distances and angles between the emitting metal ion

and each C–H bond.¹² Förster's model was successful in accounting for 99% of quenching effects in erbium quinolinolates. On the other hand, for ytterbium complexes, only 50% of non-radiative deactivation was explained, hinting at additional nonradiative paths for which no clear experimental evidence could be found so far.¹³

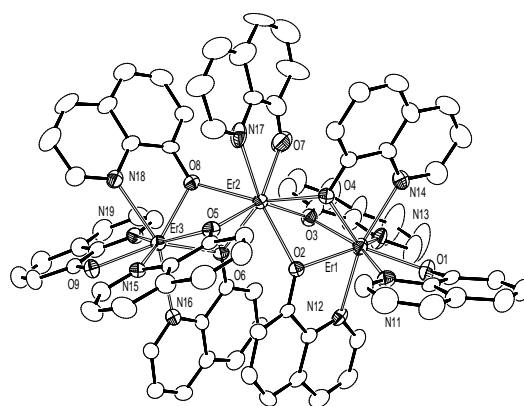


Figure 4. Molecular structure of Er_3Q_9 .

In order to reach a detailed picture of the full photocycle leading to narrow-band lanthanide emission in these complexes, the ligand-to-metal energy transfer mechanism was also studied. Ligand-to-metal sensitization quantum yield, η_{sens} , is in fact a key parameter for the design of luminescent lanthanide complexes since it critically influences the overall emission quantum yield.

Quinolinol ligands are good “light harvesters” and possess good photosensitising properties toward the NIR emissive lanthanide ions, since, in addition to broad absorption and emission bands in the visible region, have triplet state energies ($\sim 18000 \text{ cm}^{-1}$) matching well the accepting energy levels of the 4f orbitals of Er^{3+} , Nd^{3+} and Yb^{3+} . Values of η_{sens} ranging from a few percents to >95% were inferred in erbium quinolinolates.¹⁰ The high values

found for the erbium sensitization efficiency for excitation rates up to population-inversion threshold^{14a} in Er₃Q₉ and similar complexes were confirmed by the results of time-resolved studies on the intraligand and ligand to-metal excited-state temporal dynamics.^{14b} Ligand to metal energy transfer rates in erbium quinolinolates were found to be exceptionally efficient if compared to literature data of m-terphenyl-based complexes functionalized with a triphenylene antenna chromophore.¹⁵ Parallel triplet decay pathways such as oxygen quenching were inferred to be much slower than ligand-to-metal energy transfer, and therefore can only marginally influence lanthanide-ion sensitization efficiency in lanthanide quinolinolates.

For a thorough account on NIR-emissive lanthanide quinolinolates see reference 10.

The detailed understanding of the chemical/photophysical properties of this class of lanthanide-based materials has been crucial for the development of the work described in this thesis. In particular, two main aspects have been taken into consideration for a progress in this field: i) (multi-) functional NIR-emissive heterolanthanide complexes and ii) lanthanide-doped sol-gel glasses as NIR-emissive optical materials. A brief description of these research topics is given in the following paragraphs.

3. Heterolanthanide Assemblies

As previously mentioned, lanthanide ions possess many peculiar physical properties, including magnetism, luminescence, catalytic properties, that are widely exploited for several technologies. In this context, the most challenging frontier is represented by heterometallic assemblies, containing two or more different lanthanide cations as carriers of distinctive functionalities, where different physical properties can coexist or be in interplay thanks to intermetallic communication. These materials can include, for example: multiple emitters, directional light converters, double-functional compounds acting as MRI contrast agents and luminescent probes, systems with simultaneously activated catalytic sites.¹⁶

However, the preparation of well-defined and easily reproducible polymetallic lanthanide compounds is often a difficult task, and fully characterized mixed-lanthanide coordination compounds still represent very rare examples in the literature. Nonetheless, the extraordinary versatility of lanthanide coordination chemistry can lead to the isolation of a wide variety of coordination compounds, ranging from multi-dimensional networks to polynuclear discrete assemblies, through judicious selection of the coordinating ligands or even simply on variation of reaction conditions. This offers a unique opportunity to mix and play with different lanthanide ions in diverse architectures and to achieve tunability of physical properties through composition control and rational synthetic strategies. In such materials, different functionalities can be in fact achieved on dependence of the mutual interaction or simple superposition of

different physical properties.

In materials where intermetallic communication (magnetic coupling, electron transfer, energy transfer...) is sought, the distance between the interacting Ln ions must be reduced below 3.5-4 Å for mechanisms requiring orbital overlap (Dexter's energy transfer, magnetic exchange) or below 10 Å for efficient dipolar through-space interactions (Förster's energy transfer, magnetic dipolar interactions). A thorough discussion on heterolanthanide assemblies, pointing out the general strategies to achieve the desired (multi-) functionalities in these systems, is the subject of **Paper 1** in this thesis (see Figure 5).

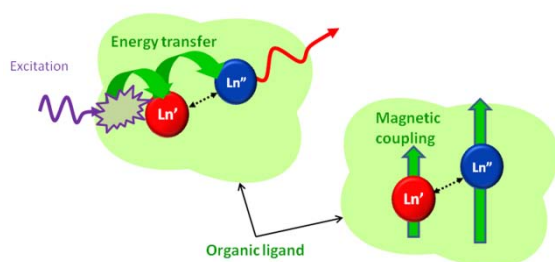


Figure 5. A schematic representation of the intermetallic communication by energy transfer or magnetic coupling between close-contact lanthanide pairs embedded in an organic framework. Reproduced from Paper 1.

In recent years there has been significant interest on Er^{3+} sensitization through resonance energy transfer (RET) from Yb^{3+} in ion-implanted/co-doped glass host materials because the absorption cross section of Yb^{3+} at 1 μm is approximately 10-times higher than that of Er^{3+} and energy transfer can occur between the $^2\text{F}_{5/2}$ level of Yb^{3+} and the resonant $^4\text{I}_{11/2}$ level of Er^{3+} . Enhancement of Er^{3+} NIR emission at 1.5 μm has been achieved in glass host Yb-Er co-doped optical fiber amplifiers.¹⁷ For

efficient Yb-to-Er RET through a Förster's mechanism, the distance between the two ions must be limited ($< 10\text{\AA}$).¹¹ However, it is often difficult to control the Er^{3+} and Yb^{3+} doping concentration accurately and homogeneously resulting in difficult quantitative analysis of RET from Yb^{3+} to Er^{3+} . A strategy to achieve composition control resorts to the encapsulation of Er and Yb in the same molecule to afford intermetallic communication between lanthanide ions at short distance in a discrete polynuclear architecture. In such heterometallic assemblies, suitable organic ligands can be introduced which can act as efficient "light harvesters", providing a supplementary excitation channel for the lanthanide ions.

The Ln_3Q_9 molecular framework, analogous to that depicted in Figure 3, is particularly suitable for preparing mixed-lanthanide complexes, providing several benefits especially in regard to NIR-emitters: i) high coordinating ability toward different Ln ions across the whole series; ii) excellent "antenna" properties of the Q ligand allowing simultaneous excitation of different NIR-emissive Ln ions upon single-wavelength irradiation; iii) short intermetallic distances (below 3.5 Å), optimal for ensuring fully efficient Yb-to-Er RET; iv) high stability and capability to undergo processing procedures (in solution or by vacuum deposition) without alterations.

The demonstration of fully efficient Yb-to-Er RET in the mixed-lanthanide Yb_2ErQ_9 complex is the subject of **Paper 2**, whereas **Paper 3** provides an extension to these studies, illustrating the full photocycle of a series of heterolanthanide $\text{Er}_x\text{Yb}_{3-x}$ quinolinolato compounds, on variation of metal composition and molecular stoichiometry. See Figures 6 and 7.

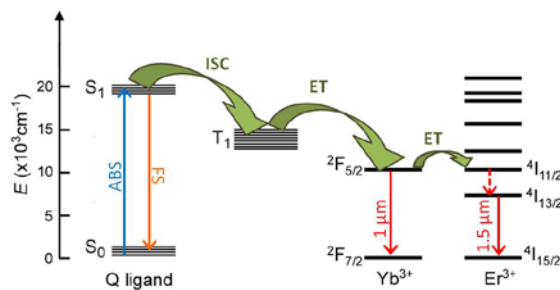


Figure 6. Jablonski diagram depicting the energy levels of the Q ligand, Yb^{3+} , and Er^{3+} and the full photocycle in trinuclear quinolinolato complexes. Dashed arrows represent nonradiative processes. Adapted from Paper 2.

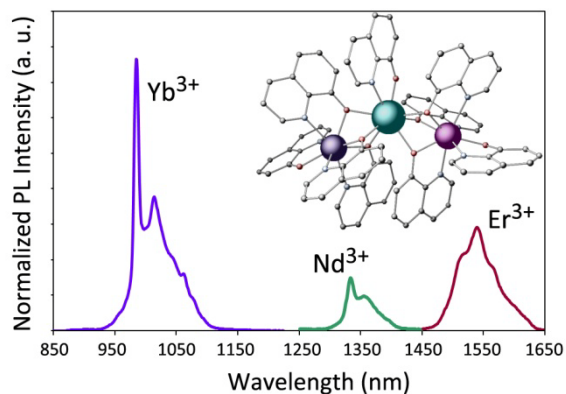


Figure 8 Broad-band NIR photoluminescence (PL) of the trilanthanide NdYbErQ_9 compound (also shown). Adapted from Paper 4.

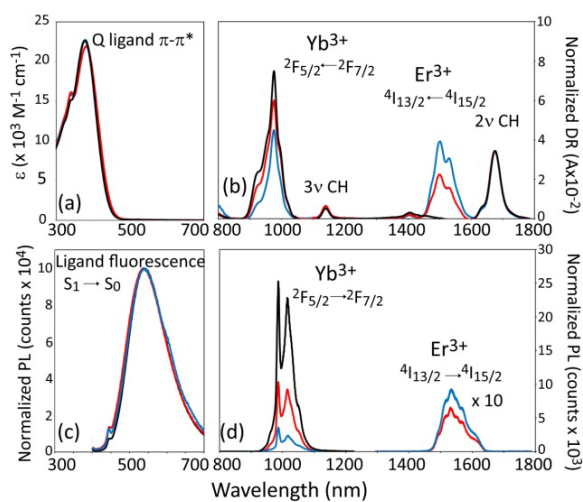


Figure 7. Absorption (above) and photoluminescence (PL, below) spectra in the visible and NIR spectral regions of trinuclear quinolinolato complexes on variation of the metal composition. Color coding: black, Yb_3Q_9 ; red, ErYb_2Q_9 ; red, Er_2YbQ_9 . Reproduced from Paper 3.

Paper 4 presents the first example of a tri-lanthanide discrete polynuclear molecule containing three NIR-emissive lanthanide ions: Nd^{3+} , Yb^{3+} and Er^{3+} . The NdYbErQ_9 complex has been investigated as a potential broad-band NIR emitter where the intensities of the three different main emissions from each lanthanide ion can be finely tuned on varying metal composition and hence molecular speciation. See Figure 8.

4. Doped Silica Glasses

The investigation of the processing potential of luminescent lanthanide complexes through the incorporation into inorganic or polymeric host matrixes is of crucial interest for the development of optical devices (amplifiers, optical waveguides, OLEDs, etc.). In general, these “hybrid” materials have superior mechanical properties and have a better processability than the pure molecular lanthanide complexes. In addition, embedding a lanthanide complex in a host matrix is also beneficial for overcoming the poor thermal stability and low mechanical strength of coordination complexes.¹⁸

Silica glasses doped with luminescent lanthanide inorganic salts are suitable materials to be used for the fabrication of several optical devices, such as lasers and optical fibres,¹⁹ as they are highly transparent and homogeneous and feature good mechanical properties. Moreover, the silica matrix hardly influences the energy levels of the lanthanide ions and has also a negligible absorption coefficient at the excitation or emission wavelengths used in photoluminescence experiments.

Lanthanide-doped silica glasses can be prepared through the convenient *sol-gel process*, which offers several advantages over the traditional melt preparation. The most important one arise from the fact that sol-gel glasses, being prepared through a solution process, can hold a higher concentration of dopants than melt glasses, without losing their amorphous character. Moreover, they are generally of better purity and can be fabricated at much lower temperatures. The sol-gel process can be used to prepare materials in different

shapes, from bulk samples (monoliths) to thin films and fibers. Optical properties achievable in sol-gel materials include chemical sensing, graded refractive indexes, optical waveguiding and amplification, frequency doubling, and lasing.²⁰

The use of lanthanide complexes with organic ligands in place of traditional inorganic salts and oxides of the optically active lanthanides, offer the additional advantage to improve the solubility of the active emitters into the host matrix affording materials of high optical homogeneity.

For an exhaustive review of lanthanide-based luminescent hybrid materials see reference 18.

In **Paper 5**, studies on the incorporation of an Yb quinolinolate complex into a silica *bulk* sol-gel glass are discussed, with a thorough investigation of the photophysical properties of this hybrid material. See Figure 9.

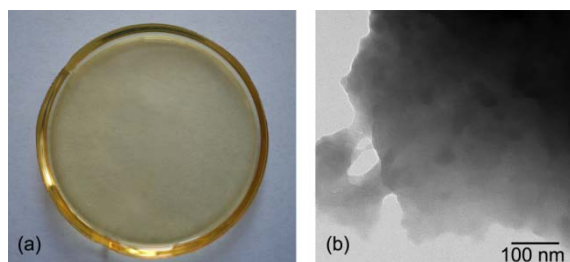


Figure 9. Bulk sol gel glass doped with an ytterbium quinolinolate complex, of high optical and compositional homogeneity at macroscopic (a) and nanometric (b, TEM micrography) level. Reproduced from Paper 5.

Silica doped sol-gel glasses are also advantageous for the preparation of co-doped Er/Yb materials. Most of the co-doped Er/Yb glassy/polymeric materials so far studied in view of their potential applications, especially as NIR optical waveguides and amplifiers, are usually

prepared through techniques (ion sputtering/implantation, beam lithography...) that do not allow a precise control of the distribution, concentration and relative position of the two lanthanide ions. These requirements can be nonetheless met through the incorporation of preformed polynuclear heterolanthanide complexes where the two optically-active ions are held at a fixed intermetallic separation, into silica glasses *via* the mild sol-gel solution technique. In this way it would be possible to take advantage of the molecular approach for functional heterolanthanide assemblies while fabricating optical materials useful for direct applications. This point is addressed in **Paper 3**, where preliminary investigations on the incorporation of heterolanthanide Er/Yb quinolinolates into silica thin films are presented as a molecular approach to achieve controlled metal-to-metal energy transfer in NIR-emissive optical materials.

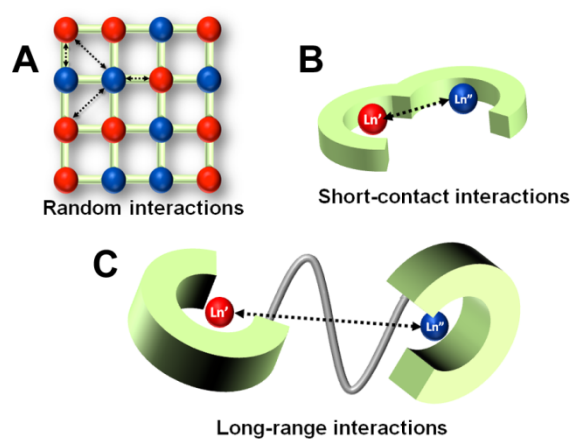
References

1. European Commission, Report on critical raw materials, May 2014.
2. a) Huang, C. (Ed.), *Rare Earth Coordination Chemistry, Fundamentals and Applications*, Wiley, **2010**; b) Bünzli, J.-C. G.; Piguët, C. *Chem. Soc. Rev.*, 2005, **34**, 1048.
3. a) Heffern, M. C.; Matosziuk, L. M.; Meade, T. J. *Chem. Rev.*, **2014**, *114*, 4496; b) Woodruff, D. N.; Winpenny, R. E. P.; Layfield, R. A. *Chem. Rev.*, **2013**, *113*, 5110; c) Ferbinteanu, M.; Kajiwara, T.; Choi, K.-Y.; Nojiri, H.; Nakamoto, A.; Kojima, N.; Cimpoesu, F.; Fujimura, Y.; Takaishi, S.; Yamashita, M. *J. Am. Chem. Soc.*, **2006**, *128*, 9008; c) Bünzli, J.-C. G.; Eliseeva, S. V. *J. Rare Earths*, **2010**, *28*, 824.
4. a) Kitagawa, T.; Hattori, K.; Shuto, K.; Yasu, M.; Kobayashi, M.; Horiguchi, M. *Electron. Lett.*, **1992**, *28*, 1818; b) Feuchter, T.; Mwcuania, E. K.; Wang, J.; Reekie, L.; Wilkinson, J. S. *IEEE Photonics Technol. Lett.*, **1992**, *4*, 542; c) Yan, Y. C.; Faber, A. J.; de Waal, H.; Polman, A.; Kik, P. G. *Appl. Phys. Lett.*, **1997**, *71*, 2922; d) Kozanecki, A.; Sealy, B. J.; Homewood, K. *J. Alloys Compd.*, **2000**, *300–301*, 61; e) Wong, S. F.; Pun, E. Y. B.; Chung, P. S. *IEEE Photonics Technol. Lett.*, **2002**, *14*, 80.
5. a) Joubert, M. F.; Remillieux, A.; Jacquier, B.; Mugnier, J.; Boulard, B.; Perrot, O.; Jacoboni, C.; *J. Non-Cryst. Solids*, **1995**, *184*, 341; b) Huang, C. H.; McCaughan, L. *IEEE Photonics Technol. Lett.*, **1997**, *9*, 599.
6. a) Kuriki, K.; Koike, Y.; Okamoto, Y. *Chem. Rev.*, **2002**, *102*, 2347; b) Slooff, L. H.; Van Blaaderen, A.; Polman, A.; Hebbink, G. A.; Klink, S. I.; Van Veggel, F. C. J. M.; Reinhoudt, D. N.; Hofstraat, J. W. *J. Appl. Phys.*, **2002**, *91*, 3955.
7. a) Curry, R. J.; Gillin, W. P. *Appl. Phys. Lett.*, **1999**, *75*, 1380; b) Gillin, W. P.; Curry, R. J. *Appl. Phys. Lett.*, **1999**, *74*, 798; c) Curry, R. J.; Gillin, W. P. *Synth. Met.*, **2000**, *35*, 111; d) Curry, R. J.; Gillin, W. P.; Knights, A. P.; Gwilliam, R. *Opt. Mater.* **2001**, *17*, 161; e) Penna, S.; Reale, A.; Pizzoferrato, R.; Tosi Beleffi, G. M.; Musella, D.; Gillin, W. P. *Appl. Phys. Lett.*, **2007**, *91*, 021106; f) Kawamura, Y.; Wada, Y.; Hasegawa, Y.; Iwamuro, M.; Kitamura, T.; Yanagida, S. *Appl. Phys. Lett.*, **1999**, *74*, 3245; g) Blyth, R. I. R.; Thompson, J.; Zou, Y.; Fink, R.; Umbach, E.; Gigli, G.; Cingolani, R. *Synth. Met.*, **2003**, *139*, 207; h) Khreis, O. M.; Curry, R. J.;

- Somerton, M.; Gillin, W. P. *J. Appl. Phys.*, **2000**, *88*, 777; i) Khreis, O. M.; Gillin, W. P.; Somerton, M.; Curry, R. J. *Org. Electron.*, **2001**, *2*, 45; l) Iwamuro, M.; Adachi, T.; Wada, Y.; Kitamura, T.; Yanagida, S. *Chem. Lett.*, **1999**, 539.
8. a) Iwamuro, M.; Adachi, T.; Wada, Y.; Kitamura, T.; Nakashima, N.; Yanagida, S. *Bull. Chem. Soc. Jpn.* **2000**, *73*, 1359; b) Van Deun, R.; Fias, P.; Driesen, K.; Binnemans, K.; Gorller-Walrand, C. *Phys. Chem. Chem. Phys.*, **2003**, *5*, 2754; c) Magennis, S. W.; Ferguson, A. J.; Bryden, T.; Jones, T. S.; Beeby, A.; Samuel, I. D. W. *Synth. Met.*, **2003**, *138*, 463; d) Thompson, J., Blyth, R. I. R.; Gigli, G.; Cingolani, R. *Adv. Funct. Mater.*, **2004**, *14*, 979; e) Beeby, A.; Clarkson, I. M.; Dickins, R. S.; Faulkner, S.; Parker, D.; Royle, L.; de Sousa, A. S.; Williams, J. A. G.; Woods, M. *J. Chem. Soc., Perkin Trans.*, **1999**, *2*, 493; f) Comby, S.; Bünzli, J. -C. G. in: Gschneidner, K. A. Jr., Bünzli, J. -C. G.; Pecharsky, V. (Eds.), *Handbook on the Physics and Chemistry of Rare Earths*, Elsevier B.V., Amsterdam, **2007**, *37*, Chapter 235.
9. a) Van Deun, R.; Fias, P.; Nockemann, P.; Schepers, A.; Parac-Vogt, T. N.; Van Hecke, K.; Van Meervelt, L.; Binnemans, K. *Inorg. Chem.*, **2004**, *43*, 8461; b) Artizzu, F.; Deplano, P.; Marchiò, L.; Mercuri, M. L.; Pilia, L.; Serpe, A.; Quochi, F.; Orrù, R.; Cordella, F.; Meinardi, F.; Tubino, R.; Mura, A.; Bongiovanni, G. *Inorg. Chem.* **2005**, *44*, 840; c) Artizzu, F.; Deplano, P.; Marchiò, L.; Mercuri, M. L.; Pilia, L.; Serpe, A.; Quochi, F.; Orrù, R.; Cordella, F.; Saba, M.; Mura, A.; Bongiovanni, G. *Adv. Funct. Mater.*, **2007**, *17*, 2365.
10. Artizzu, F.; Mercuri, M. L.; Serpe, A.; Deplano, P. *Coord. Chem. Rev.*, **2011**, *255*, 2514 and references therein.
11. a) Förster, T. *Discuss. Faraday Soc.*, **1959**, *27*, 7; b) Förster, T. *Annalen der Physik*, **1948**, *2*, 55, english translation (1993).
12. Quochi, F.; Orrù, R.; Cordella, F.; Mura, A.; Bongiovanni, G.; Artizzu, F.; Deplano, P.; Mercuri, M. L.; Pilia, L.; Serpe, A. *J. Appl. Phys.*, **2006**, *99*, 053520.
13. Artizzu, F.; Quochi, F.; Saba, M.; Marchiò, L.; Espa, D.; Serpe, A.; Mura, A.; Mercuri, M. L.; Bongiovanni, G.; Deplano, P. *ChemPLUSChem*, **2012**, *77*, 240.
14. a) Quochi, F.; Artizzu, F.; Saba, M.; Cordella, F.; Mercuri, M. L.; Deplano, P.; Loi, M. A.; Mura, A.; Bongiovanni, G. *J. Phys. Chem. Lett.*, **2010**, *1*, 141; b) Quochi, F.; Saba, M.; Artizzu, F.; Mercuri, M. L.; Deplano, P.; Mura, A.; Bongiovanni, G.; *J. Phys. Chem. Lett.*, **2010**, *1*, 2733.
15. Klink, S. I.; Grave, L.; Reinhoudt, D. N.; Van Veggel, F. C. J. M.; Werts, M. H. V.; Geurts, F. A. J.; Hofstraat, J. W. *J. Phys. Chem. A*, **2000**, *104*, 5457.
16. a) Piguet, C.; Bünzli, J. -C. G. *Chem. Rev.*, **2002**, *102*, 1897; b) Piguet, C.; Bünzli, J. -C. G. *Chem. Soc. Rev.*, **1999**, *28*, 347; c) Tsubouchi, A.; Bruce, T. C. *J. Am. Chem. Soc.*, **1994**, *116*, 11614; d) Ragunathan, K. G.; Schneider, H. -J. *Angew. Chem., Int. Ed. Engl.*, **1996**, *35*, 1219.
17. a) Strohhöfer, C.; Polman, A. *Opt. Mater.* **2003**, *21*, 705; b) Dong, B.; Q. Feng, Z.; Cao, B. S.; Zheng, J. Z. *J. Sol-Gel Sci. Technol.* **2009**, *50*, 383; c) Wong, W. H.; Pun, E. Y. B.; Chan, K. S. Er³⁺-Yb³⁺ *Appl. Phys. Lett.* **2004**, *84*, 176; d) Chryssou, C. E.; Di Pasquale, F.; Pitt, C. W. *J. Lightwave Technol.* **2001**, *19*, 345; e) Chiasera, A.; Tosello, C.; Moser, E.; Montagna, M.; Belli, R.; Goncalves, R. R.; Righini, G. C.; Pelli, S.; Chiappini, A.; Zampedri, L.; Ferrari, M. *J. Non-Cryst. Solids*, **2003**, *322*, 289.
18. Binnemans, K. *Chem. Rev.*, **2009**, *109*, 4283.
19. a) Wu, F.; Machewirth, D.; Snitzer, E.; Sigel, G. H. *J. Mater. Res.*, **1994**, *9*, 2703; b) Wu, F.; Puc, G.; Foy, P.; Snitzer, E.; Sigel, G. H. Jr. *Mat. Res. Bull.*, **1993**, *28*, 637; c) Polman, A.; Jacobson, D. C.; Eaglesham, D. J.; Kistler, R. C.; Poate, J. M. *J. Appl. Phys.*, **1991**, *70*, 3778; d) Weber, M. J. *J. Non-Cryst. Solids*, **1990**, *123*, 208.
20. Costa, V. C.; Lochhead, M. J.; Bray, K. L. *Chem. Mater.*, **1996**, *8*, 783.

Paper 1

Tailoring Functionality through Synthetic Strategy in Heterolanthanide Assemblies



Three classes of heterolanthanide assemblies, multi-dimensional frameworks (**A**), discrete polynuclear molecules (**B**) and preformed coordinated units connected by a linker (**C**), are discussed (see figure). Potential functionalities arising from the distance-dependent coexistence or interplay of physical properties carried by the different lanthanide ions are pointed out.


 CrossMark
 click for updates

 Cite this: *Inorg. Chem. Front.*, 2015,
 2, 213

 Received 30th October 2014,
 Accepted 14th January 2015

DOI: 10.1039/c4qi00188e

rsc.li/frontiers-inorganic

Tailoring functionality through synthetic strategy in heterolanthanide assemblies

 Flavia Artizzu,^{*a,b} Francesco Quochi,^b Angela Serpe,^a Elisa Sessini^a and Paola Deplano^{a,b}

An overview of the different strategies proposed for the preparation of heterolanthanide assemblies suitable to work as (multi-) functional materials, highlighting their structure/property relationship, is provided. Three classes of compounds are selected: multi-dimensional coordination frameworks, polynuclear discrete molecules and flexible large molecules formed by two or more coordinating units connected by a linker. Synthetic approaches and potential functionalities are discussed on the basis of lanthanide ion discrimination and the structural arrangement of the heterometallic assembly.

Introduction

Lanthanide (Ln) ions nowadays belong to the class of “critical metals”, materials whose availability is essential for high-technology, green and defense applications, but vulnerable to politically or economically driven fluctuations in supply.¹ Their very peculiar luminescent and magnetic properties, related to the nature of their 4f core-like electrons, are in fact exploited in several fields ranging from high-tech devices to biomedical applications. Correspondingly, lanthanide compounds have been widely studied in view of their numerous potential applications, depending on the nature of the lanthanide ion, such as, for example, MRI contrast agents (Gd³⁺), catalysts, magnetic materials with large anisotropy and reduced quantum tunneling of the magnetisation (Dy³⁺, Tb³⁺), luminescent materials for solar energy conversion, optical imaging, bioprobes, sensors, visible emitters for display and lighting technology (Eu³⁺, Tb³⁺, Sm³⁺) and near-infrared (NIR) emitters for lasers, optical fibers and amplifiers (Er³⁺, Nd³⁺, Yb³⁺).^{2,3}

In this context, the most challenging frontier is represented by heterometallic assemblies containing two or more different lanthanide cations as carriers of distinctive functionalities, where different physical properties can coexist or be in interplay thanks to intermetallic communication. These materials can include, for example: multiple emitters, directional light converters, double-function compounds acting as MRI contrast agents and luminescent probes, and systems with simultaneously activated catalytic sites.^{4,5}

However, the preparation of well-defined and easily reproducible polymetallic lanthanide compounds is often a difficult task, and fully characterized mixed-lanthanide coordination compounds still represent very rare examples in the literature. Nonetheless, the extraordinary versatility of lanthanide coordination chemistry, which obeys completely different rules from those common to transition metal ions, is basically related to the lack of orbital directionality, the strong Lewis acid character and the tendency to reach high coordination numbers of the Ln ions. These factors can lead to the isolation of a wide variety of coordination compounds, ranging from multi-dimensional networks to polynuclear discrete assemblies, through judicious selection of the coordinating ligands or even simply through the variation of the reaction conditions. This offers a unique opportunity to mix and play with different lanthanide ions to create diverse architectures and to achieve tunability of their physical properties through composition control and rational synthetic strategies. In fact, depending on the desired resulting functionality and potential applications of the material, tailored synthetic approaches, leading to specific coordination frameworks, can be selected.

The aim of this article is therefore to provide an overview, covering the most significant literature on the different strategies that have been proposed for the preparation of heterolanthanide assemblies, shedding light on the structure/property relationship of these materials.

Discussion

A. General considerations

Coordination chemistry can provide several benefits for the use of Ln ions in functional materials. Among them, the following are worth highlighting: (i) luminescent Ln ions, exhibiting intrinsically weak absorptivity, can take advantage

^aDipartimento di Scienze Chimiche e Geologiche, University of Cagliari, SS 554 Bivio per Sestu, I-09042 Monserrato-Cagliari, Italy. E-mail: f.artizzu@unica.it

^bDipartimento di Fisica, University of Cagliari, SS 554 Bivio per Sestu, I-09042 Monserrato-Cagliari, Italy

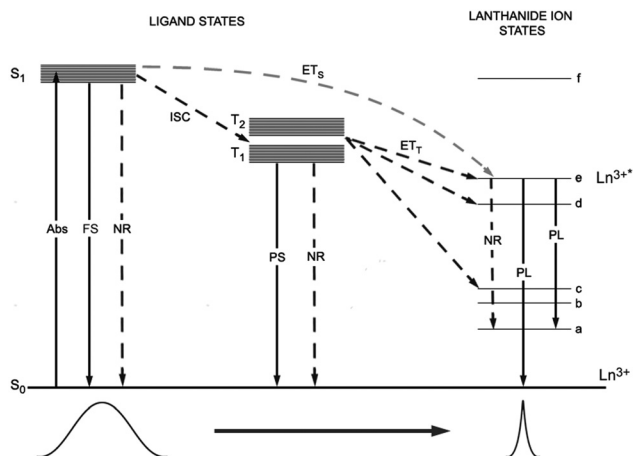


Fig. 1 A Jablonski diagram depicting the sensitisation mechanism of a Ln ion through resonance energy transfer from an organic ligand. The ligand is photoexcited to the singlet level S_1 , then intersystem-crossing (ISC) occurs to lower-lying excited triplet states (T_1 , T_2) that are suitable to feed the Ln^{3+} upper levels by direct energy transfer (ET). Alternatively, ligand-to-metal ET can occur directly from the S_1 state. FS = fluorescence; PL = photoluminescence; NR = non-radiative decay; PS = phosphorescence.

of indirect optical pumping through resonance energy transfer (sensitisation) from a suitable organic ligand acting as an antenna chromophore (see Fig. 1); (ii) magnetic anisotropy of some lanthanide ions can be tuned by changing the coordination symmetry,^{4a,6a} and the magnetic coupling between paramagnetic centers can be mediated by covalent or non-covalent interactions of organic moieties;^{6b} (iii) metal encapsulation with organic ligands improves Ln solubility into host matrices, providing processing versatility. The electronic, optical and magnetic properties of Ln ions are significantly affected by the structural constraints of the metal ion site (geometry, symmetry, nature of the first and second coordination spheres, nature of the metal ions, and site accessibility). Consequently, careful design of the coordination architecture for the selective incorporation of Ln ions is crucial for achieving programmed functionalities.⁴ Moreover, for application purposes, synthesised compounds should be: (i) fully characterised, for a detailed understanding of the structure/property relationship; (ii) highly reproducible; (iii) kinetically inert and thermodynamically stable; and (iv) processable without alterations.

Basically, two considerations should be taken into account for the design of functional heterolanthanide systems: (i) whether different physical properties are intended to be cooperative or simply superimposed and (ii) if functionality has to be achieved in the bulk materials or at a molecular level.

When dealing with the first point, one has to bear in mind that, for efficient intermetallic communication (magnetic coupling, electron transfer, energy transfer), the distance between the interacting Ln ions must be reduced below 3.5–4 Å for mechanisms requiring orbital overlap (Dexter energy transfer, magnetic exchange) or below 10 Å for efficient dipolar through-space interactions (Förster resonance energy transfer, magnetic dipolar interactions), see Fig. 2.^{4a,7,8}

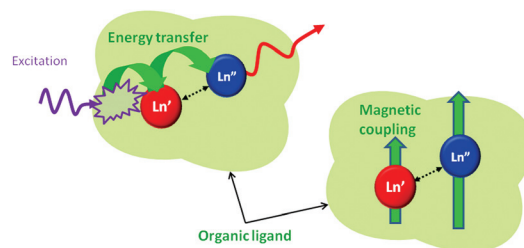


Fig. 2 A schematic representation of the intermetallic communication by energy transfer or magnetic coupling between close-contact lanthanide pairs embedded in an organic framework.

Intermetallic separation control can be achieved through the use of bridging ligands/atoms, multi-compartmental flexible receptors or by programmed supramolecular interactions, such as hydrogen bonding, π -stacking between adjacent coordinated ligands, or halogen bonding. This is definitely a crucial factor to be considered, as undesired and uncontrolled interactions between Ln ions, especially energy transfer, may severely alter the properties exhibited by the system and hamper their interpretation.

The second point that has to be addressed more generally concerns the intended final application purpose for these multifunctional materials. To give some practical examples, while several technological applications (*e.g.* in photonic devices), take general advantage of the properties of a material processed in bulk as long as sample homogeneity is ensured, on the other hand, exploitation of single-molecule properties is clearly compulsory for certain uses (*e.g.* as bioassays and catalysts), *i.e.* when simultaneous independent functionalities of active centres interacting with an external matrix are sought. This brings to attention one of the biggest challenges in the design of heterolanthanide polynuclear arrays, *i.e.* the achievement of metal composition and speciation control at the molecular level aimed at obtaining purely heterometallic compounds. In fact, the discrimination of trivalent Ln cations is severely hampered by the close similarity of their chemical behaviour and ionic radii along the series. Therefore, statistical metal distribution over available alike coordination sites inevitably governs the synthesis of heterolanthanide compounds. While this can certainly be advantageous in some cases, especially when dealing with materials intended to be used as solid state or processed samples, it represents a severe limitation when single-molecule properties are sought. Some synthetic approaches have been proposed in this regard in recent years, essentially based on two main concepts: self assembly by size selectivity or multi-step sequential metallation. However, very rare examples of purely heterometallic molecules have been isolated so far, leaving large room for improvement and for the further development of methods of general validity.

In light of these considerations, three main classes of heterolanthanide assemblies can be discussed: multi-dimensional frameworks such as metal-organic-frameworks (MOFs) and chain polymers; polynuclear discrete molecules; and large molecules formed by two or more coordinating units connected by a linker.

B. Multi-dimensional frameworks

Lanthanide-containing coordination polymers (CPs) have been investigated in the last decade in view of their potential applications in gas storage, sensing, heterogeneous catalysis, chemical separation and drug delivery.⁹ These materials offer the opportunity to mix lanthanide ions in a framework consisting of repeating equivalent coordinating units, so that the metal properties are independent to the occupied coordination sites. This makes heterolanthanide CPs interesting in view of a random statistical distribution of Ln ions over the coordination framework that provides homogeneity of the structural features and the physical properties across the bulk material. Moreover, these architectures allow the modulation of inter-metallic distances through an appropriate selection of the organic linker, so that cooperative or superimposed independent functionalities between active metal centres can, in principle, be achieved.

CPs are usually prepared through one-step reactions of the selected Ln salts in a desired stoichiometric amount and an organic linker (by reaction in solution, diffusion into gels, or by molten salt or solvothermal syntheses). However, post-synthetic modifications have also been used, in which Ln ions are incorporated into a preformed organic framework, to prevent structural alterations.^{9f,10}

Heterolanthanide multi-dimensional networks, have so far been studied mainly in view of their luminescence properties. Recently, heterolanthanide MOFs have been smartly proposed as NIR or Vis luminescent barcodes, taking advantage of the narrow, non-overlapping and easily distinguishable emission lines of Ln ions (Fig. 3).^{10–13}

In these materials, organic antenna ligands can be introduced, enabling the simultaneous emission of different lanthanide ions upon single-wavelength excitation. A wide variety of barcodes can thus be obtained simply by varying the metal stoichiometry, so long as the optically active Ln centres are homogeneously distributed across the framework and kept

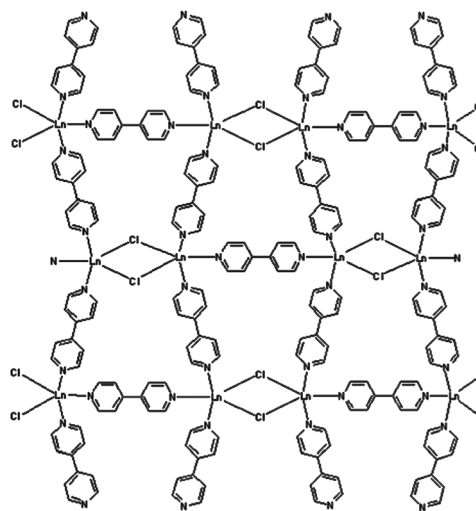


Fig. 4 The structure of ${}^2[\text{Gd}_{2-x-y}\text{Eu}_x\text{Tb}_y\text{Cl}_6(\text{bipy})_3]\cdot 2\text{bipy}$. Reproduced from ref. 13.

far enough apart (*e.g.* by using large organic linkers) to avoid undesired and uncontrolled intermetallic energy transfers that can significantly affect the emission properties. In this regard, the non-luminescent Gd^{3+} ion has been used as a codopant in ${}^2[\text{Gd}_{2-x-y}\text{Eu}_x\text{Tb}_y\text{Cl}_6(\text{bipy})_3]\cdot 2\text{bipy}$ MOF, to dilute the two communicating Tb^{3+} and Eu^{3+} ions, separated by a short bipy ligand (Fig. 4), allowing the modulation of the emission colour, resulting from the overlap of the green Tb^{3+} emission (${}^5\text{D}_4 \rightarrow {}^7\text{F}_J$, $J = 6-3$) and the red Eu^{3+} one (${}^5\text{D}_0 \rightarrow {}^7\text{F}_J$, $J = 0-4$), on varying the metal content.¹³ Interestingly, it has also been observed that Gd^{3+} codoping can enhance the luminescence of $\text{Ln}^{3+}:\text{Y}_2\text{WO}_6$ ($\text{Ln} = \text{Sm}, \text{Eu}, \text{Dy}$) microstructures.¹⁴

Another proposed application for mixed Ln CPs relies on their use as luminescent thermometric probes. In fact, it is well known that luminescence intensity decreases when temperature increases as a consequence of the thermal deactivation of excited states. In the heterolanthanide ${}^\infty[\text{Ln}(\text{L})_2(\text{NO}_3)_2]\cdot \text{Cl}\cdot 2\text{H}_2\text{O}$ ($\text{Ln} = \text{Eu}, \text{Tb}$, and Gd ; $\text{L} = 1,4\text{-bis}(\text{pyridinil-4-carboxylato})\text{-1,4-dimethylbenzene}$) CP (Fig. 5a), temperature sensitivity in the luminescence is observed as the $\text{Tb} \rightarrow \text{Eu}$ energy transfer efficiency is thermally enhanced (from 22.64% at 25 K to 34.41% at 200 K).

The emission intensity ratio $I_{\text{Tb}}/I_{\text{Eu}}$ (${}^5\text{D}_4 \rightarrow {}^7\text{F}_5$, Tb^{3+} , 544 nm to ${}^5\text{D}_0 \rightarrow {}^7\text{F}_2$, Eu^{3+} , 613 nm), can therefore be used as a self-referenced signal probe for temperature (Fig. 5).¹⁵

In light of these few examples, it is clear that heterolanthanide CPs are promising for several applications in view of the functionalities attainable in these materials. Among the numerous figures of merit, such as their structural porosity (for uses as host matrices), they can also incorporate a high density of active metal centres homogeneously dispersed across the bulk material. However, little control can be achieved in the Ln distribution, so mixed Ln CPs can best perform as “diluted” materials where independent physical properties carried by different Ln^{3+} ions are superimposed. The numerous possible distance-dependent Ln–Ln interactions

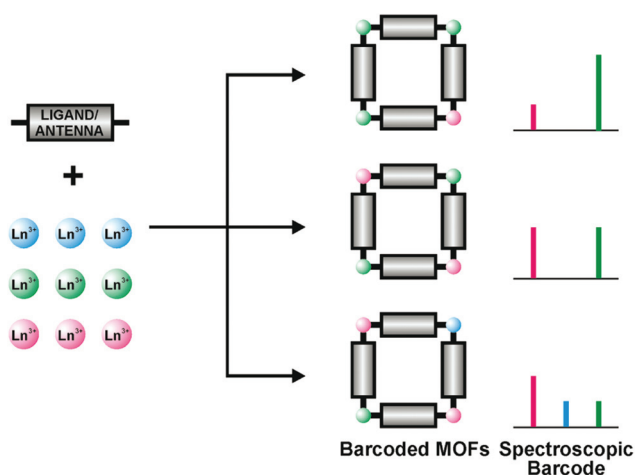


Fig. 3 A schematic representation of a Ln-based barcoded material. Reproduced with permission from ref. 11. Copyright 2009 American Chemical Society.

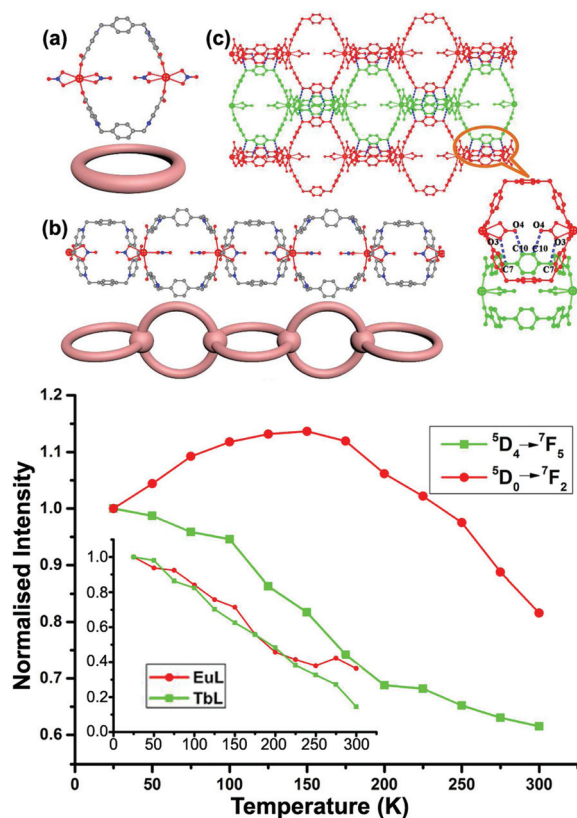


Fig. 5 Above. Structure of the heterometallic Eu–Tb ∞ [Ln(L) $_2$ (NO $_3$) $_2$].Cl·2H $_2$ O CPs: (a) Ring-like structure unit. (b) One dimensional chain structure and the simplified diagram. (c) Two dimensional supramolecular layer. All the hydrogen atoms, chlorine atoms, and water molecules have been omitted for clarity. Blue dot line: hydrogen bond. Below. Luminescent response to the temperature for Eu (red) and Tb (green) compared with the trends for the corresponding homometallic CPs (in the inset). Adapted from ref. 15.

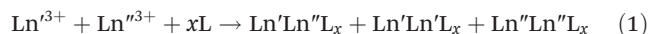
can in fact be difficult to control so that recognition and quantification of the resulting properties may be complicated.

C. Discrete polynuclear molecules

Discrete polynuclear complexes can offer several advantages for the development of functional molecular materials for application purposes. In fact, they can often be easily processed through convenient, easy-to-handle, solution methods or by techniques commonly used for the fabrication of technological devices, such as vacuum deposition, without altering their properties.¹⁶ In addition, unlike CPs, control of the separation between the lanthanide ions and their relative positions, is, in principle, feasible through judicious chemical design. This means that it would be possible to achieve controlled efficient energy transfer or magnetic coupling between different Ln ions sitting at short distances in rigid, preorganized positions in the same molecular architecture. This can be accomplished through the use of small bridging coordinating units such as CN $^-$, oxalate,^{4a} ligands having suitable bridging atoms,^{7,17–19} multi-compartmental macrocycles,^{4,20} and flexible multidentate ligands.^{8,21–24} Some significant examples

of ligands used to prepare polynuclear heterolanthanide complexes with short intermetallic separation and their coordination modes are reported in Chart 1.^{4,7,17–24}

Generally, the easiest and least time/resources-consuming synthetic approach for heterolanthanide polynuclear assemblies, consists of a one-pot reaction between the selected metal salts and the ligand(s) in suitable ratios, taking advantage of the very similar reactivity of the Ln ions across the series. The corresponding downside is that, in the absence of some metal selectivity restrictions, statistical mixtures of homo- and heterolanthanide complexes are invariably obtained. In general, for a bimetallic complex with ligand L:^{4,7,18–23}



Relative abundances of 50% for the heterometallic, and 25% for the homometallic species, are predicted for a 1:1 Ln $^{\text{r}}$:Ln $^{\text{n}}$ molar ratio, while this statistical distribution can be tuned on varying metal composition. Following this reaction scheme, heterobimetallic compounds such as [Er $_x$ Yb $_{3-x}$ (Q) $_9$],⁷ (ligand I, Chart 1), [Er $_x$ Yb $_{0.6}$ (Ba) $_6$ (Phen) $_2$] and [ErYb-(Pba) $_6$ (Phen) $_2$],¹⁹ (ligand III, Chart 1), have been obtained. [La $_{1-x}$ Ln $^{\text{n}}$ (L 2)(NO $_3$) $_4$].1.2CH $_3$ OH (Ln $^{\text{n}}$ = Tb, Eu) complexes with the macrocyclic ligand L 2 (IV, Chart 1), have been prepared in a similar procedure with the La:Tb and La:Eu ratios in the reaction mixtures being 8:2 and 9:1, respectively.^{20a} Likewise, a series of mixed lanthanide compounds [Ln $^{\text{r}}_{1-x}$ Ln $^{\text{n}}$ (L 7)(NO $_3$) $_2$]. n CH $_3$ OH (Ln $^{\text{r}}$ = Gd or Lu; Ln $^{\text{n}}$ = Eu or Tb) have been isolated with the acyclic Schiff base ligand L 7 (V, Chart 1).^{21a} A slight modification of the aforementioned synthetic pathway (1) allows the use of Ln acetylacetonate complexes, [Ln(acac) $_3$].H $_2$ O as precursor materials. Direct reaction of Ln $^{\text{r}}$ and Ln $^{\text{n}}$ precursors in a 1:1 molar ratio in solution yields dimeric species [Ln $^{\text{r}}\text{Ln}^{\text{n}}$ (acac) $_6$] (Ln $^{\text{r}}$ = Tb, Ln $^{\text{n}}$ = Eu), linked by oxo-bridges (ligand II, Chart 1),¹⁸ whereas when using the salen ligand (VI, Chart 1) as a unit assembler, [Ln $^{\text{r}}\text{Ln}^{\text{n}}$ (salen) $_2$ (acac) $_2$] (Ln $^{\text{r}}$ = Er, Ln $^{\text{n}}$ = Yb) is formed.^{21b}

Small deviations in the statistical abundances of the molecular species have occasionally been observed as a consequence of the differences in their reactivities upon ligand coordination to the Ln ions belonging to the first (La–Eu), or the second (Gd–Lu) half of the series.^{25a} Instead, for the mixed lanthanide compounds [Ln $^{\text{r}}_x\text{Ln}^{\text{n}}_{2-x}$ (L 8)(DMF) $_5$]. n DMF (Ln $^{\text{r}}$ = Eu, Tb; Ln $^{\text{n}}$ = Nd, Tb, Gd, Ho) with the macrocyclic *p*-*tert*-butylcalix[8]arene ligand L 8 (VII, Chart 1), ICP-AES determination of the Ln $^{3+}$ content shows a clear selectivity of the ligand for ions in the middle of the lanthanide series.^{20b} Lanthanide ions can, in fact, be solely discriminated on the basis of a continuous and smooth decrease in their ionic radii (lanthanide contraction) that barely drops, about 15%, on going from La $^{3+}$ to Lu $^{3+}$, with a \sim 1% variation between two successive lanthanides with a relative maximum (cusp) corresponding to the half-filled 4f 7 shell of Gd $^{3+}$ (Fig. 6).²⁶ To address this point, the most reasonable route relies on polynuclear architectures where coordination sites are inequivalent, *i.e.*, by tailoring binding sites for the specific recognition of Ln ions. This task

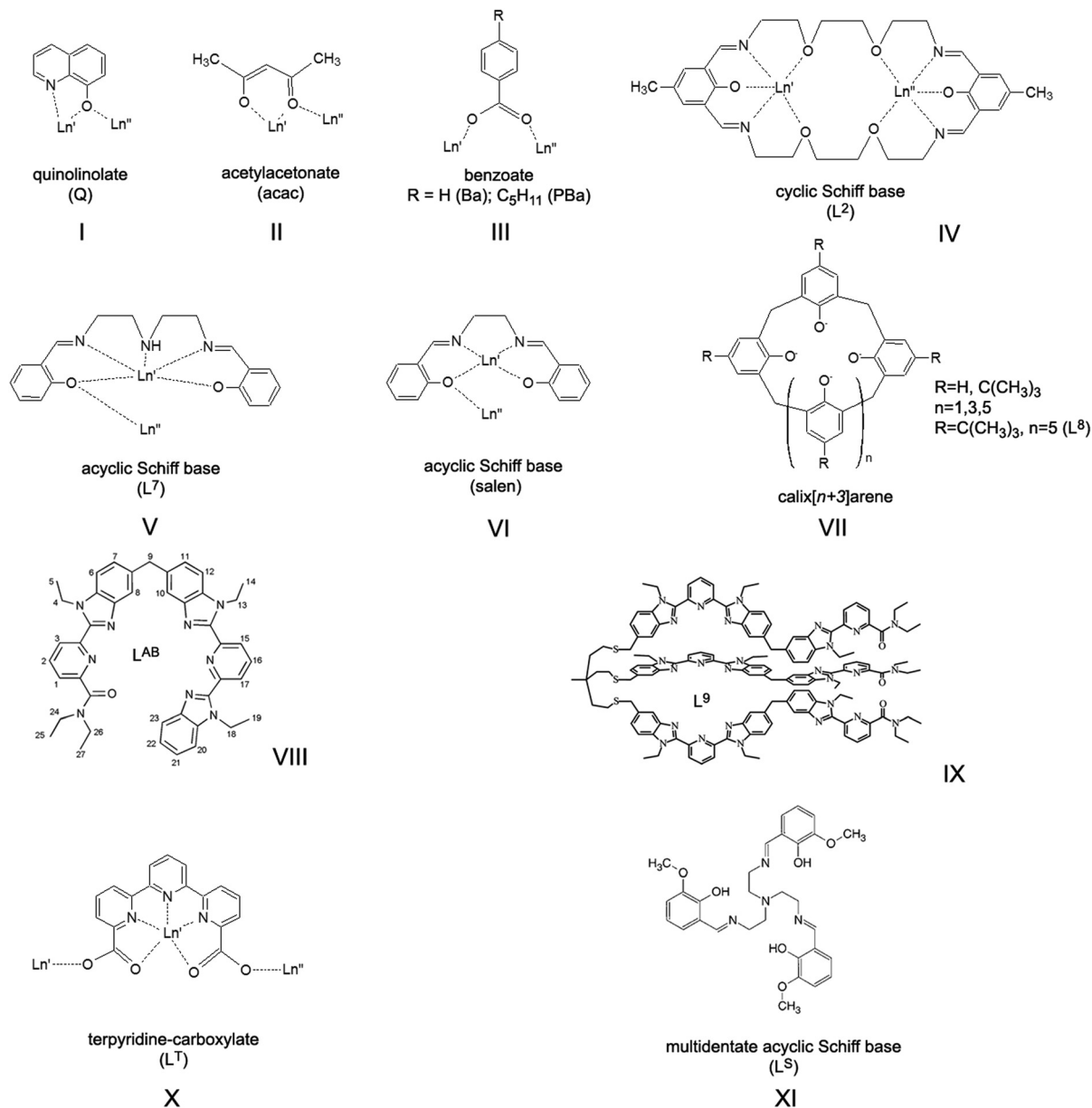


Chart 1

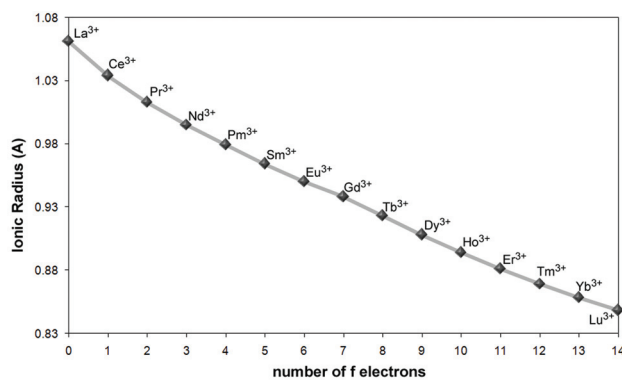


Fig. 6 The ionic radii of trivalent lanthanide ions with a coordination number of six.²⁶

can be particularly complicated in view of the flexible coordination behavior of the Ln ions, for which coordination numbers ranging from 6 to 12 are likely to be observed.

This has so far limited the strive toward pure discrete heterolanthanide complexes through simple one-pot reactions, and only very few examples are to be mentioned in this regard. In particular, Bünzli and coworkers have extensively investigated bimetallic helicates with flexible multidentate ligands as selective dinucleating agents.²² Specifically, ligand L^{AB} (VIII, Chart 1), has been elegantly designed to host two Ln ions in two different cavities formed after self-assembly of a triple-stranded helicate [Ln'Ln''(L^{AB})₃]⁶⁺. This synthetic approach takes advantage of the templating effect arising from the N₂O coordination moiety, favoring the complexation of small

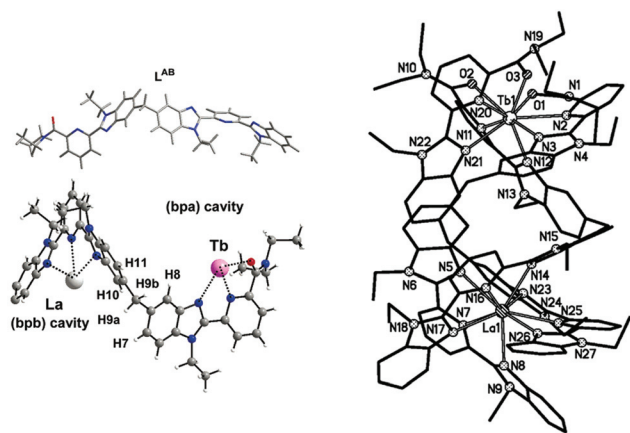
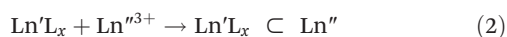


Fig. 7 Left, the L^{AB} ligand structure and coordination modes and right, the crystal structure of the $[LaTb(L^{AB})_3]^{6+}$ complex. Adapted with permission from ref. 22b. Copyright 2004. American Chemical Society.

lanthanides, and the more rigid N_3 binding unit, which, on the other hand, is better suited for large lanthanides (La–Gd) due to the stabilisation of the ligand wrapping around the ion (see Fig. 7). Accurate molecular speciation studies in solution by means of mass spectrometry and NMR have evidenced the remarkably high yield (90%) of the thermodynamic formation of the heterometallic complex in the case of a La–Lu pair, having the largest ionic radius difference ($\Delta_{La-Lu} = 0.18 \text{ \AA}$). For other lanthanide pairs, the size selectivity significantly decreases as the difference in ionic radii decreases. However, this size discriminating effect still remains the most relevant example reported in the literature so far in the case of one-pot syntheses. Unfortunately, ligand conformational flexibility, giving rise to head-to-head-to-head (HHH) and symmetrical head-to-head-to-tail (HHT) isomers, has hampered further investigations of these systems. Similar results have been more recently predicted by Piguet and his group, for the $[LaLu(L^9)]^{6+}$ complex with a tripodal ligand IX in Chart 1.

Very recently, relevant ion-size-driven control of molecular speciation has been reported in the case of the trimetallic $[Nd_yEr_xYb_{3-(x+y)}(Q)_9]$ compound which shows multiple NIR emissions upon single-wavelength excitation of the Q ligand. Results obtained from XRD structural studies, EDX and ICP-mass analyses and ESI-mass spectrometry, have evidenced that the lighter and larger Nd^{3+} ion can be chemically discriminated from the heavier and almost “vicariant” Er^{3+} and Yb^{3+} ions and helps to control molecular speciation, leading to an approximately 90% formation of the heterometallic species $[NdLn_2(Q)_9]$ ($Ln = Er, Yb$).^{7b}

A second synthetic approach makes use of preformed lanthanide complexes with peripheral binding arms (see ligands X and XI, Chart 1) that are able to react with a second lanthanide ion:^{8,17,24}



Following this route, a few examples of pure heterometallic species have been isolated and structurally characterised, such

as the $[Lu \subset (EuL^T)_6](Otf)_9$ complex, with the terpyridine derivative ligand X (Chart 1) and the $[(YbLa)L^S(NO_3)_2]_2 \cdot [La(NO_3)_5(H_2O)]$ complex with the multidentate acyclic Schiff base ligand L^S (XI, Chart 1).^{8a,17,24} However, an excess of the Ln^{n3+} salt is often necessary to ensure product formation, leading to cocrystallisation of multiple species. Moreover, due to complex lability, dissociation and scrambling effects, mixtures of homo- and heterometallic species are likely to occur, and accurate studies of molecular speciation in solution (by NMR and mass spectrometry) are needed to ensure that the considered product is the stable thermodynamic one rather than a kinetic intermediate.^{4a,24}

The evident limit of both of the described synthetic strategies is represented by the mandatory requirement of pairing lanthanide ions with a relevant difference between their ionic radii to reach for high selectivity. Unfortunately, the very rare examples available in the literature of highly discriminated, structurally characterised, heterometallic complexes, usually comprise optically and magnetically silent lanthanide ions such as La^{3+} and Lu^{3+} , to take advantage of the extreme limits of ionic radii along the series (La^{3+} is the largest, first term of the Ln series whereas Lu^{3+} places right at the end being the heaviest and smallest lanthanide ion). This points out the stringent need to further develop suitable synthetic methods and ligands for achieving a better tunability of the selectivity properties with the aim to couple selected optically/magnetically active lanthanide ions in purely heterometallic assemblies that show programmed functionalities.

Intermetallic communication in discrete polynuclear architectures. Costes and coworkers⁸ have studied interlanthanide magnetic coupling in a series of hetero-bi-lanthanide complexes with the ligand L^S (XI, Chart 1). In these compounds, the $Ln' \cdots Ln''$ separation, predicted on the basis of the only structurally characterised $[YbLa(L^S)(NO_3)_2]_2 \cdot [La(NO_3)_5(H_2O)]$ complex, lies below 4 \AA . This has allowed the identification of unusual intramolecular ferromagnetic interactions between the Yb–Gd, Gd–Nd and Gd–Ce pairs.

However, the investigation of the magnetic properties of heterolanthanide pairs embedded in the same coordination framework has so far been limited, whereas the intermetallic resonance energy transfer (RET) in luminescent compounds has attracted more attention in past years for the development of directional molecular light converters. In this regard, it has to be pointed out that, since energy transfer requires energy matching of excited levels, only selected couples of lanthanide ions can give rise to efficient interplay of optical properties. Among them, $Tb \rightarrow Eu$ and $Yb \rightarrow Er$ RET mechanisms have been studied the most, respectively in visible ($Eu^{3+} \ ^5D_0 \rightarrow \ ^7F_j$, 615 nm) and near-infrared ($Er^{3+} \ ^4I_{13/2} \rightarrow \ ^4I_{15/2}$, 1540 nm) luminescent materials (Fig. 8). This phenomenon can, in fact, be of particular importance for the enhanced excitation of poorly ligand-sensitised Ln ions or as a diagnostic tool for assessing intermetallic distances, for example for the investigation of protein structures.²⁷

The RET from a donor (Ln') to an acceptor (Ln'') is in fact a dipolar distance-dependent through space mechanism

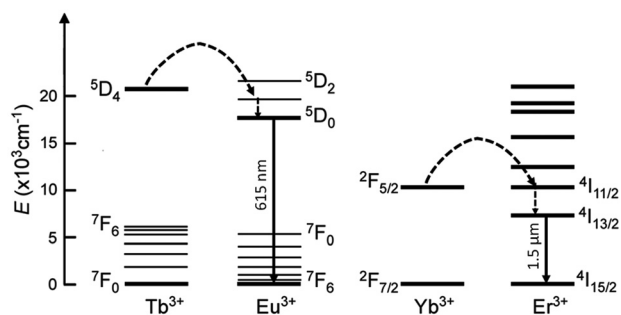


Fig. 8 Simplified resonance energy transfer mechanisms in the Tb → Eu and Yb → Er pairs. Dashed arrows represent non-radiative processes.

(Förster RET), whose effectiveness, η_{RET} , is mainly regulated through the interlanthanide separation R and the Förster radius R_0 (which can be determined spectroscopically²⁸ and can be calculated through use of the following equations:

$$\eta_{\text{RET}} = \frac{1}{1 + \frac{\tau_{\text{RET}}}{\tau_0}} \quad (3)$$

$$\frac{1}{\tau_{\text{RET}}} = \frac{1}{\tau_0} \left(\frac{R_0}{R} \right)^6 \quad (4)$$

where τ_{RET} is the RET time constant and τ_0 is the experimental decay time of the donor in the absence of the acceptor.

It must be pointed out that, for an accurate assessment of interlanthanide RET efficiency, a close investigation of molecular speciation is crucial to determine the τ_{RET} value for purely heterometallic molecules. Among the few relevant examples reported in the literature, a remarkable Tb → Eu $\eta_{\text{RET}} = 76\%$ value was found for a triple-stranded helicate with a symmetrical derivative of ligand **VIII** in Chart 1, where the distance between the two lanthanide ions lies around 9 Å.^{22c} Recently, a fully efficient Yb → Er RET at the molecular level has been demonstrated in trinuclear Yb₂ErQ₉ (Q = quinolinolate, ligand **I**, Chart 1), where the intermetallic separation is below 3.5 Å.^{7a} The Er³⁺ sensitisation is in this case the result of a two step process involving ligand photoexcitation followed by efficient RET to Yb and then to Er. This latter example is of particular significance as lanthanide quinolinolates have been studied for a long time as luminescent active centers in optoelectronic devices and their processing potential is therefore well known.^{16b-d,25b} See Fig. 9.

As already pointed out in this paper, full disclosure of the optical or magnetic properties resulting in functional/multi-functional lanthanide systems requires the knowledge of their structural arrangement. Moreover, it is crystal clear that the final properties of the product, obtained following the above described synthetic approaches, will result from the independent contribution of the different species of which it consists, *i.e.* a superposition of the properties of hetero- and homo-metallic molecules weighted to their respective amounts in the sample.^{7b} While purely heterometallic compounds are certainly advantageous for practical applications to ensure

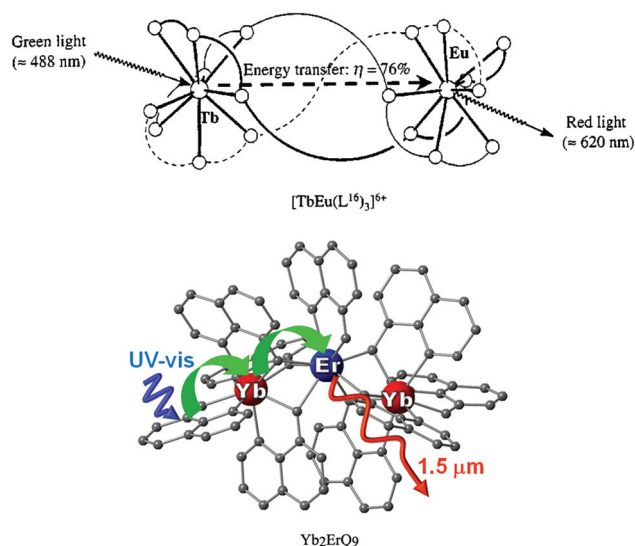
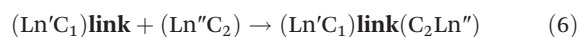
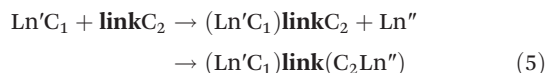


Fig. 9 Schematic representations of the light conversion in a Tb–Eu triple-stranded helicate (above) and in a trinuclear Yb₂ErQ₉ complex. Adapted with permission from ref. 22c and 7. Copyright 1993, 2013. American Chemical Society.

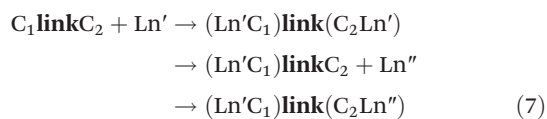
homogeneity and control of the emission signal at the molecular level, nonetheless programmed speciation of hetero- and homo-metallic mixtures (*e.g.* by varying reactant stoichiometry in the synthetic procedure) can be useful for achieving tunability of the different Ln emission intensities in broadband emitters. This latter approach can therefore be parallel to that described for multi-dimensional coordination polymers, with the additional advantage of the higher processability of small molecules.

D. Preformed coordinated units connected with a linker

The most effective strategy for affording purely heterometallic assemblies relies on multi-step synthetic procedures involving preformed coordinating units (C_n) connected with a covalent linker (**link**), according to the following proposed reaction pathways:^{29–31}



The downside of these smart synthetic approaches, however, is that the completeness of the reaction leading to the formation of covalent bonding between the organic moieties cannot be effectively controlled. Therefore, a mixture of the desired heterometallic complex and the starting precursors is likely to result,³¹ and additional separation steps (*e.g.* by chromatography) are required to isolate the pure product. A variation of reaction schemes (5) and (6) is represented by sequential metallation/selective demetallation/metallation steps:³²



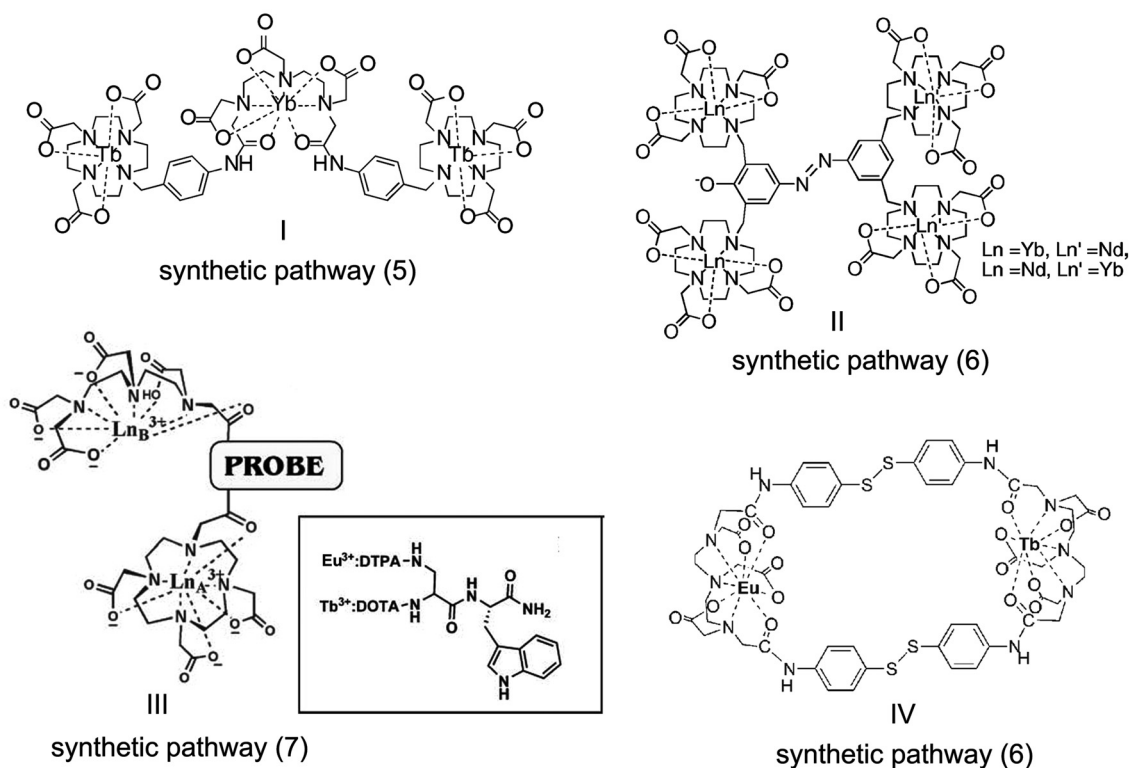


Chart 2

This reaction pathway takes advantage of the decomplexation behaviour of the C₂ unit under specific conditions, in that it is efficient enough to leave a coordination site free to accommodate a second Ln' cation, with a high yield.³²

A few examples of these quite large and flexible assemblies prepared according to the above mentioned synthetic pathways are reported in Chart 2. Unfortunately, no X-ray diffraction studies are available so far, likely as a consequence of ligand fluxionality, so intermetallic distances can be only assessed through molecular structure modelling. In particular, interesting conclusions can be drawn from the structural arrangement of the Tb–Eu complex **IV**, Chart 2, on the basis of photophysical studies. In fact, estimation of the Tb → Eu RET efficiency (66%) from the experimental determination of the Tb³⁺ emission lifetime in the hetero- and in the corresponding homodimetallic complex (τ_{RET} and τ_0 , respectively, see eqn (3)), is in better accordance (eqn (4)) with a *pseudo-endo* molecular configuration (Fig. 10b) rather than a *protracted* arrangement (Fig. 10a), where the estimated intermetallic distance is much higher (7.8 Å and 17.8 Å for the two configurations, respectively).

In the case of the Tb–Eu complex **III** in Chart 2, an interesting emission spectral change upon the variation of solvent polarity is observed, *i.e.* enhancement of the Eu³⁺ luminescence intensity and the corresponding decrease of the Tb³⁺ emission when passing from water to alcohols. A possible explanation for this phenomenon may rely on molecule fluxionality and configurational changes leading to a shorter inter-

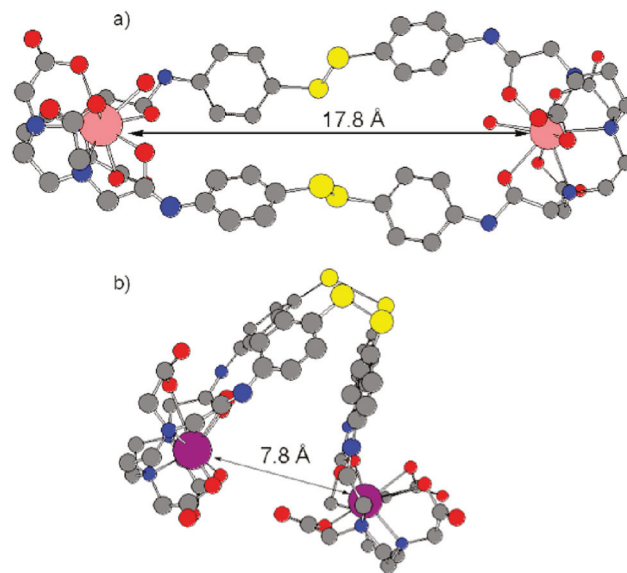


Fig. 10 Structural models for complex **IV**, Chart 2 in *protracted* (a) and *pseudo-endo* (b) configurations. Reproduced with permission from ref. 31. Copyright 2011 American Chemical Society.

metallic separation in less polar solvents and consequently an enhanced Tb → Eu RET. This makes complex **III** a potential ratiometric probe for solvent polarity.

These flexible polynuclear molecules bearing specific coordination sites are therefore suitable for achieving, in

principle, purely heterometallic assemblies through accurate ligand design and rational synthesis. However, the lack of the structural control over intermetallic distances and the coordination environments in these systems makes them ideal candidates when independent active sites in a single molecule are sought, for example for multiple emissive bioprobes, double-function MRI contrast agents and luminescent sensors, and catalysts with multi-active sites.

Conclusions

Heterolanthanide coordination compounds are extremely promising materials, with the potentiality of showing multifunctionality depending on the nature of the Ln ions and optical or/and magnetic properties, and are of interest for several applications. The rich and versatile chemistry of the f-elements allows the preparation of a variety of coordination edifices through ligand design and rational synthetic strategies. Three main classes of compounds have been selected on the basis of their structural arrangement, which determines the interplay or coexistence of the physical properties (related to the entity of metal separation), and their application as bulk materials or single-molecules.

Multi-dimensional frameworks, where Ln ions are randomly distributed over the available coordination sites can best perform as “diluted” bulk materials where functionality results from a superposition of different properties related to non-interacting active metal centres. These kind of edifices have been successfully proposed as luminescent barcodes where tunability of emission lines can be achieved by varying the metal content.

Conversely, discrete and rigid heterometallic molecules offer the potential advantage of controlling intermetallic communication (magnetic coupling, resonance energy transfer) between Ln ions sitting at short distances and in fixed positions in the same, solution-processable, molecular architecture. A variety of magnetically active materials or directional light converters can be obtained in this way. However, in this context, the big chemical challenge is represented by severe limits in the discrimination of Ln ions, and synthetic approaches that often lead to the isolation of statistical mixtures of hetero- and homometallic species. Whereas these multi-speciated compounds can be nonetheless of interest for applications as bulk materials (e.g. as tunable broadband emitters in photonic devices), a step toward the isolation of purely heterometallic molecules can be made by taking into account a third class of coordination assemblies. These are usually large and flexible architectures consisting of preformed coordinating units, hosting different Ln ions, connected with an organic linker. Efficient discrimination of Ln ions can in principle be achieved through programmed synthesis and ligand design. However, the flexibility and fluxionality of these systems hamper the control of intermetallic communication. Therefore these assemblies can be proposed for applications

where specific functionalities of independent active sites embedded in a single-molecule, can be exploited.

It is evident that the potentialities of heterometallic assemblies look well beyond the examples described in this paper, and a wide variety of (multi-) functional materials can be explored. This should stimulate the strive for a deeper understanding and further development of the complex coordination chemistry of the lanthanides. For this reason, a precise study, corroborated by robust experimental analyses on solid state and solution samples, of all of the equilibria involved in the selected reaction pathway, to reach a detailed picture of molecular speciation and therefore the reactivity of the different Ln ions, must not be neglected. Despite this point generally seeming to be only barely addressed in the literature, it is, nonetheless, of basic importance, not only to achieve fully characterised functional materials for application purposes, but also to provide a theoretical and experimental background for improving methodologies for the recovery and separation of these metals. This is of crucial importance to exploit the recycling of Ln-based end-life devices as a secondary source for these elements in view of their current “critical raw materials”¹ status.

Acknowledgements

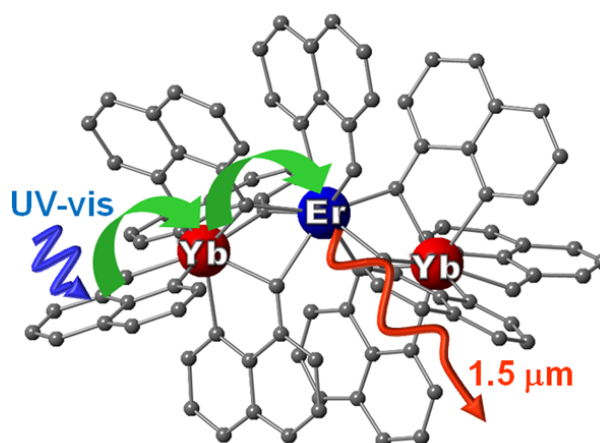
The Regione Autonoma della Sardegna (CRP-17571) and Banco di Sardegna Foundation are gratefully acknowledged for financial support.

Notes and references

- 1 European Commission, Report on critical raw materials, May 2014.
- 2 (a) *Rare Earth Coordination Chemistry, Fundamentals and Applications*, ed. C. Huang, Wiley, 2010; (b) J.-C. G. Bünzli and C. Piguet, *Chem. Soc. Rev.*, 2005, **34**, 1048.
- 3 (a) M. C. Heffern, L. M. Matosziuk and T. J. Meade, *Chem. Rev.*, 2014, **114**, 4496; (b) D. N. Woodruff, R. E. P. Winpenny and R. A. Layfield, *Chem. Rev.*, 2013, **113**, 5110; (c) M. Ferbinteanu, T. Kajiwara, K.-Y. Choi, H. Nojiri, A. Nakamoto, N. Kojima, F. Cimpoesu, Y. Fujimura, S. Takaishi and M. Yamashita, *J. Am. Chem. Soc.*, 2006, **128**, 9008; (d) J.-C. G. Bünzli and S. V. Eliseeva, *J. Rare Earths*, 2010, **28**, 824.
- 4 (a) C. Piguet and J.-C. G. Bünzli, *Chem. Rev.*, 2002, **102**, 1897; (b) C. Piguet and J.-C. G. Bünzli, *Chem. Soc. Rev.*, 1999, **28**, 347.
- 5 (a) A. Tsubouchi and T. C. Bruice, *J. Am. Chem. Soc.*, 1994, **116**, 11614; (b) K. G. Ragunathan and H.-J. Schneider, *Angew. Chem., Int. Ed. Engl.*, 1996, **35**, 1219.
- 6 (a) S. Floquet, N. Ouali, B. Bocquet, G. Bernardinelli, D. Imbert, J.-C. G. Bünzli, G. Hopfgartner and C. Piguet, *Chem. – Eur. J.*, 2003, **9**, 1860; (b) F. Artizzu, K. Bernot, A. Caneschi, E. Coronado, J. M. Clemente-Juan, L. Marchiò,

- M. L. Mercuri, L. Pilia, A. Serpe and P. Deplano, *Eur. J. Inorg. Chem.*, 2008, 3820.
- 7 (a) F. Artizzu, F. Quochi, L. Marchiò, E. Sessini, M. Saba, A. Serpe, A. Mura, M. L. Mercuri, G. Bongiovanni and P. Deplano, *J. Phys. Chem. Lett.*, 2013, 4, 3062; (b) F. Artizzu, F. Quochi, L. Marchiò, R. Fonseca Correia, M. Saba, A. Serpe, A. Mura, M. L. Mercuri, G. Bongiovanni and P. Deplano, *Chem. – Eur. J.*, 2015, DOI: 10.1002/chem.201405634.
- 8 (a) J.-P. Costes, F. Dahan, A. Dupuis, S. Lagrave and J.-P. Laurent, *Inorg. Chem.*, 1998, 37, 153; (b) J.-P. Costes and F. Nicodème, *Chem. Commun.*, 2002, 3442.
- 9 (a) R. B. Getman, Y.-S. Bae, C. E. Wilmer and R. Q. Snurr, *Chem. Rev.*, 2012, 112, 703; (b) M. P. Suh, H. J. Park, T. K. Prasad and D.-W. Lim, *Chem. Rev.*, 2012, 112, 782; (c) L. E. Kreno, K. Leong, O. K. Farha, M. Allendorf, R. P. Van Duyne and J. T. Hupp, *Chem. Rev.*, 2012, 112, 1105; (d) J.-R. Li, J. Scully and H.-C. Zhou, *Chem. Rev.*, 2012, 112, 869; (e) P. Horcajada, R. Gref, T. Baati, P. K. Allan, G. Maurin, P. Couvreur, G. Férey, R. E. Morris and C. Serre, *Chem. Rev.*, 2012, 112, 1232; (f) N. Stock and S. Biswas, *Chem. Rev.*, 2012, 112, 933.
- 10 Y. Lu and B. Yan, *J. Mater. Chem. C*, 2014, 2, 7411.
- 11 K. A. White, D. A. Chengelis, K. A. Gogick, J. Stehman, N. L. Rosi and S. Petoud, *J. Am. Chem. Soc.*, 2009, 131, 18069.
- 12 X. Fan, S. Freslon, C. Daiguebonne, G. Calvez, L. Le Pollès, K. Bernot and O. Guillou, *J. Mater. Chem. C*, 2014, 2, 5510.
- 13 P. R. Matthes, C. J. Höller, M. Mai, J. Heck, S. J. Sedlmaier, S. Schmiechen, C. Feldmann, W. Schnick and K. Müller-Buschbaum, *J. Mater. Chem.*, 2012, 22, 10179.
- 14 A. M. Kaczmarek, K. Van Hecke and R. Van Deun, *Inorg. Chem.*, 2014, 53, 9498.
- 15 X. Meng, S.-Y. Song, X.-Z. Song, M. Zhu, S.-N. Zhao, L.-L. Wu and H.-J. Zhang, *Inorg. Chem. Front.*, 2014, DOI: 10.1039/x0xx00000x.
- 16 (a) L. Armelao, S. Quici, F. Barigelletti, G. Accorsi, G. Bottaro, M. Cavazzini and E. Tondello, *Coord. Chem. Rev.*, 2010, 254, 487; (b) F. Artizzu, F. Quochi, M. Saba, D. Loche, A. Serpe, M. L. Mercuri, A. Mura, G. Bongiovanni and P. Deplano, *Dalton Trans.*, 2012, 41, 13147; (c) C. Chen, D. Zhang, T. Li, D. Zhang, L. Song and Z. Zhen, *Appl. Phys. Lett.*, 2009, 94, 041119; (d) S. Penna, A. Reale, R. Pizzoferrato, G. M. Tosi Belleffi, D. Musella and W. P. Gillin, *Appl. Phys. Lett.*, 2007, 91, 021106.
- 17 H. B. Xu, J. G. Deng, L. Y. Zhang and Z. N. Chen, *Cryst. Growth Des.*, 2013, 13, 849.
- 18 F. Tanaka and T. Ishibashi, *J. Chem. Soc., Faraday Trans.*, 1996, 92, 1105.
- 19 (a) L. Song, Q. Wang, D. Tang, X. Liu and Z. Zhen, *New J. Chem.*, 2007, 31, 506; (b) L. Song, X. Liu, Z. Zhen, C. Chen and D. Zhang, *J. Mater. Chem.*, 2007, 17, 4586.
- 20 (a) K. D. Matthews, I. A. Kahwa and D. J. Williams, *Inorg. Chem.*, 1994, 33, 1382; (b) J.-C. G. Bünzli, P. Froidevaux and J. M. Harrowfield, *Inorg. Chem.*, 1993, 32, 3306.
- 21 (a) R. C. Howell, K. V. N. Spence, I. A. Kahwa, A. J. P. White and D. J. Williams, *J. Chem. Soc., Dalton Trans.*, 1996, 961; (b) T. Gao, Y. Yang, W. B. Sun, G. M. Li, G. F. Hou, P. F. Yan, J. T. Lia and D. D. Din, *CrystEngComm*, 2013, 15, 6213.
- 22 (a) N. André, R. Scopelliti, G. Hopfgartner, C. Piguet and J.-C. G. Bünzli, *Chem. Commun.*, 2002, 214; (b) N. André, T. B. Jensen, R. Scopelliti, D. Imbert, M. Elhabiri, G. Hopfgartner, C. Piguet and J.-C. G. Bünzli, *Inorg. Chem.*, 2004, 43, 515; (c) C. Piguet, J.-C. G. Bünzli, G. Bernardinelli, G. Hopfgartner and A. F. William, *J. Am. Chem. Soc.*, 1993, 115, 8197.
- 23 (a) P. E. Ryan, G. Canard, S. Koeller, B. Bocquet and C. Piguet, *Inorg. Chem.*, 2012, 51, 10012; (b) G. Canard, S. Koeller, G. Bernardinelli and C. Piguet, *J. Am. Chem. Soc.*, 2008, 130, 1025.
- 24 X.-Y. Chen, Y. Bretonnière, J. Pécaut, D. Imbert, J.-C. G. Bünzli and M. Mazzanti, *Inorg. Chem.*, 2007, 46, 625.
- 25 (a) S. Petoud, J.-C. G. Bünzli, F. Renaud, C. Piguet, K. J. Schenk and G. Hopfgartner, *Inorg. Chem.*, 1997, 36, 5750; (b) F. Artizzu, M. L. Mercuri, A. Serpe and P. Deplano, *Coord. Chem. Rev.*, 2011, 255, 2514.
- 26 F. A. Cotton and G. Wilkinson, *Advanced Inorganic Chemistry*, 5th edn, Wiley, N.Y., 1988, ch. 20, p. 21.
- 27 D. Chaudhuri, W. e W. Horrocks Jr., J. C. Amburgey and D. J. Weber, *Biochemistry*, 1997, 36, 9674.
- 28 Experimental R_0 values reported in the literature are usually in the range 7–10 Å.
- 29 S. Faulkner and S. J. A. Pope, *J. Am. Chem. Soc.*, 2003, 125, 10526.
- 30 M. P. Placidi, A. J. L. Villaraza, L. S. Natrajan, D. Sykes, A. M. Kenwright and S. Faulkner, *J. Am. Chem. Soc.*, 2009, 131, 9916.
- 31 D. J. Lewis, P. B. Glover, M. C. Solomons and Z. Pikramenou, *J. Am. Chem. Soc.*, 2011, 133, 1033.
- 32 M. S. Tremblay and D. Sames, *Chem. Commun.*, 2006, 4116.

Fully Efficient Direct Yb-to-Er Energy Transfer at Molecular Level in a Near-Infrared Emitting Heterometallic Trinuclear Quinolinolato Complex



Combined chemical/photophysical studies on the mixed Yb–Er trinuclear lanthanide quinolinolato compound Yb_2ErQ_9 and on the corresponding Yb_3Q_9 analogue have been performed. In the mixed-metal molecular species, the ligands, acting as a bridge, allow the two metals to lie at optimal distance for direct Yb-to-Er resonance energy transfer, which reaches nearly unitary efficiency. The obtained results show that polynuclear lanthanide complexes provide a suitable strategy for achieving effective erbium sensitization in solution-processable molecular materials.

Fully Efficient Direct Yb-to-Er Energy Transfer at Molecular Level in a Near-Infrared Emitting Heterometallic Trinuclear Quinolinolato Complex

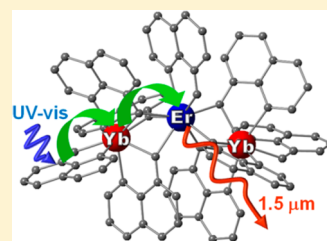
Flavia Artizzu,^{*,†,‡,||} Francesco Quochi,^{‡,||} Luciano Marchiò,[§] Elisa Sessini,[†] Michele Saba,[‡] Angela Serpe,[†] Andrea Mura,[‡] Maria Laura Mercuri,[†] Giovanni Bongiovanni,[‡] and Paola Deplano^{*,†}

[†]Dipartimento di Scienze Chimiche e Geologiche and INSTM and [‡]Dipartimento di Fisica, University of Cagliari, SS 554 Bivio per Sestu, I-09042 Monserrato-Cagliari, Italy

[§]Dipartimento di Chimica, University of Parma, Parco Area delle Scienze 17A, I-43100 Parma, Italy

Supporting Information

ABSTRACT: Combined chemical/photophysical studies on the mixed Yb–Er trinuclear lanthanide quinolinolato compound Yb_2ErQ_9 and on the corresponding Yb_3Q_9 analogue have been performed. In the mixed-metal molecular species, the ligands, acting as a bridge, allow the two metals to lie at optimal distance for direct Yb-to-Er resonance energy transfer, which reaches nearly unitary efficiency. The obtained results show that polynuclear lanthanide complexes provide a suitable strategy for achieving effective erbium sensitization in solution-processable molecular materials.



SECTION: Molecular Structure, Quantum Chemistry, and General Theory

Lanthanide ions emitting in the near-infrared (NIR) region are of considerable current interest for various applications in the telecommunication or biomedical fields.^{1–3} In fact, these ions exhibit emission peaks wavelengths falling in telecom windows and suitable penetration of the radiation in biological tissue. However, the very small absorption coefficients of the lanthanide-based absorption transitions require the use of highly efficient light-harvesting “antennas” for resonance energy transfer (RET) to the higher energy levels of these emitting ions. In recent years there has been significant interest in Er³⁺ sensitization through RET from Yb³⁺ in ion-implanted/codoped glass host materials because the absorption cross section of Yb³⁺ at 1 μm is approximately 10 times higher than that of Er³⁺ and energy transfer can occur between the ²F_{5/2} level of Yb³⁺ and the resonant ⁴I_{11/2} level of Er³⁺. Enhancement of Er³⁺ NIR emission at 1.5 μm has been achieved in glass host Yb–Er codoped optical fiber amplifiers.^{4–8} For efficient Yb-to-Er RET through a Förster’s mechanism, the distance between the two ions must be limited.⁹ However, it is often difficult to control the Er³⁺ and Yb³⁺ doping concentration accurately and homogeneously, resulting in difficult quantitative analysis of RET from Yb³⁺ to Er³⁺.² A strategy to achieve composition control can rely on the encapsulation of Er and Yb in the same molecule to afford intermetallic communication between lanthanide ions at short distance in a discrete polynuclear architecture.

So far there has been very limited work on mixed lanthanide complexes for NIR luminescence,^{10–16} and, to the best of our knowledge, there are only a couple of very recent reports of mixed Yb–Er heterobimetallic molecular complexes.^{10,11} Erbium emission enhancement was found in some of the

very few reported cases of codoped Yb–Er compounds such as mononuclear Er and Yb complexes stoichiometrically cocrystallized¹² or equimolar mixture forming dimers in solutions of noncoordinating solvents¹³ and polymeric structures.^{14,15} In these compounds, however, Yb-to-Er RET can only be observed for samples in the solid state or in solution/suspension of selected solvents. This hampers the processing potential of these materials through convenient, easy-to-handle, solution methods such as the sol–gel process¹⁷ or by techniques commonly used for the fabrication of electroluminescent devices such as vacuum deposition.^{18–20}

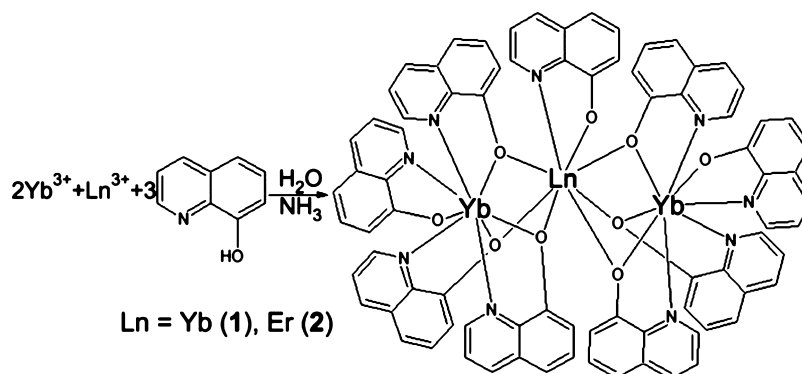
Because of its coordinating properties and bridging ability toward lanthanide ions, the 8-quinolinolato (Q) ligand is a good candidate to prepare polynuclear discrete lanthanide complexes in which the metal centers lie at short distances (within few angstroms) from each other.^{21–26} In the trinuclear Er₃Q₉^{23,24} and Ho₃Q₉²⁵ complexes the Q ligands fully saturate the metal coordination sphere and prevent water molecules (the most important quenchers for NIR emission) from directly binding to the lanthanide ion. Moreover, it has been demonstrated that 8-quinolinolato ligands are highly efficient light-harvesting “antennas” for RET to the higher energy levels of NIR-emitting lanthanide ions (sensitized emission).^{27–32}

Herein we report a novel trinuclear mixed Yb–Er quinolinolato (Q) complex, Yb_2ErQ_9 , in which fully efficient direct Yb-to-Er energy transfer is demonstrated at molecular

Received: August 9, 2013

Accepted: August 27, 2013

Scheme 1. Synthesis of 1 and 2



level in a solution-processable emissive material. To add further support to our findings, results are compared with those found for the complex Yb_3Q_9 whose trinuclear structural arrangement is newly demonstrated here.

The syntheses of Yb_3Q_9 (1) and Yb_2ErQ_9 (2) were carried out following the synthetic procedure already optimized for the preparation of Er_3Q_9 .^{23,24} 1 was synthesized using YbCl_3 as starting material through a one-pot reaction, whereas the mixed complex 2 was similarly prepared by adding Yb and Er salts in 2:1 molar ratio to the ligand solution. Microcrystalline pure products were obtained after recrystallization from CH_3CN . See Scheme 1.

Analytical data for these compounds (elemental analysis, vibrational spectroscopy in the mid- and far-infrared) compare well with those of the analogous Er_3Q_9 complex, suggesting the same stoichiometry and trinuclear structural arrangement for 1 and 2, which also have similar powder X-ray diffraction patterns (Supporting Information).

EDX analysis on crystalline samples confirms the purity and homogeneity of the compounds and provides evidence of Yb:Er molar ratio close to 2:1 in 2 (Supporting Information). The ESI-mass spectra of 1 and 2 (Figure 1) show the presence of

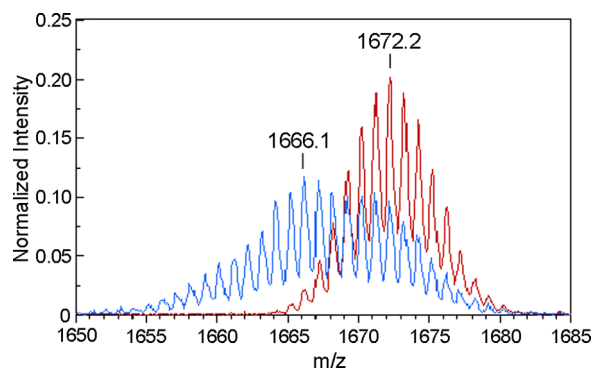


Figure 1. Expanded region of the ES(+) mass spectrum of 1 (red) and 2 (blue) in $\text{CH}_3\text{CN}/\text{MeOH}$ 3/1.

peaks related to $[\text{Ln}_3\text{Q}_9]^+$ fragments similarly to results found for Er_3Q_9 ,²³ clearly demonstrating that both compounds possess a trinuclear structure that is also preserved in solution. The most intense peak in the spectrum of 2 is related to the mixed species $[\text{Yb}_2\text{ErQ}_9]^+$ ($m/z=1666.54$), confirming the coexistence of Yb and Er in the same discrete molecular architecture. The asymmetric shape of this peak hints at a statistical mixture of Yb/Er trinuclear species in the sample. (See the Supporting Information.)

Taking the molecular structure of Er_3Q_9 as model,²³ it is then possible to reasonably assume an intermetallic $\text{Yb}^{3+}\cdots\text{Er}^{3+}$ distance of ~ 3.5 Å. Such short distance will prove crucial to allow for efficient intermetallic communication through RET between the two metals.

All of the spectroscopic and photophysical studies on the investigated compounds were performed on diluted (10^{-3} M) solutions of the strongly coordinating dimethyl sulfoxide (DMSO) solvent to ensure that the observed properties are related to isolated molecules rather than to aggregates or clusters.¹³ The NIR absorption and photoluminescence (PL) spectra of 1 and 2 are reported in Figure 2 and compared with

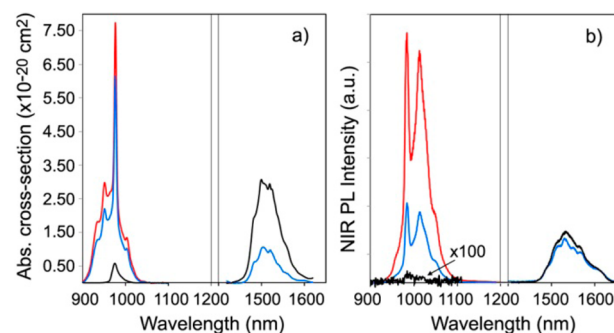


Figure 2. NIR absorption (a) and PL (b) spectra of 1 (red) and 2 (blue) compared with Er_3Q_9 (black) in DMSO solution. Er absorption cross sections at $1.5 \mu\text{m}$ are corrected for solvent effects (Supporting Information). PL spectra, obtained after ligand excitation at 392 nm, are normalized to the same complex concentration (10^{-3} M) and laser fluences.

the analogous Er_3Q_9 complex. Absorption and emission bands are related to intrashell f–f transitions of Yb^{3+} and Er^{3+} , which are slightly broadened due to small crystal field effects that partially remove the degeneracy of lanthanide f levels. 1 shows one absorption peak whose most intense line is centered at 977 nm and corresponds to the fundamental ${}^2\text{F}_{5/2} \leftarrow {}^2\text{F}_{7/2}$ transition of Yb^{3+} ($\sigma_{\text{Yb}}[{}^2\text{F}_{5/2} \leftarrow {}^2\text{F}_{7/2}] = 2.6 \times 10^{-20} \text{ cm}^2$). Two absorption bands are instead recognized for 2, which are attributed to the ${}^2\text{F}_{5/2} \leftarrow {}^2\text{F}_{7/2}$ transition of Yb^{3+} ($1 \mu\text{m}$, $\sigma_{\text{Yb}}[{}^2\text{F}_{5/2} \leftarrow {}^2\text{F}_{7/2}] = 2.8 \times 10^{-20} \text{ cm}^2$) and to the ${}^4\text{I}_{13/2} \leftarrow {}^4\text{I}_{15/2}$ transition of Er^{3+} at $\sim 1.5 \mu\text{m}$ ($\sigma_{\text{Er}}[{}^4\text{I}_{13/2} \leftarrow {}^4\text{I}_{15/2}] = 1.0 \times 10^{-20} \text{ cm}^2$). The $\text{Er}^{3+} {}^4\text{I}_{11/2} \leftarrow {}^4\text{I}_{15/2}$ transition at 980 nm is hidden by Yb absorption in 2 but is clearly visible in the spectrum of Er_3Q_9 ($\sigma_{\text{Er}}[{}^4\text{I}_{11/2} \leftarrow {}^4\text{I}_{15/2}] = 0.2 \times 10^{-20} \text{ cm}^2$). See the Supporting Information. The Yb radiative lifetimes, representing the oscillator strength of the emitter in the absence of deactivating

processes, are retrieved from absorption cross sections through the Strickler–Berg equation.³³ The obtained values $\tau_{\text{rad}} = 620 \mu\text{s}$ for **1** and $\tau_{\text{rad}} = 550 \mu\text{s}$ for **2** are in accordance with those determined for similar ytterbium quinolinolato complexes^{29,30,34} although significantly lower than “literature values” commonly accepted.³⁵

Upon excitation in the ligand lowest absorption band at 392 nm (see the Supporting Information), **1** shows NIR PL at $\sim 1 \mu\text{m}$ related to the $\text{Yb}^{3+} \text{F}_{5/2} \rightarrow \text{F}_{7/2}$ transition, while **2** displays dual NIR luminescence due to the coexistence of Yb^{3+} (977 nm, $\text{F}_{5/2} \rightarrow \text{F}_{7/2}$) and Er^{3+} (1530 nm, $\text{I}_{13/2} \rightarrow \text{I}_{15/2}$). The very weak erbium emission at 980 nm ($\text{I}_{11/2} \rightarrow \text{I}_{15/2}$), recognizable in the spectrum of Er_3Q_9 , is probably covered by the Yb^{3+} band. Noticeably, in **2** the intensity of ytterbium luminescence is $\sim 30\%$ that observed for an equimolar solution of **1**, whereas erbium emission is almost as intense as in Er_3Q_9 , where the erbium atomic ratio 1:3 between the two compounds. These findings hint at effective energy transfer taking place in **2** between Yb and Er, which can be better quantified through time-resolved spectroscopic studies. The NIR emission dynamics at 1 and $1.5 \mu\text{m}$ of **1** and **2** excited at 392 nm are reported in Figure 3 and compared with Er_3Q_9 as reference.

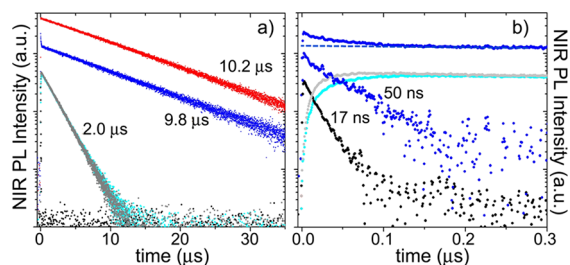


Figure 3. (a) NIR decay dynamics of **1** (red), **2** (blue), and Er_3Q_9 (black) at $1 \mu\text{m}$ and of **2** (cyan) and Er_3Q_9 (gray) at $1.5 \mu\text{m}$. (b) NIR dynamics on a short time scale of **2** (blue) and Er_3Q_9 (black) at $1 \mu\text{m}$ and of **2** (cyan) and Er_3Q_9 (gray) at $1.5 \mu\text{m}$. The short-lived component of the signal of **2** is retrieved by subtracting the long-lived component attributed to Yb_3Q_9 (dashed line). Single-exponential decay time constants are also displayed. Excitation wavelength was 392 nm. Intensities are normalized to the same complex concentration (10^{-3} M) and laser fluences.

Erbium emission is detected for **2** at $1.5 \mu\text{m}$ with the same dynamics as Er_3Q_9 ($\tau = 2.0 \mu\text{s}$). The $\text{Er}^{3+} \text{I}_{13/2}$ level in Er_3Q_9 is fed through relaxation from the higher $\text{I}_{11/2}$ level, which gives a ultrafast decay at 980 nm ($\tau = 17 \text{ ns}$), shown in Figure 3b. A monoexponential decay of Yb emission is observed for **1** at 980 nm yielding a time constant of $\tau_{\text{Yb}} = 10.2 \mu\text{s}$, so that the intrinsic quantum yield of Yb can be calculated as $\Phi_{\text{Yb}} = \tau_{\text{Yb}}/\tau_{\text{rad}} = 1.6 \times 10^{-2}$, in agreement with values already observed for analogous Yb quinolinolates.^{29–32} For **2**, two signal components are clearly distinguishable at $1 \mu\text{m}$ with associated time constants differing by almost three orders of magnitude. The longer decay signal yields approximately the same time constant as **1** ($\tau_{\text{Yb}} = 9.8 \mu\text{s}$) and can therefore be attributed to the presence of Yb_3Q_9 species in the sample. These results show that PL measurements provide useful information, not easily retrievable from conventional analytical characterization methods, of the statistical composition of **2**, which, for a nominal Yb:Er 2:1 atomic ratio, should consist of a mixture of mixed Yb–Er species, which are predominant ($\sim 44\%$ Yb_2ErQ_9 and 22% YbEr_2Q_9), and homometallic ones (ca. 30% Yb_3Q_9 and a negligible amount of Er_3Q_9). In fact, the intensity of the

longer decay component in **2** is $\sim 30\%$ of the signal of **1**, in agreement with the Yb_3Q_9 fraction in the sample. The shorter decay component of **2** can therefore be easily extrapolated by subtracting the long-lived component to the observed decay curve, as shown in Figure 3b, and a time constant of $\tau_{\text{YbEr}} = 50 \text{ ns}$ can be retrieved through monoexponential fitting. This lifetime is longer than that related to the $\text{I}_{11/2}$ level of Er^{3+} , and its intensity is about one order of magnitude higher. Therefore this ultrafast decay signal can be reliably entirely attributed to the ytterbium $\text{F}_{7/2}$ decay strongly quenched ($\Phi_{\text{Yb}} = 9.1 \times 10^{-5}$) by efficient direct energy transfer to the resonant $\text{I}_{11/2}$ level of Er^{3+} , as schematically depicted in Figure 4. These

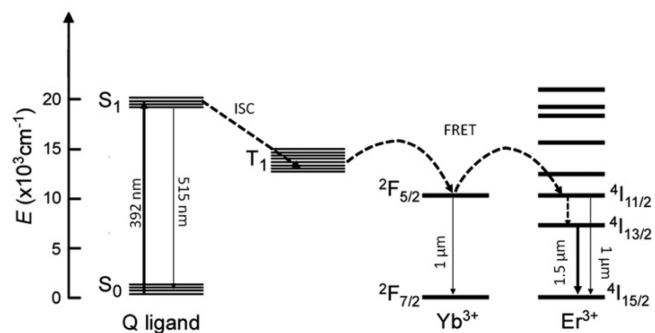


Figure 4. Jablonski diagram depicting the energy levels of the Q ligand, Yb^{3+} , and Er^{3+} and the full photocycle in trinuclear quinolinolato complexes. Dashed arrows represent nonradiative processes. Thick arrows indicate the mechanism of Yb-sensitized Er emission in mixed Yb–Er Q-complex.

considerations find further support in the analysis of the Er $1.5 \mu\text{m}$ signal rise times in Er_3Q_9 and **2**, which are compatible with the ultrafast decay time constants detected at $1 \mu\text{m}$ in the two cases (Figure 3b).

Taking into account the fact that erbium emission intensities are practically equal for equimolar solutions of **2** and Er_3Q_9 , in both emission spectra (Figure 2b) and transient PL experiments (Figure 3) in a low-excitation regime of 0.1 excitations per complex (per pulse), it can be reasonably inferred that Yb-to-Er RET in the mixed molecular system is nearly quantitative. This also sounds more realistic when considering that the ultralow lifetime of the Er $\text{I}_{11/2}$ level prevents energy back transfer to Yb. The emission spectral feature observed at $1 \mu\text{m}$ for **2** (Figure 2b) can consequently be attributed solely to the Yb_3Q_9 species. The quantum efficiency of RET can be easily quantified through the formula:

$$\eta_{\text{RET}} = \frac{1}{1 + \frac{\tau_{\text{RET}}}{\tau_{\text{Yb}}}}$$

where τ_{RET} ($= 50 \text{ ns}$) represents the Yb-to-Er RET time constant and τ_{Yb} is the lifetime of Yb emission in the absence of erbium energy acceptors. This calculation yields 99.5% efficiency of Yb-to-Er energy transfer in the mixed species. Even taking into account the inhomogeneous composition of **2**, which retains dual luminescence at 1 and $1.5 \mu\text{m}$ due to the coexistence of Yb_3Q_9 , an overall statistical average $\eta_{\text{RET}} \approx 70\%$ is predictable, which is still higher than estimations made for $\text{Yb}^{3+}\text{-Er}^{3+}$ codoped Al_2O_3 waveguides.^{4,5} By modeling this process as a dipole–dipole Förster’s resonance energy transfer (FRET)⁹ and taking a reliable estimation of Yb⋯Er distance as $r = 3.5 \text{ \AA}$, it is then possible to calculate the Förster’s radius of

$R_0 \approx 10 \text{ \AA}$, and the time constant of donor(Yb)–acceptor(Er) FRET, $\tau_{\text{RET}} \approx 20 \text{ ns}$, which is consistent with the value observed experimentally (Supporting Information).

The validity of the Förster's model for explaining Yb-to-Er energy transfer in molecular systems is further supported by results reported by Zhong et al.¹² for cocrystallized Er and Yb mononuclear complexes. In that case, taking an average Yb...Er distance of $r = 11.75 \text{ \AA}$ in the crystal packing, $\tau_{\text{RET}} = 1.4 \text{ ms}$ and $\eta_{\text{RET}} = 6.1\%$ are calculated for the solid state, in accordance with experimental data. Concerning the other example of mixed Yb–Er heteropolynuclear complexes studied by Xu et al.,¹⁰ where $r = 3.5 \text{ \AA}$ (av.), Yb-to-Er FRET time constants of $\tau_{\text{RET}} = 3.5$ and 3.7 \mu s were found in Er_2Yb_2 and Yb_2Er_2 isomers, respectively. These times are rather slow and comparable to the lifetime of $\text{Yb } ^2\text{F}_{5/2} \rightarrow ^2\text{F}_{7/2}$ emission, likely robustly quenched by the presence of OH bridging groups in the Gd_2Yb_2 (1.94 \mu s) and Yb_2Gd_2 (2.55 \mu s) reference analogs, where no intermetallic FRET is possible. This leads to an estimation of $\eta_{\text{RET}} = 35\text{--}41\%$. These efficiencies are quite low if compared with our findings, hinting at indirect energy-transfer process between Yb and Er.

In conclusion, we have prepared and studied two trimetallic lanthanide (Ln = Yb, Er) quinolinolato complexes possessing the general stoichiometry Ln_3Q_6 , the ytterbium complex (1), and the mixed Yb–Er analogue (2). ESI-mass spectrometry confirms that Yb and Er coexist in the same molecular structure in 2, and 2:1 Yb:Er ratio was further established by EDX analysis. The results of spectroscopic and time-resolved studies clearly provide evidence of direct Yb-to-Er energy transfer with nearly unity efficiency at molecular level in the mixed species. Because Yb emission is so efficiently quenched by FRET to Er, this process would likely not suffer from other competitive deactivating channels such as vibrational quenching by CH groups and even water molecules.³¹ These studies will therefore provide a relevant strategy for achieving effective erbium sensitization in polynuclear complexes, where the two metals lie at short distance in the same molecular structure. It must be remarked that the encapsulation of Yb and Er in the same molecule affords a suitable precursor that can be easily processed in solution to obtain doped optical waveguides and amplifiers with controlled composition and donor–acceptor distances within the Förster's radius. Further studies are in progress in our laboratory to optimize synthetic methods to obtain pure mixed Yb–Er complexes suitable to be processed for achieving these goals.

■ ASSOCIATED CONTENT

Supporting Information

Experimental section, FT-IR spectra, powder XRD patterns, EDX analysis, visible spectroscopy and PL transients, ESI-mass analysis, and Förster's model. This material is available free of charge via the Internet at <http://pubs.acs.org>.

■ AUTHOR INFORMATION

Corresponding Author

*Email: fartizzu@unica.it (F.A.); deplano@unica.it (P. D.).

Author Contributions

†F.A. and F.Q. contributed equally.

Notes

The authors declare no competing financial interest.

■ ACKNOWLEDGMENTS

The Regione Autonoma della Sardegna is gratefully acknowledged for financial support through POR Sardegna FSE 2007-2013, L.R.7/2007 "Promozione della ricerca scientifica e dell'innovazione tecnologica in Sardegna" (CRP-17571). We thank Dr. D. Loche for powder XRD characterization, Dr. G. Mula for NIR absorption measurements, and Drs. E. Musu and S. Podda (Laboratorio di Telemicroscopia Industriale, Sardegna Ricerche) for EDX analyses.

■ REFERENCES

- Bünzli, J.-C. G.; Piguet, C. Taking Advantage of Luminescent Lanthanide Ions. *Chem. Soc. Rev.* **2005**, *34*, 1048–1077.
- Bünzli, J.-C. G.; Eliseeva, S. V. Lanthanide NIR Luminescence for Telecommunications, Bioanalyses and Solar Energy Conversion. *J. Rare Earths* **2010**, *28*, 824–842.
- Eliseeva, S. V.; Bünzli, J.-C. G. Lanthanide Luminescence for Functional Materials and Bio-Sciences. *Chem. Soc. Rev.* **2010**, *39*, 189–227.
- Strohhofer, C.; Polman, A. Absorption and Emission Spectroscopy in Er^{3+} – Yb^{3+} Doped Aluminum Oxide Waveguides. *Opt. Mater.* **2003**, *21*, 705–712.
- Dong, B.; Feng, Z. Q.; Cao, B. S.; Zheng, J. Z. $\text{Yb}^{3+} \rightarrow \text{Er}^{3+}$ Energy Transfer in Al_2O_3 and Temperature Characteristic of Near-Infrared Photoluminescence. *J. Sol-Gel Sci. Technol.* **2009**, *50*, 383–386.
- Wong, W. H.; Pun, E. Y. B.; Chan, K. S. Er^{3+} – Yb^{3+} Codoped Polymeric Optical Waveguide Amplifiers. *Appl. Phys. Lett.* **2004**, *84*, 176–178.
- Chryssou, C. E.; Di Pasquale, F.; Pitt, C. W. Improved Gain Performance in Yb^{3+} -Sensitized Er^{3+} -Doped Alumina (Al_2O_3) Channel Optical Waveguide Amplifiers. *J. Lightwave Technol.* **2001**, *19*, 345–349.
- Chiasera, A.; Tosello, C.; Moser, E.; Montagna, M.; Belli, R.; Goncalves, R. R.; Righini, G. C.; Pelli, S.; Chiappini, A.; Zampedri, L.; Ferrari, M. $\text{Er}^{3+}/\text{Yb}^{3+}$ -Activated Silica–Titania Planar Waveguides for EDPWAs Fabricated by RF-Sputtering. *J. Non-Cryst. Solids* **2003**, *322*, 289–294.
- Förster, T. Transfer Mechanism of Electronic Excitation. *Discuss. Faraday Soc.* **1959**, *27*, 7–17.
- Xu, H. B.; Deng, J. G.; Zhang, L. Y.; Chen, Z. N. Structural and Photophysical Studies on Geometric ($\text{Er}_2\text{Yb}_2/\text{Yb}_2\text{Er}_2$) and Configurational ($\text{EuTb}_3/\text{Eu}_3\text{Tb}$) Isomers of Heterotetranuclear Lanthanide(III) Complexes. *Cryst. Growth Des.* **2013**, *13*, 849–857.
- Gao, T.; Yang, Y.; Sun, W. B.; Li, G. M.; Hou, G. F.; Yan, P. F.; Lia, J. T.; Din, D. D. Syntheses, Structure and Near-Infrared (NIR) Luminescence of Er_2 , Yb_2 , ErYb of Homodinuclear and Heterodinuclear Lanthanide(III) Complexes Based on Salen Ligand. *CrystEngComm* **2013**, *15*, 6213–6220.
- Zhong, Q.; Wang, H.; Qian, G.; Wang, Z.; Zhang, J.; Qiu, J.; Wang, M. Novel Stoichiometrically Erbium-Ytterbium Cocrystalline Complex Exhibiting Enhanced Near-Infrared Luminescence. *Inorg. Chem.* **2006**, *45*, 4537–4543.
- Tanaka, F.; Ishibashi, T. Energy Transfer between Lanthanide Ions in Dinuclear Complexes. *J. Chem. Soc., Faraday Trans.* **1996**, *92*, 1105–1110.
- White, K. A.; Chengelis, D. A.; Gogick, K. A.; Stehman, J.; Rosi, N. L.; Petoud, S. Near-Infrared Luminescent Lanthanide MOF Barcodes. *J. Am. Chem. Soc.* **2009**, *131*, 18069–18071.
- Song, L.; Hu, J.; Wang, J.; Liu, X.; Zhen, Z. Novel Perfluorodiphenylphosphinic Acid Lanthanide (Er or Er–Yb) Complex with High NIR Photoluminescence Quantum Yield. *Photochem. Photobiol. Sci.* **2008**, *7*, 689–693.
- Faulkner, S.; Pope, S. J. A. Lanthanide-Sensitized Lanthanide Luminescence: Terbium-Sensitized Ytterbium Luminescence in a Trinuclear Complex. *J. Am. Chem. Soc.* **2003**, *125*, 10526–105267.

- (17) Artizzu, F.; Quochi, F.; Saba, M.; Loche, D.; Serpe, A.; Mercuri, M. L.; Mura, A.; Bongiovanni, G.; Deplano, P. Silica Sol-Gel Glasses Incorporating Dual-Luminescent Yb Quinolinolato Complex: Processing, Emission and Photosensitising Properties of the 'Antenna' Ligand. *Dalton Trans.* **2012**, 41, 13147–13153.
- (18) Curry, R. J.; Gillin, W. P. 1.54 μm Electroluminescence from Erbium(III) Tris(8-hydroxyquinoline) (ErQ)-Based Organic Light-Emitting Diodes. *Appl. Phys. Lett.* **1999**, 75, 1380–1382.
- (19) Gillin, W. P.; Curry, R. J. 1.54 μm Erbium (III) Tris(8-Hydroxyquinoline) (ErQ): A Potential Material for Silicon Compatible 1.5 μm Emitters. *Appl. Phys. Lett.* **1999**, 74, 798–800.
- (20) Khreis, O. M.; Gillin, W. P.; Somerton, M.; Curry, R. J. 980 nm Electroluminescence from Ytterbium Tris(8-Hydroxyquinoline). *Org. Electron.* **2001**, 2, 45–51.
- (21) Artizzu, F.; Mercuri, M. L.; Serpe, A.; Deplano, P. NIR-Emissive Erbium–Quinolinolate Complexes. *Coord. Chem. Rev.* **2011**, 255, 2514–2529.
- (22) Van Deun, R.; Fias, P.; Nockemann, P.; Schepers, A.; Parac-Vogt, T. N.; Van Hecke, K.; Van Meervelt, L.; Binnemans, K. Rare-Earth Quinolinates: Infrared-Emitting Molecular Materials with a Rich Structural Chemistry. *Inorg. Chem.* **2004**, 43, 8461–8469.
- (23) Artizzu, F.; Deplano, P.; Marchiò, L.; Mercuri, M. L.; Pilia, L.; Serpe, A.; Quochi, F.; Orrù, R.; Cordella, F.; Meinardi, F.; et al. Structure and Emission Properties of Er_3Q_6 (Q = 8-Quinolinolate). *Inorg. Chem.* **2005**, 44, 840–842.
- (24) Artizzu, F.; Deplano, P.; Marchiò, L.; Mercuri, M. L.; Pilia, L.; Serpe, A.; Quochi, F.; Orrù, R.; Cordella, F.; Saba, M.; et al. New Insights on Near-Infrared Emitters Based on Er-Quinolinolate Complexes: Synthesis, Characterisation, Structural and Photophysical Properties. *Adv. Funct. Mater.* **2007**, 17, 2365–2376.
- (25) Leary, S. G.; Deacon, G. B.; Junk, P. C. The Synthesis of a Homoleptic Lanthanoid Complex of the 8-Quinolinolate Ion Directly from the Metal. *Z. Anorg. Allg. Chem.* **2005**, 631, 2647–2650.
- (26) Bozoklu, G.; Marchal, C.; Pecaut, J.; Imbert, D.; Mazzanti, M. Structural and Photophysical Properties of Trianionic Nine-Coordinated Near-IR Emitting 8-Hydroxyquinoline-Based Complexes. *Dalton Trans.* **2010**, 39, 9112–9123.
- (27) Quochi, F.; Saba, M.; Artizzu, F.; Mercuri, M. L.; Deplano, P.; Mura, A.; Bongiovanni, G. Ultrafast Dynamics of Intersystem Crossing and Resonance Energy Transfer in Er(III)-Quinolinolate Complexes. *J. Phys. Chem. Lett.* **2010**, 1, 2733–2737.
- (28) Quochi, F.; Artizzu, F.; Saba, M.; Cordella, F.; Mercuri, M. L.; Deplano, P.; Loi, M. A.; Mura, A.; Bongiovanni, G. Population Saturation in Trivalent Erbium Sensitized by Organic Molecular Antennae. *J. Phys. Chem. Lett.* **2010**, 1, 141–144.
- (29) Artizzu, F.; Quochi, F.; Saba, M.; Marchiò, L.; Espa, D.; Serpe, A.; Mura, A.; Mercuri, M. L.; Bongiovanni, G.; Deplano, P. Dual Emitting $[\text{Yb}(\text{5,7ClQ})_2(\text{H5,7ClQ})_2\text{Cl}]$: Chemical and Photophysical Properties. *ChemPlusChem* **2012**, 77, 240–248.
- (30) Shavaleev, N. M.; Scopelliti, R.; Gumy, F.; Bünzli, J.-C. G. Surprisingly Bright Near-Infrared Luminescence and Short Radiative Lifetimes of Ytterbium in Hetero-Binuclear Yb-Na Chelates. *Inorg. Chem.* **2009**, 48, 7937–7946.
- (31) Shavaleev, N. M.; Scopelliti, R.; Gumy, F.; Bünzli, J.-C. G. Modulating the Near-Infrared Luminescence of Neodymium and Ytterbium Complexes with Tridentate Ligands Based on Benzoxazole-Substituted 8-Hydroxyquinolines. *Inorg. Chem.* **2009**, 48, 2908–2918.
- (32) Albrecht, M.; Osetskaya, O.; Klankermayer, J.; Frohlich, R.; Gumy, F.; Bünzli, J.-C. G. Enhancement of Near-IR Emission by Bromine Substitution in Lanthanide Complexes with 2-Carboxamide-8-Hydroxyquinoline. *Chem. Commun.* **2007**, 1834–1836.
- (33) Strickler, S. J.; Berg, R. A. Relationship between Absorption Intensity and Fluorescence Lifetime of Molecules. *J. Chem. Phys.* **1962**, 37, 814–822.
- (34) Bünzli, J.-C. G.; Chauvin, A.-S.; Kim, H. K.; Deiters, E.; Eliseeva, S. V. Lanthanide Luminescence Efficiency in Eight- and Nine-Coordinate Complexes: Role of the Radiative Lifetime. *Coord. Chem. Rev.* **2010**, 254, 2623–2633.
- (35) Werts, M. H. V.; Jukes, R. T. F.; Verhoeven, J. W. The Emission Spectrum and the Radiative Lifetime of Eu^{3+} in Luminescent Lanthanide Complexes. *Phys. Chem. Chem. Phys.* **2002**, 4, 1542–1548.

Supporting Information

Fully Efficient Direct Yb-to-Er Energy Transfer at Molecular Level in a Near-Infrared Emitting Heterometallic Trinuclear Quinolinolato Complex

*Flavia Artizzu, Francesco Quochi, Luciano Marchiò, Elisa Sessini, Michele Saba, Angela Serpe,
Andrea Mura, Maria Laura Mercuri, Giovanni Bongiovanni and Paola Deplano*

Experimental Section

General

All the reagents and solvents were purchased from Aldrich and used without further purification. Electronic UV-Vis-NIR: Diffuse reflectance (DR) on KBr pellets and Teflon films and absorption spectra were collected using a Varian Cary 5 and a Perkin Elmer Lambda 950 spectrophotometers. Vibrational FTIR spectra on KBr (MIR, 4000-400 cm^{-1}) and polyethylene (FIR, 400-50 cm^{-1}) pellets were collected using a Bruker Equinox 55 spectrophotometer. Elemental analysis data were collected using a Carlo Erba mod. EA1108 CHNS analyzer. Mass spectra were obtained with a Micromass ZMD spectrometer operating in positive ionization mode.

Syntheses

Synthesis of 1: Few drops of NH_3 28% up to a final concentration of $2.0 \times 10^{-2} \text{ mol dm}^{-3}$ ($\text{pH} \cong 10$) were added to a mixture of 8-hydroxy-quinoline (0.145 g, 1 mmol) in H_2O (100 mL) under mixing. After 30 min a water solution of $\text{YbCl}_3 \cdot 6\text{H}_2\text{O}$ (0.129 g, 0.33 mmol) was added to the above mixture which is allowed to react for 2 days until the white solid due to the unreacted ligand disappears. A yellow precipitate is formed, collected by filtration, washed with water, NaOH 0.1 M, water, and dried in oven at 120°C (almost quantitative yield). Analytical results are in agreement with $\text{Yb}_3\text{Q}_9 \cdot 3\text{H}_2\text{O}$ formulation. CHN Found (Calculated for $\text{C}_{81}\text{H}_{60}\text{Yb}_3\text{N}_9\text{O}_{12}$): C% 52.18(52.01), H% 3.35(3.23), N% 6.82(6.74). The solid was then dissolved in warm CH_3CN , the solvent was roto-evaporated to incipient precipitation and after several days yellow microcrystals of Yb_3Q_9 were obtained (yield 46%). CHN Found (Calculated for $\text{C}_{81}\text{H}_{54}\text{Yb}_3\text{N}_9\text{O}_9 \cdot \text{CH}_3\text{CN}$): C% 54.07 (53.67); H% 3.20 (3.09); N% 7.56 (7.54). FT-IR, cm^{-1} : 3047 m, 1601 m, 1571 s, 1498 vs, 1466 vs, 1424 mw, 1383 s, 1318 s, 1276 m, 1231 m, 1174 w, 1109 vs, 1035 w, 907 w, 823 m, 804 m, 788 m, 732 s, 648 m, 607 m, 592 w; 571 w, 504 m, 490 m, 458 w, 419 mw, 397 m, 384 m, 376 m, 353 m, 335 vw, 326 w, 315 vw, 303 w, 290 w, 280 m, 266 w, 253 m, 247 m, 226 m, 203 m, 177 m, 151 ms, 140 m, 132 m, 121 m, 101m 90 m 80 mw, 74 mw, 57 mw. UV-Vis-NIR absorption, nm, [$\text{mol}^{-1} \text{ dm}^3 \text{ cm}^{-1}$], DMSO: 340[$1.43 \cdot 10^4$], 379[$2.09 \cdot 10^4$], 977 ($^2\text{F}_{5/2} \rightarrow ^2\text{F}_{7/2}$) [20]; Diffuse reflectance, nm: 262, 344, 385; 928, 952, 979 ($^2\text{F}_{7/2} \rightarrow ^2\text{F}_{5/2}$), 1147(3vC-H), 1683 (2vC-H). ESI-Mass ($\text{CH}_3\text{CN}/\text{CH}_3\text{OH}$ 3/1), m/z: 1671.87 [Yb_3Q_8^+].

Synthesis of 2: Synthesis was carried out following the same procedure described for **1**, by adding to a solution containing 1 mmol of the ligand, a mixture of 0.22 mmol of $\text{YbCl}_3 \cdot 6\text{H}_2\text{O}$ and 0.11 mmol of $\text{ErCl}_3 \cdot 6\text{H}_2\text{O}$ in water. A yellow precipitate is formed, collected by filtration, washed with water, NaOH 0.1 M, water, and dried in oven at 120°C (almost quantitative yield). CHN Found (Calculated for $\text{C}_{81}\text{H}_{54}\text{Yb}_2\text{ErN}_9\text{O}_9 \cdot 3\text{H}_2\text{O}$): C% 52.25(52.17), H% 3.38(3.24), N% 6.87(6.76). Yellow microcrystals were obtained after recrystallization from CH_3CN (yield 38%). CHN Found (Calculated for $\text{C}_{81}\text{H}_{54}\text{Yb}_2\text{ErN}_9\text{O}_9 \cdot 3\text{H}_2\text{O}$): FT-IR, cm^{-1} : 3047 m, 1601 m, 1571 s, 1498 vs, 1466 vs, 1424 mw, 1383 s, 1318 s, 1276 m, 1231 m, 1174 w, 1109 vs, 1035 w, 907 w, 823 m, 804 m, 788 m, 732 s, 648 m, 607 m, 592 w; 571 w, 504 m, 489 m, 458 w, 419 mw, 397 m, 384 m, 377 m, 353 m, 335 vw, 326 w, 315 vw, 303 w, 289 w, 280 m, 267 w, 253 m, 247 m, 226 m, 203 m, 177 m, 151 ms, 140 m, 132 m, 121 m, 105 m, 101 m, 89 m, 80 mw, 74 mw, 57 mw. UV-Vis-NIR absorption, nm, [$\text{mol}^{-1} \text{ dm}^3 \text{ cm}^{-1}$], DMSO: 340[$1.43 \cdot 10^4$], 379[$2.10 \cdot 10^4$], 977 ($^2\text{F}_{5/2} \rightarrow ^2\text{F}_{7/2}$) [20], 1504 [3.5]; Diffuse reflectance, nm: 262, 344, 385; 928, 952, 979 ($^2\text{F}_{7/2} \rightarrow ^2\text{F}_{5/2}$), 1147(3vC-H), 1506, 1533 ($^4\text{I}_{13/2} \rightarrow ^4\text{I}_{15/2}$), 1683 (2vC-H). ESI-Mass ($\text{CH}_3\text{CN}/\text{CH}_3\text{OH}$ 3/1), m/z: 1666.54 [$\text{Yb}_2\text{ErQ}_8^+$].

SEM-EDX and X-ray powder diffraction

SEM-EDX analyses were performed with a FEI Dual Beam Nova NanoLab 600i equipped with a EDAX Genesis microanalyzer.

Wide-angle XRD-patterns on microcrystalline powder samples were recorded with a Panalytical Empyrean diffractometer equipped with a graphite monochromator and a X'Celerator linear detector. The scans were collected within the range $5\text{-}90^\circ$ (2θ) using $\text{Cu K}\alpha$ radiation.

Photoluminescence measurements

Photoluminescence (PL) was excited at 392 nm wavelength by the frequency-doubled output pulses of a regenerative Ti:Sapphire amplifier (Quantronix INTEGRA C) running at repetition frequency of 1 kHz. Vis PL decay transients were captured by a streak camera (Hamamatsu C5680) equipped with an imaging spectrometer (Acton SpectraPro

2300i). NIR PL was wavelength dispersed by an Acton SpectraPro 2300i spectrometer; optical spectra and decay transients were detected using, respectively, an InGaAs CCD (Andor iDus) and an InGas photomultiplier (Hamamatsu H10330A-75) connected to a 1 GHz digitizing oscilloscope (Tektronik TDS 5104). In order to minimize nonlinear effects possibly taking place in doubly excited complexes, photoexcitation fluences were kept below the level of 0.1 excitation per complex per laser pulse in all experiments. According to Poissonian statistics, an average excitation level of 0.1 yields a fractional population of doubly excited complexes of ca. 5×10^{-3} . CW visible PL spectra were recorded using a Horiba Jobin-Yvon FluoroMax-4 spectrofluorimeter.

Vibrational Spectroscopy

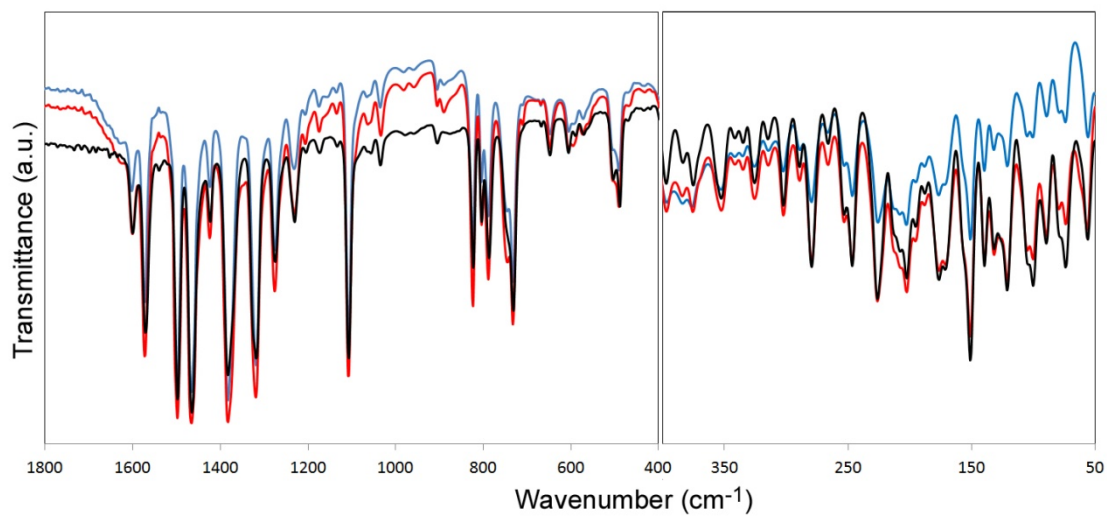


Figure SI1. FT-IR spectra of **1** (red), **2** (blue) and Er₃Q₉ (black) in the MIR (4000-400 cm⁻¹, KBr pellet) and in the FIR (400-50 cm⁻¹, polyethylene pellet).

Powder X-ray diffraction

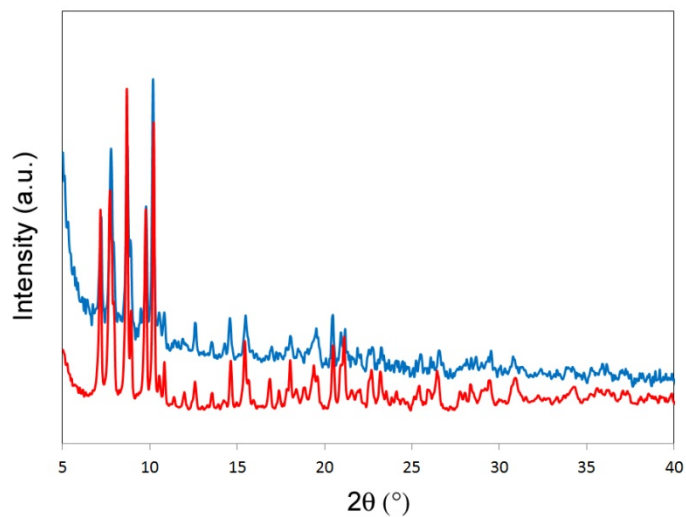


Figure SI2. Powder XRD in the 5-40° angle (2θ) of **1** (red) and **2** (blue).

SEM-EDX analysis

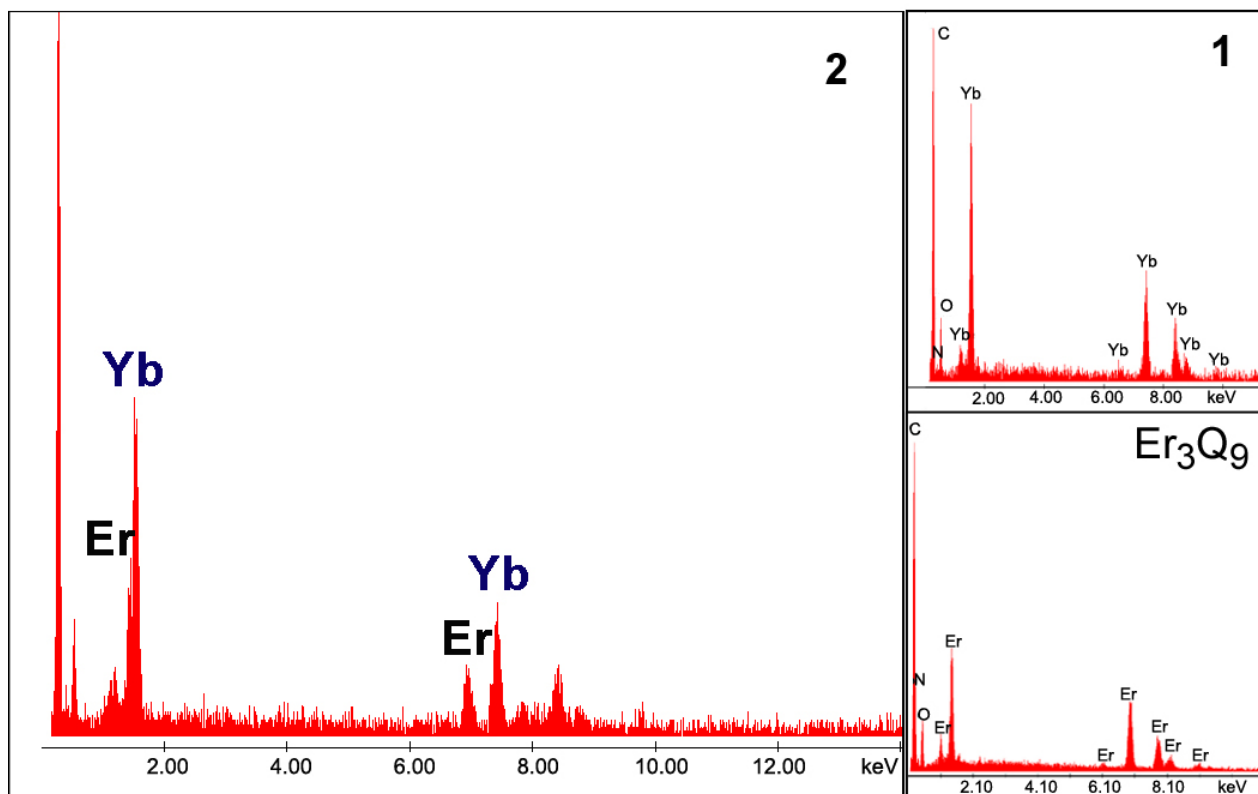


Figure S13. X-ray energy dispersive spectra for **2**, **1** and Er₃Q₉.

Table S11. EDX analysis results for **2**.

EDAX Element Table	ZAF Normalized :	Quantification, Default	Standardless,			
Element,	Wt	%,	At	%,	K-Ratio, Z,	A,
ErL,	33.40,	34.16,	0.3309,	1.0030,	0.9879,	1
YbL,	66.60,	65.84,	0.6684,	0.9984,	1.0052,	1
Total,	100.000,		100			
Element,	Net	Inte.,	Bkgd	Inte.,	Inte.	Error, P/B
ErL,	17.70,	4.10,	6.43,	4.32		
YbL,	33.10,	4.50,	4.38,	7.36		

Measurements were performed on several batches of **2**, and EDX data were acquired on at least three spots per each sample, yielding very good reproducibility.

ESI-Mass analysis

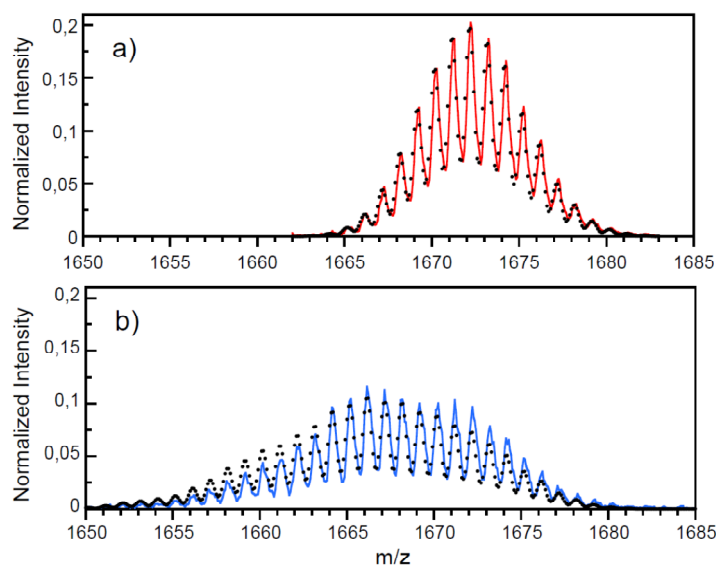


Figure SI4. Normalized mass spectra of **1** (a) and **2** (b) showing the isotopic distribution. Dots represent calculated distributions for Yb_3Q_9 (a) and for a statistical mixture of Yb_2ErQ_9 (44%), YbEr_2Q_9 (22%), Yb_3Q_9 (30%) and Er_3Q_9 (4%) (b), assuming that the $[(\text{Er-Yb})\text{Q}_8]^+$ fragmentation yield is independent of the Er and Yb number of occurrences in the fragment.

Erbium absorption cross-section

For accurate evaluation of erbium absorption cross-section at about $1.5 \mu\text{m}$, anhydrous dimethylsulfoxide solvent was used to limit the amount of water in the solution and the concentration of the complex was pushed up to the solubility limit (10^{-2} M). The spectrum of **2** (1 cm cuvette pathlength) was then compared to that of an equimolar solution of **1** in which an absorption feature appears in the region 1400-1620 nm (see Figure SI5). The intensity of this feature does not change upon dilution of **1** and is also observed in the spectrum of the pure solvent. Therefore it can be attributed to weak vibrational harmonic bands of solvent or small amount of water contamination. The corrected spectrum of **2** at about $1.5 \mu\text{m}$ was then obtained by subtracting the spectrum of **1**. This method was also used for Er_3Q_9 (results published in ref. 28). The same absorption cross-section per erbium atom was found for **2** and Er_3Q_9 ($\sigma_{\text{Er}}[{}^4\text{I}_{13/2} \leftarrow {}^4\text{I}_{15/2}] = 1.0 \cdot 10^{-20} \text{ cm}^2$).

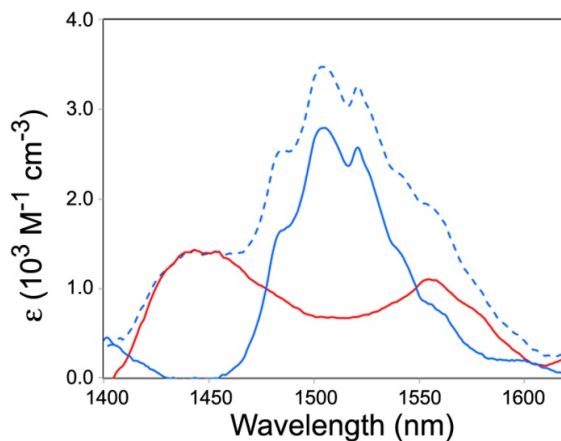


Figure SI5. Absorption spectra of **1** (red) and **2** (dashed blue line) in the 1400-1620 nm region. The continuous blue line represents the erbium ${}^4\text{I}_{13/2} \leftarrow {}^4\text{I}_{15/2}$ absorption band corrected for solvent effects (see text).

Ligand-centered optical properties

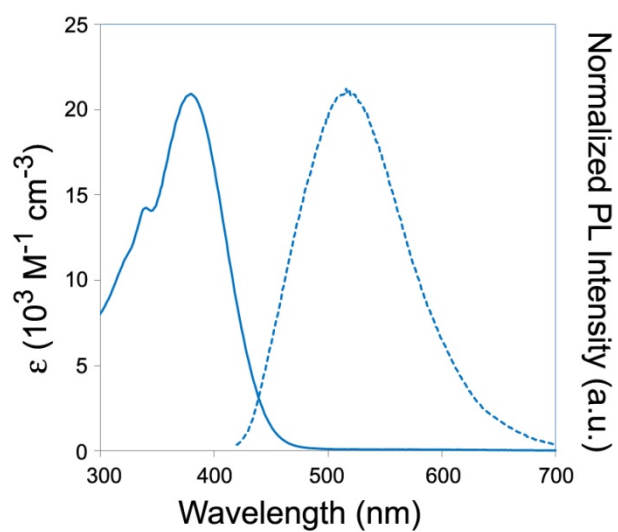


Figure SI6. Ligand absorption and normalized PL spectra for **2** in DMSO solution. Complex **1** shows the same spectral features in the visible region.

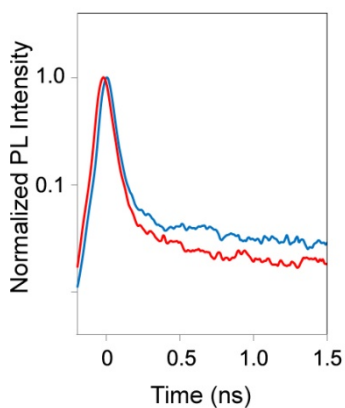
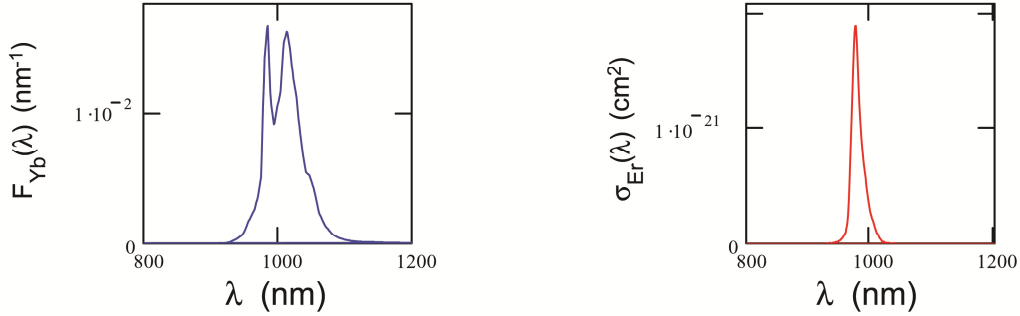


Figure SI7. Normalized visible emission transients for **1** (red) and **2** (blue) excited at 392 nm. The ultrafast (resolution limited) initial decay of the visible emission is traced back to intersystem crossing depopulating the photoexcited ligand-centered singlet states.

Förster's model

$$J = \int F_{Yb}(\lambda) \sigma_{Er}(\lambda) \lambda^4 d\lambda$$

Overlap integral between the emission band of the donor ($F_{Yb}(\lambda)$) and the absorption band of the acceptor ($\sigma_{Er}(\lambda)$)



$$J \cdot 10^{35} = 3.36 \cdot 10^{-3} \text{ cm}^6$$

Donor-Acceptor overlap integral

$$R_0 = \sqrt[6]{\frac{9\kappa_j^2}{128\pi^5 n^4} \int F_{Yb}(\lambda) \sigma_{Er}(\lambda) \lambda^4 d\lambda}$$

where κ^2 ($= 0.667$) is a geometrical factor that depends on the relative orientation between the donor-acceptor transition dipoles, and n is the refractive index of the medium (1.478 for DMSO)

$$R_0 = 1.01 \cdot 10^{-7} \text{ cm}$$

Förster's radius

$$k_{RET} = \frac{1}{\tau_{RET}} = \frac{1}{\tau_{Yb}} \left(\frac{R_0}{R_{Yb-Er}} \right)^6$$

Förster's energy transfer rate constant ($k_{RET \text{ YbEr}}$) and time constant ($\tau_{RET \text{ YbEr}}$). τ_{Yb} ($= 10 \mu\text{s}$) is the decay time of the donor (Yb) in the absence of the acceptor (Er), R_{Yb-Er} ($= 3.5 \text{ \AA}$) is the donor-acceptor distance.

$$\tau_{RET \text{ YbEr}} = 1.71 \cdot 10^{-8} \text{ s}$$

Förster's energy transfer time constant (Model)

$$\eta_{RET} = \frac{1}{1 + \frac{\tau_{RET}}{\tau_{Yb}}}$$

$$\eta_{RET \text{ YbEr}} = 0.998$$

Förster's energy transfer efficiency (Model)

$$\tau_{RET} = \frac{1}{1/\tau_{YbEr} - 1/\tau_{Yb}}$$

where τ_{YbEr} ($= 50 \cdot 10^{-9} \text{ s}$) represents the lifetime of Yb feeding the $\text{Er}^4 \text{I}_{1/2}$ level

$$\tau_{RET \text{ YbEr}} = 5.03 \cdot 10^{-8} \text{ s}$$

Energy transfer time constant (Experimental)

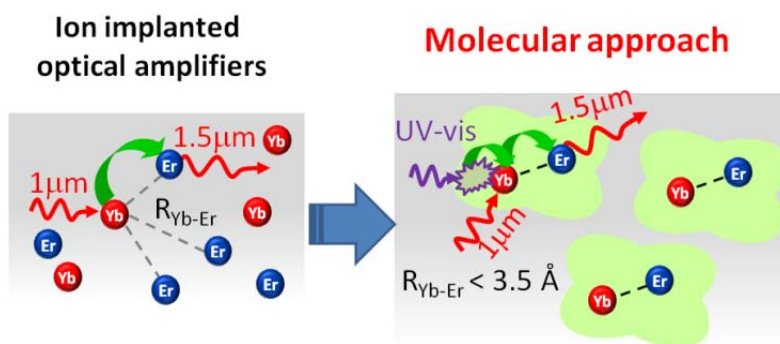
$$\eta_{RET} = \frac{1}{1 + \frac{\tau_{RET}}{\tau_{Yb}}}$$

$$\eta_{RET \text{ YbEr}} = 0.995$$

Energy transfer efficiency (Experimental)

Paper 3

Light Conversion Control in NIR-Emissive Optical Materials based on Heterolanthanide Er_xYb_{3-x} Quinolinolato Molecular Components



Heterolanthanide Er/Yb trinuclear quinolinolato complexes have been thoroughly investigated as promising optically-active molecular dopants for controlled ligand-to-metal and metal-to-metal energy transfer processes in NIR-luminescent hybrid materials.

Manuscript under revisions. Chemistry of Materials., 2015.

Light Conversion Control in NIR-Emissive Optical Materials based on Heterolanthanide Er_xYb_{3-x} Quinolinolato Molecular Components

Flavia Artizzu,^{a,b,*} Francesco Quochi,^{b,*} Luciano Marchiò,^c Cristiana Figus,^b Danilo Loche,^a Matteo Atzori,^a Valerio Sarritzu,^b Rik Van Deun,^d Michele Saba,^b Angela Serpe,^a Andrea Mura,^b Maria Laura Mercuri,^a Giovanni Bongiovanni^b and Paola Deplano^{b,*}

^aDipartimento di Scienze Chimiche e Geologiche, University of Cagliari, SS 554 Bivio per Sestu, I-09042, Monserrato-Cagliari, Italy.

^bDipartimento di Fisica, University of Cagliari, SS 554 Bivio per Sestu, I-09042, Monserrato-Cagliari, Italy.

^cDipartimento di Chimica, University of Parma, Parco Area delle Scienze 17/A, I-43100, Parma, Italy

^dL3- Luminescent Lanthanide Lab, f-Element Coordination Chemistry, Department of Inorganic and Physical Chemistry, Ghent University, Krijgslaan 281-S3, B-9000 Ghent, Belgium

ABSTRACT: Homo- and heterobimetallic homoleptic complexes of general formula Er_xYb_{3-x}Q₉ (Q = 8-quinolinolato; x = 0, **1**; x = 1, **2**; x = 2, **3**) and the corresponding heteroleptic complexes Er_xYb_{3-x}Q₈NO₃ (x = 0, **1b**; x = 1, **2b**; x = 2, **3b**), where one Q ligand is replaced by a nitrate anion, have been synthesized, and fully characterized by means of compositional (EDX, ICP-mass and ESI-mass spectrometry) and structural (X-ray diffraction) investigations to study the effects of ligand substitution and variation of metal composition on their chemical and photophysical properties. Advanced spectroscopic and photophysical studies in the visible and NIR spectral regions have allowed to reach a detailed picture of the photocycle leading to narrow-band lanthanide luminescent emission, providing evidence of highly efficient ligand-to-metal and metal-to-metal (Yb-to-Er) resonance energy transfers, thanks to the short intermetallic distances in heterolanthanide molecular species. Highly homogeneous silica thin films doped with **2**, have shown to retain the optical properties of the dopant complex in solution, proving the suitability of this class of complexes for preparing Er/Yb codoped optical materials, for potential applications as waveguides or amplifiers, with controlled composition and distribution of the optically active metals.

Introduction

Near-infrared (NIR) emitting lanthanide ions (Ln) are of remarkable interest in view of the several potential applications ranging from optical technologies to biomedical fields.¹⁻² Among them, Yb³⁺ and Er³⁺ play a special role in telecom technologies, as their emission can be exploited for signal amplification in the so-called first and third-communication windows, at 1 μm and 1.5 μm wavelengths, respectively. Doped silica fibers such as EDFAs (Erbium Doped Fiber Amplifiers) are currently used for optical amplification in the long-haul communication systems operating in the 1.5 μm spectral window. However, for effective optical pumping of intrinsically weakly-absorbing lanthanide ions, highly efficient light-harvesting “antennas” are required for resonance energy transfer (RET) to the higher energy levels of these metal emitters. Er³⁺ sensitization through RET from Yb³⁺, featuring a 10-times higher absorption cross section, has proved to be a smart strategy to achieve enhancement of Er³⁺ emission at 1.5 μm in Yb-Er co-doped glassy optical fiber amplifiers.³⁻⁸ For efficient Yb-to-Er RET through the distance-dependent, through-space Förster’s mechanism, the two optically active ions must lie at close distance (< 10 Å).⁹ Most of the co-doped Er/Yb materials so far studied in view of their potential applications, es-

pecially as NIR optical waveguides and amplifiers, consist of inorganic glassy or polymeric matrixes where the two optically-active ions are incorporated through diverse techniques such as ion implantation, sputtering, electron beam lithography, melting techniques, or *via* the sol-gel process, to cite the most popular.³⁻⁸ However, controlled co-doping of inorganic or polymeric matrixes with lanthanide inorganic salts or oxides is usually limited by solubility reasons or intrinsic difficulties in regulating the distribution and relative positions of the two intercommunicating ions into the host matrix. A viable route to address this challenging task relies on the use of easily-processable discrete polynuclear molecules where selected lanthanide ions are held together in fixed positions in a pre-designed molecular architecture allowing controlled intermetallic RET between two closely spaced optically-active ions. The incorporation of the lanthanide ions into an organic framework can help to overcome solubility restraints in inorganic/organic hosts while improving the thermal stability and mechanical strength of coordination complexes compared to conventional inorganic or polymeric materials. Moreover, in these heterometallic assemblies, suitable organic ligands can be introduced as efficient “light harvesters”, providing a supplementary excitation channel for the lanthanide ions. In this

way it would be possible to take advantage of the molecular approach for functional heterolanthanide assemblies while fabricating optical materials useful for direct applications.

Recently, it has been demonstrated that the Ln_3Q_9 ($\text{Q} = 8$ -quinolinolato) framework is particularly suitable for preparing heteronuclear-lanthanide complexes,¹⁰ providing several benefits especially in regard to NIR-emitters: i) high coordinating ability toward different Ln ions across the whole series;^{11–15} ii) excellent “antenna” properties of the Q ligand allowing simultaneous excitation of different NIR-emissive Ln ions upon single-wavelength irradiation in the easily accessible visible region;^{16–17} iii) short intermetallic distances (below 3.5 Å), optimal for ensuring fully efficient Yb-to-Er RET;^{9–15} iv) high stability and capability to undergo processing procedures (in solution or by vacuum deposition) without alterations.^{18–25}

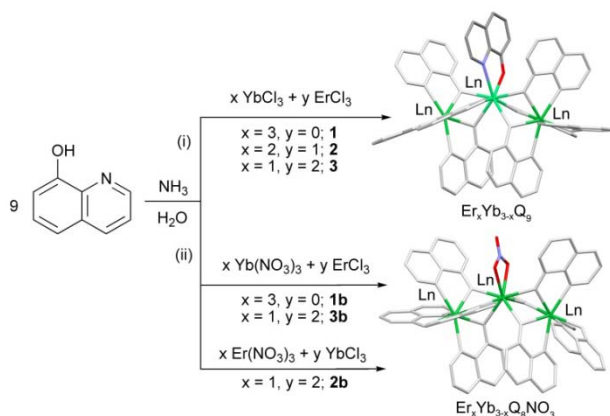
In order to further explore and clarify the chemical/photophysical properties of mixed Er/Yb quinolinolates, a thorough study on the structure/properties relationship upon slight structural modifications (replacement of one Q ligand) and variation of metal composition, has been performed, and results compared to those observed for the corresponding trinuclear homometallic Yb quinolinolato analogs as useful references. In addition, the potential of this class of compounds as functional molecular materials for photonic applications has been investigated through the incorporation of these complexes into silica thin films.

Results and discussion

Synthesis, structural and analytical characterization

The investigated compounds have been prepared through a one-pot reaction between the selected metal salts and the ligand in suitable ratios, taking advantage of the very similar reactivity of the erbium and ytterbium ions, both belonging to the second half of the lanthanide series, according to the reaction pathways (i) and (ii) illustrated in Scheme 1.

Scheme 1. Reaction pathways



Homoleptic $\text{Er}_x\text{Yb}_{3-x}\text{Q}_9$ complexes have been synthesized with the procedure already described for the Er_3Q_9 and mixed lanthanide (Yb, Er, Nd) complexes,^{10,12} by directly reacting the deprotonated Q ligand with chloride (or acetate) salts of Yb and Er ions in selected molar ratios ($x = 0, 1; x = 1, 2; x = 2, 3$ reaction pathway (i), Scheme 1). $\text{Er}_x\text{Yb}_{3-x}\text{Q}_9$ formulations are in agreement with analytical and spectroscopic data (see Experimental Section). The molecular structure of **2** has been re-

cently reported elsewhere¹⁰ and the isostructurality of compounds **1** and **3** with respect to **2** was confirmed by powder XRD measurements performed on microcrystalline samples obtained after recrystallization in CH_3CN (Figure S1, Supporting Information).

Instead, when using, as metal source, salts of the more coordinating nitrate anion in the presence of two equivalents of the chloride salt of a second lanthanide ion, heteroleptic complexes of general formula $\text{Er}_x\text{Yb}_{3-x}\text{Q}_8\text{NO}_3$ have been isolated ($x = 0, \mathbf{1b}; x = 1, \mathbf{2b}; x = 2, \mathbf{3b}$; reaction pathway (ii), Scheme 1), as confirmed by analytical and spectroscopic data (see Experimental Section). Single crystals suitable for X-ray structural analysis have been obtained for **1b** after recrystallization in CH_3CN . The molecular structure of **1b** is shown in Figure 1.

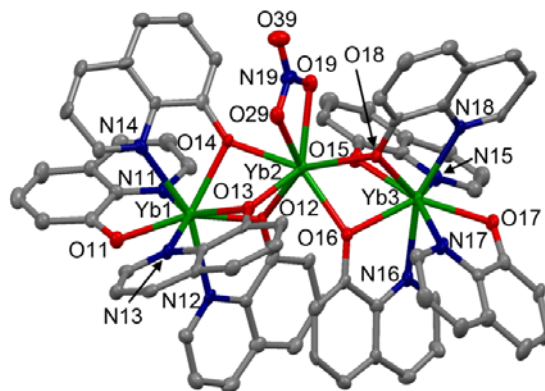


Figure 1. Molecular structure of **1b** with H atoms omitted for clarity.

The molecule, which can be formulated as $\text{Yb}_3\text{Q}_8\text{NO}_3$, presents a trinuclear structural arrangement similar to the analogous homoleptic Ln_3Q_9 complexes,^{12–15} with a nitrate anion replacing one quinolinolato ligand chelating the central Yb^{3+} ion. The three coordination sites are inequivalent, and the two outer metals are in a N_4O_4 environment through coordination of four quinolinolato ligands, whereas the inner metal is octacoordinated by six oxygen atoms of bridging μ^2 -quinolinolato ligands and two oxygen atoms of a κ^2 - NO_3 anion. Interestingly, the $\text{Yb}(1)\text{-Yb}(2)\text{-Yb}(3)$ angle is 139.6° and is remarkably wider than in the analogous homoleptic Ln_3Q_9 complexes obtained with the synthetic method (i) in Scheme 1, Er_3Q_9 (133.5°),¹² ErYb_2Q_9 (133.4°) and NdErYbQ_9 (132.4°),¹⁰ and slightly smaller than that found for Yb_3Q_9 (140.3°).¹⁴ It is also worth noting that the $\text{Yb}(1)\cdots\text{Yb}(2)$ and $\text{Yb}(2)\cdots\text{Yb}(3)$ distances in **1b** are 3.414 Å and 3.407 Å, and are noticeably shorter than those found in the homoleptic Yb_3Q_9 (3.459 and 3.458 Å)¹⁴ and also in the mixed ErYb_2Q_9 (**2**, 3.475 Å and 3.478 Å)¹⁰ complexes. Moreover, the difference in the metal separation lengths between Er_3Q_9 (3.488 and 3.495 Å)¹² and **1b** significantly exceeds the difference of erbium and ytterbium ionic radii ($\Delta r_{\text{Er-Yb}}^{\text{CN=8}} = 1.9$ pm). This may be likely ascribed to the lower steric hindrance of the nitrate anion coordinated to the central metal with respect to the quinolinolato ligand, allowing the metal centers to sit at closer proximity in the trinuclear molecular framework. As far as the molecular crystal packing is concerned, the presence of the coordinated nitrate anion does not induce significant differences in terms

of supramolecular interactions with the surrounding molecules with respect to those exchanged in their homoleptic analogues. The isostructurality of compounds **2b** and **3b** with respect to **1b** was confirmed by powder-XRD measurements on microcrystalline samples obtained after recrystallization in CH₃CN (Figure S1, Supporting Information). Main crystallographic parameters and most significant bond lengths for **1b** are reported in Tables 1 and 2, respectively.

Table 1. Summary of X-ray crystallographic data for **1b**.

Empirical Formula	C ₇₂ H ₄₇ N ₉ O ₁₁ Yb ₃
Colour, habit	Yellow, Block
Crystal system, space group	Triclinic P-1
a, b, c (Å)	12.7218(8), 15.1809(10), 18.0938(11)
•, •, • (deg.)	95.563(2), 103.475(2), 111.631(2)
V (Å³)	3093.6(3)
Z, • (calc) (Mg/m³)	2, 1.861
T (K), • (Å)	125(2), 0.71073
μ (mm⁻¹)	4.570
• range (deg.)	2.36 to 25.03
No. of rflcn/unique	40882/10916
Goof	1.002
Final R indices	R1=0.0524, wR2=0.1106
[I>2sigma(I)]	

Table 2. Selected bond lengths for **1b**.

N(11)-Yb(1)	2.425(9)	O(16)-Yb(3)	2.315(6)
N(12)-Yb(1)	2.466(9)	O(17)-Yb(3)	2.237(7)
N(13)-Yb(1)	2.489(8)	O(18)-Yb(3)	2.325(7)
N(14)-Yb(1)	2.472(9)	O(12)-Yb(2)	2.347(7)
N(15)-Yb(3)	2.485(8)	O(13)-Yb(2)	2.251(6)
N(16)-Yb(3)	2.436(9)	O(14)-Yb(2)	2.305(7)
N(17)-Yb(3)	2.445(9)	O(15)-Yb(2)	2.240(7)
N(18)-Yb(3)	2.433(8)	O(16)-Yb(2)	2.269(7)
O(11)-Yb(1)	2.219(7)	O(18)-Yb(2)	2.395(7)
O(12)-Yb(1)	2.301(6)	O(19)-Yb(2)	2.382(7)
O(13)-Yb(1)	2.304(7)	O(29)-Yb(2)	2.393(7)
O(14)-Yb(1)	2.339(6)	Yb(2)-Yb(1)	3.4139(7)
O(15)-Yb(3)	2.295(7)	Yb(2)-Yb(3)	3.4071(7)

ICP-mass analysis on solution samples have been employed to accurately assess metal composition in mixed Er/Yb compounds, and the following stoichiometrical formulations have been retrieved: Er_{0.89}Yb_{2.11}Q₉ (**2**); Er_{1.92}Yb_{1.08}Q₉ (**3**); Er_{0.88}Yb_{2.12}Q₈NO₃ (**2b**); Er_{1.95}Yb_{1.05}Q₈NO₃ (**3b**). These results

evidence a small excess (2-4%) of Yb content with respect to expected stoichiometrical metal ratios, Er:Yb 2:1 (**2**, **2b**) or 1:2 (**3**, **3b**), used in the synthetic procedures. Results are quite consistent, with only small variations, within the series of four independent samples, pointing out a slightly stronger affinity of Yb³⁺ upon coordination to the 8-quinolinolato ligand, likely relatable to its slightly smaller ionic radius compared to Er³⁺.

Generally, when using one-pot synthetic approaches for the preparation of heterolanthanide compounds, in the absence of some metal selectivity restrictions, statistical metal distribution over the available coordination sites leading to mixtures of homo- and hetero-lanthanide species is predictable.²⁶⁻²⁷ For this reason, in order to reach a detailed picture of molecular speciation of the mixed Er/Yb compounds, and explore the reactivity of the different Ln ions upon ligand coordination, positive ion mode ESI-mass experiments have been performed, and corresponding spectra for **2**, **2b**, **3** and **3b**, are reported in Figure 2. As expected, for all the samples, two peaks are dominant. The peak at highest m/z (1640-1680 m/z) corresponds to an isotopic distribution of [Er_xYb_{3-x}Q₈]⁺ (x = 0-3) species as a consequence of the fragmentation of one Q ligand for **2** and **3** (Figure 2a) and a nitrate anion for **2b** and **3b** (Figure 2b) from the parent molecule. The second peak at 1045-1075 m/z is related to [Er_xYb_{2-x}Q₅]⁺ (x = 0-2) fragments. It is worth noting that in the spectra of Er_xYb_{3-x}Q₉ complexes no peaks of significant intensity can be attributed to [Er_xYb_{3-x}Q₇NO₃]⁺ (x = 0-3) or [Er_xYb_{2-x}Q₄NO₃]⁺ (x = 0-2) fragments (see Supporting Information). This suggests that the chelating ligand at the central coordination site in the trinuclear complexes is the most weakly bound, in agreement with previous results supported by TD-DFT calculations on similar compounds.¹⁴ The isotopic distribution of the parent peak for all the mixed complexes, reveals that the most predominant species is [ErYb₂Q₈]⁺ (m/z=1666.2) for **2**, **2b** and [Er₂YbQ₈]⁺ (m/z=1660.2) for **3**, **3b** and confirms that multiple species with different metal ratios are present in the samples. Experimental spectra are in fact in good agreement with models (dotted lines, Figure 2) calculated by taking into account the molecular speciation estimated for a statistical distribution of the metals across the three coordination sites, on the basis of ICP-mass metal compositional analysis. Relative abundances of homo- and hetero-metallic species constituting samples **2**, **3**, **2b** and **3b** are reported in Table 3.

Table 3. Relative abundances of molecular species with different Er/Yb atomic ratios in heterolanthanide compounds **2**, **3**, **2b** and **3b**.

Compound	<i>Er_xYb_{3-x} metal composition</i>			
	<i>x = 1</i>	<i>x = 2</i>	<i>x = 0</i>	<i>x = 3</i>
2	44%	18%	35%	3%
2b	44%	18%	35.5%	2.5%
3	25%	44%	5%	26%
3b	24%	44.5%	4%	27.5%

Given the close similarity of Er³⁺ and Yb³⁺ ionic radii, these results are not surprising, although it has been recently ob-

served that a remarkable size discriminating effect controls molecular speciation in heterolanthanide quinolinolates when a larger ion such as neodymium, is mixed with smaller lanthanides belonging to the second half of the series.¹⁰

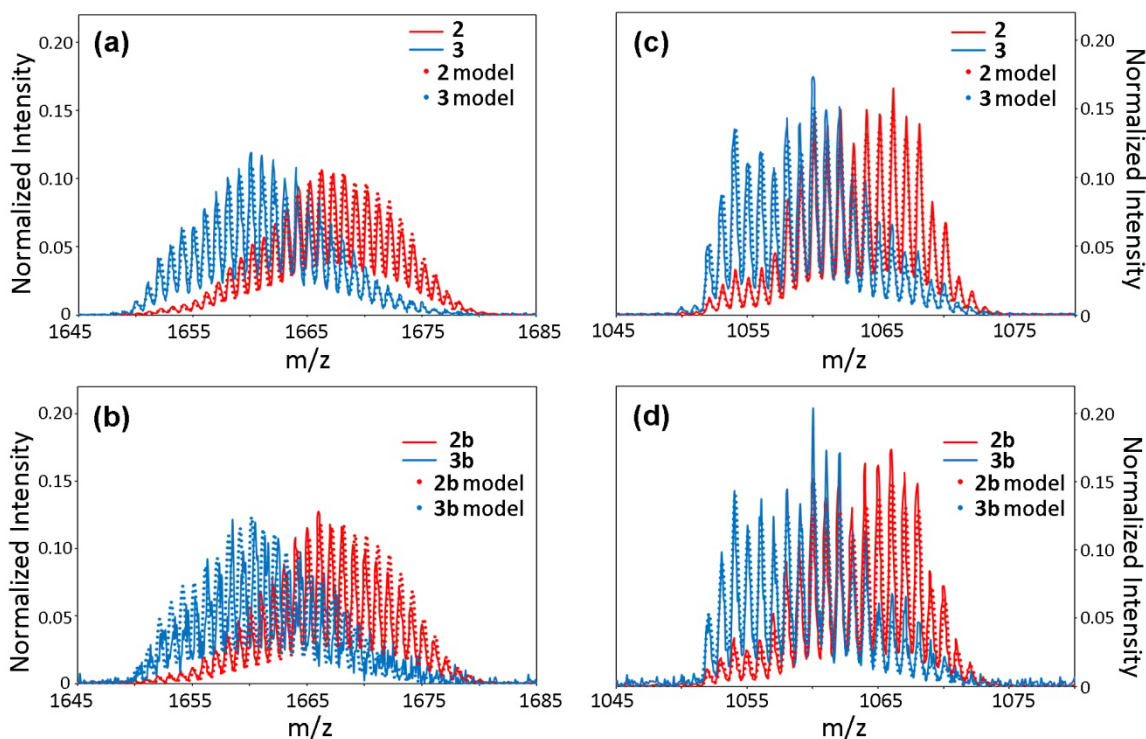


Figure 2. ESI-mass spectra of heterolanthanide compounds, showing the $[\text{Er}_x\text{Yb}_{3-x}\text{Q}_8]^+$ (**2-3**, panel a; **2b-3b**, panel b) and the $[\text{Er}_x\text{Yb}_{2-x}\text{Q}_5]^+$ (**2-3**, panel c; **2b-3b**, panel d) fragments. Dotted lines represent model isotopic distribution functions for a statistical molecular speciation of $\text{Er}_{0.89}\text{Yb}_{2.11}\text{Q}_9$ (**2**); $\text{Er}_{1.92}\text{Yb}_{1.08}\text{Q}_9$ (**3**); $\text{Er}_{0.88}\text{Yb}_{2.12}\text{Q}_8\text{NO}_3$ (**2b**) and $\text{Er}_{1.95}\text{Yb}_{1.05}\text{Q}_8\text{NO}_3$ (**3b**). Integrated intensities are normalized to unity.

For **2b** and **3b**, the agreement between the experimental isotopic distribution and the statistical model of the $[\text{Er}_x\text{Yb}_{2-x}\text{Q}_5]^+$ fragment, most likely involving the central metal ion (Figure 2d), indicates that the nitrate anion in the central position can coordinate either erbium or ytterbium regardless of the starting metal salt (see reaction pathway (ii), Scheme 1), proving that ligand scrambling effects take place during the synthesis. Actually, no results on positional control of a specific lanthanide ion over the three available coordination sites have been so far achieved through templating syntheses by using different lanthanide salts as starting materials. Additional attempts made by using acetate or triflate salts of Er^{3+} or Yb^{3+} , mixed with two equivalent of Yb^{3+} or Er^{3+} chlorides, respectively, invariably afforded $\text{Er}_x\text{Yb}_{3-x}\text{Q}_9$ complexes as statistical mixtures of homo- and hetero-metallic species (see Experimental Section). The close similarity of the chemical behavior, reactivity and size of the two NIR-emissive erbium and ytterbium ions, that can be considered as “vicariants”, leads to similar occupancies of these metal ions over the available coordination sites in the crystal lattice in trinuclear quinolinolato complexes.¹⁰ SEM-EDX semi-quantitative punctual analyses on crystalline sam-

ples confirmed the homogeneity of metal distribution, with reproducible metal atomic ratios for several different crystals (Table S2, Supporting Information). This allows a continuous tuning of the molecular speciation simply by varying the stoichiometry of the metals in the synthesis, while ensuring unaltered compositional homogeneity in the sample.

Spectroscopic studies and photophysical properties

Absorption, solid state diffuse reflectance (DR) and photoluminescence (PL) spectra in the UV-Vis and NIR regions for **1**, **2** and **3**, are reported in Figure 3, whereas corresponding spectra for compounds **1b**, **2b** and **3b** can be found in Figure S3 in the Supporting Information.

For all the compounds, the absorption spectrum in the visible region is dominated by the typical intense and broad band related to a π - π^* transition of the quinolinolato ligand with intraligand charge transfer (ILCT) character (Figure 3a).²⁸ In the 800-1800 nm spectral window, DR spectra have been acquired on crystalline samples, to avoid interference due to strong sol-

vent absorption (Figure 3b). The narrow bands related to intrashell f-f transitions of Yb^{3+} (${}^2\text{F}_{5/2} \rightarrow {}^2\text{F}_{7/2}$, 1 μm) and Er^{3+} (${}^4\text{I}_{13/2} \rightarrow {}^4\text{I}_{15/2}$, 1.5 μm) are resolved into a fine structure as a consequence of the splitting of the energy levels manifolds due to crystal field effects. These transitions are particularly sensitive to the chemical coordination environment and observed bands shapes are slightly different for **1**, **2** and **3** with respect to compounds **1b**, **2b**, **3b** (Figure S3b, Supporting Information), where the replacement of the central Q ligand with a nitrate anion changes the molecular symmetry. The bands at 1680 and 1140 nm in the DR spectra are attributed to the second and third harmonic of the stretching vibration of ligand aromatic CH groups and can serve as useful internal reference for normalizing the spectra of isostructural complexes. DR spectroscopy can therefore be used as a supplementary diagnostic tool for a rough estimation of the amount of erbium and ytterbium ions in the samples through comparison of the intensities of the related integrated peaks.

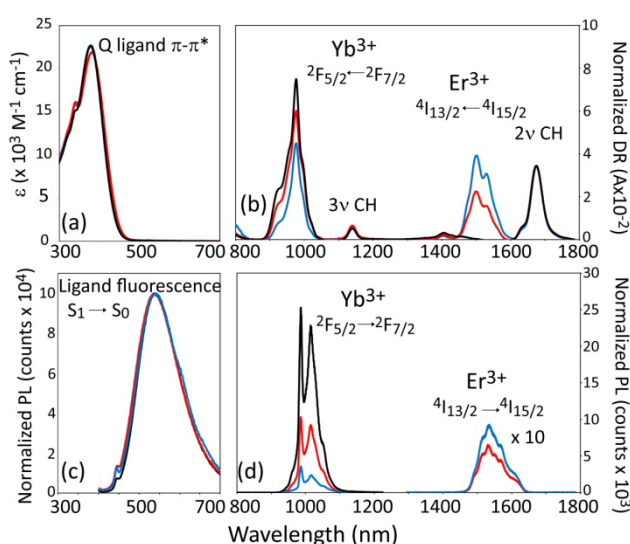


Figure 3. (a) Absorbance spectra in DMSO solution showing the broad band related to the Q ligand in the Uv-Vis region; (b) diffuse reflectance (DR) spectra of crystalline samples in the Vis-NIR region showing lines related to intrashell f-f transitions of Er^{3+} and Yb^{3+} and ligand CH stretching overtones; (c) Ligand fluorescence and (d) PL spectra in the NIR region, of DMSO solutions excited at $\lambda=392$ nm. Color coding: **1** (black), **2** (red) and **3** (blue). Spectroscopic labels of Er^{3+} and Yb^{3+} transitions are also indicated. DR spectra are normalized to the 2v CH band. PL spectra are normalized for absorbed power at excitation wavelength.

All the investigated compounds display photoluminescence in the Visible and in the NIR regions upon single-wavelength irradiation in the ligand lowest absorption band in the near-UV. Broad ligand-centered emission attributed to radiative decay from the excited singlet state S_1 to the ground state S_0 is detected in the green region of the visible spectrum (Figure 3c). Simultaneous photoluminescence from Yb^{3+} and Er^{3+} upon single-wavelength irradiation is also observed in the NIR spectral window as a consequence of RET from the excited ligand to the upper energy levels of the lanthanide ions, which

become sensitized (Figure 3d). Yb^{3+} (${}^2\text{F}_{5/2} \rightarrow {}^2\text{F}_{7/2}$, 1 μm) and Er^{3+} (${}^4\text{I}_{13/2} \rightarrow {}^4\text{I}_{15/2}$, 1.5 μm) emission bands are resolved into a fine structure and are Stokes-shifted with respect to DR spectra. The observed NIR-PL spectroscopic features in mixed Er/Yb compounds arise from the contribution of the different species in the samples, where only the fraction of homolanthanide molecular species (Yb_3Q_9 , Er_3Q_9) yields independent emission from the metals, whereas intermetallic communication occurring in heterometallic Er/Yb molecules affects the intensity of the emission bands in the NIR.⁹

A multi-step photocycle, involving intra-ligand, ligand-to-metal and metal-to-metal energy transfer processes is in fact responsible for narrow-band lanthanide emission in this class of mixed-lanthanide complexes. This mechanisms, which can be simply depicted through a Jablonski diagram, reported in Figure 4, can be briefly summarized as follows. After ligand excitation in the first singlet excited state S_1 , intersystem crossing (ISC) to excited triplet T_1 becomes competitive with ligand fluorescence ($S_1 \rightarrow S_0$) due to the heavy atom effect induced by coordination to the lanthanide ions. The excited triplet T_1 is then likely to feed, by Förster's RET, the upper energy levels of Yb^{3+} and Er^{3+} . As a consequence of the perfect energy match between the ${}^2\text{F}_{5/2}$ and the ${}^4\text{I}_{11/2}$ levels of Yb^{3+} and Er^{3+} , metal-to-metal RET can occur between these two ions, adding a supplementary step to the photocycle.

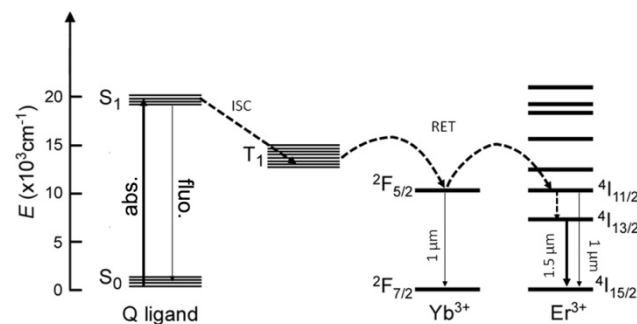


Figure 4. Jablonski diagram depicting the energy levels of the Q ligand, Yb^{3+} , and Er^{3+} ions and the full photocycle in trinuclear quinolinolato complexes. Dashed arrows represent nonradiative processes. Thick arrows indicate the mechanism of Yb-sensitized Er emission in mixed Er/Yb Q-complex. abs. = ligand absorption; fluo. = ligand fluorescence; ISC = intersystem crossing; RET = resonance energy transfer.

Advanced time-resolved photophysical studies in the visible and NIR spectral windows have been performed to investigate the most competitive processes that lead to narrow-band NIR emission in heterolanthanide Er/Yb compounds and evaluate their efficiency.

Ligand-centered dynamics and ligand-to-metal energy transfer. Combined transient PL and photoinduced excited-state absorption (ESA) experiments with subpicosecond photoexcitation in the fundamental absorption band of the ligand at 392 nm for **1**, **2**, **3** in diluted ($\sim 5 \times 10^{-4}$ M) DMSO solution are summarized in Figure 5. Corresponding graphs for **1b**, **2b**, **3b** are reported in Figure S4 in the Supporting Information. Related

time constants for all the investigated compounds are compared in Figure 6.

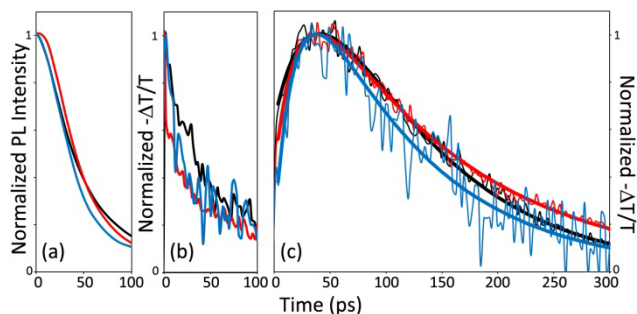


Figure 5. (a) Transient PL in the 400-700 nm region; (b) transient ESA probed in the region 430-440 nm showing ligand singlet decay dynamics and (c) ESA signal attributed to ligand triplet dynamics in the region 560-570 nm and curve fitting (thick lines). Excitation wavelength was $\lambda = 392$ nm. Color coding: **1** (black), **2** (red) and **3** (blue). Signal intensities are normalized to unity.

After photoexcitation, time-resolved PL measurements spectrally integrated over the fluorescence emission spectrum (400-700 nm spectral window), show that the ligand excited state S_1 decays monoexponentially on an ultrafast timescale (Figure 5a). Decay time constants are close to the instrumental temporal resolution limit ($\tau_{\text{fluo}} \sim 50$ ps) for all the investigated compounds (Figure 6), as expected for this class of complexes, where the presence of the heavy lanthanide ion favors the intra-ligand ISC mechanism.¹⁶⁻¹⁷ ESA experiments probed in the 430-440 nm spectral window (Figure 5b) show signals attributable to excited singlet, with prompt risetimes followed by ultrafast relaxation. Singlet decay occurs with time constants (τ_S) in agreement with the resolution limited ones retrieved from transient PL (see Figure 6). When probing in the 560-570 nm region, where the singlet signal is almost undetectable, the dynamics related to ligand triplet excited states can be determined (Figure 5c). Triplet population shows an ultrafast activation complementary to the excited singlet decay, with similar time constants that can be reliably attributed to the singlet-triplet intersystem crossing process (τ_{T^*} , Figure 6). Triplet decay is ultrafast, and curve fitting yields triplet lifetimes (τ_T) in the range 100-150 ps (Figure 6), in agreement with previous reports for erbium and ytterbium quinolinolate complexes.¹⁶⁻¹⁷

By comparing these findings with the $\tau_T = 1.4$ ns value previously found for the analogous Gd_3Q_9 complex,¹⁶⁻¹⁷ where upper gadolinium levels lie too high in energy to be fed through indirect excitation from the ligand, it can be deduced that the excited triplet is strongly quenched by ligand-to-metal energy transfer. Therefore, lanthanide sensitization is extremely efficient in all the investigated compounds. The triplet lifetime can then be considered as the time constant of the ligand-to-metal RET process. Time constants and related experimental errors, details of kinetic equations and curve fitting procedure are reported in the Supporting Information.

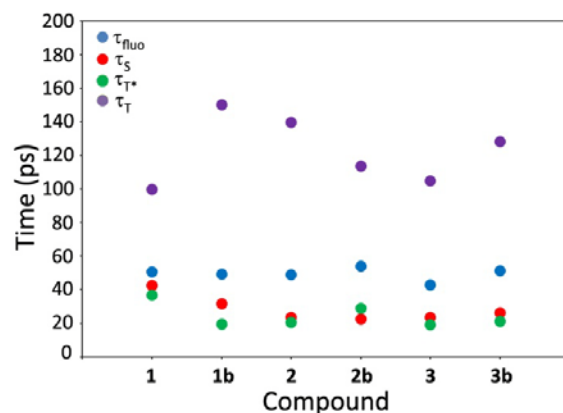


Figure 6. Time constants of the ligand-centered dynamics in the visible spectral region: ligand fluorescence lifetime, τ_{fluo} , blue dots; excited singlet decay time constant from ESA experiments, τ_S , red dots; excited triplet risetime, τ_{T^*} , green dots and excited triplet decay time, τ_T , purple dots, as retrieved from ESA experiments. Errors fall in the range 0.4-7 ps (see Table S3, Supporting Information).

Metal-centered dynamics and metal-to-metal energy transfer. Time-resolved photoluminescence studies showing the metal-centered dynamics in the NIR spectral region for **1**, **2** and **3** in diluted ($\sim 5 \times 10^{-4}$ M) DMSO solution are summarized in Figure 7. Corresponding data for **1b**, **2b** and **3b** are reported in Figure S5 in the Supporting Information. Figure 8 summarizes the decay time constants for the Er^{3+} and Yb^{3+} dynamics for all the investigated compounds.

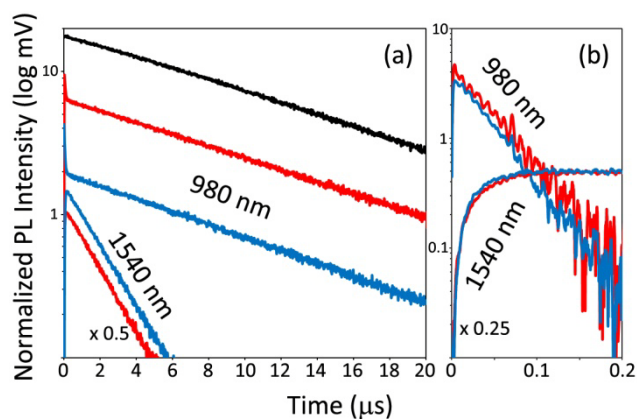


Figure 7. (a) NIR decay dynamics of **1** (black), **2** (red), and **3** (blue) at 980 and 1540 nm. (b) NIR dynamics on a short time scale of **2** (red) and **3** (blue): decay traces at 980 nm and at 1540 nm have been obtained by subtracting the long-lived component attributed to Yb_3Q_9 and the Er_3Q_9 contribution, respectively. Signal intensities are plotted on a logarithmic scale. Excitation wavelength was 392 nm. Intensities are normalized for absorbed power at excitation wavelength.

A monoexponential decay, related to $\text{Yb}^{3+} {}^2F_{5/2} \rightarrow {}^2F_{7/2}$ emission at 980 nm is detected for **1** (black line, Figure 7a), with a time constant $\tau_{\text{Yb}} \sim 11$ μs (Figure 8). For the mixed Er-Yb compounds **2** and **3**, two distinct decay dynamics are observed

at 980 and 1540 nm, due to the coexistence of Yb³⁺ and Er³⁺ in the samples (Figure 7a, **2**, red line, **3** blue line). The signal at 1540 nm arises from erbium ⁴I_{13/2} • ⁴I_{15/2} radiative emission and decays monoexponentially for both **2** and **3** with the same dynamics as Er₃Q₉,^{9,12} (τ_{Er} ~ 2 μs, red dots, Figure 8). As described in Figure 4, this emission is most likely consequent to the population of the erbium ⁴I_{13/2} level after non-radiative cascade from the upper lying ⁴I_{9/2} level. The difference of 1540 nm signal intensities between **2** and **3**, reflects the composition of the two samples (Table 3), and in particular, the amount of Yb₃Q₉ not giving rise to emission at 1540 nm. Instead, for the decay trace at 980 nm, two components are clearly distinguishable with lifetimes differing for almost three orders of magnitude, as retrieved by double-exponential fitting. The longer-lived component, showing a similar dynamics as **1** (τ_{Yb} ~ 10 μs, blue dots, Figure 8) can be attributed to Yb³⁺ ²F_{5/2} • ²F_{7/2} emission from the fraction of Yb₃Q₉ species present in the two samples and can be weighted accordingly (Table 3). Conversely, the ultrafast decay component is likely due to the strong quenching of ytterbium ²F_{5/2} level induced by resonant Yb-to-Er (²F_{5/2} • ⁴I_{9/2}) energy transfer, as depicted in Figure 4.⁹ This observation becomes more evident from a closer inspection of the ytterbium and erbium dynamics on a shorter timescale as reported in Figure 7b, where the contributions of Yb₃Q₉ and Er₃Q₉ fractions in the two samples are subtracted from the signals at 980 and 1540 nm, respectively (see Figure S6, Supporting Information for details). Therefore, the resulting components are to be solely attributed to the “pure” heterometallic Er/Yb species. The erbium signal rising at 1540 nm appears to be complementary to the ytterbium decay at 980 nm, in good agreement with the dynamics expected on the basis of a Yb-to-Er RET. This is further corroborated by the comparison of related time constants in the inset of Figure 8 (980 nm decay time, τ_{Yb*}, purple dots; 1540 nm risetime, τ_{Er*}, green dots), that fall in the 30-50 ns range for all the investigated compounds.

The dynamics of the process leading to erbium ⁴I_{13/2} population is therefore ultrafast, and, noteworthy, it is slightly slower than that observed in the homometallic Er₃Q₉ complex (τ = 21 ns, dashed line in the inset of Figure 8), as a consequence of the direct involvement of excited Yb³⁺ in the Er³⁺ sensitization mechanism in heterolanthanide species.⁹ The shortening of intermetallic distances in **2b** and **3b** with respect to **2** and **3** seems to lead to a slightly faster trend in Yb-to-Er RET dynamics. However, the small differences in the donor-acceptor separation, which is well below the Förster’s radius (R₀ ~ 10 Å) in all the investigated compounds, fall beyond any possible discrimination of related quantum efficiencies on the basis of the Förster’s theory.⁹

Moreover, the corrected signals at 1540 nm for compounds **2** and **3** in Figure 7b (and **2b** - **3b**, Figure S5b, Supporting Information), are of the same intensity, suggesting that erbium sensitization in heterometallic species is quantitative and independent of the number of erbium ions in the samples when exciting in a linear regime of 0.1 excitations per complex.⁹

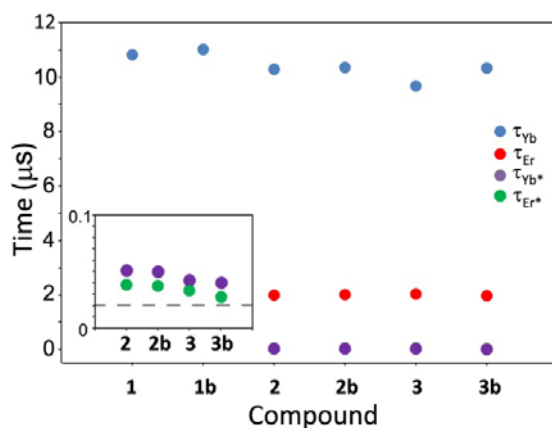


Figure 8. Time constants of the metal-centered dynamics in the NIR spectral region: ytterbium decay time for radiative emission at 980 nm, τ_{Yb}, blue dots; erbium emission decay time at 1540 nm, τ_{Er}, red dots; time constant of the Yb-to-Er RET, τ_{Yb*}, purple dots; erbium signal risetime at 1540 nm τ_{Er*}, green dots. Dashed line in the inset represents erbium signal risetime at 1540 nm in Er₃Q₉. Errors fall in the range 0.4-10 ns (see Table S4, Supporting Information).

The efficiency of the metal-to-metal resonant energy transfer (η_{RET}) can be easily estimated by taking into account the decay time of the donor (Yb³⁺) in the absence (τ_{Yb}) and in the presence (τ_{Yb*}) of the acceptor (Er³⁺), by considering the latter parameter as the time constant of Yb-to-Er RET, according to the following equation:

$$\eta_{\text{RET}} = \frac{1}{1 + \frac{\tau_{\text{Yb}^*}}{\tau_{\text{Yb}}}}$$

Therefore, almost quantitative (~99.5%) Yb-to-Er RET efficiency is found for all the heterolanthanide complexes investigated in this work, thanks to the short intermetallic distances in the trinuclear molecular framework (<3.5 Å).^{10,12-15}

Energy back transfer from Er to Yb is prevented by the ultra-short lifetime of the Er ⁴I_{11/2} level as observed in Er₃Q₉ (17 ns).⁹ From all these considerations, it is then possible to conclude that in hetero-lanthanide Er-Yb molecular assemblies, where the two lanthanide ions are held at a short distance between each other, Yb-to-Er RET is strongly favored and takes place as the only competitive mechanism, leading to erbium ⁴I_{13/2} • ⁴I_{15/2} emission as the final step.

As a final remark, it is interesting to note that no significant differences in ytterbium (or erbium) luminescence lifetimes are found for **1** and **1b** (**2**, **3** and **2b**, **3b**) in DMSO solution, despite the replacement of one Q ligand with the nitrate anion and therefore the lower number of CH groups, that are known to act as efficient vibrational quenchers towards NIR emitters.²⁹⁻³¹ For crystalline samples of **1** and **1b**, where solvent effects are ruled out, the observed emission lifetime at 980 nm, τ_{Yb} (**1b**) = 11.29 μs, is noticeably longer than τ_{Yb}(**1**) = 10.10 μs (see Figure S7, Supporting Information) in agreement with the

lower number of CH quenchers (48 vs. 54). In solution, this observation may be hampered by the lability of the bond at the central ligand, which may be likely replaced by coordinating dimethylsulfoxide molecules.

Decay constants with related experimental errors and curve fitting procedures are reported in the Supporting Information.

Er/Yb-doped silica thin films

In order to investigate the processing potential of heterolanthanide Er/Yb quinolinolato complexes, experiments on the incorporation of compound **2** into silica thin films have been performed. Homogeneous and transparent doped thin films (see Figure S8 in the Supporting Information) have been prepared by dipcoating or dropcasting a *sol* solution, containing a mixture of alkoxysilane precursors, and the complex dissolved in ethanol, on a quartz support. Different alkoxysilanes (glycidoxy-propyl-trimethoxy-silane, GLYMO, and a mixture of tetramethoxysilane, TMOS, and isobutyl-trimethoxy-silane, ITMS, see Experimental Section) have been used as starting precursors, to investigate potential matrix effects on the optical properties of the final material.

The best results in terms of optical response have been obtained when using GLYMO as precursor, and corresponding NIR PL spectra and dynamics are reported in Figure 9. The doped GLYMO-based film retains the main optical properties of **2**, showing dual NIR luminescence at 1 and 1.5 μm , after photoexcitation at 355 nm. The spectral profiles of Yb^{3+} and Er^{3+} emissions, shown in Figure 9a (blue line, Yb^{3+} , red line, Er^{3+}), are very similar to those observed for **2** in solution (Figure 3d). This indicates that the coordination sphere of both ions, and consequently the molecular framework, remains mostly unaltered as the complex is embedded into the silica host matrix. The NIR emission dynamics, shown in Figure 9b, confirms that Yb-to-Er RET still takes place in the doped film, as evidenced by the ultrafast component of the Yb^{3+} 980 nm decay trace (see inset of Figure 9b, blue line). The longer-lived fraction of the 980 nm decay, has a double-exponential dynamics and curve fitting yields the following time constants: $\tau_{\text{Yb1}} = 1.48 \mu\text{s}$ (60%) and $\tau_{\text{Yb2}} = 6.57 \mu\text{s}$ (40%). Similar observations can be made for the Er^{3+} decay at 1540 nm (red line, Figure 9), for which $\tau_{\text{Er1}} = 0.41 \mu\text{s}$ (60%) and $\tau_{\text{Er2}} = 1.81 \mu\text{s}$ (40%) are retrieved from double-exponential fitting. These results seem to suggest that two different populations of complexes exist in the host matrix, whose luminescence lifetimes are slightly shortened to different extent by second sphere quenching interactions with the silica backbone, as already observed for an analogous Yb quinolinolate-doped silica-glass material.²¹ It must be remarked that repeated measurements have shown that the same optical features are flawlessly reproduced throughout the film, proving the optimal dispersion of the dopant compound in the silica matrix.

Data for the TMOS/ITMS-based film are summarized in Figure S9 in the Supporting Information. Further investigations on the effects of silica matrixes based on different alkoxysilane precursors on the optical/photophysical properties of thin

films incorporating NIR emitting lanthanide complexes, are currently being performed in our laboratories.

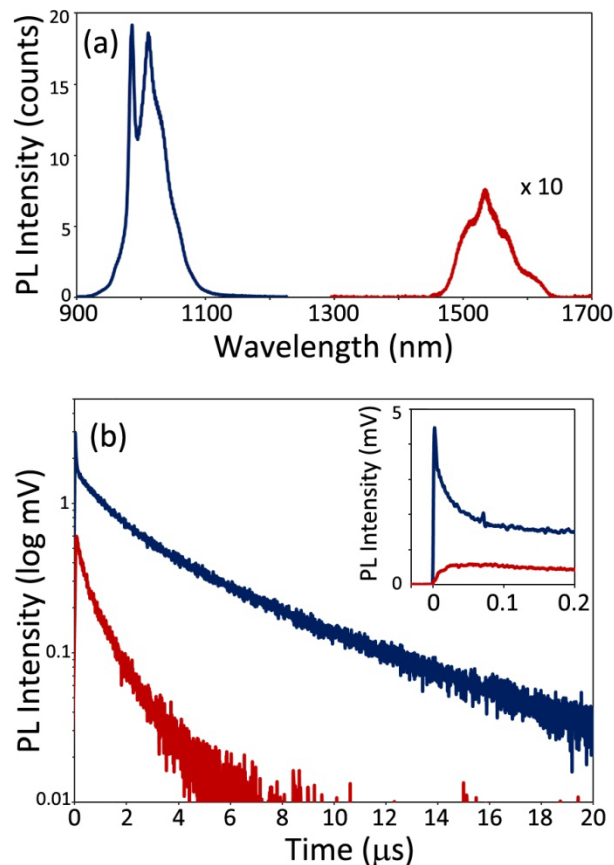


Figure 9. NIR PL studies of a GLYMO-based silica thin film doped with **2**: (a) PL spectrum showing the emission bands related to $\text{Yb}^{3+} {}^2\text{F}_{5/2} \rightarrow {}^2\text{F}_{7/2}$ (blue) and $\text{Er}^{3+} {}^4\text{I}_{13/2} \rightarrow {}^4\text{I}_{15/2}$ (red) transitions; (b) NIR dynamics at 980 nm (blue) and 1540 nm (red) plotted on a logarithmic scale. In the inset of panel (b) signal intensities in the 0-200 ns time range are reported on a linear scale. Excitation wavelength was 355 nm.

Conclusions

In conclusion, we have reported a detailed combined chemical/photophysical study on a series of trinuclear homo- (Yb) and heterolanthanide (Er, Yb) quinolinolato complexes as promising optically-active components of Er/Yb codoped NIR-emissive materials. On dependence of the starting metal salts used in the synthesis, homoleptic complexes of general formula $\text{Er}_x\text{Yb}_{3-x}\text{Q}_9$ ($x = 0, \mathbf{1}; x = 1, \mathbf{2}; x = 2, \mathbf{3}$; chloride, acetate or triflate salts) and the corresponding heteroleptic complexes $\text{Er}_x\text{Yb}_{3-x}\text{Q}_8\text{NO}_3$ ($x = 0, \mathbf{1b}; x = 1, \mathbf{2b}; x = 2, \mathbf{3b}$; mixture of chloride and nitrate salts), have been synthesized and characterized. XRD structural studies on **1b** have shown that this complex has a trinuclear $\text{Yb}_3\text{Q}_8\text{NO}_3$ molecular arrangement, where the central ytterbium is chelated by a nitrate anion, allowing a remarkable shortening of intermetallic distances with

respect to the Yb₃Q₉ analog. Metal compositional analysis on the heterometallic compounds, performed by ICP-mass measurements, has evidenced metal ratios close to the expected ones on the basis of the stoichiometric amounts used in the synthesis, with only a slightly favored affinity (2-4%) of Yb³⁺ with respect to Er³⁺ upon coordination to the Q ligand. Model analysis of ESI-mass spectra shows that, for the mixed metal compounds **2**, **2b**, **3** and **3b**, the relative abundance of heterometallic Er/Yb molecular species with respect to the homometallic ones, is consistent with predictions made on the basis of the relative amounts of Er³⁺ and Yb³⁺ ions in each sample, statistically distributed over the molecular coordination sites. These observations point out the “vicariant” chemical behavior of ytterbium and erbium ions toward coordination regardless of the starting metal salt used in the synthetic procedure, and that molecular speciation can be varied according to the metal stoichiometry established in the synthetic procedure.

Spectroscopic and time-resolved photophysical studies in the visible and NIR spectral regions have allowed a full disclosure of the photocycle leading to narrow-band lanthanide emission in these systems. Ligand-centered dynamics in the visible has been studied by means of time-resolved photoluminescence and photoinduced absorption experiments, which have confirmed that the Q ligand is able to sensitize Yb³⁺ and Er³⁺ with high efficiency, through a two-step mechanism involving excited triplet levels. Mixed Er/Yb compounds show simultaneous dual luminescence at 1 and 1.5 μm upon single-wavelength irradiation in the ligand lowest absorption band, as a result of the weighted contribution of the different hetero- and homometallic species in the samples. These spectral features can therefore be finely modulated by tuning the molecular speciation simply on variation of the Er/Yb metal ratio. Time-resolved studies in the NIR provide evidence that the excited Yb³⁺ is directly quenched by RET to Er³⁺ and that this process is favored by the shorter intermetallic distances in heteroleptic complexes. Yb-to-Er RET is quantitative and emission intensity at 1540 nm is independent of the number of erbium ions in the sample.

In the solid state, a noticeable increase of the Yb³⁺ emission lifetime is observed in the heteroleptic **1b** complex with respect to the homoleptic analog **1**, as a consequence of the lowering of the number of CH quenching groups in the surroundings of the emitting lanthanide ion. ESI-mass spectrometry provided evidence that the trinuclear structure is preserved in solution as [Er_xYb_{3-x}Q₈]⁺ (x = 0-3) species, likely resulting from the fragmentation of the labile central coordinated ligand.

Finally, it has been demonstrated that these kind of complexes can be easily processed through mild solution techniques, such as the sol-gel method, without alterations. Highly transparent and homogeneous silica thin films doped with **2** have been prepared, showing the same optical properties of the incorporated complex in solution. This strategy opens new perspectives for the development of NIR-emitting codoped Er/Yb materials such as optical waveguides and amplifiers, while taking advantage of the effective molecular approach for the control

of light conversion processes in functional heterolanthanide assemblies.

Experimental Section

General

All the reagents and solvents were purchased from Aldrich and used without further purification.

Syntheses

Synthesis of 1 and 1b: Few drops of NH₃ 28% up to a final concentration of 2.0×10⁻² mol dm⁻³ (pH ≅ 10) were added to a suspension of 8-hydroxy-quinoline (0.145 g, 1 mmol) in H₂O (100 mL) under stirring. After 30 min a water solution of YbCl₃·6H₂O (**1**, 0.129 g, 0.33 mmol) or Yb(NO₃)₃·6H₂O (**1b**, 0.154 g, 0.33 mmol) was added to the above mixture, which was allowed to react for 2 days until the white solid due to the unreacted ligand disappears. A yellow precipitate formed, which was collected by filtration, washed with water, NaOH 0.1 M, water, and dried in oven at 60°C overnight (almost quantitative yield). The solid was then dissolved in warm CH₃CN, the solvent was roto-evaporated to incipient precipitation and after several days yellow microcrystals of **1** and **1b** were obtained. X-ray diffraction data were collected on single crystals of **1b** for structural studies. *Analytical and spectroscopic data for 1.* CHN Found (Calculated for C₈₁H₅₄Yb₃N₉O₉·3H₂O): C% 52.18 (52.01), H% 3.35 (3.23), N% 6.82 (6.74). FT-IR, cm⁻¹: 3047 m, 1601 m, 1571 s, 1498 vs, 1466 vs, 1424 mw, 1383 s, 1318 s, 1276 m, 1231 m, 1174 w, 1109 vs, 1035 w, 907 w, 823 m, 804 m, 788 m, 732 s, 648 m, 607 m, 592 w; 571 w, 504 m, 490 m, 458 w, 419 mw, 397 m, 384 m, 376 m, 353 m, 335 vw, 326 w, 315 vw, 303 w, 290 w, 280 m, 266 w, 253 m, 247 m, 226 m, 203 m, 177 m, 151 ms, 140 m, 132 m, 121 m, 101m 90 m 80 mw, 74 mw, 57 mw. UV-Vis-NIR absorption, nm, [mol⁻¹ dm³ cm⁻¹], DMSO: 381 [2.25·10⁴], 977 (Yb³⁺ ²F_{5/2}• ²F_{7/2}) [20]; Diffuse reflectance, nm: 262, 344, 385; 928, 952, 979 (²F_{7/2}• ²F_{5/2}), 1147 (3vC-H), 1678 (2vC-H). ESI-Mass (CH₃CN/CH₃OH 3/1), m/z: 1671.87 [Yb₃Q₈]⁺. *Analytical and spectroscopic data for 1b.* CHN Found (Calculated for C₇₂H₄₈Yb₃N₉O₁₁·3H₂O): C% 47.75 (48.36), H% 3.25 (3.04), N% 7.14 (7.05). FT-IR, cm⁻¹: 3047 m, 1601 m, 1571 s, 1498 vs, 1466 vs, 1424 mw, 1383 s, 1318 s, 1276 m, 1231 m, 1174 w, 1109 vs, 1035 w, 907 w, 823 m, 804 m, 788 m, 732 s, 648 m, 607 m, 592 w; 571 w, 504 m, 490 m, 458 w, 419 mw. UV-Vis-NIR absorption, nm, [mol⁻¹ dm³ cm⁻¹], DMSO: 378[2.06×10⁴], 977 (Yb³⁺ ²F_{5/2}• ²F_{7/2}). Diffuse reflectance, nm: 262, 344, 385; 928, 952, 979 (Yb³⁺ ²F_{7/2}• ²F_{5/2}), 1147 (3vC-H), 1678 (2vC-H). ESI-Mass (CH₃CN/CH₃OH 3/1), m/z: 1671.87 [Yb₃Q₈]⁺.

Synthesis of 2, 3, 2b, 3b: Syntheses were carried out following the same procedure described for **1** and **1b**, by adding to a solution containing 1 mmol of the deprotonated ligand, a mixture of 0.22 mmol of LnCl₃·6H₂O (Ln = Yb, **2**, **2b**; Er, **3**, **3b**) and 0.11 mmol of LnCl₃·6H₂O (Ln = Er, **2**; Yb, **3**) or Ln(NO₃)₃·6H₂O (Ln = Er, **2b**; Yb, **3b**) in water. A yellow precipitate formed, and it was then collected by filtration, washed

with water, NaOH 0.1 M, water, and dried in oven at 60°C overnight (yield > 95%). Yellow microcrystals were obtained after recrystallization from CH₃CN. *Analytical and spectroscopic data for 2.* CHN Found (Calculated for C₈₁H₅₄ErYb₂N₉O₉·3H₂O): C% 52.25 (52.17), H% 3.38 (3.24), N% 6.87 (6.76). FT-IR, cm⁻¹: 3047 m, 1601 m, 1571 s, 1498 vs, 1466 vs, 1424 mw, 1383 s, 1318 s, 1276 m, 1231 m, 1174 w, 1109 vs, 1035 w, 907 w, 823 m, 804 m, 788 m, 732 s, 648 m, 607 m, 592 w; 571 w, 504 m, 489 m, 458 w, 419 mw, 397 m, 384 m, 377 m, 353 m, 335 vw, 326 w, 315 vw, 303 w, 289 w, 280 m, 267 w, 253 m, 247 m, 226 m, 203 m, 177 m, 151 ms, 140 m, 132 m, 121 m, 105 m, 101 m, 89 m, 80 mw, 74 mw, 57 mw. UV-Vis-NIR absorption, nm, [mol⁻¹ dm³ cm⁻¹], DMSO: 379 [2.20·10⁴], 522 (Er³⁺ ²H_{11/2}·⁴I_{15/2}), 652 (Er³⁺ ⁴F_{9/2}·⁴I_{15/2}), 977 (Yb³⁺ ²F_{5/2}·²F_{7/2} and Er³⁺ ⁴I_{11/2}·⁴I_{15/2}) [20], 1540 (Er³⁺ ⁴I_{13/2}·⁴I_{15/2}) [3.5]; Diffuse reflectance, nm: 262, 344, 385, 521 (Er³⁺ ²H_{11/2}·⁴I_{15/2}), 653 (Er³⁺ ⁴F_{9/2}·⁴I_{15/2}), 802 (Er³⁺ ⁴I_{4/2}·⁴I_{15/2}), 979 (Yb³⁺ ²F_{5/2}·²F_{7/2} and Er³⁺ ⁴I_{11/2}·⁴I_{15/2}), 1147(3v C–H), 1533 (Er³⁺ ⁴I_{13/2}·⁴I_{15/2}), 1678 (2v C–H). ICP-mass (atomic ratios, average on 5 repeated measurements): Er:Yb 1:2.36. ESI-Mass (CH₃CN/CH₃OH 3/1), m/z: 1666.5 [ErYb₂Q₈]⁺. The same product was obtained when reacting two equivalents of Yb³⁺ chloride with one equivalent of Er³⁺ acetate or triflate. *Analytical and spectroscopic data for 3.* CHN Found (Calculated for C₈₁H₅₄Er₂YbN₉O₉·3H₂O): C% 51.80 (52.33), H% 3.34 (3.25), N% 6.60 (6.78). FT-IR, cm⁻¹: 3047 m, 1602 m, 1570 s, 1498 vs, 1466 vs, 1425 mw, 1383 s, 1318 s, 1278 m, 1232 m, 1173 w, 1109 vs, 1035 w, 907 w, 824 m, 804 m, 788 m, 732 s, 648 m, 607 m, 592 w; 571 w, 504 m, 489 m, 458 w, 419 mw. UV-Vis-NIR absorption, nm, [mol⁻¹ dm³ cm⁻¹], DMSO: 381 [2.25·10⁴], 522 (Er³⁺ ²H_{11/2}·⁴I_{15/2}), 652 (Er³⁺ ⁴F_{9/2}·⁴I_{15/2}), 977 (Yb³⁺ ²F_{5/2}·²F_{7/2} and Er³⁺ ⁴I_{11/2}·⁴I_{15/2}); Diffuse reflectance, nm: 262, 344, 385, 521 (Er³⁺ ²H_{11/2}·⁴I_{15/2}), 653 (Er³⁺ ⁴F_{9/2}·⁴I_{15/2}), 802 (Er³⁺ ⁴I_{4/2}·⁴I_{15/2}), 979 (Yb³⁺ ²F_{5/2}·²F_{7/2} and Er³⁺ ⁴I_{11/2}·⁴I_{15/2}), 1147(3v C–H), 1533 (Er³⁺ ⁴I_{13/2}·⁴I_{15/2}), 1678 (2v C–H). ICP-mass (atomic ratios, average on 5 repeated measurements): Er:Yb 1:0.56. ESI-Mass (CH₃CN/CH₃OH 3/1), m/z: 1660.1 [Er₂YbQ₈]⁺. The same product was obtained when reacting two equivalents of Er³⁺ chloride with one equivalent of Yb³⁺ acetate or triflate. *Analytical and spectroscopic data for 2b.* CHN Found (Calculated for C₇₂H₄₈ErYb₂N₉O₁₁·3H₂O): C% 49.77 (48.51), H% 2.82 (3.05), N% 6.44 (7.07). FT-IR, cm⁻¹: 3049 m, 1602 m, 1571 s, 1499 vs, 1466 vs, 1423 mw, 1382 s, 1318 s, 1277 m, 1230 m, 1173 w, 1109 vs, 1036 w, 908 w, 822 m, 804 m, 788 m, 732 s, 649 m, 606 m, 590 w; 571 w, 504 m, 490 m, 457 w, 420 mw. UV-Vis-NIR absorption, nm, [mol⁻¹ dm³ cm⁻¹], DMSO: 378 [2.09·10⁴], 522 (Er³⁺ ²H_{11/2}·⁴I_{15/2}), 652 (Er³⁺ ⁴F_{9/2}·⁴I_{15/2}), 977 (Yb³⁺ ²F_{5/2}·²F_{7/2} and Er³⁺ ⁴I_{11/2}·⁴I_{15/2}); Diffuse reflectance, nm: 262, 344, 385, 521 (Er³⁺ ²H_{11/2}·⁴I_{15/2}), 653 (Er³⁺ ⁴F_{9/2}·⁴I_{15/2}), 802 (Er³⁺ ⁴I_{4/2}·⁴I_{15/2}), 979 (Yb³⁺ ²F_{5/2}·²F_{7/2} and Er³⁺ ⁴I_{11/2}·⁴I_{15/2}), 1147 (3· C–H), 1533 (Er³⁺ ⁴I_{13/2}·⁴I_{15/2}), 1678 (2v C–H). ICP-mass (atomic ratios, average on 5 repeated measurements): Er:Yb 1:2.44. ESI-Mass (CH₃CN/CH₃OH 3/1), m/z: 1666.5 [ErYb₂Q₈]⁺. *Analytical and spectroscopic data for 3b.* CHN Found (Calculated for C₇₂H₄₈Er₂YbN₉O₁₁·3H₂O): C% 49.23 (48.67), H% 2.81 (3.06), N% 6.62 (7.09). FT-IR, cm⁻¹: 3048 m, 1602 m, 1571 s, 1499 vs, 1466 vs, 1423 mw, 1382 s, 1318 s, 1277 m, 1230 m, 1171 w, 1109 vs, 1036 w, 909 w, 822 m,

804 m, 787 m, 732 s, 650 m, 606 m, 590 w; 571 w, 504 m, 490 m, 457 w, 420 mw. UV-Vis-NIR absorption, nm, [mol⁻¹ dm³ cm⁻¹], DMSO: 378 [2.06·10⁴], 522 (Er³⁺ ²H_{11/2}·⁴I_{15/2}), 652 (Er³⁺ ⁴F_{9/2}·⁴I_{15/2}), 977 (Yb³⁺ ²F_{5/2}·²F_{7/2} and Er³⁺ ⁴I_{11/2}·⁴I_{15/2}); Diffuse reflectance, nm: 262, 344, 385, 521 (Er³⁺ ²H_{11/2}·⁴I_{15/2}), 653 (Er³⁺ ⁴F_{9/2}·⁴I_{15/2}), 802 (Er³⁺ ⁴I_{4/2}·⁴I_{15/2}), 979 (Yb³⁺ ²F_{5/2}·²F_{7/2} and Er³⁺ ⁴I_{11/2}·⁴I_{15/2}), 1147 (3v C–H), 1533 (Er³⁺ ⁴I_{13/2}·⁴I_{15/2}), 1678 (2v C–H). ICP-mass (atomic ratios, average on 5 repeated measurements): Er:Yb 1:0.54. ESI-Mass (CH₃CN/CH₃OH 3/1), m/z: 1660.1 [Er₂YbQ₈]⁺.

Preparation of silica thin films doped with 2

GLYMO thin film: The sol precursor was prepared by mixing GLYMO with EtOH and H₂O (molar ratio = 1:9:5) under stirring at room temperature (RT) for 24 hours. Subsequently, a volume of 2.5 mL of **2** in EtOH (5×10⁻⁴ M) was added to 7.5 mL of the sol precursor and the mixture was maintained under stirring at 50 °C for 1 hour. Transparent sol was obtained. Films were prepared by the dip coating or drop casting method. After preparation all films were dried at room temperature for 48 h. Quartz slides were employed as substrates for film preparation. Before coating, the substrates were cleaned through water soap, distilled water, acetone and finally rinsed with isopropanol. PL measurements have been performed on dropcasted films.

TMOS/ITMS thin film: The precursor sol solution was prepared by mixing 8 mL of absolute ethanol, 8 mL of TMOS, 8 mL of ITMS and 4 mL H₂O in a round-bottom flask (molar ratio: ITMS:TMOS:EtOH:H₂O = 1:1.3:3.3:5.4). This mixture was maintained 1 day under stirring at room temperature (~22°C). Afterwards, 2 mL of a 5×10⁻⁴ M solution of **2** in EtOH were added to 3 mL of the sol solution and the mixture was maintained under stirring at 50°C for 1 h. The obtained sol was then dropcasted on a glass support and let drying at room temperature.

Analytical data and spectroscopic characterization

Elemental analysis: C, H, N analyses were performed with a Flash 2000 Fisher Scientific Thermo Electron Analyzer. *Electronic UV-Vis-NIR:* Diffuse reflectance (DR) on Teflon films and solution absorption spectra were collected using a Agilent Cary 5000 spectrophotometer. *Vibrational spectroscopy:* FTIR spectra on KBr pellets were collected using a Bruker Equinox 55 spectrophotometer. *ICP-mass determinations:* 220mg of a DMSO solution (5×10⁻⁴M, approx) of the selected sample, were introduced in a TFM vessel containing a mixture of HNO₃ (65%, 4 mL), H₂O₂ (30%, 0.5 mL) and H₂O (bidistilled, 4 mL) thus treated in a Milestone Ethos 1 Microwave digester, equipped with a HPR1000/10S high pressure segmented rotor, ATC-400CE automatic temperature control and Terminal 640 with easyCONTROL software. The treatment was performed by applying a microwave program consisting of two steps each lasting 10 minutes, at the temperature of 200 °C and microwave power up to 1000W. The samples were prepared for the analysis by diluting the digested solutions with 5% HNO₃ (suprapur grade) blank and then the metals were determined using a quadrupole ICP-MS Varian mod. RT equipped with a 90° reflecting ion mirror (Varian, Mulgrave, Australia), a Micromist glass low flow concentric nebulizer, a Peltier-cooled (3°C) double pass glass spray chamber and a glass torch, with

respect to 4-points external aqueous calibration plots in the 0.1–25 $\mu\text{g L}^{-1}$ range for each metal (Correlation Coefficients > 0.999990, Limit of Detection (LoD) for the different analytes: 0.5–5 ng L^{-1}). Instrumental parameters and measured isotopes are listed in Table S1 in the Supporting Information. *ESI-mass*: Mass spectra were obtained with a Micromass ZMD spectrometer operating in positive ionisation mode. *SEM-EDX*. SEM-EDX analyses were performed with a FEI Dual Beam Nova NanoLab 600i equipped with a EDAX Genesis microanalyser.

Structural and crystallographic studies

X-ray powder diffraction. Wide-angle XRD-patterns on microcrystalline powder samples were recorded with a Panalytical Empyrean diffractometer equipped with a graphite monochromator and a X'Celerator linear detector. The scans were collected within the range 5–40° (2 θ) using Cu K α radiation.

Data collection and structure determination for 1b. A clear colourless needle-like specimen of **1b** of approximate dimensions 0.011×0.019×0.099 mm was used for the X-ray crystallographic analysis. The X-ray intensity data were measured on a Bruker D8 VENTURE system equipped with a multilayer monochromator and a Mo K α Incoatec microfocus sealed tube ($\lambda = 0.71073 \text{ \AA}$). This instrumental set-up was well suited for the collection of the small crystal sample. A total of 777 frames were collected, which were integrated with the Bruker SAINT software package using a narrow-frame algorithm.³² The integration of the data using a triclinic unit cell yielded a total of 40882 reflections to a maximum θ angle of 25.03° (0.84 \AA resolution), Table 1. Data were corrected for absorption effects using the multi-scan method (SADABS V2012/1).^{33–34} The calculated minimum and maximum transmission coefficients (based on crystal size) were 0.660 and 0.951. The structure was solved and refined using XS and XL included in the APEX2 software suite,^{35–36} using the space group P -1. The largest peak and hole in the final difference electron density synthesis were 2.484 $\text{e}/\text{\AA}^3$ and -1.253 $\text{e}/\text{\AA}^3$, respectively. CCDC 1054887 contain the supplementary crystallographic data.

Photophysical studies

Absorption and photoluminescence (PL) studies, except for doped thin films and crystalline samples, were performed on diluted (5×10^{-4} M) solutions of the strongly coordinating dimethyl sulfoxide (DMSO) solvent to ensure that the observed properties are related to isolated molecules rather than to aggregates or clusters. CW visible PL spectra were recorded using a Horiba Jobin-Yvon FluoroMax-4 spectrofluorimeter. Transient PL was excited at 392 nm wavelength by the frequency-doubled, 130-fs-long output pulses of a regenerative Ti:Sapphire amplifier (Quantronix INTEGRA C) running at repetition frequency of 1 kHz. For silica thin films, PL in the NIR was excited at 355 nm wavelength using the 310-ps-long output pulses of a passively Q-switched powerchip laser running at repetition frequency of 1 kHz. Vis PL decay transients were captured by a streak camera (Hamamatsu C5680) equipped with a grating spectrometer (Acton SpectraPro 2300i). NIR PL was wavelength dispersed by an Acton SpectraPro 2300i spectrometer; optical spectra and decay transients

were detected using, respectively, an InGaAs CCD (Andor iDus) and a photomultiplier (Hamamatsu H10330A-75) connected to a 1 GHz digitising oscilloscope (Tektronik TDS 5104). In order to minimize nonlinear effects possibly taking place in doubly excited complexes, photoexcitation fluences were kept below the level of 0.1 excitations per complex per laser pulse in all experiments. Transient photoinduced absorption was measured by broadband synchronous pulses obtained by supercontinuum generation in a sapphire plate. The optical probe beam transmitted through the sample was spectrally dispersed using a SpectraPro 2300i spectrograph and detected by a charge-coupled device (Andor NEWTON). Pump-probe time delay was varied using a motorized optical delay stage. Photoinduced absorption is measured as the differential transmission signal $\Delta T/T = (T - T_0)/T_0$, where T (T_0) is the transmitted probe pulse energy in presence (absence) of the pump pulse(s). PL measurements on crystalline samples were performed with an Edinburgh Instruments FLSP920 spectrofluorimeter equipped with a photomultiplier detector (Hamamatsu R5509-72 NIR PMT) and using a 450W xenon lamp as the steady state excitation source for NIR spectra and a Continuum Surelite I-10 Nd:YAG laser system (10 Hz repetition rate) using the third harmonic $\lambda_{\text{exc}} = 355 \text{ nm}$ for time-resolved dynamics.

ASSOCIATED CONTENT

Supporting Information. ICP-mass setup details, powder XRD patterns, EDX analysis, supplementary ESI-mass, spectroscopic and PL data, details of kinetic equations and curve fitting procedures. This information is available free of charge via the Internet at <http://pubs.acs.org>.

AUTHOR INFORMATION

Corresponding Author

*Email: f.artizzu@unica.it (F.A.), francesco.quoichi@dsf.unica.it (F. Q.), deplano@unica.it (P.D.)

ACKNOWLEDGMENT

The Regione Autonoma della Sardegna (CRP-17571) and Banco di Sardegna Foundation are gratefully acknowledged for financial support. The authors thank Dr. A. Rigoldi for for ICP-mass and Drs. S. Podda and E. Musu (Laboratorio di Telemicroscopia Industriale, Sardegna Ricerche) for SEM-EDX analyses. The authors thank Dr. Holger Ott of Bruker AXS (Karlsruhe) for the single crystal data collection. RVD thanks the Flemish Hercules Foundation (project AUGÉ/09/024 “Advanced Luminescence Setup”) for funding.

REFERENCES

- (1) Bunzli, J.-C. G.; Piguet, C. *Chem. Soc. Rev.* **2005**, *34*, 1048.
- (2) Eliseeva, S. V.; Bunzli, J.-C. G. *Chem. Soc. Rev.* **2010**, *39*, 189.
- (3) Strohhofer, C.; Polman, A. *Opt. Mater.* **2003**, *21*, 705.
- (4) Chryssou, C. E.; Di Pasquale, F.; Pitt, C. W. *J. Lightwave Technol.* **2001**, *19*, 345.
- (5) Chiasera, A.; Tosello, C.; Moser, E.; Montagna, M.; Belli, R.; Goncalves, R. R.; Righini, G. C.; Pelli, S.; Chiappini, A.; Zampedri, L.; Ferrari, M. *J. Non-Cryst. Solids* **2003**, *322*, 289.
- (6) Wong, W. H.; Pun, E. Y. B.; Chan, K. S. *Appl. Phys. Lett.* **2004**, *84*, 176.
- (7) L. D. da Vila, L. Gomes, L. V. G. Tarelho, S. J. L. Ribeiro, Y. Messadeq *J. Appl. Phys.* **2003**, *93*, 3873.

- (8) Dong, B.; Feng, Z. Q.; Cao, B. S.; Zheng, J. Z. *J. Sol-Gel Sci. Technol.* **2009**, *50*, 383.
- (9) Artizzu, F.; Quochi, F.; Marchiò, L.; Sessini, E.; Saba, M.; Serpe, A.; Mura, A.; Mercuri, M. L.; Bongiovanni, G.; Deplano, P. *J. Phys. Chem. Lett.*, **2013**, *4*, 3062.
- (10) Artizzu, F.; Quochi, F.; Marchiò, L.; Fonseca Correia, R.; Saba, M.; Serpe, A.; Mura, A.; Mercuri, M. L.; Bongiovanni, G.; Deplano, P. *Chem. Eur. J.*, **2015**, *21*, 3882.
- (11) Van Deun, R.; Fias, P.; Nockemann, P.; Schepers, A.; Parac-Vogt, T. N.; Van Hecke, K.; Van Meervelt, L.; Binnemans, K. *Inorg. Chem.*, **2004**, *43*, 8461.
- (12) Artizzu, F.; Deplano, P.; Marchiò, L.; Mercuri, M. L.; Pilia, L.; Serpe, A.; Quochi, F.; Orrù, R.; Cordella, F.; Meinardi, F.; Tubino, R.; Mura, A.; Bongiovanni, G. *Inorg. Chem.*, **2005**, *44*, 840.
- (13) Leary, S. G.; Deacon, G. B.; Junk, P. C. *Z. Anorg. Allg. Chem.* **2005**, *631*, 2647.
- 14(14) Baranov, E. V.; Fukin, G. K.; Balashova, T. V.; Pushkarev, A. P.; Grishin, I. D.; Bochkarev, M. N. *Dalton Trans.* **2013**, *42*, 15699;
- (15) Chilton, N. F.; Deacon, G. B.; Gazukin, O.; Junk, P. C.; Kersting, B.; Langley, S. K.; Moubaraki, B.; Murray, K. S.; Schleife, F.; Shome, M.; Turner, D. R.; Walker, J. A. *Inorg. Chem.* **2014**, *53*, 2528.
- (16) Quochi, F.; Saba, M.; Artizzu, F.; Mercuri, M. L.; Deplano, P.; Mura, A.; Bongiovanni, G.; *J. Phys. Chem. Lett.*, **2010**, *1*, 2733.
- (17) Artizzu, F.; Quochi, F.; Saba, M.; Marchiò, L.; Espa, D.; Serpe, A.; Mura, A.; Mercuri, M. L.; Bongiovanni, G.; Deplano, P. *ChemPLUSChem*, **2012**, *77*, 240.
- (18) Curry, R. J.; Gillin, W. P. *Appl. Phys. Lett.* **1999**, *75*, 1380.
- (19) Khreis, O. M.; Gillin, W. P.; Somerton, M.; Curry, R. J. *Org. Electron.* **2001**, *2*, 45.
- (20) Penna, S.; Reale, A.; Pizzoferrato, R.; Tosi Beleffi, G. M.; Musella, D.; Gillin, W. P. *Appl. Phys. Lett.* **2007**, *91*, 021106.
- (21) Figus, C.; Quochi, F.; Artizzu, F.; Piana, G.; Saba, M.; Mercuri, M. L.; Serpe, A.; Deplano, P.; Mura, A.; Bongiovanni, G. *AIP Conf. Proc.* **2014**, *1624*, 37.
- (22) Artizzu, F.; Quochi, F.; Saba, M.; Loche, D.; Serpe, A.; Mercuri, M. L.; Mura, A.; Bongiovanni, G.; Deplano, P. *Dalton Trans.*, **2012**, *41*, 13147.
- (23) Binnemans, K. *Chem. Rev.* **2009**, *109*, 4283.
- (24) Armelao, L.; Quici, S.; Barigelletti, F.; Accorsi, G.; Bottaro, G.; Cavazzini M.; Tondello, E. *Coord. Chem. Rev.*, **2010**, *254*, 487.
- (25) O'Riordan, A.; Van Deun, R.; Mairiaux, E.; Moynihan, S.; Fias, P.; Nockemann, P.; Binnemans, K.; Redmond, G. *Thin Solid Films*, **2008**, *516*, 5098.
- (26) Artizzu, F.; Quochi, F.; Serpe, A.; Sessini, E.; Deplano, P. *Inorg. Chem. Front.*, **2015**, *2*, 213.
- 27(27) Piguet, C.; Bünzli, J.-C. G. *Chem. Rev.*, **2002**, *102*, 1897;
- (8c) Piguet, C.; Bünzli, J.-C. G. *Chem. Soc. Rev.*, **1999**, *28*, 347.
- 28(28) Ballardini, R.; Varani, G.; Indelli, M. T.; Scandola, F. *Inorg. Chem.*, **1986**, *25*, 3858.
- (29) Scholten, J.; Rosser, G. A.; Wahsner, J.; Alzakhem, N.; Bischof, C.; Stog, F.; Beeby, A.; Seitz M. *J. Am. Chem. Soc.*, **2012**, *134*, 13915;
- (30) Monguzzi, A.; Milani, A.; Mech, A.; Brambilla, L.; Tubino, R.; Castellano, C.; Demartin, F.; Meinardi, F.; Castiglioni, C. *Synth. Met.*, **2012**, *161*, 2693.
- (31) Quochi, F.; Orrù, R.; Cordella, F.; Mura, A.; Bongiovanni, G. Artizzu, F.; Deplano, P.; Mercuri, M. L.; Pilia, L.; Serpe, A. *J. Appl. Phys.*, **2006**, *99*, 053520.
- (32) Bruker, SAINT V8.34A. Bruker AXS Inc., Madison, Wisconsin, USA., **2007**.
- (33) Bruker, SADABS V2012/1. Bruker AXS Inc., Madison, Wisconsin, USA, **2001**.
- (34) Krause, L.; Herbst-Irmer, R.; Sheldrick, G. M.; Stalke D. *J. Appl. Cryst.*, **2015**, *48*, 3.
- (35) Sheldrick, G. M. *Acta Crystallogr., Sect. A: Found. Crystallogr.*, **2008**, *64*, 112.
- (36) Sheldrick, G. M. *Acta Crystallogr., Sect. C: Structural Chemistry*, **2015**, *71*, 3.

Light Conversion Control in NIR-Emissive Optical Materials based on Heterolanthanide Er_xYb_{3-x} Quinolinolato Molecular Components

Flavia Artizzu, Francesco Quochi, Luciano Marchiò, Cristiana Figus, Danilo Loche, Matteo Atzori, Valerio Sarritzu, Rik Van Deun, Michele Saba, Angela Serpe, Andrea Mura, Maria Laura Mercuri, Giovanni Bongiovanni and Paola Deplano

Supporting Information

Analytical and structural data

ICP-Mass

Table S1. Equipment and settings for ICP-mass lanthanides determination on digested samples.

Spectrometer	ICP-MS Varian mod. RT
Plasma (Ar)	
Plasma flow	17.50 L min ⁻¹
Auxiliary flow	1.65 L min ⁻¹
Sheat gas flow	0.22 L min ⁻¹
Nebulizer flow	1.10 L min ⁻¹
Sampling depth	7 mm
Power	1.4 kW
Pump rate	3 rpm
Stabilisation delay	10 sec
Ion Optics	
Ion Lens Voltages	Optimized for mul tielement
Interface cones	analysis
Analysis modes	Nickel
Scan mode	
Scans/Replicate	Peak hopping
Replicates/Sample	20
Dwell time	5
Analytical mass	50 ms
	¹⁶⁶ Er, ¹⁶⁷ Er, ¹⁷¹ Yb, ¹⁷² Yb, ¹⁷³ Yb

Powder-XRD

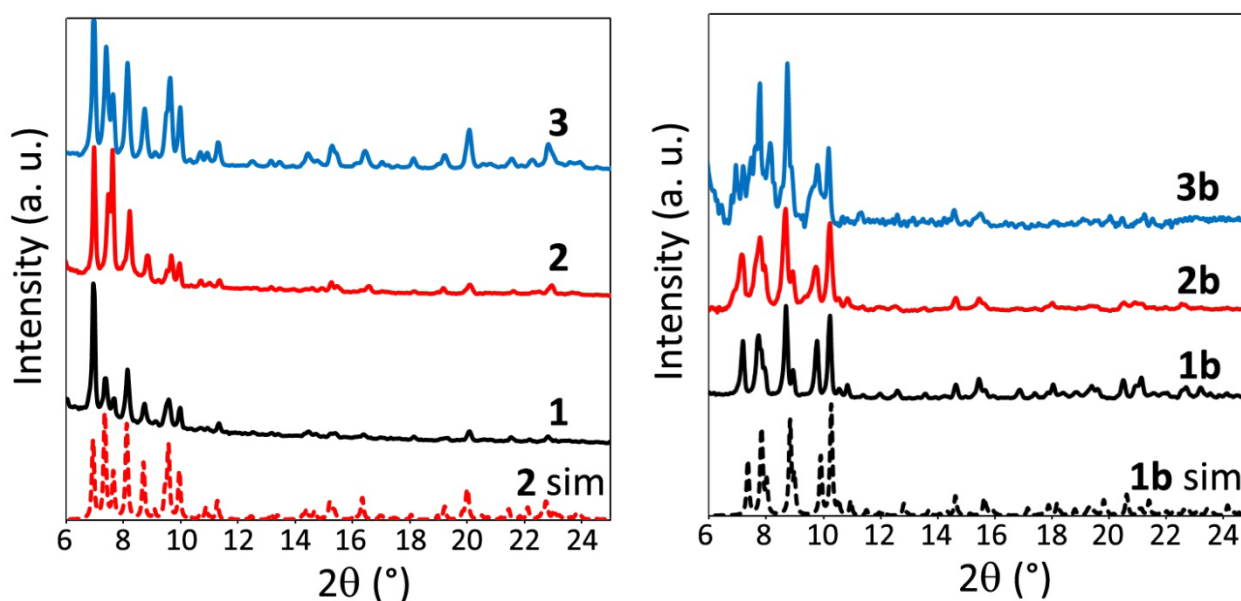


Figure S 1. Left: Experimental powder-XRD patterns for **1** (black), **2** (red) and **3** (blue) and comparison with the powder diffractogram of **2** (dashed red line) simulated from crystallographic data (see ref. 10). Right: Experimental powder-XRD patterns for **1b** (black), **2b** (red) and **3b** (blue) and comparison with the powder diffractogram of **1b** (dashed black line) simulated from crystallographic data. Differences in peaks intensities are related to preferential orientations.

SEM-EDX

Table S2. Metal atomic ratios of heterolanthanide complexes retrieved from EDX analysis.

Sample	Er:Yb ratio ^a
2	1:2.17
3	1:0.50
2b	1:2.31
3b	1:0.61

^aaverages of punctual analyses on three different crystals in the samples

ESI-mass

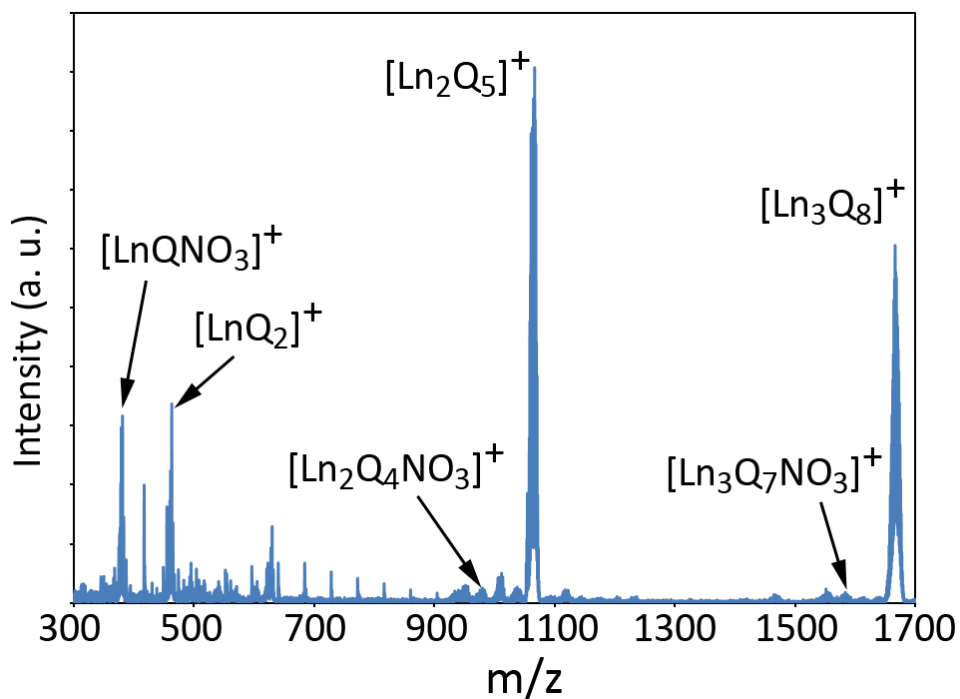


Figure S2. ESI-mass spectrum of **2b** in the range 300-1700 m/z with peaks assignments. m/z values for maximum intensities: $[\text{Ln}_3\text{Q}_8]^+ = 1666$; $[\text{Ln}_3\text{Q}_7\text{NO}_3]^+ = 1583$; $[\text{Ln}_2\text{Q}_5]^+ = 1066$; $[\text{Ln}_2\text{Q}_4\text{NO}_3]^+ = 979$; $[\text{LnQ}_2]^+ = 461$; $[\text{LnQNO}_3]^+ = 380$, (Ln = Er, Yb). The spectrum of **3b** was too noisy to recognize specific peaks apart the most intense $[\text{Ln}_3\text{Q}_8]^+$ and $[\text{Ln}_2\text{Q}_5]^+$ ones.

Vis and NIR Spectroscopy

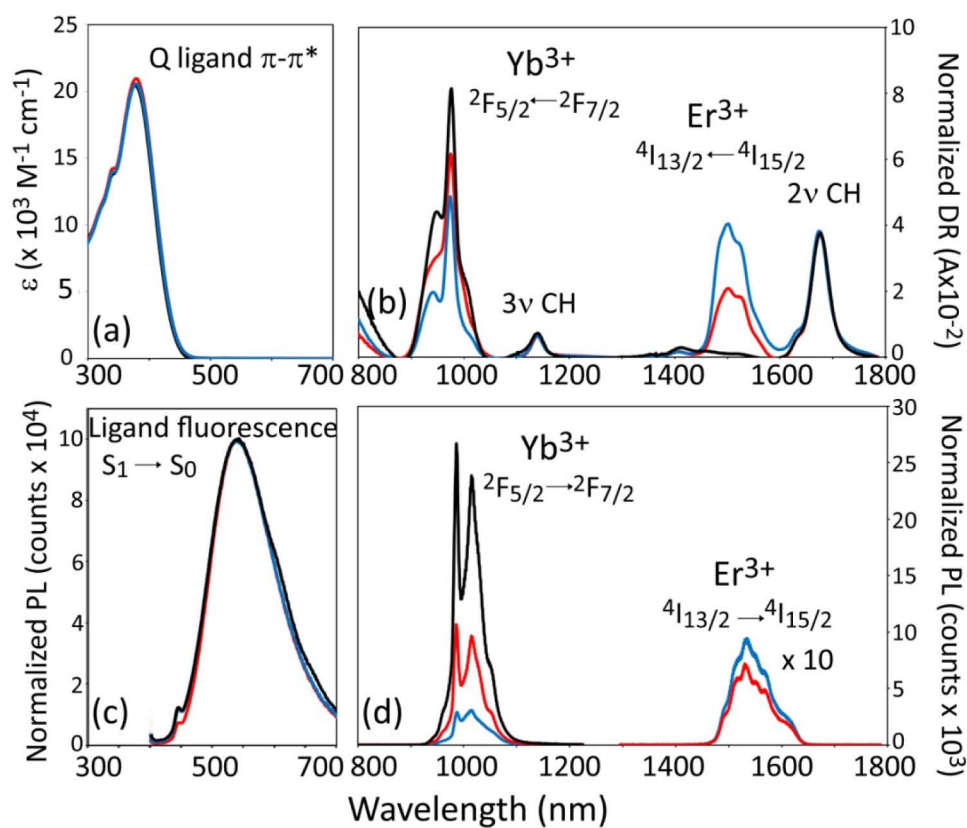


Figure S3. (a) Absorbance spectra in DMSO solution showing the broad band related to the Q ligand in the Uv-Vis region; (b) diffuse reflectance (DR) spectra of crystalline samples in the Vis-NIR region showing lines related to intrashell f-f transitions of Er³⁺ and Yb³⁺ and ligand CH stretching overtones; (c) Ligand fluorescence and (d) PL spectra in the NIR region, of DMSO solutions excited at $\lambda=392$ nm. Color coding: **1b** (black), **2b** (red) and **3b** (blue). Spectroscopic labels of Er³⁺ and Yb³⁺ transitions are also indicated. DR spectra are normalized to the 2v CH band. PL spectra are normalized for absorbed power at excitation wavelength.

Ligand-centered dynamics

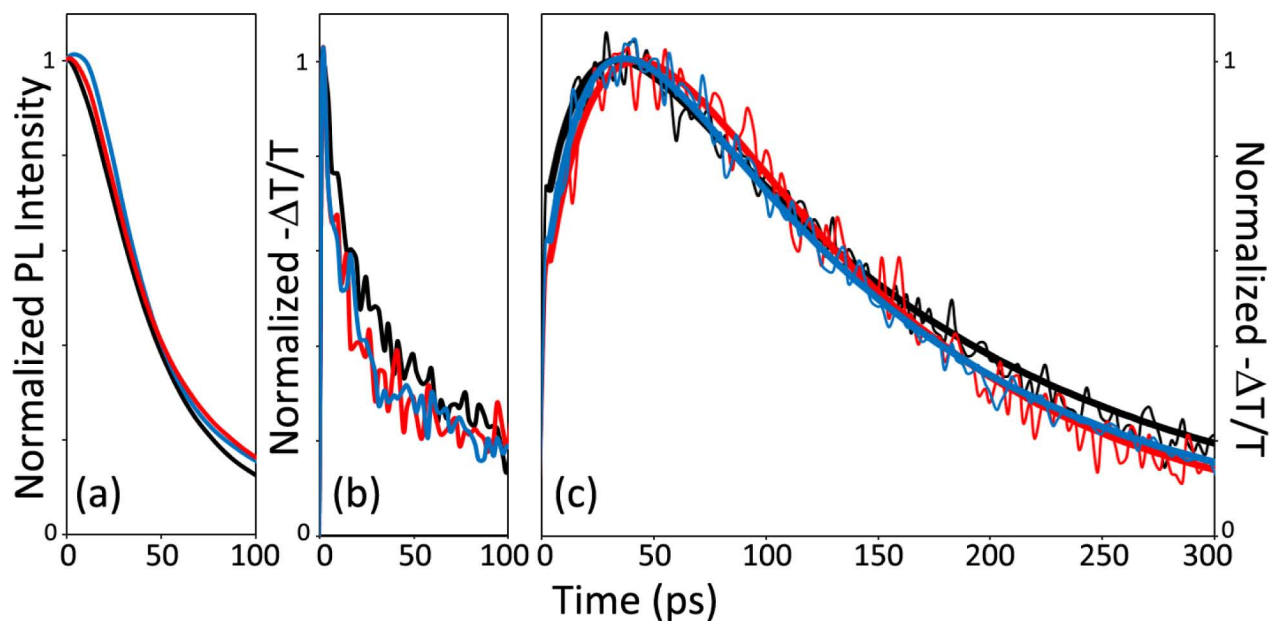


Figure S4. (a) Transient PL in the 400-700 nm region; (b) transient ESA probed in the region 430-440 nm showing ligand singlet decay dynamics and (c) ESA signal attributed to ligand triplet dynamics in the region 560-570 nm and curve fitting (thick lines). Excitation wavelength was $\lambda = 392$ nm. Color coding: **1b** (black), **2b** (red) and **3b** (blue). Signal intensities are normalized to unity.

Table S3. Time constants for transient photoluminescence (PL) and excited state absorption (ESA) dynamics in the visible region.

Sample	PL	τ_s (ps) [§]	ESA	τ_T (ps) [§]
	τ_{fluo} (ps) [§]		τ_{ISC} (ps) [§]	
1	50.6(0.6)	42.6(4.1)	37.1(2.5)	99.6(2.9)
1b	49.2(0.4)	31.9(3.0)	20.0(1.5)	150.2(2.2)
2	49.1(0.5)	23.5(4.3)	20.8(0.9)	139.8(1.6)
2b	54.1(0.8)	22.5(2.7)	29.2(2)	113.6(2.9)
3	43.0(0.4)	23.5(4.4)	19.4(3.6)	104.9(6.8)
3b	51.5(0.8)	26.5(3.8)	21.5(1.1)	128.2(1.7)

[§]Experimental uncertainties are reported in brackets

Excited singlet and triplet kinetics

Excited singlet and triplet population dynamics is modeled on the basis of the following rate equation model:

$$\frac{dN_S}{dt} = -\frac{N_S}{\tau_S} \quad (1.1)$$

$$\frac{dN_T}{dt} = +\frac{N_S}{\tau_S} - \frac{N_T}{\tau_T} \quad (1.2)$$

where $N_{S(T)}$ is the excited singlet (triplet) population, and $\tau_{S(T)}$ is the singlet (triplet) lifetime. Owing to the experimental observations, we assume that: (i) singlet de-excitation via intersystem crossing to the triplet state is much faster than all other singlet de-excitation mechanisms and hence τ_S coincides with intersystem crossing time constant; (ii) triplet is quenched with nearly 100% efficiency through lanthanide (Ln) energy sensitization, so that τ_T practically coincides with the Ln sensitization time constant. Singlet are only excited by ultrafast pumping at $t = 0$, hence $N_T(0) = 0$. Given the initial conditions, the solution is:

$$N_S(t) = N_S(0) \exp(-t / \tau_S) \quad (2.1)$$

$$N_T(t) = \frac{\tau_T}{\tau_T - \tau_S} N_S(0) [1 - \exp(-t / \tau_S + t / \tau_T)] \cdot \exp(-t / \tau_T) \quad (2.2)$$

Metal-centered dynamics

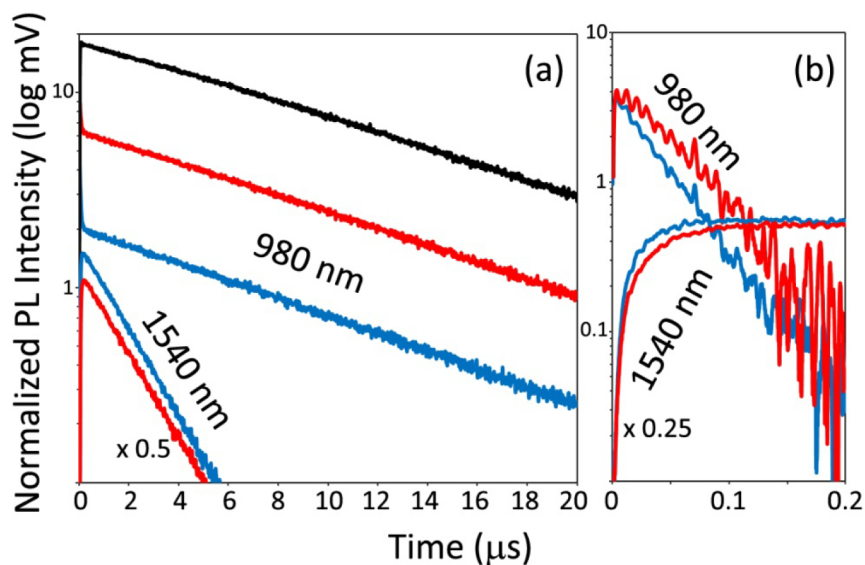


Figure S5. (a) NIR decay dynamics of **1b** (black), **2b** (red), and **3b** (blue) at 980 and 1540 nm. (b) NIR dynamics on a short time scale of **2b** (red) and **3b** (blue): the decay trace at 980 nm nm has been obtained by subtracting the long-lived component attributed to $\text{Yb}_3\text{Q}_8\text{NO}_3$ contribution. For the signal at 1540 nm, the contribution of the Er homometallic species has been estimated by taking into account the dynamics of Er_3Q_9 , and subtracted to the observed signal. Signal intensities are plotted on a logarithmic scale. Excitation wavelength was 392 nm. Intensities are normalized for absorbed power at excitation wavelength.

Table S4. Time constants for transient photoluminescence (PL) dynamics in the NIR region.

Sample	τ_{Yb} (μs) [§]	τ_{Er} (μs) [§]	τ_{Yb^*} (ns) [§]	τ_{Er^*} (ns) [§]
1	10.83(0.01)	-	-	-
1b	11.02(0.01)	-	-	-
2	10.29(0.02)	1.99(0.01)	51.4(0.4)	38.8(0.1)
2b	10.36(0.01)	2.00(0.01)	50.4(0.4)	37.5(0.1)
3	9.68(0.01)	2.04(0.01)	42.4(0.2)	33.5(0.1)
3b	10.34(0.01)	1.98(0.01)	41.7(0.1)	27.8(0.1)

[§]Experimental uncertainties are reported in brackets

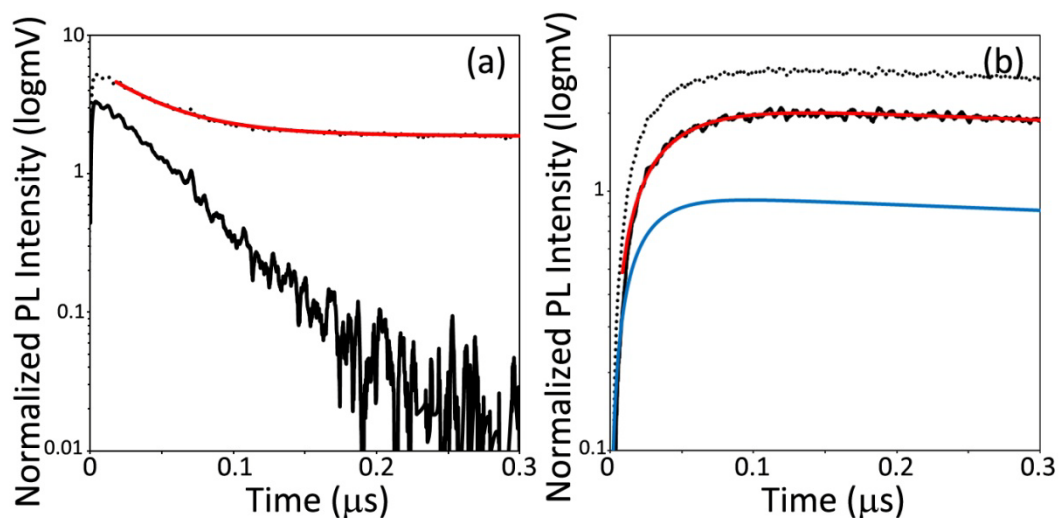


Figure S6. Example of curve fitting and subtraction procedure for contribution of homometallic species of signals at 980 and 1540 nm for compound **3**. (a) Observed signal at 980 nm (dotted line), curve fit for the long-lived component (red line), and resulting short-lived component (black line) after subtraction of the long-lived one retrieved through fitting procedure; (b) Observed signal at 1540 nm (dotted line), estimated contribution of Er homometallic species retrieved from curve fitting of Er₃Q₉ 1540 nm signal, weighted for the predicted amount in the sample (blue line), resulting component after subtraction (black line) and curve fitting (red line).

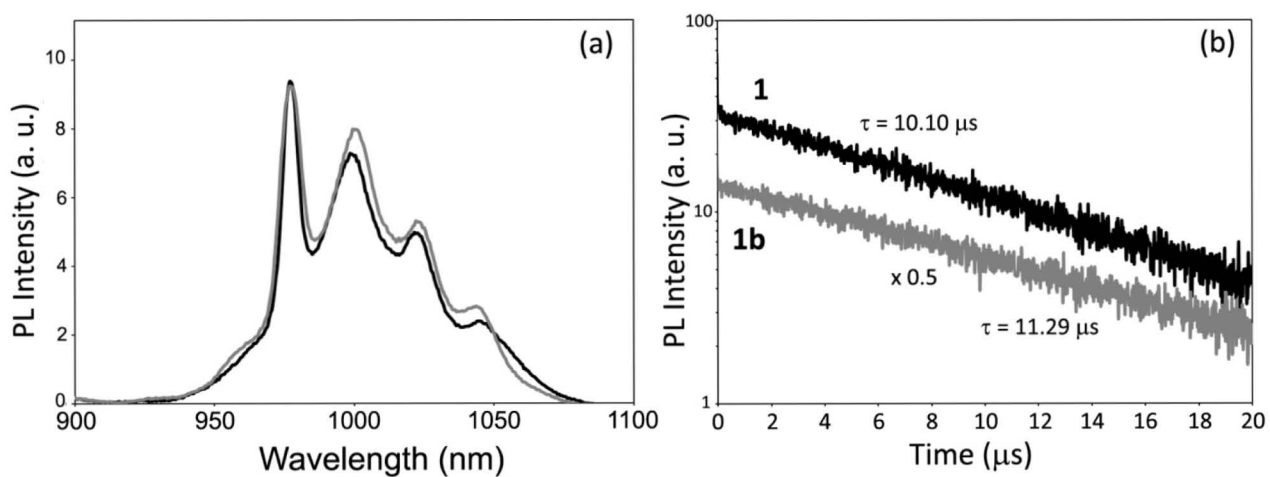


Figure S7. (a) PL spectra in the 900-1000 nm region, showing the $\text{Yb}^{3+} \ ^2\text{F}_{5/2} \rightarrow \ ^2\text{F}_{7/2}$ emission and (b) decay dynamics at 980 nm and relative time constants for **1** (black) and **1b** (grey) in the crystalline state.

Silica thin films doped with 2.



Figure S8. Picture of a GLYMO-based silica thin film doped with **2** obtained by dip coating.

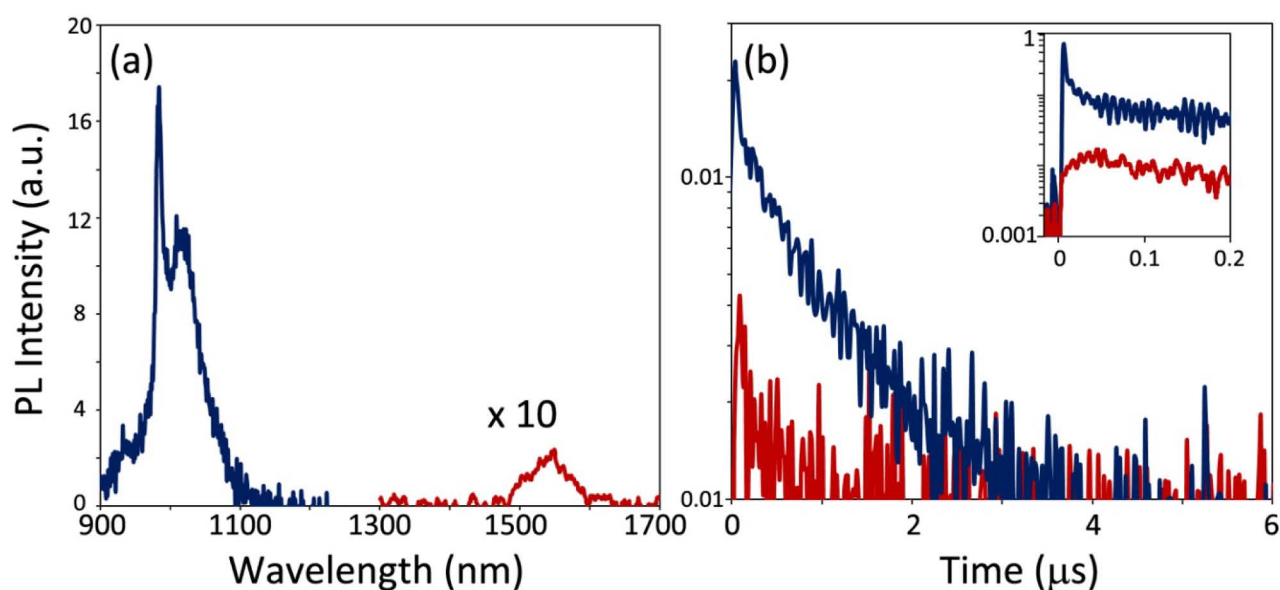
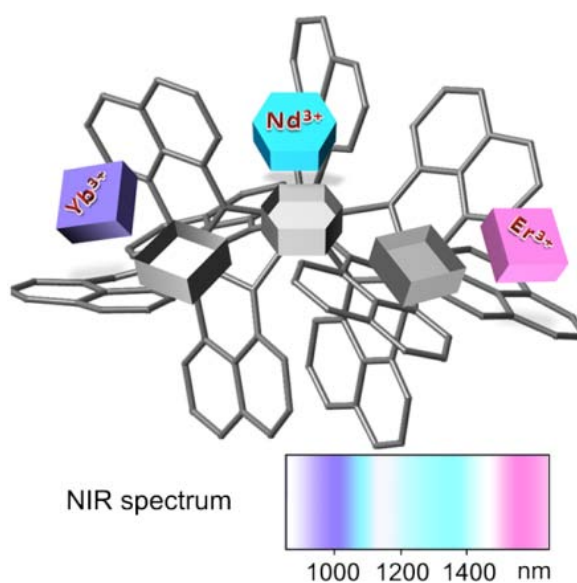


Figure S9. NIR PL studies of a TMOS/ITMS-based silica thin film doped with **2**: PL spectrum showing the emission bands related to $\text{Yb}^{3+} \ ^2\text{F}_{5/2} \rightarrow \ ^2\text{F}_{7/2}$ (blue) and $\text{Er}^{3+} \ ^4\text{I}_{13/2} \rightarrow \ ^4\text{I}_{15/2}$ (red) transitions (a), and NIR dynamics in the 0-6 μs (b) and 0-200 ns (inset of panel b) time ranges at 980 nm (blue) and 1540 nm (red). Signal intensities in panels (b) are plotted on a logarithmic scale. Excitation wavelength was 355 nm.

Paper 4

Ln_3Q_9 as a Molecular Framework for Ion-Size-Driven Assembly of Heterolanthanide (Nd, Er, Yb) Multiple Near-Infrared Emitters



Relevant ion size effects allow the control of metal composition in heterolanthanide quinolinolates. A unique example of heterotrimetallic Nd-Er-Yb complex with multiple NIR emission is reported.

CHEMISTRY

A European Journal

www.chemeurj.org



Review

Nanorattles or Yolk-Shell Nanoparticles – What Are They, How Are They Made, and What Are They Good For?
M. Priebe and K. M. Fromm

CEUJED 21 (10) 3833–4164 (2015) · ISSN 0947-6539 · Vol. 21 · No. 10 · 2015

A Journal of



ChemPubSoc
Europe

2015-21/10




Supported by
ACES

WILEY-VCH

The Three Graces of Canova illustrates an assembly of three entities, each carrier of its own virtue, which become one in the embrace to the central figure, governing the unit composition. Similarly, the Ln_3Q_9 molecular framework assembles three different NIR-

luminescent lanthanide ions, in which the central position seems to be carved out for the neodymium ion, linking all of them together by quinolinolato bridges. The multiple composition of this unit allows the individual lanthanide emissions to become combined.

Lanthanides | Hot Paper |

 **Ln₃Q₉ as a Molecular Framework for Ion-Size-Driven Assembly of Heterolanthanide (Nd, Er, Yb) Multiple Near-Infrared Emitters**Flavia Artizzu,^{*[a, b]} Francesco Quochi,^[b] Luciano Marchiò,^[c] Raquel Fonseca Correia,^[a] Michele Saba,^[b] Angela Serpe,^[a] Andrea Mura,^[b] Maria Laura Mercuri,^[a] Giovanni Bongiovanni,^[b] and Paola Deplano^{*[a]}

Abstract: A unique example of discrete molecular entity Nd_yEr_xYb_{3-(x+y)}Q₉ (**1**) (Q = quinolinolato) containing three different lanthanides simultaneously emitting in three different spectral regions in the NIR, ranging from 900 to 1600 nm, has been synthesized and fully characterized. A simple molecular strategy based on tuning metal composition in the Ln₃Q₉ framework, which contains inequivalent central and terminal coordination sites, has allowed a satisfactory ion-size-driven control of molecular speciation close to 90%. In **1** the central position of the larger Nd ion is well distinguished from the terminal ones of the smaller Yb³⁺ and Er³⁺, which are almost “vicariants” as found in the heterobimetallic Er_xYb_{3-x}Q₉ (**2**). The Ln₃Q₉ molecular architecture, which allows communication between the ions, has proved to afford multiple NIR emission in **1** and **2**, and is promising to develop a variety of multifunctional materials through the variation of the Ln composition.

Lanthanide ions play a crucial role in modern technology due to their very peculiar luminescent and magnetic properties related to the nature of their 4f core-like electrons.^[1] Heterometallic coordination compounds containing two or more different lanthanide cations are therefore attractive as they can lead to multifunctional materials in which different physical properties can be combined in the same architecture and enhanced properties may be achieved through intermetallic communication.^[2,3]

However, the design of polymetallic lanthanide compounds with well-defined and easily reproducible structures is a challenge, and fully characterized mixed-lanthanide coordination compounds still represent very rare examples in the literature. Among them, heteropolymetallic metal-organic frameworks and coordination polymers, have been very recently proposed as near-infrared- or visible-luminescent barcodes.^[4] In such compounds, different lanthanide ions are randomly distributed over the coordination network, thanks to the similarity of ionic radii and chemical behavior, and their emission properties are simultaneously displayed. However, little control can be achieved on the distribution and distances between the different metals resulting in “diluted” materials in which independent physical properties carried by different Ln³⁺ are superimposed. Instead, to ensure efficient intermetallic communication, the distance between the lanthanide ions and their relative positions should be controlled.^[2b,3,5] In addition, for application purposes, functional materials that can be easily processed without altering their properties through convenient, easy-to-handle, solution methods^[6] or by techniques commonly used for the fabrication of technological devices, such as vacuum deposition, are strongly desirable. In this context, discrete polynuclear molecules in which Ln³⁺ ions are connected through bridging atoms, could fit all these requirements much more easily than multidimensional coordination networks or suspensions/solutions of aggregates/clusters or even larger and heavy polymetallic assemblies.^[4,7,8]


We present here a simple molecular strategy for achieving effective interplay of optical properties of near-infrared (NIR) luminescent functional materials by mixing Yb³⁺, Er³⁺, and Nd³⁺ in heterometallic trinuclear lanthanide quinolinolato (Q) complexes of general formula Ln₃Q₉, a class of coordination compounds that have been investigated for use as active centers into optical silica fiber amplifiers and are also of interest in view of their magnetic properties.^[9,10] In these luminophores, the Q ligand is particularly efficient as light-harvesting “antenna” for all the NIR lanthanide emitters (Er³⁺, Yb³⁺, Nd³⁺), thanks to resonance energy transfer (RET) to lanthanide ion’s higher levels (sensitized emission), to overcome the very small absorption coefficients of the lanthanide-based line-like parity-forbidden intrashell transitions.^[10,11]

The heterotrimetallic Nd_yEr_xYb_{3-(x+y)}Q₉ (**1**) and the heterobimetallic Er_xYb_{3-x}Q₉ (**2**) complexes, were obtained by using a mixture of salts of the selected NIR emitting lanthanide ions, Er³⁺, Yb³⁺, and Nd³⁺, and the ligand in the suitable molar

[a] Dr. F. Artizzu, Dr. R. F. Correia, Dr. A. Serpe, Prof. M. L. Mercuri, Prof. P. Deplano
Dipartimento di Scienze Chimiche e Geologiche
University of Cagliari, SS 554 Bivio per Sestu
09042, Monserrato-Cagliari (Italy)
E-mail: f.artizzu@unica.it
deplano@unica.it

[b] Dr. F. Artizzu, Dr. F. Quochi, Dr. M. Saba, Prof. A. Mura, Prof. G. Bongiovanni
Dipartimento di Fisica, University of Cagliari
SS 554 Bivio per Sestu, I-09042, Monserrato-Cagliari (Italy)

[c] Dr. L. Marchiò
Dipartimento di Chimica, University of Parma
Parco Area delle Scienze 17 A, I-43100, Parma (Italy)

 Supporting information for this article is available on the WWW under <http://dx.doi.org/10.1002/chem.201405634>.

ratios through a one-pot reaction optimized for Ln_3Q_9 complexes ($\text{Ln} = \text{Er},^{[10a]} \text{Yb},^{[3]} \text{Gd}^{[11a]}$). X-ray results on single crystals, supported also by powder-XRD experiments (see Supporting Information), show that **1** and **2** are both isostructural with the analogous trinuclear Er_3Q_9 complex.^[10a] The molecular structure of **1** is chosen here as representative and reported in Figure 1, whereas structural data for **2** can be found in the Supporting Information.

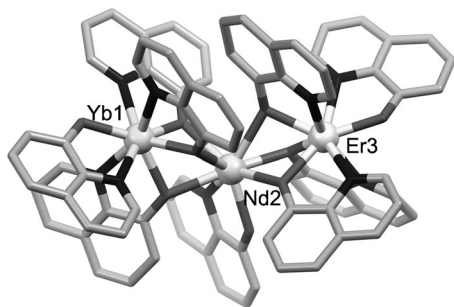


Figure 1. Molecular structure of **1**. Hydrogen atoms were removed for clarity.

In the homoleptic Ln_3Q_9 molecules, the central and terminal coordination sites are inequivalent, and the two outer metals have a N_4O_4 coordination environment, while the inner one has a NO_7 environment. X-ray structural refinement parameters for **1** (Table S4 in the Supporting Information), allow for a reliable attribution of the central position to the “light” and larger Nd ion that can be well distinguished from the “heavy” Yb^{3+} and Er^{3+} ions, which in turn occupy the terminal sites. The intermetallic distances of 3.586 Å for $\text{Ln1}\cdots\text{Nd2}$ and 3.573 Å for $\text{Nd2}\cdots\text{Ln3}$ ($\text{Ln} = \text{Er}, \text{Yb}$) are in this case significantly longer than those determined for **2** (see later) and also for Er_3Q_9 ^[10a] and Yb_3Q_9 ^[10e] in agreement with the differences in ionic radii between these ions. From electron density maps reported in Table S4 (in the Supporting Information) and relative discussion, the best description of this complex is NdErYbQ_9 .

Instead the close similarity of erbium and ytterbium electronic densities hampers a clear discrimination between these two ions by X-ray diffraction and no significant differences in the structure refinement parameters for the different metal occupancies are found for **2** (Table S5 in the Supporting Information). However, intermetallic distances, 3.475 Å for $\text{Ln1}\cdots\text{Ln2}$ and 3.478 Å for $\text{Ln2}\cdots\text{Ln3}$, are slightly shorter than the homonuclear Er_3Q_9 (3.488 and 3.495 Å).^[10a] These geometric considerations, together with analytical data (vide infra), are in support of a mixed metal molecular composition ErYb_2Q_9 , as discussed in detail in the Supporting Information.

It must be remarked that the isostructurality of these trinuclear quinolinolato complexes with Ln ions belonging both to the first and second half of the lanthanide series, is a rare case,^[12] and allows great versatility for mixing, at a molecular level, Ln ions as carriers of different functionalities, without altering the molecular architecture. Moreover, the short intermetallic distances found in **1** and **2**, both between adjacent and also between terminal Ln ions ($\text{Ln1}\cdots\text{Ln3}$ separation is 6.549 Å

for **1** and 6.386 Å for **2**) lie well below the Förster’s resonance energy transfer radius R_0 of about 10 Å and are thus optimal to ensure fully efficient intermetallic communication between the NIR-emissive Yb and Er ions.^[3,4]

Due to the close composition–structure–property relationship in these kinds of heterometallic functional molecular materials, the accurate determination of metal composition is crucial for achieving a satisfactory insight into these systems. To this end, ICP-mass analysis on solution samples has proven to be a valuable technique. Metal ratios of Nd:Er:Yb 1:1.14:1.27 were found for **1** after repeated measurements on several independent batches of the compound. A similar trend can be observed for **2** ($\text{Yb}/\text{Er} = 2.36$), hinting to a slightly stronger affinity of Yb^{3+} upon coordination to the 8-quinolinolato ligand, likely connected to its slightly smaller ionic radius compared to Er^{3+} .^[2a] The purity and homogeneity of the compounds have been verified by SEM-EDX semi-quantitative punctual analyses (see Supporting Information) on different single crystals, which have shown reproducible metal atomic ratios close to expected values. Compositional analysis on single molecules has then been done by electrospray (ESI) mass spectrometry experiments in positive ion mode. The ESI-mass spectra, reported in Figure 2, show the presence of peaks related to $[\text{Ln}_3\text{Q}_9]^+$ fragments clearly demonstrating that the trinuclear structure is preserved in solution. The most intense peaks are related to the mixed species, $[\text{NdErYbQ}_9]^+$ ($m/z = 1637.9$, **1**) and $[\text{ErYb}_2\text{Q}_9]^+$ ($m/z = 1666.2$, **2**), confirming the coexistence of the three NIR-emissive lanthanide ions Nd^{3+} , Er^{3+} and Yb^{3+} in the same discrete molecular architecture.

Analysis of the ESI-mass spectrum of **1** (Figure 2, upper panel) provides clear evidence of the presence of one neodymium ion in each single molecule, in agreement with XRD structural data. In the experimental spectrum (curve a), the

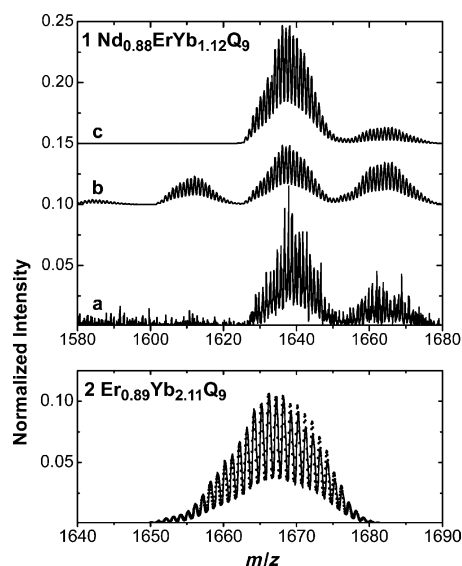


Figure 2. Expanded region of the ES(+) mass spectrum of: **1**, experimental spectrum (a) and model spectra for Nd in a fixed central site (c) and for a statistical metal distribution of Nd, Er and Yb (b) according to atomic ratios retrieved from ICP-mass analysis; **2**, experimental spectrum (black curve) and model spectrum (dots), see text.

most intense peak corresponds to a convolution of isotopic patterns of heterometallic $[\text{NdLn}_2\text{Q}_8]^+$ ($\text{Ln} = \text{Er}, \text{Yb}$) species, while the residual fragments at higher m/z values, related to molecules containing only Yb and Er, are ascribable to the excess of these two ions in the sample, as shown by ICP-mass data. Moreover, no fragments relative to species containing more than one neodymium ion are observed, providing further support to the central molecular site as preferential for the larger Nd^{3+} with respect to the Er^{3+} and Yb^{3+} ions, sitting in the two equivalent peripheral positions. To corroborate these observations, two models for the $\text{Nd}_{0.88}\text{ErYb}_{1.12}\text{Q}_9$ composition, retrieved from ICP-mass analysis, have been compared. Figure 2 (upper panel) clearly points out that, while experimental data significantly differ from a statistical model spectrum obtained for a random and independent metal occupancy over three molecular sites (curve b), they can nonetheless be adequately described (curve c) by applying some constraints, that is, by assuming one Nd^{3+} ion per molecule and statistical occupancies for Yb^{3+} and Er^{3+} over the two remaining sites. These conclusions allow to estimate, for this heterotrimeric system, a molecular speciation of only three predominant configurations: NdErYbQ_9 (ca. 44%), NdYb_2Q_9 (ca. 25%) and NdEr_2Q_9 (ca. 19%). This size-discriminating effect is very relevant here that it leads to relative abundance (ca. 88%) of heterometallic Nd-Ln_2 ($\text{Ln} = \text{Er}, \text{Yb}$; $\Delta r_{\text{Nd-Er}}^{\text{CN}=8} = 10.5$ pm and $\Delta r_{\text{Nd-Yb}}^{\text{CN}=8} = 12.4$ pm) molecules comparable to the best result (90%) found in the literature in the case of one-pot synthetic strategies, for the thermodynamic formation of heterobimetallic La-Lu ($\Delta r_{\text{La-Lu}}^{\text{CN}=8} = 18.3$ pm) triple-stranded helicate.^[13,14] It is worth noting that size selectivity of substituted quinolinolato ligands towards lanthanide ions has been already observed in the case of mononuclear complexes.^[15] The experimental spectrum of **2** can be satisfactorily fitted for $\text{Er}_{0.89}\text{Yb}_{2.11}\text{Q}_9$ composition, on the basis of a statistical occupancy model of erbium and ytterbium ions over the three possible molecular sites (dotted curve, Figure 2, lower panel). This provides further evidence of the analogous chemical behavior of Er^{3+} and Yb^{3+} that can be considered as “vicariants”, on dependence of their very similar ionic radii ($\Delta r_{\text{Er-Yb}}^{\text{CN}=8} = 1.9$ pm).

Optical properties of the complexes have been also investigated to check for the coexistence of multiple emissions due to the presence of the different lanthanide ions. The absorption spectra of **1** and **2**, featuring a broad and intense absorption related to ligand $\pi-\pi^*$ transitions and numerous sharp peaks originated from intrashell f-f transitions of Nd, Er, and Yb ions, are shown in Figure 3 a and b.

Upon ligand excitation in its lowest absorption band, some residual emission in the green ($\lambda_{\text{max}} = 520$ nm) related to ligand fluorescence is detected for both the compounds (Figure 3 c). After resonance energy transfer from ligand excited triplet states to the upper energy levels of the lanthanide ions, photoluminescence at 1 and 1.5 μm , due to $\text{Yb}^{3+} {}^2\text{F}_{7/2} \rightarrow {}^2\text{F}_{5/2}$ and $\text{Er}^{3+} {}^4\text{I}_{13/2} \rightarrow {}^4\text{I}_{15/2}$ transitions respectively, is simultaneously detected for **2**, as shown in Figure 3 d (blue). In the case of **1**, three emission bands covering almost the entire NIR spectrum from 900 to 1650 nm are observed as a result of the simultaneous excitation and radiative decay of Nd^{3+} (${}^4\text{F}_{3/2} \rightarrow {}^4\text{I}_{9/2}$ 890 nm,

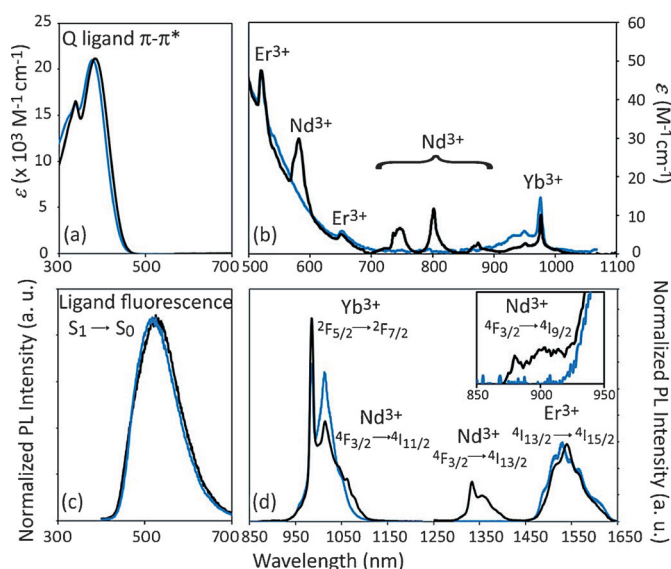


Figure 3. Absorbance spectrum of **1** (black) and **2** (blue) in DMSO solution showing a) the broad band related to the Q ligand in the UV-Vis region and b) lines related to intrashell f-f transitions of Nd^{3+} , Er^{3+} , and Yb^{3+} in the Vis-NIR. c) Ligand fluorescence and d) PL spectra in the NIR region, of DMSO solutions of **1** (black) and **2** (blue) excited at $\lambda = 355$ nm. Spectroscopic labels of Nd^{3+} , Er^{3+} , and Yb^{3+} transitions are also indicated. PL spectra have been normalized for solution absorption at excitation wavelength and laser power.

${}^4\text{F}_{3/2} \rightarrow {}^4\text{I}_{11/2}$ 1070 nm, ${}^4\text{F}_{3/2} \rightarrow {}^4\text{I}_{13/2}$ 1350 nm), Er^{3+} (${}^4\text{I}_{13/2} \rightarrow {}^4\text{I}_{15/2}$ 1540 nm), and Yb^{3+} (${}^2\text{F}_{5/2} \rightarrow {}^2\text{F}_{7/2}$ 980 nm), see Figure 3 d, black curve. Crystal field effects split the energy levels manifolds of the f-states resulting in band broadening and resolution into a fine structure on dependence on the symmetry of the coordination environment around the lanthanide ion. Consequently, Yb and Er emission bands in **1** and **2** display slightly different shapes likely related to the different coordination sites (central and/or peripheral) occupied by these ions in the two samples.

The observed PL spectroscopic features originate from the contribution of the different species in the two samples. However, it is interesting to note that Er emission bands in **1** and **2** are equally intense, suggesting that efficient Yb-Er energy transfer, already demonstrated for the bimetallic Yb-Er case,^[3] takes place similarly in the trimetallic complex. The observed Yb^{3+} residual emission can be ascribed to the fraction of molecules not containing erbium, although, in **1**, other phenomena such as Nd to Yb energy transfer, currently under investigation, cannot be ruled out. These features make **1** a potential broad-band NIR emitter for which the intensities of the three different main emissions can be finely tuned on varying metal composition and hence molecular speciation.

In conclusion, we have synthesized and fully characterized two heterometallic complexes of NIR emitting lanthanide ions, with a trinuclear structure of general formula Ln_3Q_9 . Complex **1** represents, to the best of our knowledge, the first example of a discrete molecular unit containing three different NIR-luminescent lanthanide ions, Nd^{3+} , Er^{3+} , and Yb^{3+} , simultaneously emitting upon ligand excitation at a single wavelength.

From results obtained from XRD structural studies, EDX and ICP-mass analyses, and ESI-mass spectrometry, it can be deduced that the lighter and larger Nd^{3+} ion can be chemically discriminated from the heavier and almost "vicariants" Er^{3+} and Yb^{3+} and helps in controlling molecular speciation and metal distribution across the coordination sites in polynuclear discrete molecules, in which the metals sit at short distances from each other. This would be particularly useful for achieving controlled intermetallic communication and tunability of physical properties in solution-processable functional molecular materials through a rational and easy-to-handle synthetic strategy simply by controlling reactant stoichiometry. Studies on the energy-transfer mechanisms between the different NIR-emitting lanthanide ions are currently being performed in our laboratories as well as the investigation of their processing potential through mild solution techniques in order to explore potential applications as doped optical waveguides and amplifiers.

As final remark, we note that the described molecular strategy provides a powerful tool for obtaining a variety of multifunctional compounds, beyond those for photophysical applications,^[10g] simply on variation of the Ln ions as carriers of functionality.

Experimental Section

Details of the synthesis and characterization of **1** and **2** can be found in the Supporting Information. CCDC 1026425 (**1**) and 1026426 (**2**) contain the supplementary crystallographic data for this paper. These data can be obtained free of charge from The Cambridge Crystallographic Data Centre via www.ccdc.cam.ac.uk/data_request/cif.

Acknowledgements

The Regione Autonoma della Sardegna (CRP-17571) and Banco di Sardegna Foundation are gratefully acknowledged for financial support. The authors thank Dr. D. Loche for powder XRD characterization, Dr. A. Rigoldi for ICP-mass analyses, Dr. S. Podda (Laboratorio di Telemicroscopia Industriale, Sardegna Ricerche) for SEM-EDX, Dr. A. Cardini for providing the laser source.

Keywords: heterometallic complexes • lanthanides • luminescence • multifunctional materials • structure elucidation

- [1] a) *Rare Earth Coordination Chemistry, Fundamentals and Applications* (Ed.: C. Huang), Wiley, Singapore, 2010; b) J.-C. G. Bünzli, C. Piguet, *Chem. Soc. Rev.* 2005, 34, 1048; c) M. C. Heffern, L. M. Matosziuk, T. J. Meade, *Chem. Rev.* 2014, 114, 4496; d) D. N. Woodruff, R. E. P. Winpenny,

- R. A. Layfield, *Chem. Rev.* 2013, 113, 5110; e) J.-C. G. Bünzli, S. V. Eliseeva, *J. Rare Earths* 2010, 28, 824.
 [2] a) C. Piguet, J.-C. G. Bünzli, *Chem. Soc. Rev.* 1999, 28, 347; b) J.-P. Costes, F. Dahan, A. Dupuis, S. Lagrave, J.-P. Laurent, *Inorg. Chem.* 1998, 37, 153.
 [3] F. Artizzu, F. Quochi, L. Marchiò, E. Sessini, M. Saba, A. Serpe, A. Mura, M. L. Mercuri, G. Bongiovanni, P. Deplano, *J. Phys. Chem. Lett.* 2013, 4, 3062.
 [4] T. Förster, *Discuss. Faraday Soc.* 1959, 27, 7.
 [5] a) K. A. White, D. A. Chengelis, K. A. Gogick, J. Stehman, N. L. Rosi, S. Petoud, *J. Am. Chem. Soc.* 2009, 131, 18069; b) X. Fan, S. Freslon, C. Dai-guebonne, G. Calvez, L. Le Pollès, K. Bernot, O. Guillou, *J. Mater. Chem. C* 2014, 2, 5510; c) Y. Lu, B. Yan, *J. Mater. Chem. C* 2014, 2, 7411.
 [6] a) L. Armelao, S. Quici, F. Barigelletti, G. Accorsi, G. Bottaro, M. Cavazzini, E. Tondello, *Coord. Chem. Rev.* 2010, 254, 487; b) F. Artizzu, F. Quochi, M. Saba, D. Loche, A. Serpe, M. L. Mercuri, A. Mura, G. Bongiovanni, P. Deplano, *Dalton Trans.* 2012, 41, 13147; c) C. Chen, D. Zhang, T. Li, D. Zhang, L. Song, Z. Zhen, *Appl. Phys. Lett.* 2009, 94, 041119.
 [7] a) Q. Zhong, H. Wang, G. Qian, Z. Wang, J. Zhang, J. Qiu, M. Wang, *Inorg. Chem.* 2006, 45, 4537; b) F. Tanaka, T. Ishibashi, *J. Chem. Soc. Faraday Trans.* 1996, 92, 1105.
 [8] a) S. Faulkner, S. J. A. Pope, *J. Am. Chem. Soc.* 2003, 125, 10526; b) M. S. Tremblay, D. Sames, *Chem. Commun.* 2006, 4116; c) D. J. Lewis, P. B. Glover, M. C. Solomons, Z. Pikramenou, *J. Am. Chem. Soc.* 2011, 133, 1033.
 [9] a) R. J. Curry, W. P. Gillin, *Appl. Phys. Lett.* 1999, 75, 1380; b) O. M. Khreis, W. P. Gillin, M. Somerton, R. J. Curry, *Org. Electron.* 2001, 2, 45; c) S. Penna, A. Reale, R. Pizzoferrato, G. M. Tosi Beleffi, D. Musella, W. P. Gillin, *Appl. Phys. Lett.* 2007, 91, 021106.
 [10] a) F. Artizzu, P. Deplano, L. Marchiò, M. L. Mercuri, L. Pilia, A. Serpe, F. Quochi, R. Orrù, F. Cordella, F. Meinardi, R. Tubino, A. Mura, G. Bongiovanni, *Inorg. Chem.* 2005, 44, 840; b) R. Van Deun, P. Fias, P. Nockemann, A. Schepers, T. N. Parac-Vogt, K. Van Hecke, L. Van Meervelt, K. Binne-mans, *Inorg. Chem.* 2004, 43, 8461; c) F. Artizzu, P. Deplano, L. Marchiò, M. L. Mercuri, L. Pilia, A. Serpe, F. Quochi, R. Orrù, F. Cordella, M. Saba, A. Mura, G. Bongiovanni, *Adv. Funct. Mater.* 2007, 17, 2365; d) F. Artizzu, M. L. Mercuri, A. Serpe, P. Deplano, *Coord. Chem. Rev.* 2011, 255, 2514; e) S. G. Leary, G. B. Deacon, P. C. Junk, *Z. Anorg. Allg. Chem.* 2005, 631, 2647; f) E. V. Baranov, G. K. Fukin, T. V. Balashova, A. P. Pushkarev, I. D. Grishin, M. N. Bochkarev, *Dalton Trans.* 2013, 42, 15699; g) N. F. Chilton, G. B. Deacon, O. Gazukin, P. C. Junk, B. Kersting, S. K. Langley, B. Moubarak, K. S. Murray, F. Schleife, M. Shome, D. R. Turner, J. A. Walker, *Inorg. Chem.* 2014, 53, 2528; h) M. Iwamuro, T. Adachi, Y. Wada, T. Kitamura, S. Yanagida, *Chem. Lett.* 1999, 539.
 [11] a) F. Quochi, M. Saba, F. Artizzu, M. L. Mercuri, P. Deplano, A. Mura, G. Bongiovanni, *J. Phys. Chem. Lett.* 2010, 1, 2733; b) F. Artizzu, F. Quochi, M. Saba, L. Marchiò, D. Espa, A. Serpe, A. Mura, M. L. Mercuri, G. Bongio-vanni, P. Deplano, *ChemPlusChem* 2012, 77, 240.
 [12] X. Y. Chen, X. Yang, B. J. Holliday, *Inorg. Chem.* 2010, 49, 2583.
 [13] a) N. André, R. Scopelliti, G. Hopfgartner, C. Piguet, J.-C. G. Bünzli, *Chem. Commun.* 2002, 214; b) N. André, T. B. Jensen, R. Scopelliti, D. Imbert, M. Elhabiri, G. Hopfgartner, C. Piguet, J.-C. G. Bünzli, *Inorg. Chem.* 2004, 43, 515; c) G. Canard, S. Koeller, G. Bernardinelli, C. Piguet, *J. Am. Chem. Soc.* 2008, 130, 1025.
 [14] ICP-mass analyses performed on **1** as crude product and recrystallized sample gave approximately the same results, ruling out selective crys-tallization effects.
 [15] F. Artizzu, K. Bernot, A. Caneschi, E. Coronado, J. M. Clemente-Juan, L. Marchiò, M. L. Mercuri, L. Pilia, A. Serpe, P. Deplano, *Eur. J. Inorg. Chem.* 2008, 3820.

Received: October 14, 2014

Published online on December 4, 2014

CHEMISTRY

A **European** Journal

Supporting Information

© Copyright Wiley-VCH Verlag GmbH & Co. KGaA, 69451 Weinheim, 2015

Ln₃Q₉ as a Molecular Framework for Ion-Size-Driven Assembly of Heterolanthanide (Nd, Er, Yb) Multiple Near-Infrared Emitters

Flavia Artizzu,^{*,[a, b]} Francesco Quochi,^[b] Luciano Marchiò,^[c] Raquel Fonseca Correia,^[a]
Michele Saba,^[b] Angela Serpe,^[a] Andrea Mura,^[b] Maria Laura Mercuri,^[a]
Giovanni Bongiovanni,^[b] and Paola Deplano^{*,[a]}

chem_201405634_sm_miscellaneous_information.pdf

Supporting Information

Color Figures

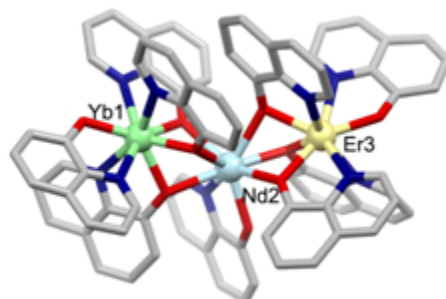


Figure 1. Molecular structure of **1**. Hydrogen atoms were removed for clarity. Color codes: red, oxygen, blue, nitrogen, gray, carbon.

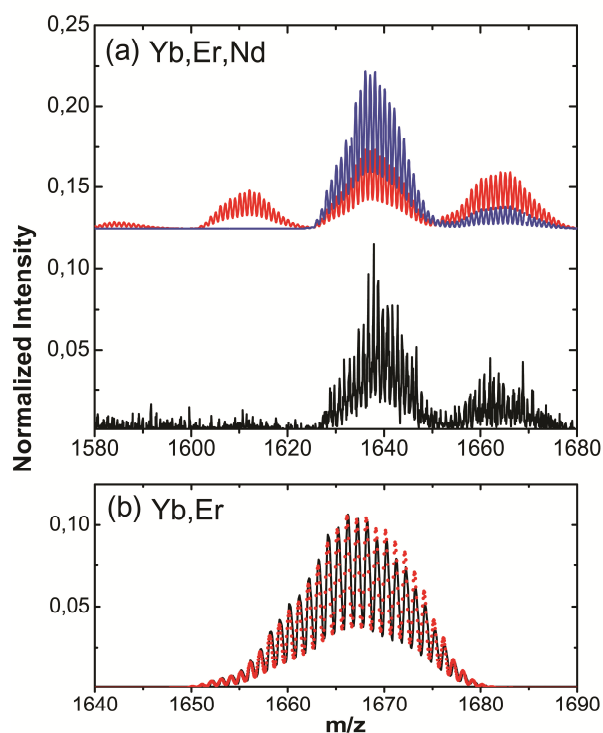


Figure 2. Expanded region of the ES(+) mass spectrum of: (a) **1**, experimental spectrum (black) and model spectra for Nd in a fixed central site (blue) and for a statistical metal distribution of Nd, Er and Yb (red) according to atomic ratios retrieved from ICP-mass analysis; (b) **2**, experimental spectrum (black) and model spectrum for a statistical metal distribution (red dots).

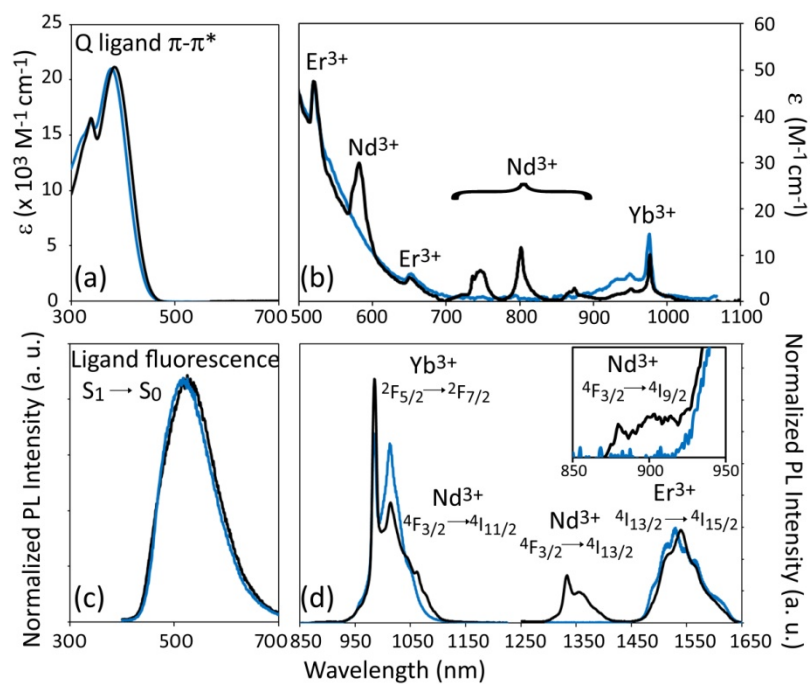


Figure 3. Absorbance spectrum of **1** (black) and **2** (blue) in DMSO solution showing (a) a broad band related to the Q ligand in the UV-Vis region and, (b), lines related to intrashell f-f transitions of Nd^{3+} , Er^{3+} and Yb^{3+} in the Vis-NIR. (c) Ligand fluorescence and (d) PL spectra in the NIR region, of DMSO solutions of **1** (black) and **2** (blue) excited at $\lambda=355$ nm. Spectroscopic labels of Nd^{3+} , Er^{3+} and Yb^{3+} transitions are also indicated. PL spectra have been normalized for solution absorption at excitation wavelength and laser power.

Experimental Section

General

All the reagents and solvents were purchased from Aldrich and used without further purification.

Syntheses

Synthesis of 1: Few drops of NH₃ 28% up to a final concentration of 2.0×10^{-2} mol dm⁻³ (pH \cong 10) were added to a mixture of 8-hydroxy-quinoline (0.145 g, 1 mmol) in H₂O (100 mL) under mixing. After 30 min a water solution containing 0.11 mmol of NdCl₃·6H₂O, 0.11 mmol of YbCl₃·6H₂O, and 0.11 mmol of ErCl₃·6H₂O in 15 mL of water was added to the above mixture which is allowed to react at reflux for 2 days until the white solid due to the unreacted ligand disappears. A yellow precipitate was formed, collected by filtration, washed with water, NaOH 0.1 M, water, and dried in oven at 60°C (yield > 95%). Analytical results are in agreement with NdErYbQ₉·3H₂O formulation. CHN Found (Calculated for C₈₁H₅₄Yb₂ErN₉O₉·3H₂O): C% 52.71(52.99), H% 3.38(3.29), N% 6.80(6.87). ICP-mass on crude product (average on 3 repeated measurements, atomic ratios): Nd:Er:Yb 1:1.17:1.25. Yellow crystals suitable for X-ray structural studies were obtained after recrystallization from CH₃CN. FT-IR, cm⁻¹: 3050 m, 16031 m, 1571 s, 1499 vs, 1468 vs, 1424 mw, 1382 s, 1319 s, 1276 m, 1230 m, 1172 w, 1110 vs, 1034 w, 905 w, 824 m, 804 m, 787 m, 732 s, 648 m, 605 m, 593 w; 571 w, 505 m, 488 m, 456 w, 420 mw. UV-Vis-NIR absorption, nm, [mol⁻¹ dm³ cm⁻¹], DMSO: 340[$1.4 \cdot 10^4$], 379[$2.1 \cdot 10^4$], 522 (Er³⁺ ²H_{11/2}←⁴I_{15/2}), 584 (Nd³⁺ ²G_{7/2}+²G_{5/2}←⁴I_{9/2}), 655 (Er³⁺ ⁴F_{9/2}←⁴I_{15/2}), 746 (Nd³⁺ ⁴F_{7/2}+⁴S_{3/2}←⁴I_{9/2}), 802 (Nd³⁺ ⁴F_{5/2}+²H_{9/2}←⁴I_{9/2} and Er³⁺ ⁴I_{4/2}←⁴I_{15/2}) [10], 875 (Nd³⁺ ⁴F_{5/2}+²H_{9/2}←⁴I_{9/2}), 977 (Yb³⁺ ²F_{5/2}→²F_{7/2} and Er³⁺ ⁴I_{11/2}←⁴I_{15/2}) [10], 1540 (Er³⁺ ⁴I_{13/2}←⁴I_{15/2}). Diffuse reflectance, nm: 262, 344, 385; 520 (Er³⁺ ²H_{11/2}←⁴I_{15/2}), 583 (Nd³⁺ ²G_{7/2}+²G_{5/2}←⁴I_{9/2}), 651 (Er³⁺ ⁴F_{9/2}←⁴I_{15/2}), 737 (Nd³⁺ ⁴F_{7/2}+⁴S_{3/2}←⁴I_{9/2}), 804 (Nd³⁺ ⁴F_{5/2}+²H_{9/2}←⁴I_{9/2} and Er³⁺ ⁴I_{4/2}←⁴I_{15/2}), 871 (Nd³⁺ ⁴F_{5/2}+²H_{9/2}←⁴I_{9/2}), 979 (Yb³⁺ ²F_{5/2}→²F_{7/2} and Er³⁺ ⁴I_{11/2}←⁴I_{15/2}), 1147 (3vC-H), 1533 (Er³⁺ ⁴I_{13/2}←⁴I_{15/2}), 1683 (2vC-H). ICP-mass (atomic ratios, average on 5 repeated measurements): Nd:Er:Yb 1:1.14:1.27. ESI-Mass (CH₃CN/CH₃OH 3/1), m/z: 1666.54 [ErYb₂Q₈⁺].

Synthesis of 2: Synthesis was carried out following the same procedure described for 1, by adding to a water solution (100 mL) containing 1 mmol of the ligand, a mixture of 0.22 mmol of YbCl₃·6H₂O and 0.11 mmol of Er(CH₃COO)₃·6H₂O dissolved in 15 mL of water. A yellow precipitate was formed, collected by filtration, washed with water, NaOH 0.1 M, water, and dried in oven at 60°C (yield > 95%). Analytical results are in agreement with ErYb₂Q₉·3H₂O formulation. CHN Found (Calculated for C₈₁H₅₄Yb₂ErN₉O₉·3H₂O): C% 52.35(52.17), H% 3.30(3.24), N% 6.88(6.76). Yellow crystals suitable for X-ray structural studies were obtained after recrystallization from CH₃CN. FT-IR, cm⁻¹: 3047 m, 1601 m, 1571 s, 1498 vs, 1466 vs, 1424 mw, 1383 s, 1318 s, 1276 m, 1231 m, 1174 w, 1109 vs, 1035 w, 907 w, 823 m, 804 m, 788 m, 732 s, 648 m, 607 m, 592 w; 571 w, 504 m, 489 m, 458 w, 419 mw. UV-Vis-NIR absorption, nm, [mol⁻¹ dm³ cm⁻¹], DMSO: 340[$1.4 \cdot 10^4$], 379[$2.1 \cdot 10^4$], 522 (Er³⁺ ²H_{11/2}←⁴I_{15/2}), 652 (Er³⁺ ⁴F_{9/2}←⁴I_{15/2}), 977 (Yb³⁺ ²F_{5/2}←²F_{7/2} and Er³⁺ ⁴I_{11/2}←⁴I_{15/2}) [20], 1540 (Er³⁺ ⁴I_{13/2}←⁴I_{15/2}); Diffuse reflectance, nm: 262, 344, 385, 521 (Er³⁺ ²H_{11/2}←⁴I_{15/2}), 653 (Er³⁺ ⁴F_{9/2}←⁴I_{15/2}), 802 (Er³⁺ ⁴I_{4/2}←⁴I_{15/2}), 979 (Yb³⁺ ²F_{5/2}←²F_{7/2} and Er³⁺ ⁴I_{11/2}←⁴I_{15/2}), 1147(3v C-H), 1533 (Er³⁺ ⁴I_{13/2}←⁴I_{15/2}), 1683 (2v C-H). ICP-mass (atomic ratios, average on 5 repeated measurements): Er:Yb 1:2.36. ESI-Mass (CH₃CN/CH₃OH 3/1), m/z: 1666.54 [ErYb₂Q₈⁺].

Analytical data and spectroscopy.

Elemental analysis: data were collected using a Flash 2000 Fisher Scientific Thermo Electron Analyzer. **ESI-mass:** Mass spectra were obtained with a Micromass ZMD spectrometer operating in positive ionisation mode. **Electronic UV-Vis-NIR:** Diffuse reflectance (DR) on Teflon films and solution absorption spectra were collected using a Varian Cary 5 spectrophotometer. **Vibrational spectroscopy:** FTIR spectra on KBr pellets were collected using a Bruker Equinox 55 spectrophotometer.

ICP- Mass Spectrometry

Sample preparation and ICP-MS determinations: 220mg of a DMSO solution ($5 \cdot 10^{-4}$ M, approx) of the selected sample, were introduced in a TFM vessel containing a mixture of HNO₃ (65%, 4 mL), H₂O₂ (30%, 0.5 mL) and H₂O (bidistilled, 4 mL) thus treated in a Milestone Ethos 1 Microwave digester, equipped with a HPR1000/10S high pressure segmented rotor, ATC-400CE automatic temperature control and Terminal 640 with easyCONTROL software. The treatment was performed by applying a microwave program consisting of two steps each lasting 10 minutes, at the temperature of 200 °C and microwave power up to 1000W. The samples were prepared for the analysis by diluting the digested solutions with 5% HNO₃ (suprapur grade) blank and then the metals were determined using a quadrupole ICP-MS Varian mod. RT equipped with a 90° reflecting ion mirror (Varian, Mulgrave, Australia), a Micromist glass low flow concentric nebulizer, a Peltier-cooled (3°C) double pass glass spray chamber and a glass torch, with respect to 4-points external aqueous calibration plots in the 0.1-25 μg L⁻¹ range for each metal (Correlation Coefficients > 0.999990, Limit of Detection (LoD) for the different analytes: 0.5-5 ng L⁻¹). The instrumental parameters and the measured isotopes are listed in Table S1.

Table S1. Equipment and settings for the lanthanides determination on digested samples.

Spectrometer	ICP-MS Varian mod. RT
Plasma (Ar)	
Plasma flow	17.50 L min ⁻¹
Auxiliary flow	1.65 L min ⁻¹
Sheat gas flow	0.22 L min ⁻¹
Nebulizer flow	1.10 L min ⁻¹
Sampling depth	7 mm
Power	1.4 kW
Pump rate	3 rpm
Stabilisation delay	10 sec
Ion Optics	
Ion Lens Voltages	Optimized for multielement analysis
Interface cones	Nickel
Analysis modes	
Scan mode	Peak hopping
Scans/Replicate	20
Replicates/Sample	5
Dwell time	50 ms
Analytical mass	¹⁴³ Nd, ¹⁴⁶ Nd, ¹⁶⁶ Er, ¹⁶⁷ Er, ¹⁷¹ Yb, ¹⁷² Yb, ¹⁷³ Yb

SEM-EDX and X-ray powder diffraction

SEM-EDX analyses were performed with a FEI Dual Beam Nova NanoLab 600i equipped with a EDAX Genesis microanalyser.

Wide-angle XRD-patterns on microcrystalline powder samples were recorded with a Panalytical Empyrean diffractometer equipped with a graphite monochromator and a X'Celerator linear detector. The scans were collected within the range 5-90° (2θ) using Cu Kα radiation.

Photoluminescence measurements

Photoluminescence (PL) was excited at 355 nm wavelength using the 310-ps-long output pulses of a passively Q-switched powerchip laser running at repetition frequency of 1 kHz. NIR PL was wavelength dispersed by an Acton SpectraPro 2300i spectrometer; optical spectra and decay transients were detected using, respectively, an InGaAs CCD (Andor iDus) and an InGas photomultiplier (Hamamatsu H10330A-75) connected to a 1 GHz digitising oscilloscope (Tektronik TDS 5104). In order to minimize nonlinear effects possibly taking place in doubly excited complexes, photoexcitation fluences were kept below the level of 0.1 excitation per complex per laser pulse in all experiments. According to Poissonian statistics, an average excitation level of 0.1 yields a fractional population of doubly excited complexes of ca. 5×10^{-3} . CW visible PL spectra were recorded using a Horiba Jobin-Yvon FluoroMax-4 spectrofluorimeter. All the absorption and photoluminescence (PL) studies were performed on diluted ($5 \cdot 10^{-4}$ M) solutions of the strongly coordinating dimethyl sulfoxide (DMSO) solvent to ensure that the observed properties are related to isolated molecules rather than to aggregates or clusters.

Crystallographic data

Data Collection and Structure Determination.

Single-crystal data were collected on a Bruker Smart APEXII area-detector diffractometers (Mo $K\alpha$; $\lambda = 0.71073 \text{ \AA}$). Cell parameters were refined from the observed setting angles and detector positions of selected strong reflections. Intensities were integrated from several series of exposure frames that covered the sphere of reciprocal space.ⁱ A multiscan absorption correction was applied to the data using the program SADABS.ⁱⁱ The structures were solved by direct methods (SIR2004ⁱⁱⁱ) and refined with full-matrix least-squares (SHELXL-97),^{iv} using the Wingx software package.^v In both structures, the solvent of crystallization could not be properly located and it was treated by means of the PLATON/SQUEEZE program.^{vi} Graphical material was prepared with the and Mercury 3.0^{vii} program. CCDC 1026425-1026426 contain the supplementary crystallographic data for this paper.

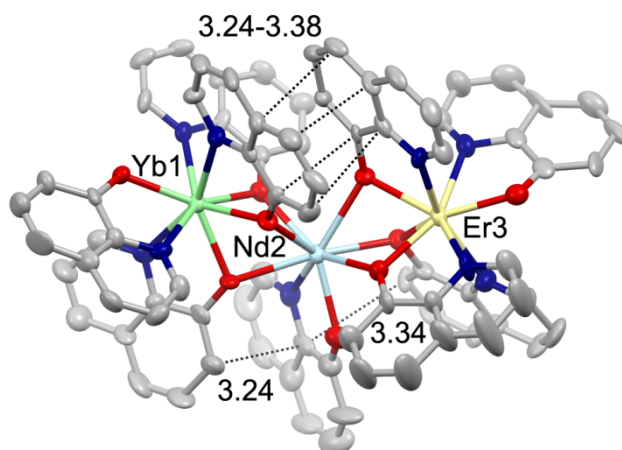


Figure S1. Molecular drawing of **1** with thermal ellipsoids depicted at the 30% probability level. Hydrogen atoms are omitted for clarity. Dashed lines indicate intramolecular π - π interactions (in \AA). Color codes: red, oxygen, blue, nitrogen, gray, carbon.

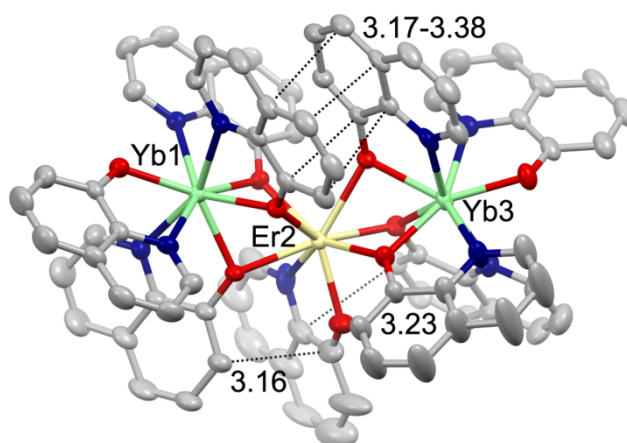


Figure S2. Molecular drawing of **2** with thermal ellipsoids depicted at the 30% probability level. Hydrogen atoms are omitted for clarity. Dashed lines indicate intramolecular π - π interactions (in \AA). Color codes: red, oxygen, blue, nitrogen, gray, carbon.

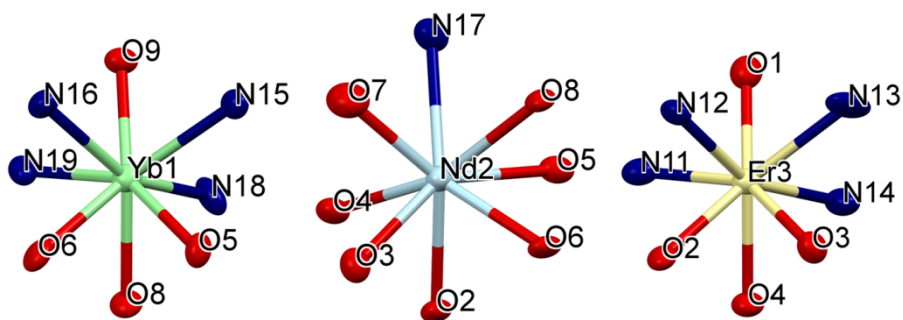


Figure S3. Coordination geometry of the three metal ions in **1**. The metals exhibit a distorted square antiprismatic geometry.

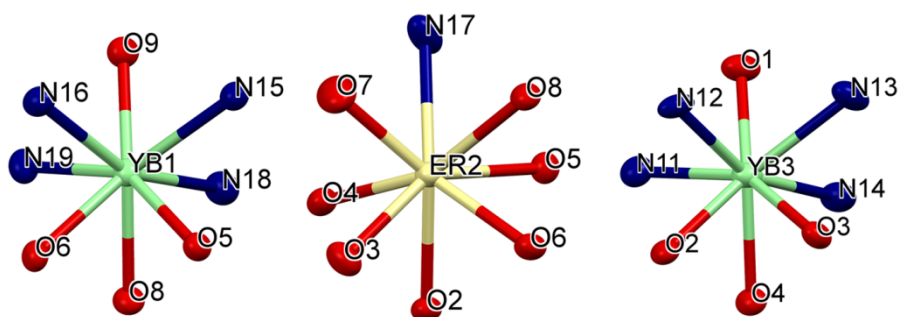


Figure S4. Coordination geometry of the three metal ions in **2**. The metals exhibit a distorted square antiprismatic geometry.

In the homoleptic Ln_3Q_9 molecules, each metal presents a distorted antiprismatic geometry with the two outer metals bound by four nitrogen and four oxygen atoms whereas the inner metal is coordinated by a nitrogen and seven oxygen atoms. The molecules are bent and the Ln(1)–Ln(2)–Ln(3) angles of 132.4° for **1** and 133.4° for **2** are close to the value found for Er_3Q_9 (133.5°).

Table S2. Summary of crystallographic data for **1·2CH₃CN** and **2·2CH₃CN**

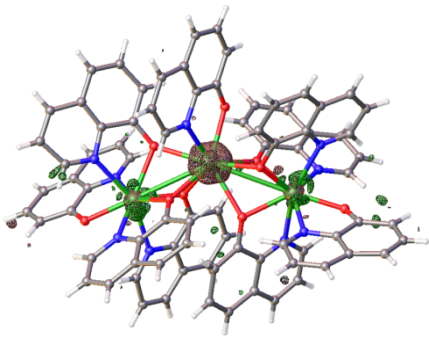
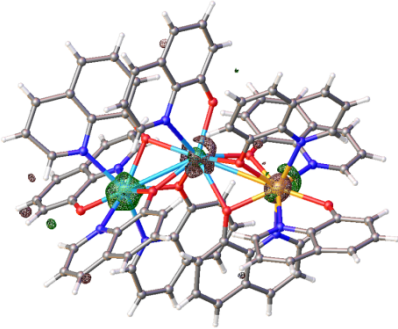
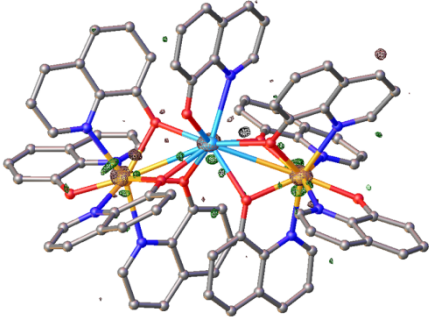
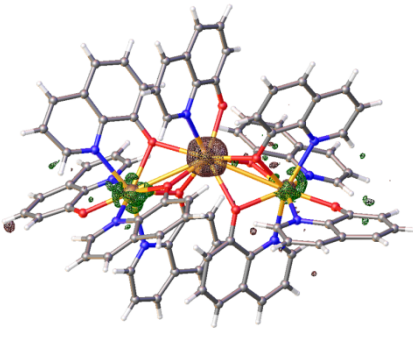
	1·2CH₃CN	1·2CH₃CN
Colour, habit	Yellow, Block	Yellow, Block
Crystal system, space group	Triclinic P-1	Triclinic P-1
a, b, c (Å)	12.292(4), 16.932(5), 18.278 (6)	12.314(1), 16.751(1), 18.195 (2)
α, β, γ (deg.)	83.339(6), 78.749(6), 83.481(6)	83.391(3), 79.250(1), 83.909(2)
V (Å³)	3690(2)	3648.9(5)
Z, ρ(calc) (Mg/m³)	2, 1.678	2, 1.723
T (K), λ (Å)	293(2), 0.71073	293(2), 0.71073
μ (mm⁻¹)	3.145	3.750
θ range (deg.)	1.14 to 24.58	1.60 to 26.63
No.of rflcn/unique	38296/12286	44942/15243
Goof	0.988	1.005
Final R indices [I>2σ(I)]	R1=0.0624, wR2=0.0856	R1=0.0347, wR2=0.0755

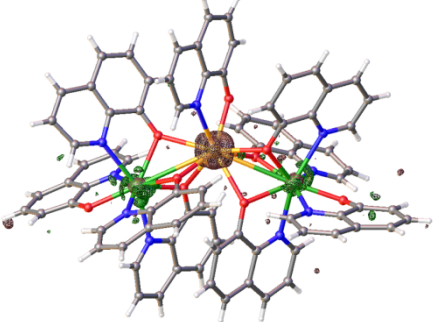
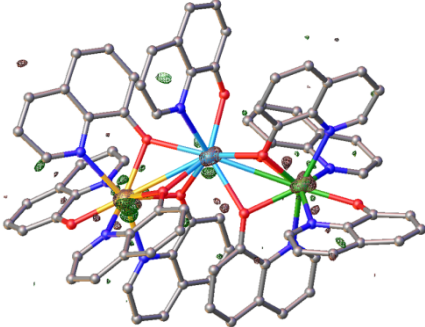
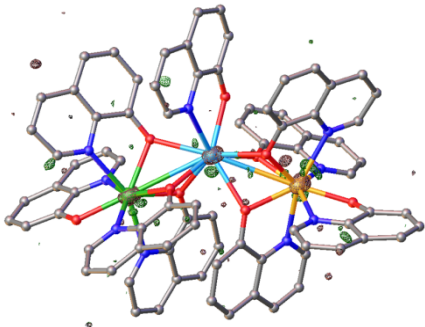
Table S3. Selected bond lengths for **1·2CH₃CN** and **2·2CH₃CN**

	1·2CH₃CN	2·2CH₃CN
N(11)-Ln(3)	2.49(1)	2.475(4)
N(12)-Ln(3)	2.519(9)	2.489(4)
N(13)-Ln(3)	2.48(1)	2.494(4)
N(14)-Ln(3)	2.50(1)	2.462(4)
N(15)-Ln(1)	2.524(9)	2.516(4)
N(16)-Ln(1)	2.497(9)	2.457(4)
N(17)-Ln(2)	2.65(1)	2.508(5)
N(18)-Ln(1)	2.444(9)	2.470(4)
N(19)-Ln(1)	2.44(1)	2.461(4)
O(1)-Ln(3)	2.224(8)	2.236(3)
O(2)-Ln(3)	2.295(7)	2.285(3)
O(2)-Ln(2)	2.534(7)	2.476(3)
O(3)-Ln(3)	2.287(8)	2.285(3)
O(3)-Ln(2)	2.389(8)	2.304(3)
O(4)-Ln(2)	2.434(7)	2.339(3)
O(4)-Ln(3)	2.339(7)	2.348(3)
O(5)-Ln(1)	2.315(7)	2.303(3)
O(5)-Ln(2)	2.425(8)	2.308(3)
O(6)-Ln(1)	2.195(7)	2.314(3)
O(6)-Ln(2)	2.465(7)	2.387(3)
O(7)-Ln(2)	2.334(9)	2.250(4)
O(8)-Ln(1)	2.324(7)	2.306(3)
O(8)-Ln(2)	2.499(7)	2.385(3)
O(9)-Ln(1)	2.256(7)	2.243(3)
Ln(3)-Ln(2)	3.573(1)	3.4748(3)
Ln(2)-Ln(1)	3.586(1)	3.4782(3)

Table S4. Refinement of the molecular structure of **1** with different metal site occupancies, together with the F_o-F_c map (negative values of electron density are reported in red).

	1	2	3	R (%) prelim. refin.	R (%) comple te refin.	wR2	Largest diff. peak and hole $e^- \text{ \AA}^{-3}$	(F_o-F_c) map
Refine ment 1	Nd	Nd	Nd	6.96	6.94	0.1657	0.96 (0.71 Nd1)/ -1.47 (0.62 Nd2)	
2	Yb	Nd	Nd	7.15				
3	Nd	Yb	Nd	9.00	9.10	0.2932	1.82(0.45 Nd1)/ -3.53 (0.59 Yb2)	
4	Nd	Nd	Yb	7.06				
5	Yb	Yb	Nd	8.46				
6	Yb	Nd	Yb	6.20	6.30	0.1006	0.90 (0.54 Nd2)/ -0.83 (0.99 Yb3)	
7	Nd	Yb	Yb	8.36				

8	Yb	Yb	Yb	7.02	6.91	0.1663	1.06 (0.80 Yb1)/ -1.97 (0.62 Yb2)	
9	Er	Nd	Nd	6.97				
10	Nd	Er	Nd	8.57				
11	Nd	Nd	Er	6.89	6.96	0.1669	1.64 (0.52 Nd1)/ -1.13 (0.75 Er3)	
12	Er	Er	Nd	8.09				
13	Er	Nd	Er	6.12	6.19	0.0988	0.81 (0.44 Er3)/ -0.80 (1.16 Yb2)	
14	Nd	Er	Er	7.98				
15	Er	Er	Er	6.95	6.84	0.1596		
16	Yb	Er	Er	6.84				

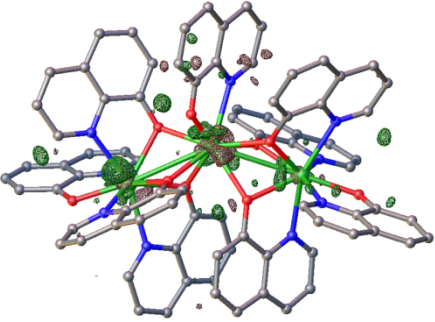
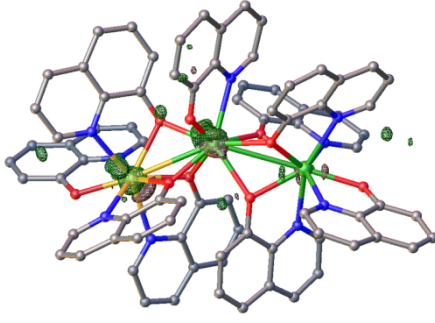
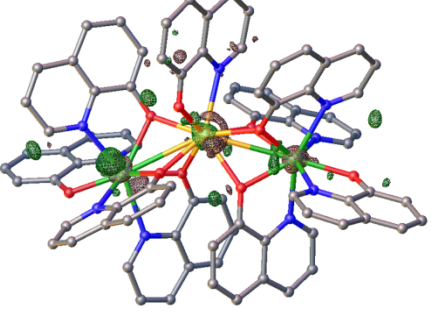
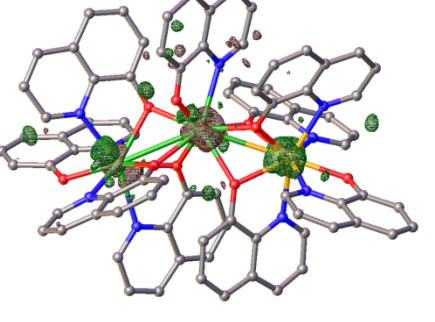
17	Er	Yb	Er	7.22				
18	Er	Er	Yb	6.81				
19	Yb	Yb	Er	7.12				
20	Yb	Er	Yb	6.72	6.65	0.1469	0.96 (0.84 Yb1)/ -1.61 (0.62 Er2)	
21	Er	Yb	Yb	7.10				
22	Er	Nd	Yb	6.12	6.29	0.1008	0.91 (0.52 Er1)/ -0.87 (0.94 Yb3)	
23	Er	Yb	Nd	8.48				
24	Nd	Er	Yb	8.04				
25	Nd	Yb	Er	8.36				
26	Yb	Nd	Er	6.20	6.24	0.0995	0.88 (0.43 Er3)/ -0.80 (1.12 Yb1)	
27	Yb	Er	Nd	8.18				

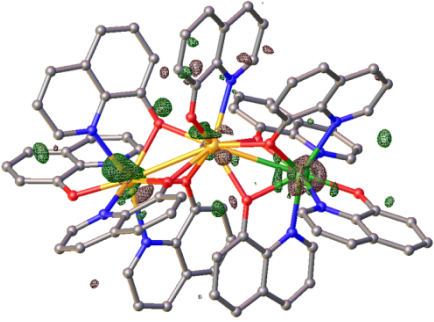
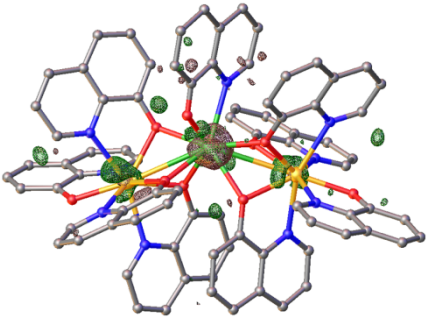
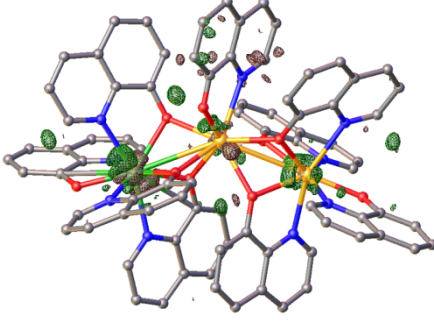
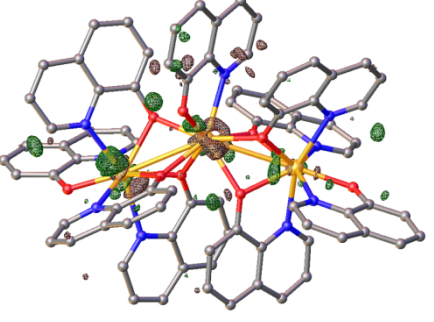
According to the refinement reported in Table S4 performed for compound **1**, the best results are obtained with the following models: **6** (YbNdYb), **13** (ErNdEr), **22** (ErNdYb), and **26** (YbNdEr). According to the $F_o - F_c$ maps it is evident that the central site is occupied by the Nd atom. In fact, when refining the structure with either with Yb (**3** (NdYbNd) and **8** (YbYbYb)) or Er (**15** (ErErEr) and **20** (YbErYb)) there is an excess of electron density on the central metal site in agreement with the greater atomic number of Yb (70) and Er (68) with respect to Nd (60). Unfortunately, no definitive assignment can be made for the metal sites 1 and 3 since the refinement **6** (YbNdYb), **13** (ErNdEr), **22** (ErNdYb), and **26**

(YbNdEr) are equally satisfactory. The molecular structure was refined with a mixed metal composition according to the complex speciation derived by the ESI-MS experiments, which give the following molecular speciation: NdErYbQ₉ (~44%), NdYb₂Q₉ (~25%) and NdEr₂Q₉ (~19%).

The model YbNdErQ₉ (refinement **26**) was preferred over ErNdYb (refinement **22**) according to the absence of appreciable residual features in the F_o-F_c map in the latter.

Table S5. Refinement of the molecular structure of **2** with different metal site occupancies, together with the F_o-F_c map (negative values of electron density are reported in red).

	1	2	3	R (%)	wR2	Largest diff. peak and hole $e/\text{\AA}^{-3}$	(F_o-F_c) map
Refinement 1	Yb	Yb	Yb	3.49	0.0822	1.51 (0.82 \AA Yb1)/ -0.97 (0.82 \AA Yb1)	
2	Er	Yb	Yb	3.60	0.0903	1.87(0.71 \AA Er1)/ -1.11 (0.71 \AA Yb2)	
3	Yb	Er	Yb	3.47	0.0755	1.35 (0.87 \AA Yb1)/ -1.20 (0.79 \AA Yb1)	
4	Yb	Yb	Er	3.62	0.0926	1.31 (0.86 \AA Yb1)/ -1.26 (0.75 \AA Yb1)	

5	Er	Er	Yb	3.48	0.0824	1.67(0.76 \AA Er1)/ -0.90 (0.63 \AA Yb3)	
6	Er	Yb	Er	3.63	0.0938	1.64(0.74 \AA Er1)/ -0.66 (0.63 \AA Yb2)	
7	Yb	Er	Er	3.50	0.0842	1.15(0.93 \AA Yb1)/ -1.48 (0.72 \AA Yb1)	
8	Er	Er	Er	3.40	0.0775	1.43(0.81 \AA Er1)/ -0.99 (0.69 \AA Er1)	

According to the seven refinement performed for compound **1**, the best results are obtained with the following models: **1** (YbYbYb), **3** (YbErYb), **5** (ErErYb), and **8** (ErErEr). Useful information concerning the proper assignment of the metals in the correct model can be obtained by the inspection of the $F_o - F_c$ map, in which negative values, representing an excess of electron density, are reported in red. According to the maps it appears that the central site is most likely occupied by the Er atom. In fact, when refining the structure with Yb, there is an excess of electron density for this model (compare refinements **1**, **4** and **6**) in agreement with the greater atomic number of Yb (70) with respect to Er (68). Unfortunately, no definitive assignment can be made for the metal sites 1 and 3 since the refinements **3** (YbErYb), **5** (ErErYb), and **8** (ErErEr) are equally satisfactorily. The molecular structure was therefore refined as YbErYbQ₉ (refinement **3**) according to the complex speciation derived by the ESI-MS experiments, which give the following molecular speciation: ErYb₂Q₉ ~44%, Er₂YbQ₉ ~18%, Yb₃Q₉ ~35% and Er₃Q₉ ~3%.

Table S6. Er-N/O bond distances (Å) according to the 70 structures found in the CCDC for a ErO₄N₄ search.

	Er-O1	Er-O2	Er-O3	Er-O4	Er-N1	Er-N2	Er-N3	Er-N4
Range	2.196-2.590	2.139-2.565	2.141-2.566	2.165-2.566	2.367-2.758	2.310-2.831	2.370-2.810	2.365-2.812
<i>Mean</i>	2.431	2.412	2.401	2.409	2.539	2.554	2.540	2.550
Mean (all)	2.413				2.546			

Table S7. Er-N/O bond distances (Å) according to the 87 structures found in the CCDC for a ErO₇N search.

	Er-O1	Er-O2	Er-O3	Er-O4	Er-O5	Er-NO6	Er-O7	Er-N
Range	2.207-2.887	2.207-2.887	2.242-2.857	2.224-2.885	2.234-2.625	2.215-2.702	2.209-2.692	2.370-2.779
<i>Mean</i>	2.396	2.415	2.386	2.421	2.409	2.396	2.393	2.545
Mean (all)	2.402							2.545

Table S8. Yb-N/O bond distances (Å) according to the 107 structures found in the CCDC for a ErO₄N₄ search.

	Yb-O1	Yb-O2	Yb-O3	Yb-O4	Yb-N1	Yb-N2	Yb-N3	Yb-N4
Range	2.138-2.543	2.164-2.714	2.125-2.773	2.164-2.609	2.309-2.884	2.302-2.719	2.290-2.865	2.302-2.685
<i>Mean</i>	2.363	2.368	2.381	2.373	2.555	2.508	2.542	2.525
Mean (all)	2.371				2.533			

Table S9. Yb-N/O bond distances (Å) according to the 48 structures found in the CCDC for a ErO₇N search.

	Yb-O1	Yb-O2	Yb-O3	Yb-O4	Yb-O5	Yb-NO6	Yb-O7	Yb-N
Range	2.254-2.695	2.235-2.576	2.208-2.498	2.184-2.533	2.149-2.606	2.207-2.568	2.179-2.709	2.284-2.668
<i>Mean</i>	2.390	2.366	2.357	2.338	2.387	2.396	2.407	2.514
Mean (all)	2.377							2.514

According to the mean values reported in Tables S6-S9, the Yb-O and Yb-N bond distances in the Yb complexes are significantly shorter than those of the Er ones, which is in agreement with the ionic radii of Er³⁺ (0.089 Å) and Yb³⁺ (0.086 Å). The trend observed for the mean values of the Ln-O and Ln-N bond distances appears to be also independent of the type of donor atoms surrounding the metal, since the LnO₄N₄ and LnO₇N provide comparable results.

If we now compare the data reported in Table S3, it appears that the central Er atoms of complex **2** exhibits greater Er-N and Er-O bond distances than the peripheral Yb atoms. This would tentatively support the refinement **3** reported in Table S5.

Powder XRD

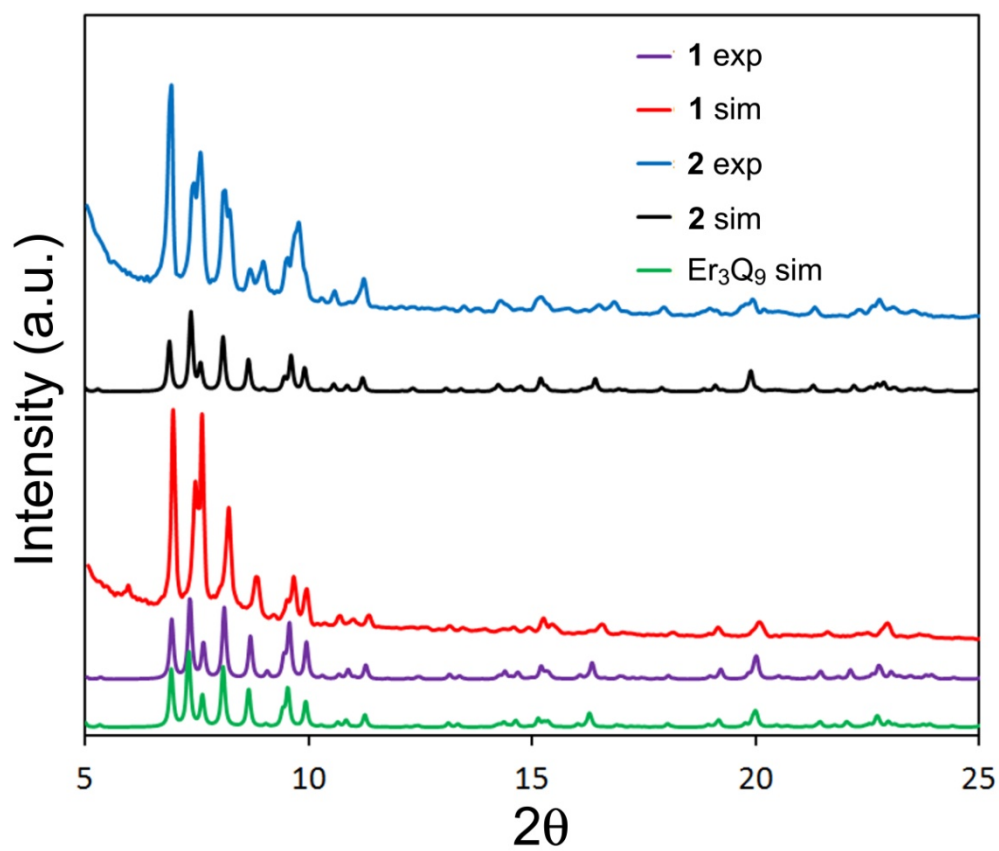


Figure S5. Experimental and simulated powder XRD patterns for **1** and **2** and comparison with the simulated diffractogram of the isostructural Er₃Q₉. Differences in peaks intensities are related to preferential orientations.

SEM-EDX

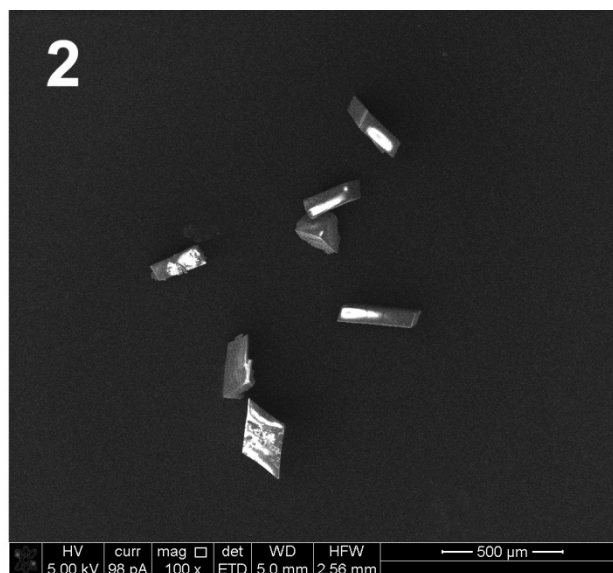
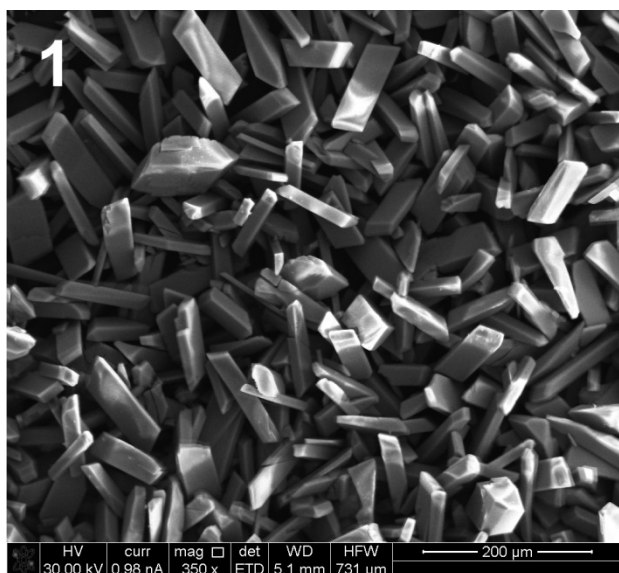


Figure S6. SEM micrographies of crystals of 1 and 2.

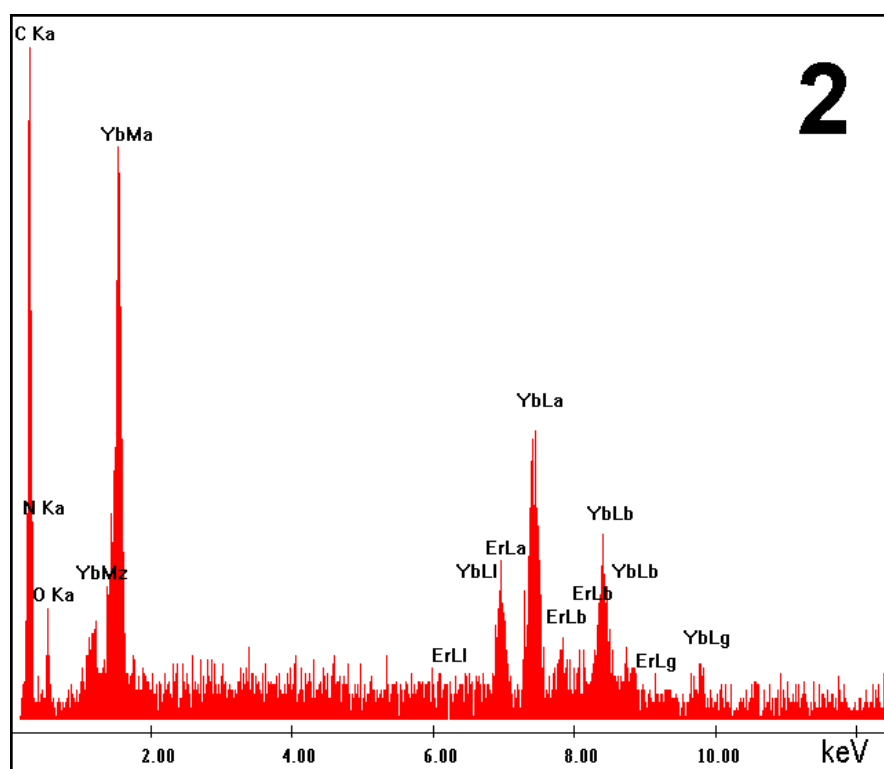
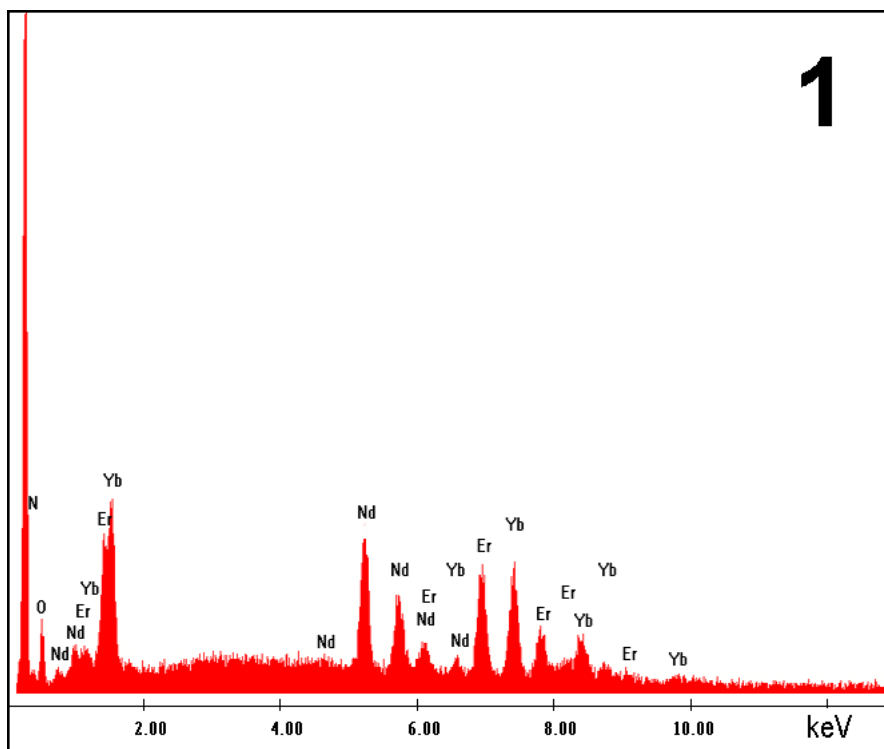


Figure S7. X-ray energy dispersive spectra for 1 and 2.

Table S10. Metal atomic percentages retrieved from EDX analysis.

Element	1 ^a	2 ^a
Nd	33.30	-
Er	33.82	31.32
Yb	35.88	68.68

^aaverages of punctual analyses on three different crystals

ESI-mass spectral analysis

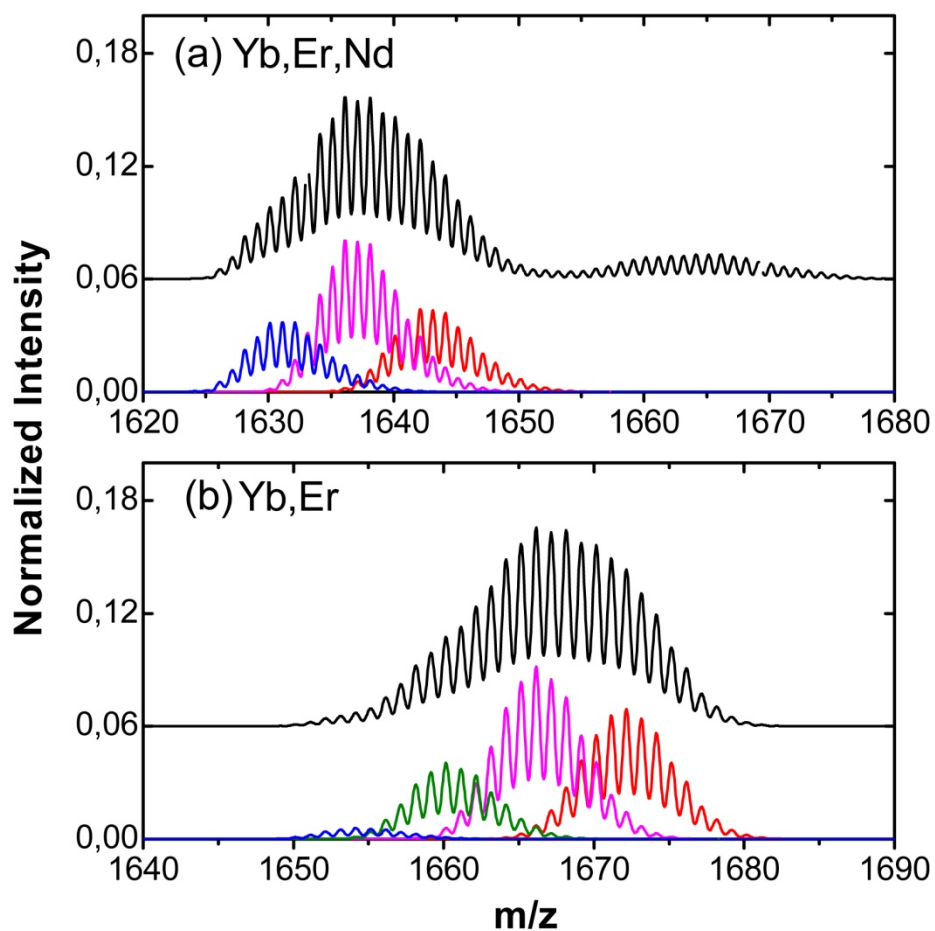


Figure S8. Model calculations of the $[Ln_3Q_8]^+$ parent peak for **1** (a) and **2** (b), showing the relative contributions of the different molecular species. Color codes and relative contributions: (a) Magenta, $NdErYbQ_8^+$ (~44%); Red, $NdYb_2Q_8^+$ (~25%); Blue, $NdEr_2Q_8^+$ (~19%); (b) Magenta, $ErYb_2Q_8^+$ (~44%); Red, $Yb_3Q_8^+$ (~35%); Green, $Er_2YbQ_8^+$ (~18%) Blue, $Er_3Q_8^+$ (~3%).

Solid state diffuse reflectance (DR) spectra

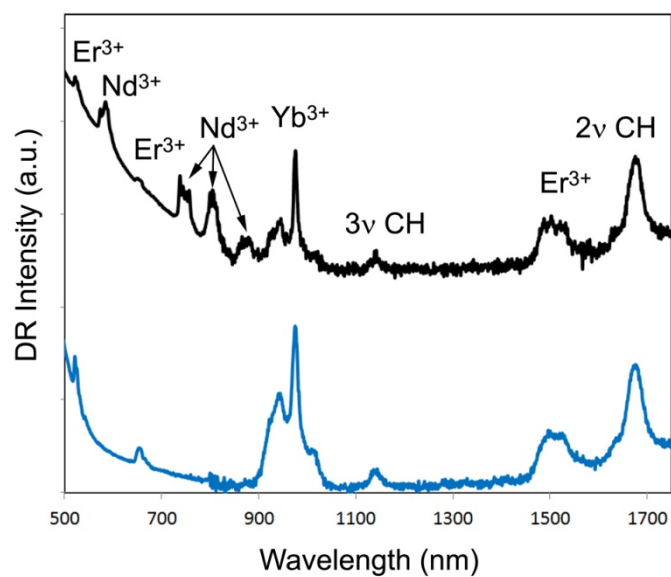


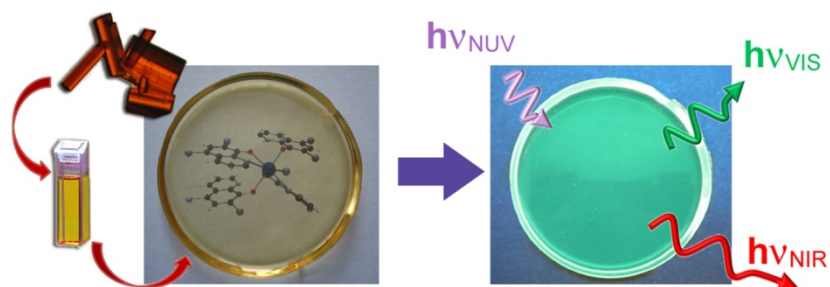
Figure S9. Diffuse reflectance (DR) spectra of **1** (black) and **2** (blue) as crystalline samples, showing narrow lanthanide absorption bands and overtones of ligand CH stretching vibrations. Since **1** and **2** are isostructural, spectra have been normalized for the 2nd harmonic of ligand CH stretching mode. See Experimental Section for bands assignments.

Reference List

- i SMART (control) and SAINT (integration) software for CCD systems, Bruker AXS, Madison, WI, USA, **1994**.
- ii. Area-Detector Absorption Correction, Siemens Industrial Automation Inc., Madison, WI, **1996**.
- iii. Burla, M. C.; Caliandro, R.; Camalli, M.; Carrozzini, B.; Cascarano, G. L.; De Caro, L.; Giacovazzo, C.; Polidori, G.; Spagna, R. SIR2004: an improved tool for crystal structure determination and refinement. *Journal of Applied Crystallography* **2005**, *38*, 381-388.
- iv. Sheldrick, G. M., SHELX97. Programs for Crystal Structure Analysis (1997) (Release 97-2). University of Göttingen, Germany.
- v. Farrugia, L. J. WinGX suite for small-molecule single-crystal crystallography. *Journal of Applied Crystallography* **1999**, *32*, 837
- vi. Spek, A. L. Structure validation in chemical crystallography. *Acta Crystallogr., Sect.D: Biol.Crystallogr.* **2009**, *D65*[2], 148
- vii. Macrae, C. F.; Edgington, P. R.; McCabe, P.; Pidcock, E.; Shields, G. P.; Taylor, R.; Towler, M.; van de Streek, J. *J. Appl. Crystallogr.* **2006**, *39*, 453.

Paper 5

Silica Sol-Gel Glasses incorporating Dual-Luminescent Yb Quinolinolato Complex: Processing, Emission and Photosensitising Properties of the 'Antenna' Ligand



Good quality $[\text{Yb}(\text{5,7ClQ})_2(\text{H5,7ClQ})_2\text{Cl}]$ doped silica sol-gel glass exhibits dual (NIR, Yb-centered and Visible, ligand-centered) luminescence upon NUV illumination.

Cite this: *Dalton Trans.*, 2012, **41**, 13147

www.rsc.org/dalton

PAPER

Silica sol–gel glasses incorporating dual-luminescent Yb quinolinolato complex: processing, emission and photosensitising properties of the ‘antenna’ ligand†‡

Flavia Artizzu,^{*a,b} Francesco Quochi,^b Michele Saba,^b Danilo Loche,^a Maria Laura Mercuri,^a Angela Serpe,^a Andrea Mura,^b Giovanni Bongiovanni^b and Paola Deplano^{*a}

Received 13th February 2012, Accepted 17th April 2012

DOI: 10.1039/c2dt30323j

The [Yb(5,7ClQ)₂(H5,7ClQ)₂Cl] (**1**) complex, that exhibits dual-luminescence in the visible (ligand-centered) and in the NIR (Yb-centered), has been incorporated into a silica sol–gel glass obtaining 1-doped glassy material which is optically transparent and homogeneous and with good mechanical properties. The doped sol–gel glass can be considered a “solid state solution” and photophysical studies demonstrate that the emissive properties of the dopant complex are preserved in the silica matrix. Observed NIR decay times fall in the μs range and are likely limited by “second-sphere” matrix interactions. The ligand-to-metal energy transfer mechanism occurs on ultrafast timescale and involves ligand triplet states. The sensitization efficiency of the antenna quinolinolato ligand toward Yb³⁺ is estimated to be as high as ~80%. The Yb natural radiative lifetime observed for **1** in MeCN–EtOH solution ($\tau_{\text{rad}} = 438 \mu\text{s}$) is the shortest reported so far for ytterbium complexes.

Introduction

Near-infrared emitting lanthanide quinolinolates are of interest in view of their possible applications as optically emitting materials at telecom wavelengths (optical fibers and amplifiers) and for medical imaging purposes.^{1–9} Near-infrared (NIR) emission related to lanthanide 4f intrashell transitions is sensitized by resonance energy transfer (RET) from the quinolinolato ligand acting as efficient “antenna” chromophore after convenient photoexcitation in the near-UV-visible spectral region. Through this indirect sensitization process, the low emission quantum yield after direct excitation of lanthanide ions, due to their intrinsic weak absorptivity, can be improved.^{10–22}

We are extensively investigating the structure–property relationship of this class of emitting molecules through combined chemical and photophysical studies to more deeply understand the decay processes affecting the quantum yield of NIR luminescence.^{20,21,23,24} It has been found that the ligand-to-metal energy transfer process occurs through a two-step mechanism involving the triplet state of the quinolinolato ligand. This mechanism results in an exceptionally efficient process leading to lanthanide (Er³⁺, Yb³⁺) sensitization efficiencies up to

population inversion threshold. These findings confirm that quinolinolato ligands are very appealing antennae for sensitizing lanthanide NIR emission.^{11,24,25}

However, the use of lanthanide chelate complexes in optical devices may be limited by poor thermal stability and low mechanical strength. These difficulties can be overcome by incorporation of lanthanide complexes into a suitable rigid matrix such as a silica host material provided that it does not significantly affect the luminescence properties of the compounds.²⁶ It is known that silica glasses doped with luminescent lanthanides are suitable materials for use in the fabrication of optical devices, such as lasers and optical fibres,²⁷ being highly transparent and homogeneous and having good mechanical properties. Moreover, the silica matrix hardly influences the energy levels of the lanthanide ions and has also a negligible absorption coefficient at the excitation wavelengths used in photoluminescence experiments. In order to check if lanthanide quinolinolate complexes are suitable dopants into silica sol–gel glasses, we have selected [Yb(5,7ClQ₂)(H5,7ClQ)₂Cl] (H5,7ClQ = 5,7-dichloroquinolinol), fully characterised chemically and photophysically in solution and the solid state,²⁴ to be incorporated into a silica sol–gel glass and report here a study on its properties. Our results on the photocycle of the resulting silica sol–gel glasses provide encouraging evidence for their prospects as large-cross section solid-state NIR emitters and amplifiers.

Experimental section

General

Chemicals. All the reagents and solvents were purchased from Aldrich and used without further purification.

^aDipartimento di Scienze Chimiche e Geologiche, Università di Cagliari, SS 554 Bivio per Sestu, I-09042, Monserrato-Cagliari, Italy.

E-mail: f.artizzu@unica.it, deplano@unica.it; Fax: (+) 39 0706754456

^bDipartimento di Fisica, Università di Cagliari, SS 554 Bivio per Sestu, I-09042, Monserrato-Cagliari, Italy

† Based on the presentation at Dalton Discussion No. 13, 10–12 September 2012, University of Sheffield, UK.

‡ Electronic supplementary information (ESI) available. See DOI: 10.1039/c2dt30323j

Spectroscopy. Absorption UV-Vis-NIR spectra of solutions and of sol-gel glass samples were collected with a Varian Cary 5 spectrophotometer. The absorption spectrum of a blank undoped sol-gel glass was taken as baseline for the 1-doped sol-gel glass spectrum. Vibrational FT-IR spectra on KBr pellets were collected with a Bruker Equinox 55 spectrophotometer.

Microscopy. Transmission electron microscopy (TEM) was done on samples drop cast from ethanolic suspension onto copper grid mounted holey carbon films, on a Hitachi H-7000 instrument running at 100 kV.

X-Ray diffraction. Wide-angle X-ray diffraction XRD patterns were recorded on a Panalytical Empyrean diffractometer equipped with a graphite monochromator on the diffracted beam and a X'Celerator linear detector. The scans were collected within the range of 10–90° (2 θ) using Cu K α radiation.

Thermal analysis. Thermal gravimetric analysis (TG) and simultaneous differential thermal analysis (DTA) were carried out on a Mettler-Toledo TGA/STDA 851. Thermal analysis data were collected in the 25–800 °C range, under oxygen flow (heating rate = 10 °C min⁻¹; flow rate = 50 mL min⁻¹).

Syntheses

Synthesis of [Yb(5,7ClQ)₂(H5,7ClQ)₂Cl] (1). Synthesis was carried out as reported in ref. 24. Electronic absorption spectroscopy, MeCN–EtOH (1 : 1) (λ_{max} /nm (10⁻³ε/mol⁻¹ dm³ cm⁻¹): 340 (9.58 ± 0.03), 381 (8.00 ± 0.02).

Synthesis of 1-doped silica sol-gel glass

Preparation of the sol mixture. 8 mL of absolute ethanol, 8 mL of tetramethoxysilane (TMOS), 8 mL of glycidoxypropyltrimethoxysilane (GLYMO) and 4 mL of water were mixed in a round-bottom flask. This mixture (sol) was maintained 1 day under stirring at room temperature.

Preparation of the doped glass. 2 mL of a 1 × 10⁻³ M solution of **1** in MeCN–EtOH 1 : 1 were added to 3 mL of the sol solution and the mixture was maintained under stirring at 50 °C for 1 h. The mixture was then transferred into a cylindrical glass vial and allowed to cool down at room temperature. Afterwards, the vial was covered with Parafilm pierced with a needle to allow the solvent to evaporate slowly. After a few days, depending on the viscosity of the sol-gel, two or three more holes were made in the Parafilm and the sample was allowed to stand at RT until the glass formed. The sample thickness was about 1 mm and the estimated concentration of **1** was ~3 × 10⁻³ M. Electronic absorption spectroscopy (λ_{max} /nm): 340, 391; FT-IR (KBr pellet, cm⁻¹): 3480w, br, 2952w, 2922w, 2885vw, 1647w, 1384s, 1207s, 1098vs, 1037vs, 906m, 855m, 797m, 758m, 694mw, 568mw, 450s. Thermal gravimetric analysis (TG) and simultaneous differential thermal analysis (DTA) show a very limited weight loss (around 1%) below 80 °C, accompanied in the DTA curve by an endothermic effect, likely due to some residual/adsorbed water. In the range 200–300 °C the weight loss is about 50% and corresponds to exothermic peaks in the DTA indicating that the weight loss in this region can be attributed to the combustion of organics, *i.e.* the aliphatic chains of the ORMOSIL and the 5,7ClQ ligand.

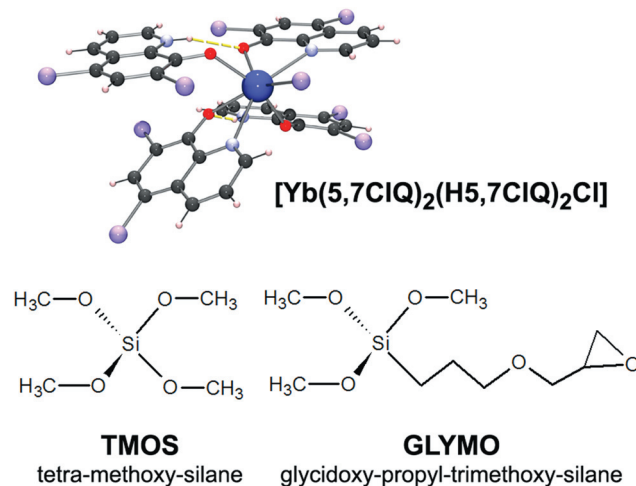
Transient optical spectroscopy

Photoluminescence (PL) and photoinduced absorption were excited at 392 nm wavelength by the frequency-doubled output pulses of a regenerative Ti:sapphire amplifier (Quantronix INTEGRA C) running at a repetition frequency of 1 kHz. The PL transient was spectrally dispersed in a 0.3 m imaging spectrograph (Acton SpectraPro 2300i) and captured by a streak camera (Hamamatsu C5680) operating in single-shot mode. Experimental data show that effective temporal resolution is ~30 ps in the operating conditions (with 70–100 s accumulation time). Photoinduced absorption was probed by broadband synchronous pulses obtained by supercontinuum generation in a sapphire plate. The optical probe beam transmitted through the sample was spectrally dispersed using a SpectraPro 2300i spectrograph and detected by a charge-coupled device (Andor NEWTON). The pump-probe time delay was varied using a motorized optical delay stage. Photoinduced absorption was measured as the differential transmission signal $\Delta T/T = (T - T_0)/T_0$, where T (T_0) is the transmitted probe pulse energy in presence (absence) of the pump pulse. Near-infrared emission transients were measured using a DC-125MHz NIR photoreceiver (NewFocus 1811) and a 1 GHz digitizing oscilloscope (Tektronik TDS 5104). Photoexcitation fluences were kept below the level of one excitation per complex per laser pulse in all experiments.

Results and discussion

Preparation of Yb-doped sol-gel glasses

The tetrakis-complex [Yb(5,7ClQ)₂(H5,7ClQ)₂Cl] (**1**), which has been fully characterised through solid-state and solution studies was selected as dopant to prepare Yb-doped sol-gel glasses.²⁴ In this complex the ytterbium ion is hepta-coordinated to four ligands, two anionic N,O chelated and two in the zwitterionic form acting as monodentate oxygen donors with a chloride completing the lanthanide coordination sphere, as shown in Scheme 1.



Scheme 1 Structures of [Yb(5,7ClQ)₂(H5,7ClQ)₂Cl] dopant complex and the silica precursors.

The silica matrix was prepared from a mixture of the two precursors shown in Scheme 1: tetramethoxysilane (TMOS) and the organically-modified silicon alkoxide (ORMOSIL), glycidoxypropyltrimethoxysilane (GLYMO). ORMOSILs are formed by a silicate backbone in which alkoxydic –OR groups are replaced by organic –R groups.²⁸ These precursors have been selected in view of the following more appealing features over the commonly used tetraalkoxysilanes such as TMOS and TEOS (tetraethoxysilane): (i) improved mechanical properties of the glass (lower shrinkage) due to the filling of the pores by bulky organic groups, (ii) high thermal stability and damage threshold upon lasing in photoluminescence experiments,²⁹ and (iii) decrease of the polarity of the material due to the formation of hydrophobic domains. As a consequence, water molecules potentially entrapped in the matrix are expected to be expelled and, at the same time, diffusion of water molecules from the environment into the porous glass should be hampered. Moreover the number of residual Si–OH groups in the silica host is reduced.^{26,30} In particular, GLYMO has been selected in view of the fact that the epoxy group is expected to react readily with water molecules, lowering the water content in the sol–gel material, and thus reducing quenching phenomena affecting NIR luminescence.^{26,30d} In addition, **1** itself being highly hydrophobic, its solubility into the organically modified sol–gel matrix is improved, leading to a homogeneous final material. This should also help in avoiding the presence of molecular aggregates and clusters, which may diminish the luminescence quantum yield through self-extinction processes (concentration effect).³¹

The preparation of the doped sol–gel glass was performed through a one-step process in which a solution of the lanthanide complex in MeCN–EtOH (1 : 1 v/v) solvent mixture was mixed with the liquid sol matrix (ethanolic mixture of TMOS and GLYMO precursors where the hydrolysis reaction was already started) at 50 °C and at neutral pH. Hydrolysis and condensation reactions in the sol–gel process were carried out without acidic or basic catalysis in order to avoid possible degradation of **1** in view of the acid–base properties of the Q ligand.³² For this reason, TMOS, which hydrolyses easily under neutral conditions, was preferred to the more commonly used TEOS (tetraethoxysilane). These optimized conditions led to the best results in terms of transparency, homogeneity and mechanical resistance of the doped glass.

The resulting doped sol solution was then added into a Teflon vial and allowed to age at room temperature. Slow solvent evaporation led to the formation of a homogeneous and transparent yellow glass as shown in Fig. 1. Sample homogeneity at nanometric level was also confirmed by TEM (Fig. 1b), and further evidence of the amorphous character of the doped glass was provided by XRD analysis, showing only the typical amorphous silica haloes (Fig. S11, ESI†).

Thermal gravimetric analysis (TG) and simultaneous differential thermal analysis (DTA) showed the presence of a very limited water content (around 1%) in the final material (Fig. S12, ESI†).

Spectroscopic studies and photophysical properties

Recent chemical and photophysical studies of **1** in DMSO solution and in the solid state have established that **1** shows

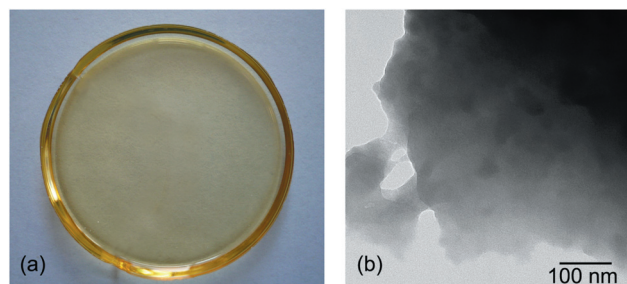


Fig. 1 (a) Sol–gel glass sample doped with **1** under white light illumination; (b) TEM image of **1**-doped sol–gel glass.

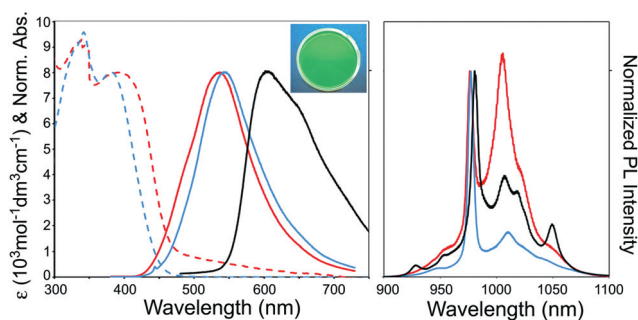


Fig. 2 UV-visible absorption spectra of **1** in MeCN–EtOH solution (dashed blue line) and in doped sol–gel glass sample (dashed red line) and normalised photoluminescence (PL) spectra in the visible and near-infrared spectral regions acquired after photo-excitation at 392 nm (MeCN–EtOH solution, blue line; sol–gel glass sample, red line; crystals, black line). Inset: **1**-doped sol–gel glass under UV light.

dual-luminescence in the visible (ligand-centered emission) and in the NIR (metal-centered luminescence) upon ligand photoexcitation in the near-UV.²⁴ Similar studies on **1**-doped sol–gel glass show that these features are preserved in the silica host material as reported below. The obtained glass sample is optically homogeneous throughout the bulk/surface.

Absorption and photoluminescence (PL) spectra in the visible and in the near-infrared regions of the **1**-doped sol–gel glass are shown in Fig. 2. Absorption and PL spectra of **1** in the MeCN–EtOH solution used for the preparation of the glass sample and PL spectra of crystals of **1** are also reported for comparison.

A summary of spectroscopic data (absorption and PL) for **1** in different matrices is reported in Table 1.

As shown in Fig. 2, the absorption spectra of the solution and of the **1**-doped sol–gel glass are both dominated by two intense ligand bands and display very similar spectral features despite a small band broadening in the glass absorption spectrum. The more intense peak near 340 nm in both spectra arises from the contribution of both the anionic and the zwitterionic forms of the quinolinolato ligand. The low-energy peak, centered at about 391 and 381 nm in the glass and solution spectrum, respectively, is attributable to a $^1(\pi-\pi)^*$ ligand-centered transition with ILCT character and closely reflects that of the deprotonated form of the ligand, as expected for closed-shell metal complexes with a high ionic character of the metal–ligand bonding.³³

Photoexcitation in the lowest ligand absorption band yields ligand-centered fluorescence $^1(\pi-\pi)^*$ in the green ($\lambda_{\max} \sim$

Table 1 Absorption and PL peak positions of **1** in different matrices

Matrix	Absorption λ_{\max}/nm	Vis PL λ_{\max}/nm
MeCN–EtOH solution	340, 381	541
DMSO solution ²⁴	343, 396	545
Doped sol–gel glass	338, 391	537
Solid state (crystals) ²⁴	351, 410, 494	603

540 nm) for both solution and doped sol–gel glass, whereas a remarkable red-shift is instead observed in the case of crystalline sample ($\lambda_{\max} = 603$ nm), that has been attributed to “excimer-like” emission due to the extensive π -stacking of **1** observed in the crystal structure.²⁴

Peak positions related to ligand-centered transitions in both absorbance and photoluminescence spectra are slightly affected by the nature of the matrix (Table 1). A weak blue shift is observed in MeCN–EtOH solution compared to solutions in more polar solvents.²⁴ Similarly, the observed hypsochromic shift of sol–gel glass fluorescence with respect to solution may be related either to a change in the complex environment in the organosilica matrix, due to the filling of the pores by organic hydrophobic chains, or to a weak rigidochromic effect.³⁴

The Yb^{3+} emission band at 1 μm due to the intrashell ${}^2\text{F}_{5/2} \rightarrow {}^2\text{F}_{7/2}$ transition, is moderately broadened and partially resolved into multiplets (Stark lines) due to the partial removal of the degeneracy of 4f ground (${}^2\text{F}_{7/2}$) and excited (${}^2\text{F}_{5/2}$) levels into $2J + 1$ terms by crystal field effects, which makes f–f transitions allowed to some extent. The observed fine structure arising from this Stark splitting is in accordance with the low-symmetry of the metal environment.³⁵ The spectral profile of **1**-doped sol–gel glass is slightly modified with respect to solution and solid state, showing an increase of the relative intensity of the peak at 1005 nm compared to the ${}^2\text{F}_{5/2}(0') \leftrightarrow {}^2\text{F}_{7/2}(0)$ transition at 977 nm. This sequence of peaks has been observed in eight-coordinated ytterbium complexes.³⁶ An increase of the coordination number of Yb in the sol–gel glass cannot be ruled out by taking into account that several potential oxygen donors are available in the organically-modified silica matrix.

Time-resolved measurements in the near-infrared under femto-second laser pulse excitation yield bi-exponential decays for both solution and **1**-doped sol–gel glass samples with similar ytterbium emission lifetimes, $\tau_{\text{obs}1} = 0.85$ μs , $\tau_{\text{obs}2} = 2.51$ μs and $\tau_{\text{obs}1} = 0.63$ μs , $\tau_{\text{obs}2} = 3.69$ μs , respectively (Fig. 3). Each constant has approximately 50% weight in both cases.

In order to compare these absolute values to those found for analogous ytterbium compounds or for **1** in other matrices,²⁴ the ytterbium intrinsic quantum yield, Φ_{Yb} , is required. Φ_{Yb} represents the ratio between the rate constants of radiative ($\kappa_{\text{rad}} = 1/\tau_{\text{rad}}$) and nonradiative excited state deactivation ($\kappa_{\text{obs}} = 1/\tau_{\text{obs}}$) processes of Yb^{3+} in a specific environment.^{37–41} The ytterbium “natural” radiative lifetime, τ_{rad} , is the intrinsic radiative strength of the emitting oscillator in the absence of nonradiative deactivation. Usually this value is taken from literature data and is assumed to be constant in different solvents.⁴² However, since it depends on several parameters, including the refractive index of the medium and the coordination environment, it seemed to us important to experimentally determine τ_{rad} for **1** in MeCN–EtOH solution from spectroscopic data (absorption cross-section, σ_{Yb})

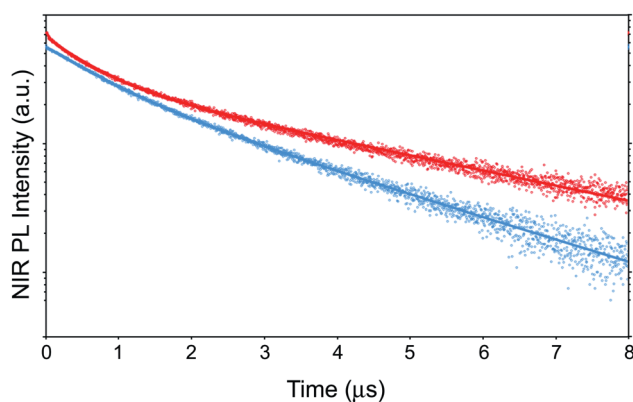


Fig. 3 Normalised NIR experimental decay of **1** as doped sol–gel glass (red dots) and in MeCN–EtOH solution (blue dots). Solid curves represent best fitting to experimental data. The emission signal is reported on a logarithmic scale.

through the Strickler–Berg equation.⁴³ The obtained value, $\tau_{\text{rad}} = 440$ μs , is the smallest ever reported for ytterbium complexes, indicating an extremely high radiative strength of Yb^{3+} in such an environment. It should also be pointed out that the shortening of τ_{rad} with respect to radiative lifetime found for **1** in anhydrous DMSO solution ($\tau_{\text{rad}} = 690$ μs) exceeds that expected on the basis of the difference in refractive indexes of the solvents and may therefore be related to a second-sphere solvent interaction.⁴⁴ The obtained results and the apparent discrepancy with literature data point out that the use of intrinsic quantum yields evaluated through ‘literature’ data should be discouraged, while the availability of experimental data is crucial to assess reliable photophysical parameters in luminescent lanthanide complexes. Experimental data and equations used for evaluating the radiative lifetime of **1** in MeCN–EtOH solution are given in ESI†.

The obtained ytterbium intrinsic quantum yield in MeCN–EtOH solution, $\Phi_{\text{YbMeCN/EtOH}} = 0.43\%$, is quite low and appreciably lower than the value found for complex **1** in anhydrous DMSO solution ($\Phi_{\text{YbDMSO}} = 1.1\%$, $\tau_{\text{obs}} = 7.85$ μs),²⁴ indicating the occurrence of significant nonradiative processes affecting the NIR emission. These low quantum yields can be, in most part, explained by taking into account quenching phenomena due to Förster resonance energy transfer (FRET)⁴⁵ from the emitting lanthanide ion to the strongly resonant oscillating C–H and/or O–H groups present in the surroundings (deactivation *via* vibrational excitation). In the case of the MeCN–EtOH solution the additional presence, with respect to anhydrous DMSO, of ethanolic OH groups and/or water molecules in the solvent mixture, will lead to increased nonradiative processes. In fact the third harmonic of stretching vibration of these groups is extremely resonant (~ 980 nm) with Yb^{3+} 1 μm luminescence and provides an important supplementary non-radiative deactivation channel (likely due to a second-sphere solvent interaction) accounting for the further shortening of τ_{obs} (Fig. 4). Similar considerations can be extended to the organically-modified sol–gel glass, where “second-sphere” quenching effects can be ascribed to the presence of aliphatic chains and hydrolysed epoxy groups of the GLYMO precursor and/or to solvent molecules potentially entrapped into the pores. Moreover a self-quenching effect may be operational, due to the high

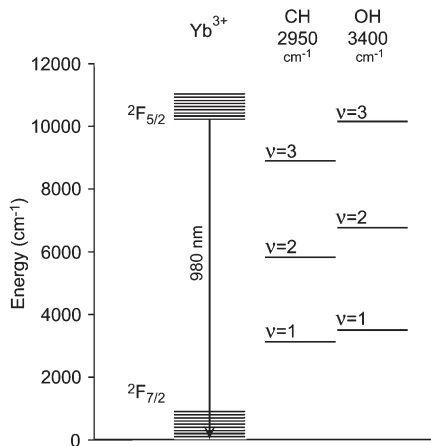


Fig. 4 Energy gaps of emitting levels of Yb^{3+} compared to the energy of vibrational modes of C–H and O–H groups and their harmonics.

concentration of the doped material in the sol–gel glass, but the observed NIR-dynamics (see Fig. 3) show only minor differences between the two curves of **1** in doped sol–gel glass and solution. Future work is addressed to overcome the quenching processes by suitably changing the starting material in order to take advantage of the promising properties of the glasses for future applications in optical devices, in terms of preparative procedures (low-cost and energy saving), and quality of the glass for optical transparency, homogeneity, mechanical strength and thermal stability.

Direct measurement of total quantum yield for NIR emission after ligand excitation in MeCN–EtOH solution yields $\Phi_{\text{tot}} = 0.30 \times 10^{-2}$.⁴⁶ The ligand-to-metal sensitization efficiency, η_{sens} , is therefore calculated through the equation:

$$\Phi_{\text{tot}} = \eta_{\text{sens}} \Phi_{\text{Yb}} \quad (1)$$

a value close to 80% is determined confirming that the upper emitting $^2\text{F}_{5/2}$ level of the ytterbium ion is efficiently populated by RET from the quinolinolato ligand.

Photophysical properties of **1** in different matrices are summarized in Table 2.

To go deeper into the ligand-to-metal energy transfer mechanism and clarify if its efficiency is maintained when incorporating **1** into the silica matrix, combined transient PL and excited state absorption (ESA) experiments with subpicosecond photoexcitation in the fundamental absorption band of the ligand have been performed. The obtained results are summarized in Fig. 5 and time constants of ligand emission dynamics and excited state kinetics are reported in Table 3.

Transient PL data are spectrally integrated over the excited singlet fluorescence emission spectrum (470–570 nm spectral window). As shown in Fig. 5a, singlet excited state decay is bi (tri)-exponential in the doped sol–gel glass (MeCN–EtOH solution) sample and is dominated by ultrafast components yielding time constants of the order of tens of ps (Table 3). These findings are in agreement with values previously found for **1** in DMSO solution and as a crystalline sample²⁴ as well as for analogous erbium quinolinolates,¹¹ suggesting that ligand singlet states are strongly deactivated by intersystem-crossing (ISC) to ligand excited triplet states favoured by the presence of the heavy lanthanide ion (heavy-atom effect). A 10% signal fraction

Table 2 Photophysical parameters of **1** in different matrices

Matrix	$\tau_{\text{obs}}/\mu\text{s}$	$\tau_{\text{rad}}/\mu\text{s}$	Φ_{tot} (%)	η_{sens} (%)
MeCN–EtOH solution	0.85(1) (~50%), 2.51(1) (~50%); av. 1.9(1)	440(20)	0.30(6)	70(20)
DMSO solution ²⁴	7.85(1)	690(35)	1.40(30)	95(5) ^a
Doped sol–gel glass	0.63(1) (~50%), 3.69(1) (~50%); av. 2.4(1)	—	—	—
Solid state (crystals) ²⁴	7.10(1)	—	—	—

^a Lies within the error bar of the calculated value: 120(30)%.

of excited singlets in **1**-doped sol–gel decays with a time constant $\tau_2 = \sim 2$ ns. This value is consistent to that observed (8.5 ns) for tris(8-quinolinolato)aluminium(III) (AlQ_3), where the heavy-atom effect is negligible, suggesting that this slower singlet decay component may originate from a small fraction of dissociated ligands dispersed in the silica matrix.¹¹ This fraction appears to be negligible in MeCN–EtOH solution, where the long-lived signal amplitude is as small as 0.3%.

Singlet and triplet dynamics have then been determined from transient absorption signals probed by differential transmission ($-\Delta T/T$) in the 600–620 nm spectral range (Fig. 5b). Curve fitting of the measured excited state kinetics confirms that singlet deactivation (SD, dashed curves in Fig. 5b) occurs on an ultrafast timescale, with decay time as fast as 5 ps in MeCN–EtOH solution (Table 3).

For both samples, triplet population shows ultrafast activation (TA) with time constants (τ_{TA}) that are inferred to be equal to singlet decay times. Curve fitting yields triplet lifetimes (τ_{TD} , Table 3) of the order of hundreds of ps that are in agreement with previous reports for erbium quinolinolates (80–100 ps), and much shorter than the value found for a gadolinium quinolinolate analogue (~ 1.4 ns),¹¹ where no ligand-to-metal energy transfer can occur due to the high energy of the Gd^{3+} first excited state.⁴⁷ These findings clearly point out that ligand excited triplets are effectively deactivated through resonant energy transfer to ytterbium upper levels. Other mechanisms, such as photo-sensitization through internal redox processes⁴⁸ or phonon-assisted energy transfer,⁴⁹ that are often invoked to account for ytterbium sensitization, seem to be less likely.

Deconvolution of the excited state absorption (ESA) experimental curve for the doped glass gives an estimated $\sim 85\%$ of excited triplets that are likely to efficiently feed ytterbium upper levels (long-dashed black curve in Fig. 5b, left panel). Bearing in mind that 90% of excited singlets decay to triplet states, these outcomes suggest that the ligand-to-metal energy transfer efficiency (η_{sens}) in **1**-doped sol–gel glass can be estimated to be as high as 70–80%, in close agreement with value calculated through eqn (1) for MeCN–EtOH solution.

We can definitely conclude that the emissive properties of **1** are preserved in the doped sol–gel glass that shows dual emission in the visible (ligand-centered) and in the NIR (metal-centered) upon antenna sensitization in the near-UV. The close similarity of spectroscopic profiles and photophysical properties of the **1**-doped sol–gel glass compared to a solution of **1** in the same solvent mixture used for the preparation of the glass

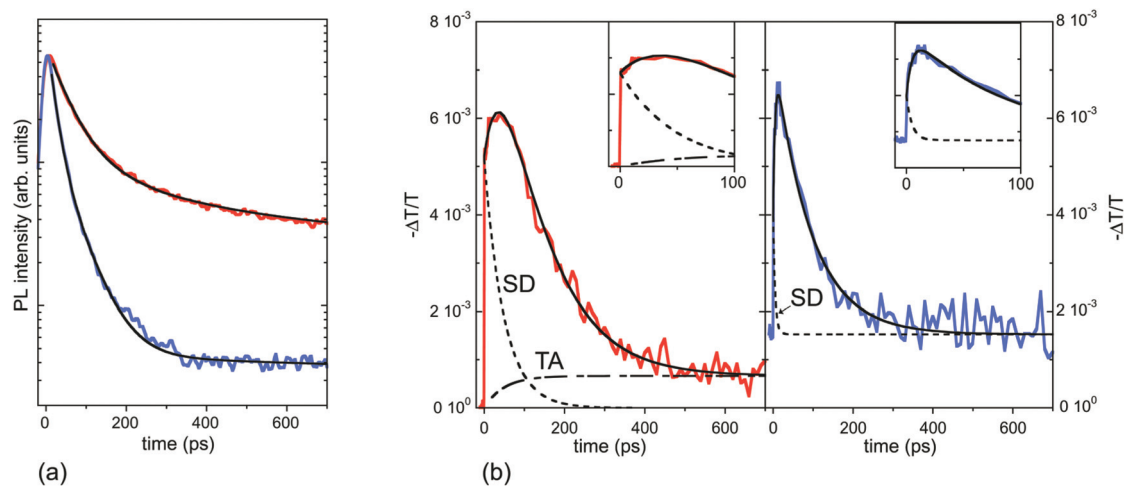


Fig. 5 (a) Transient photoluminescence of **1** in sol-gel glass (red line) and in MeCN-EtOH solution (blue line). The signal is reported on a logarithmic scale. Black solid curves are the best fit based on a bi-exponential (sol-gel glass) and tri-exponential (MeCN-EtOH solution) decay curve. (b) Transient photoinduced absorption of **1**-doped sol-gel glass (red, left) and of **1** in MeCN-EtOH solution (blue, right). Black short-dashed lines represent singlet decay components. Black long-dashed line in the left panel represents a population of long-lived triplets not involved in Yb³⁺ sensitization. In MeCN-EtOH solution, a steady-state ESA signal is found, which we trace back to triplet accumulation in dissociated ligands. This signal is also represented by the short-dashed line after singlet decay. In the insets signals are reported on the 0–100 ps timescale.

Table 3 Time constants of ligand dynamics for **1** in different matrices

Matrix	Transient PL τ /ps	ESA	
		τ_{SD} ($= \tau_{TA}$)/ps	τ_{TD} /ps
MeCN-EtOH solution	$\tau_1 < 30^a$ (85%), $\tau_2 = 52$ (15%), $\tau_3 = 5000$ (0.3%)	5	90
Doped sol-gel glass	$\tau_1 = 49$ (90%), $\tau_2 = 2100$ (10%)	49	108

^a Constant determination is resolution limited.

sample suggests that the silica matrix does not significantly affect the optical properties of the complex. The glass material, that is optically transparent, can then be considered a “solid-state solution” in which the dopant lanthanide complex is homogeneously dispersed and clustering effects that can be detrimental for the optical properties are avoided.

Conclusions

[Yb(5,7ClQ₂)(H5,7ClQ₂)₂Cl] has been selected as a prototype complex to be used as dopant in sol-gel glasses in view of the extensive knowledge available on its structure-properties relationship. Our efforts are aimed at obtaining a suitable optical material for future practical applications and for a full study of its photophysical properties in comparison with those observed for the same complex in solution or in the solid state.

It has been confirmed that the selected processing of doped glasses, based on the convenient sol-gel method, offers several advantages over the traditional melt preparation. Given that this method is a solution process, formation of the matrix can lead to a high concentration of dopant without loss of amorphous character, as demonstrated by XRD/TEM characterization. Moreover, the preparation of the sol-gel glass can be carried out under mild

conditions (temperature, pH) avoiding decomposition/degradation of the dopant complex. The obtained doped material is optically transparent and homogeneous and exhibits good mechanical strength. Optical properties achievable in sol-gel materials include graded refractive indexes, waveguiding, chemical sensing, optical amplification, frequency doubling, and lasing.⁵⁰

The obtained doped sol-gel glass can be considered a “solid state solution” whose spectroscopic and photophysical properties are very close to those observed in the precursor MeCN-EtOH solution. NIR decay times are in the μ s range and are likely limited by the presence of some residual OH quencher groups in both (silica glass and solvent) the host matrices. The ligand-to-metal sensitization efficiency has been determined to be as high as 80% in MeCN-EtOH solution and combined transient PL and ESA experiments allow estimating that the effectiveness of this mechanism is maintained in the doped sol-gel glass. It has been confirmed that ligand-to-metal energy transfer involves the triplet states of the ligand and that ISC and RET from ligand triplet states to metal occur on an ultrafast timescale.

It is worth remarking that the ytterbium radiative lifetime observed in MeCN-EtOH solution is the shortest ever reported so far and is significantly shorter (37%) than the value found for **1** in other solvents such as DMSO, indicating a strong solvent effect. This outcome dramatically points out that the correct assessment of the photophysical properties of luminescent lanthanide complexes with antenna ligands is crucially dependent on the experimental determination of photophysical parameters case by case.

These results seem encouraging since they demonstrate that photophysical properties of NIR emitting lanthanide compounds are entirely maintained when they are incorporated into silica sol-gel glasses. This study opens new perspectives into the development of optical materials based on luminescent lanthanide complexes and further work will be addressed to the design and selection of suitable precursors for the preparation and processing of these materials to improve their properties.

Acknowledgements

The Regione Autonoma della Sardegna is gratefully acknowledged for financial support through POR Sardegna FSE 2007–2013, L.R.7/2007 “Promozione della ricerca scientifica e dell’innovazione tecnologica in Sardegna” (Research Project: “Complessi di lantanidi con proprietà di luminescenza nel vicino infrarosso: studio della correlazione struttura/proprietà fotofisiche indirizzato alla fotonica molecolare” (CRP-17571) and Cofinanced Research Grant “Giovani Ricercatori” of F. Artizzu: “Complessi di lantanidi come materiali luminescenti per applicazioni in fotonica” (CRP2_502)). Thanks are due to Dr Salvatore Bullita for acquiring TEM images and to Dr Mauro Aresti and for technical support.

References

- 1 R. J. Curry and W. P. Gillin, *Appl. Phys. Lett.*, 1999, **75**, 1380.
- 2 W. P. Gillin and R. J. Curry, *Appl. Phys. Lett.*, 1999, **74**, 798.
- 3 O. M. Khreis, R. J. Curry, M. Somerton and W. P. Gillin, *J. Appl. Phys.*, 2000, **88**, 777.
- 4 O. M. Khreis, W. P. Gillin, M. Somerton and R. J. Curry, *Org. Electron.*, 2001, **2**, 45.
- 5 R. J. Curry and W. P. Gillin, *Synth. Met.*, 2000, **111–112**, 35.
- 6 R. J. Curry, W. P. Gillin, A. P. Knights and R. Gwilliam, *Opt. Mater.*, 2001, **17**, 161.
- 7 Z. R. Hong, C. J. Liang, R. G. Li, D. Zhao, D. Fan and W. L. Li, *Thin Solid Films*, 2001, **391**, 122.
- 8 Z.-F. Chen, X.-Y. Song, Y. Peng, X. Hong, Y.-C. Liu and H. Liang, *Dalton Trans.*, 2011, **40**, 1684.
- 9 Y. Kawamura, Y. Wada, M. Iwamuro, T. Kitamura and S. Yanagida, *Chem. Lett.*, 2000, 280.
- 10 F. Artizzu, M. L. Mercuri, A. Serpe and P. Deplano, *Coord. Chem. Rev.*, 2011, **255**, 2514, and references therein.
- 11 F. Quochi, M. Saba, F. Artizzu, M. L. Mercuri, P. Deplano, A. Mura and G. Bongiovanni, *J. Phys. Chem. Lett.*, 2010, **1**, 2733.
- 12 (a) M. Iwamuro, T. Adachi, Y. Wada, T. Kitamura and S. Yanagida, *Chem. Lett.*, 1999, 539; (b) M. Iwamuro, T. Adachi, Y. Wada, T. Kitamura, N. Nakashima and S. Yanagida, *Bull. Chem. Soc. Jpn.*, 2000, **73**, 1359.
- 13 (a) J. Thompson, R. I. R. Blyth, G. Gigli and R. Cingolani, *Adv. Funct. Mater.*, 2004, **14**, 979; (b) R. I. R. Blyth, J. Thompson, Y. Zou, R. Fink, E. Umbach, G. Gigli and R. Cingolani, *Synth. Met.*, 2003, **139**, 207.
- 14 A. Nonat, D. Imbert, J. Pécaut, M. Giraud and M. Mazzanti, *Inorg. Chem.*, 2009, **48**, 4207.
- 15 N. M. Shavaleev, R. Scopelliti, F. Gumy and J.-C. G. Bünzli, *Inorg. Chem.*, 2009, **48**, 2908.
- 16 G. F. de Sà, O. L. Malta, C. de Mello Donegá, A. M. Simas, R. L. Longo, P. A. Santa-Cruz and E. F. da Silva, *Coord. Chem. Rev.*, 2000, **196**, 165.
- 17 N. Sabbatini, M. Guardigli and J.-M. Lehn, *Coord. Chem. Rev.*, 1993, **123**, 201.
- 18 J. M. Lehn, *Angew. Chem., Int. Ed. Engl.*, 1990, **29**, 1304.
- 19 (a) R. Van Deun, P. Fias, P. Nockemann, A. Schepers, T. N. Parac-Vogt, K. Van Hecke, L. Van Meervelt and K. Binnemans, *Inorg. Chem.*, 2004, **43**, 8461; (b) R. Van Deun, P. Fias, P. Nockemann, K. Van Hecke, L. Van Meervelt and K. Binnemans, *Eur. J. Inorg. Chem.*, 2007, 302; (c) R. Van Deun, P. Fias, K. Driesen, K. Binnemans and C. Görller-Walrand, *Phys. Chem. Chem. Phys.*, 2003, **5**, 2754.
- 20 F. Artizzu, P. Deplano, L. Marchiò, M. L. Mercuri, L. Pilia, A. Serpe, F. Quochi, R. Orrù, F. Cordella, F. Meinardi, R. Tubino, A. Mura and G. Bongiovanni, *Inorg. Chem.*, 2005, **44**, 840.
- 21 F. Artizzu, P. Deplano, L. Marchiò, M. L. Mercuri, L. Pilia, A. Serpe, F. Quochi, R. Orrù, F. Cordella, M. Saba, A. Mura and G. Bongiovanni, *Adv. Funct. Mater.*, 2007, **17**, 2365.
- 22 H. He, L. Si, Y. Zhong and M. Dubey, *Chem. Commun.*, 2012, **48**, 1886.
- 23 F. Quochi, R. Orrù, F. Cordella, A. Mura, G. Bongiovanni, F. Artizzu, P. Deplano, M. L. Mercuri, L. Pilia and A. Serpe, *J. Appl. Phys.*, 2006, **99**, 053520.
- 24 F. Artizzu, F. Quochi, M. Saba, L. Marchiò, D. Espa, A. Serpe, A. Mura, M. L. Mercuri, G. Bongiovanni and P. Deplano, *ChemPlusChem*, 2012, **77**, 240.
- 25 F. Quochi, F. Artizzu, M. Saba, F. Cordella, M. L. Mercuri, P. Deplano, M. A. Loi, A. Mura and G. Bongiovanni, *J. Phys. Chem. Lett.*, 2010, **1**, 141.
- 26 R. Reisfeld, T. Saraidarov, M. Pietraszkiewicz and S. Lis, *Chem. Phys. Lett.*, 2001, **349**, 266.
- 27 (a) K. Binnemans, *Chem. Rev.*, 2009, **109**, 4283, and references available therein (b) F. Wu, D. Machewirth, E. Snitzer and G. H. Sigel, *J. Mater. Res.*, 2011, **9**(10), 2703; (c) F. Wu, G. Puc, P. Foy, E. Snitzer and G. H. Sigel Jr, *Mater. Res. Bull.*, 1993, **28**, 637; (d) A. Polman, D. C. Jacobson, D. J. Eaglesham, R. C. Kistler and J. M. Poate, *J. Appl. Phys.*, 1991, **70**, 3778; (e) M. J. Weber, *J. Non-Cryst. Solids*, 1990, **123**, 208.
- 28 (a) P. Judeinstein and C. Sanchez, *J. Mater. Chem.*, 1996, **6**, 511; (b) J. Portier, J.-H. Choy and M. A. Subramanian, *Int. J. Inorg. Mater.*, 2001, **3**, 581.
- 29 K. Machida, H. Li, D. Ueda, S. Inoue and G. Adachi, *J. Lumin.*, 2000, **87–89**, 1257.
- 30 (a) H. Li, S. Inoue, K. Machida and G. Adachi, *Chem. Mater.*, 1999, **11**, 3171; (b) M. Lal, S. Pakatchi, G. S. He, K. S. Kim and P. N. Prasad, *Chem. Mater.*, 1999, **11**, 3012; (c) M. Zayat, R. Pardo and D. Levy, *J. Mater. Chem.*, 2003, **13**, 2899; (d) P. Lenaerts, A. Storms, J. Mullens, J. D’Haen, C. Görller-Walrand, K. Binnemans and K. Driesen, *Chem. Mater.*, 2005, **17**, 5194; (e) A. P. Otto, K. S. Brewer and A. J. Silversmith, *J. Non-Cryst. Solids*, 2000, **265**, 176.
- 31 K. Binnemans, P. Lenaerts, K. Driesen and C. Görller-Walrand, *J. Mater. Chem.*, 2004, **14**, 191.
- 32 (a) H. Gershon, M. W. McNeil, S. G. Shulman and J. W. Parkes, *Anal. Chim. Acta*, 1972, **62**, 43; (b) F. Goldman and E. L. Wehry, *Anal. Chem.*, 1970, **42**, 1178.
- 33 R. Ballardini, G. Varani, M. T. Indelli and F. Scandola, *Inorg. Chem.*, 1986, **25**, 3858.
- 34 P. J. Giordano, S. M. Fredericks, M. S. Wrighton and D. L. Morse, *J. Am. Chem. Soc.*, 1978, **100**, 2257.
- 35 (a) H. Wang, G. Qian, M. Wang, J. Zhang and Y. Luo, *J. Phys. Chem. B*, 2004, **108**, 8084; (b) Y. Zhong, L. Si, H. He and A. G. Sykes, *Dalton Trans.*, 2011, **40**, 11389; (c) R. F. Ziessel, G. Ulrich, L. Charbonnière, D. Imbert, R. Scopelliti and J.-C. G. Bünzli, *Chem.–Eur. J.*, 2006, **12**, 5060; (d) E. G. Moore, J. Xu, S. C. Dodani, J. Jocher, A. D’Aléo, M. Seitz and K. N. Raymond, *Inorg. Chem.*, 2010, **49**, 4156.
- 36 H. He, A. G. Sykes, P. S. May and G. He, *Dalton Trans.*, 2009, 7454.
- 37 J.-C. G. Bünzli and C. Piguet, *Chem. Soc. Rev.*, 2005, **34**, 1048.
- 38 J.-C. G. Bünzli and C. Piguet, *Chem. Rev.*, 2002, **102**, 1897.
- 39 J.-C. G. Bünzli, A.-S. Chauvin, H. K. Kim, E. Deiters and S. V. Eliseeva, *Coord. Chem. Rev.*, 2010, **254**, 2623.
- 40 M. H. V. Werts, J. W. Verhoeven and J. W. Hofstraat, *J. Chem. Soc., Perkin Trans. 2*, 2000, 433.
- 41 R. F. Ziessel, G. Ulrich, L. Charbonnière, D. Imbert, R. Scopelliti and J.-C. G. Bünzli, *Chem.–Eur. J.*, 2006, **12**, 5060.
- 42 (a) M. H. V. Werts, R. T. F. Jukes and J. W. Verhoeven, *Phys. Chem. Chem. Phys.*, 2002, **4**, 1542; (b) S. I. Klink, L. Grave, D. N. Reinhoudt, F. C. J. M. Van Veggel, M. H. V. Werts, F. A. J. Geurts and J. W. Hofstraat, *J. Phys. Chem. A*, 2000, **104**, 5457.
- 43 S. J. Strickler and R. A. J. Berg, *Chem. Phys.*, 1962, **37**, 814.
- 44 N. M. Shavaleev, R. Scopelliti, F. Gumy and J.-C. G. Bünzli, *Inorg. Chem.*, 2009, **48**, 7937.
- 45 (a) T. Förster, *Discuss. Faraday Soc.*, 1959, **27**, 7; (b) T. Förster, *Ann. Phys.*, 1948, **437**, 55 (English translation, 1993).
- 46 The total quantum yield was measured by using DMSO solutions of **1** and of the isostructural erbium complex [Er(5,7ClQ)₂(H5,7ClQ)₂Cl] ($\Phi_{\text{tot}} = 0.038\%$) as suitable references. For the latter case, quantum yield has been reliably experimentally determined by the relative method using tris(2,2'-bipyridyl)ruthenium(II) Ru(bipy)₃²⁺; 2.40×10^{-3} M) in deaerated water as the referencestandard ($\Phi_{\text{tot}} = 4.2\%$, $\tau = 0.58$ μs), as described in ref. 25. Appropriate corrections to detector spectral response have been applied to account for different emission spectral ranges.
- 47 A. Strasser and A. Vogler, *Inorg. Chim. Acta*, 2004, **357**, 2345.
- 48 (a) W. D. Horrocks Jr., J. P. Bolender, W. D. Smith and R. M. Supkowski, *J. Am. Chem. Soc.*, 1997, **119**, 5972; (b) Y. Zhong, L. Si, H. He and A. G. Sykes, *Dalton Trans.*, 2011, **40**, 11389.
- 49 C. Reinhard and H. U. Güdel, *Inorg. Chem.*, 2002, **41**, 1048.
- 50 V. C. Costa, M. J. Lochhead and K. L. Bray, *Chem. Mater.*, 1996, **8**, 783.

Supplementary Information

Silica sol-gel glasses incorporating dual-luminescent Yb quinolinolato complex: processing, emission and photosensitising properties of the 'antenna' ligand

Flavia Artizzu,^{*a} Francesco Quochi,^b Michele Saba,^b Danilo Loche,^a Maria Laura Mercuri,^a Angela Serpe,^a Andrea Mura,^b Giovanni Bongiovanni^b and Paola Deplano^{*a}

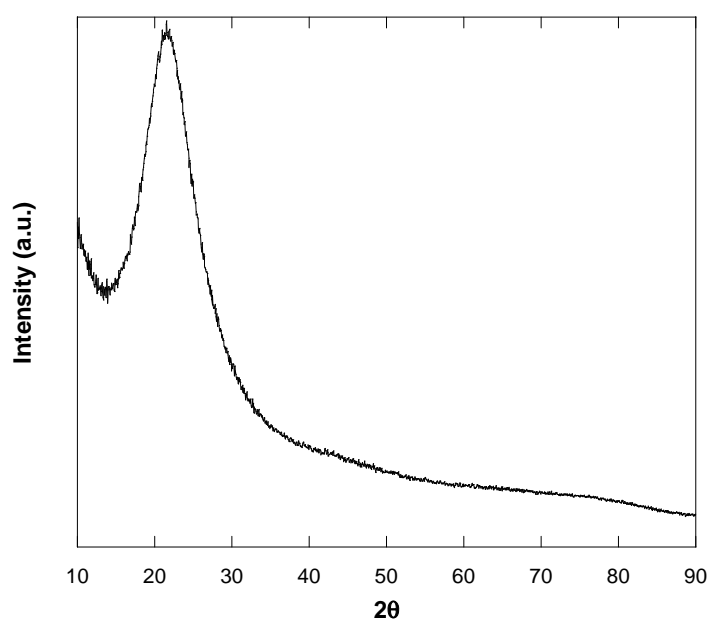


Figure S11. XRD patterns for the **1**-doped sol-gel glass, showing the amorphous silica haloes.

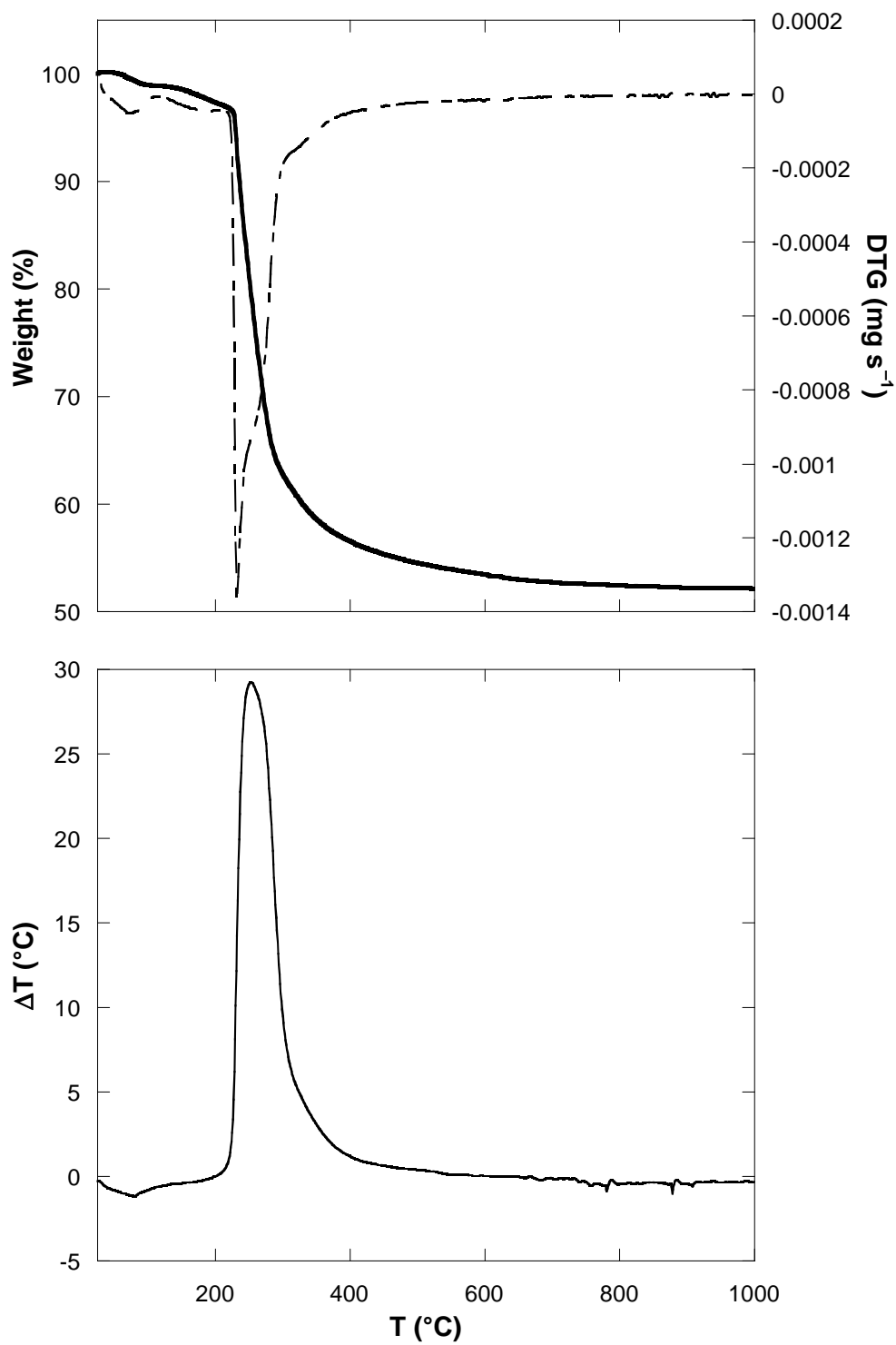


Figure SI2. TG (solid line) and DTG (dotted line) curves (top) and corresponding DTA (bottom) of **1**-doped sol-gel glass.

Evaluation of ytterbium radiative lifetime in **1** in CH₃CN/EtOH solution.

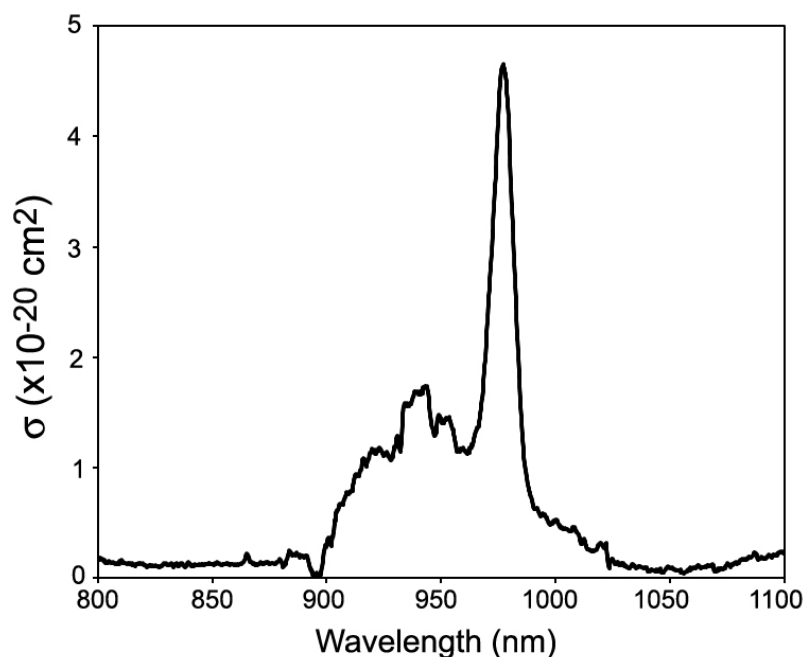


Figure SI3. Ytterbium absorption cross-section for **1** in CH₃CN/EtOH solution

Strickler-Berg Equation:

$$\tau_{\text{rad}}^{-1} = 8\pi n^2 c \frac{1}{\lambda_{\text{em}}^3} \frac{2J + 1}{2J' + 1} \int \frac{\sigma_{\text{Yb}}(\lambda)}{\lambda} d\lambda$$

where n is the refractive index of the medium ($n=1.35$ for CH₃CN/EtOH 1:1 solvent mixture), c is the speed of light in vacuum and J, J' refer to the ground and excited state respectively ($J=7/2; J'=5/2$). λ_{em}^3 is mediated over the Yb emission spectrum. σ_{Yb} is the ytterbium absorption cross-section (see Figure SI3). $\sigma_{\text{Yb}977} = 4.74 \cdot 10^{-20} \text{ cm}^2$.

Conclusions and Perspectives

Light Conversion Processes in Lanthanide-based Materials

1. Conclusions
2. Perspectives

1. Conclusions

Heterolanthanide coordination compounds are extremely promising materials with the potential of showing multi-functionality, depending on the nature of the Ln ions, of interest for several applications. The nature of the molecular edifice and structural arrangement, determines the interplay or coexistence of physical properties (related to the entity of metal separation) and applicative uses as bulk materials or single-molecules. Coordination compounds such as multi-dimensional frameworks, where Ln ions are randomly distributed over the available coordination sites, can best perform as “diluted” bulk materials where functionality results from a superposition of different properties related to non-interacting active metal centres. This kind of edifices have been successfully proposed as luminescent barcodes where tunability of emission lines can be achieved by varying the metal content. Conversely, discrete and rigid hetero-metallic molecules offer the potential advantage of controlling intermetallic communication (magnetic coupling, resonance energy transfer) between Ln ions sitting at short distance and in fixed positions in the same, solution-processable, molecular architecture. This latter point is of particular relevance for the development of optical materials such as waveguides and amplifiers working in the NIR, for which Er^{3+} emission through Yb^{3+} sensitization has been proposed as a convenient way to improve the figures of merit of erbium-based optical devices.

Spectroscopic and time-resolved studies on the heterolanthanide ErYb_2Q_9 complex, where the two optically-active Yb^{3+} and Er^{3+} ions are held at a intermetallic separation (<

3.5 Å) well below the Forster’s radius (10 Å), have provided evidence of direct Yb-to-Er resonance energy transfer (RET) with nearly unity efficiency at molecular level. Because Yb emission is so efficiently quenched by RET to Er, this process would likely not suffer from other competitive deactivating channels such as vibrational quenching by CH groups and even water molecules. These findings can suggest a relevant strategy for achieving effective erbium sensitization in polynuclear complexes, where the two metals lie at short distance in the same molecular structure.

As a progress of these studies, the full photocycle leading to narrow-band lanthanide emission in a series of heterolanthanide $\text{Er}_x\text{Yb}_{3-x}$ quinolinolato compounds, on variation of metal composition and molecular stoichiometry, has been investigated. Ligand-to-metal and metal-to-metal energy transfer processes occur with high efficiency in all the studied complexes. In particular, Yb-to-Er RET is quantitative (~100%).

Mixed Er/Yb compounds show simultaneous dual luminescence at 1 and 1.5 μm upon single-wavelength irradiation in the ligand lowest absorption band, as a result of the weighted contribution of the different hetero- and homometallic species in the samples. In fact, discrimination of Er^{3+} and Yb^{3+} ions is severely hampered by their close similarity of chemical behaviour and ionic radii. Therefore, statistical metal distribution over available alike coordination sites inevitably governs the synthesis of heterolanthanide Er/Yb compounds. This can certainly be advantageous when dealing with materials intended to be used as solid state broad-band emitters, as the spectral features can be finely modulated by tuning the molecular speciation simply on variation of the metal stoichiometry in the synthetic procedure.

Nonetheless, the strive for metal composition and speciation control at molecular level, aimed at obtaining purely heterometallic NIR-emissive compounds, can be effectively addressed through size discriminating effects when mixing a larger ion, such as Nd^{3+} , with smaller lanthanides, as Er^{3+} and Yb^{3+} . In this way, 90% control of molecular speciation can be achieved in Nd/Ln (Ln = Er, Yb) complexes, as observed when incorporating these ions in the trinuclear Ln_3Q_9 molecular framework. The trilanthanide $\text{Nd}_y\text{Er}_x\text{Yb}_{3-(x+y)}\text{Q}_9$ complex is the first example of a discrete molecular entity containing three different lanthanides simultaneously emitting in three different spectral regions in the NIR, ranging from 900 to 1600 nm, upon single wavelength excitation. Studies on Nd-to-Yb and Nd-to-Er energy transfer processes are currently in progress.

These findings open new perspectives for the control of intermetallic communication and tunability of physical properties in solution-processable functional molecular materials through a rational and easy-to-handle synthetic strategy. In this context, lanthanide-doped silica glasses, prepared through the mild sol-gel process in solution, are ideal candidates to prepare optical materials useful for practical applications such as, for example, optical waveguides and amplifiers. It has been shown that doped sol-gel glasses incorporating NIR-emitting lanthanide complexes can be considered as “solid state solutions” whose spectroscopic and photophysical properties are very close to those observed in the precursor solutions. This would be of particular importance for the development of NIR-emitting codoped Er/Yb materials, while taking advantage of the effective molecular approach for the control of light conversion processes in functional heterolanthanide assemblies.

2. Perspectives

One of the most enticing perspectives of this work relies on the investigation of NIR-emitting heterolanthanide complexes of high purity in regard to molecular speciation. A promising way to achieve this goal is definitely suggested by the experimental findings on the trimetallic $\text{Nd}_y\text{Er}_x\text{Yb}_{3-(x+y)}\text{Q}_9$ complex, which have evidenced that the Nd^{3+} ion can effectively template the synthesis of trinuclear quinolinolate complexes. The additional benefit is that Nd^{3+} is a potential good sensitizer toward both Yb^{3+} and Er^{3+} . As Nd^{3+} possesses several absorption lines spanning throughout the visible region, this would be particularly advantageous for convenient non-resonant optical pumping of the Yb $^4\text{F}_{7/2}$ - $^4\text{F}_{5/2}$ quasi two-level system. Yb emission would in fact be achieved by indirect excitation of the Nd $^4\text{F}_{3/2}$ - $^4\text{I}_{9/2}$ absorption band using the easily available high power 800 nm laser diode, while still ensuring a low quantum defect (i.e. low thermal energy dissipation). In heterolanthanide Nd-Yb complexes a “cascade” mechanism involving ligand-to-Nd and subsequent Nd-to-Yb energy transfer can be envisaged, leading to efficient Yb sensitization, as the energy gap between the ligand donating (triplet) level and the metal receiving levels is lowered with respect to homometallic Yb-complexes (Figure 1). Similar considerations also apply to Nd-Er systems.

The combination of the optical properties of Nd^{3+} with those of Yb^{3+} and Er^{3+} , represent a very promising strategy for the development of Yb-based lasers and optical amplifiers working at 1 μm , or for Er-based photonic devices for eye-safe emission at

1.5 μm . Besides these applications, multiband NIR emission can be achieved when combining these three lanthanide ions in the same assembly as in the $\text{Nd}_y\text{Er}_x\text{Yb}_{3-(x+y)}\text{Q}_9$ complex.

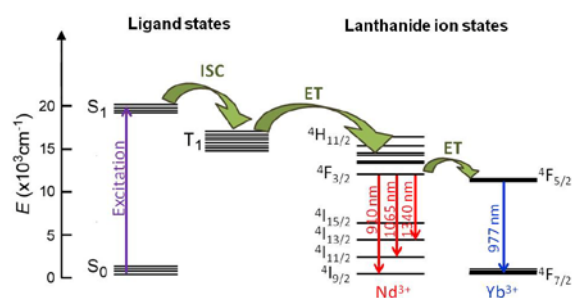


Figure 1. Jablonski diagram depicting the “cascade” mechanism of ligand-to-metal energy transfer in a Nd-Yb complex. ISC = intersystem crossing; ET = energy transfer.

In the light of these considerations, the NdYb_2Q_9 and NdEr_2Q_9 complexes are excellent candidates to investigate Nd-to-Yb and Nd-to-Er energy transfer mechanisms, whose understanding is crucial for the advancement of potential applications. This would also significantly extend the scientific literature on heterolanthanide assemblies as very rare reports can be found so far on this subject.

